

**Flow in naturally deformed ice: a
cryogenic electron microscopy and
modelling study of
the NEEM ice core**

E. N. Kuiper

**Utrecht Studies in Earth Sciences
No. 170**

Members of the dissertation committee:

Prof. dr. N. Azuma

Dept. of Mechanical Engineering, Nagaoka University of Technology
Nagaoka, Japan

Prof. dr. P. Bons

Dept. of Geosciences, Eberhard Karls University Tübingen
Tübingen, Germany

Prof. dr. D. Dahl-Jensen

Niels Bohr institute, Ice and Climate Research, University of Copenhagen
Copenhagen, Denmark

Dr. L. Hansen

Dept. of Earth Sciences, Oxford University
Oxford, United Kingdom

Prof. dr. C. Spiers

Dept. of Earth Sciences, Utrecht University
Utrecht, The Netherlands

This research was carried out at:

Dept. of Earth Sciences, Utrecht University
Princetonlaan 8a, 3584 CB, Utrecht
The Netherlands

Alfred Wegener Institute, Helmholtz Centre for Polar and Marine Research
Am Alten Hafen 26, 27568, Bremerhaven
Germany

ISBN/EAN: 978-90-6266-524-2

Copyright © 2018 Ernst-Jan Nicolaas Kuiper

All rights reserved. No part of this publication may be reproduced in any form, by print or photo print, microfilm or any other means, without written permission by the publishers.

Printed by: Gildeprint - Enschede

Flow in naturally deformed ice: a cryogenic EBSD and modelling study of the NEEM ice core

Vloei van natuurlijk gedefformeerd ijs: een cryogene EBSD- en modelleerstudie van de NEEM ijskern
(met een samenvatting in het Nederlands)

Proefschrift

ter verkrijging van de graad van doctor aan de Universiteit Utrecht op gezag van de rector magnificus, prof.dr. H.R.B.M.

Kummeling, ingevolge het besluit van het college voor promoties in het openbaar te verdedigen op vrijdag 1 februari 2019 des middags te 2.30 uur

door

Ernst-Jan Nicolaas Kuiper

geboren op 26 april 1988 te Rheden

Promotoren: Prof. dr. J. H. P. de Bresser
Prof. dr. M. R. Drury

Copromotoren: Dr. G. M. Pennock
Dr. I. Weikusat

This thesis was accomplished with financial support from the Alfred-Wegener-Institute, Helmholtz-Center for Polar- and Marine Research in the framework of the Helmholtz Junior Research group ‘The effect of deformation mechanisms for ice sheet dynamics’.

“Oud ijs glijdt beter”

Contents

Abstract	11
Chapter 1	
Introduction	13
1.1 Summary of thesis	14
1.2 General Background	15
1.2.1 Ice sheets and sea level rise	15
1.2.2 Ice in polar ice sheets	16
1.2.3 The ice single crystal.....	19
1.2.4 Recovery, recrystallization and grain growth in ice.....	20
1.2.5 The creep of polycrystalline ice	23
1.2.6 Subgrain boundaries in ice	24
1.2.7 Ice flow laws and deformation mechanisms	25
1.2.8 The NEEM ice core	28
1.2.9 Cryogenic EBSD	30
1.2.10 Flow law modelling.....	31
1.3 Scope and outline of the thesis	31
References	33
Chapter 2	
EBSD analysis of subgrain boundaries and dislocation slip systems in Antarctic and Greenland ice	41
Abstract	42
2.1 Introduction	43
2.2 Material and Methods	46
2.3 Results	48
2.3.1 Subgrain boundary types.....	48
2.3.2 Misorientation angle range used for subgrain boundaries using EBSD.....	49
2.3.3 Analysis of subgrain boundary types.....	49
2.3.3.1 Subgrain boundary traces	50
2.3.3.2 Subgrain boundary rotation axes.....	50
2.3.3.3 Combination of subgrain boundary traces and rotation axes.....	50
2.4 Discussion	52
2.4.1 CPO and dislocation creep.....	52
2.4.2 Subgrain boundaries controlled by and geometrically related to host grain crystallography	52
2.4.3 Implications on the origin of non-basal dislocations from extended dislocations	57
2.4.4 Subgrain boundaries without connection to host grain crystallography.....	59
2.4.5 Implications of SGB type and creep rate-control	60
2.5 Conclusions	61
References	62

Chapter 3

Variation in non-basal slip activity controlled by strain induced

boundary migration in the NEEM deep ice core, Greenland	71
Abstract	72
3.1 Introduction	73
3.2 Background	76
3.3 Materials and methods	78
3.4 Results	82
3.4.1 Overview of microstructures	82
3.4.2 EBSD mapped microstructures	82
3.4.2.1 SGB misorientation angles	84
3.4.2.2 SGB rotation axes	84
3.4.2.3 SGB trace	87
3.4.2.4 Analysis of SGB types	87
3.4.2.5 Combination of possible slip system and misorientation angle	88
3.5 Discussion	88
3.5.1 General discussion of SGB statistics	88
3.5.1.1 Subgrain boundary misorientation angles	90
3.5.1.2 Rotation axes	92
3.5.1.3 Slip system analysis	93
3.5.2 Misorientation angle of not-classified SGBs	96
3.6 Conclusions	97
References	98

Chapter 4

Using a composite flow law to investigate the role of grain

size on the deformation of Holocene and glacial ice in the

NEEM deep ice core, Greenland	107
Abstract	108
4.1 Introduction	110
4.2 Methods	113
4.2.1 Study site and ice microstructure	113
4.2.2 The composite flow law	114
4.2.3 Boundary conditions and input data	117
4.3 Flow law parameters	120
4.4 Results	121
4.5 Discussion	124
4.5.1 Comparison of micro-scale constant stress versus micro-scale constant strain rate model	125
4.5.2 comparing grain size distribution model end members with the mean grain size model	126
4.5.3 Stress sensitivities	127
4.5.4 Variability of predicted strain rates with depth	129
4.5.5 Microstructural evidence and CPO development	130
4.5.6 Dominance of GBS-limited creep over dislocation creep	131
4.6 Conclusions	132
References	133

Chapter 5

Using a composite flow law to investigate the role of grain size and premelting on ice deformation at high homologous temperature in the lower part of the NEEM ice core, Greenland.

	141
Abstract	142
5.1 Introduction	143
5.2 Methods	145
5.2.1 The NEEM ice core and ice microstructure data	145
5.2.2 Flow laws and flow law parameters	147
5.3 Results	149
5.3.1 Ice microstructure in the Eemian-glacial facies	149
5.3.2 Correlation mean grain diameter with type and strength of CPO.....	150
5.3.3 Transition temperature: NEEM results compared to other polar ice cores	151
5.3.4 Calculated strain rates and deformation mechanisms	152
5.4 Discussion	154
5.4.1 The role of impurities in premelted ice	154
5.4.2 The effect of premelting on ice microstructure	156
5.4.3 Setting the temperature threshold for premelting	157
5.4.4 Recrystallization and deformation mechanisms in the Eemian-glacial facies	158
5.4.5 Strain localization in the Eemian-glacial facies	159
5.5 Conclusions	161
References	162

Chapter 6

Recrystallization and deformation mechanisms in the NEEM deep ice core, Greenland

	171
Abstract	172
6.1 Introduction	174
6.2 Background NEEM ice core	176
6.3 Materials and methods	177
6.4 Results	181
6.5 Discussion	185
6.5.1 Microstructures indicating recrystallization and deformation mechanisms	185
6.5.1.1 SIBM and island grains at shallow depths	185
6.5.1.2 Recrystallization of new grains along grain boundaries by grain boundary bulging and subgrain rotation.....	187
6.5.1.3 Microstructures indicating GBS-limited creep	187
6.5.1.4 Alignment of a-axes	190
6.5.1.5 Internal strain energy by geometrically necessary dislocations as driver for SIBM	191
6.5.2 Recrystallization and deformation mechanisms in the NEEM ice core	192
6.5.2.1 The Holocene ice.....	192
6.5.2.2 The glacial ice.....	194
6.5.2.3 The Eemian-glacial facies	195
6.5.3 Discrepancy between results of flow law modelling and microstructural analysis	196
6.6 Conclusions	198
References	199

Chapter 7

Summary and suggestions for further research

Summary	208
Introduction	208
Microstructural results.....	209
Results from flow law modelling.....	210
Synthesis of the recrystallization and deformation mechanisms in the NEEM ice core	212
Suggestions for further research	213
References	215
Nederlandse samenvatting.....	217
Introductie	217
Microstructuur resultaten	218
Resultaten modelleren van vloeiwetten.....	219
Synthese van de rekristallisatie- en vervormingsmechanismen in de NEEM ijskern.....	221
Appendices	
Appendix A: EBSD sample preparation from ice core sections.....	224
A1. Remarks and preparations.....	224
A2. Logging and cutting.....	224
A3. Preparing the thick section	225
A4. Large area scanning microscope.....	226
A5. Cutting EBSD samples	227
A6. Microtoming and sublimation	228
A7. LM scan of the EBSD samples	229
A8. Packing of the EBSD samples	229
A9. Transport of the EBSD samples.....	229
References	230
Appendix B: Cryo-EBSD on polar ice in a low pressure SEM	231
B1. Remarks and preparations.....	231
B2. Installing the cryo-stage and cooling down the system.....	231
B3. Mounting the EBSD sample on the stub	232
B4. EBSD sample transfer to preparation chamber	233
B5. Sublimation and sample transfer to the SEM chamber	234
B6. SEM/EBSD work	235
B7. Removal of the EBSD sample and heating up the system	236
References	236
Appendix C: Terminologies describing ice microstructures in different fields ..	237
C1. Material science terminology	237
C2. Geological terminology	238
C3. Glaciology literature.....	239
References	241
Afterword/Acknowledgements	243
Curriculum Vitae	247
List of publications	249

Abstract

Understanding the flow of ice is essential to predict the contribution of the polar ice sheets to global mean sea level rise in the next decades and centuries. During this PhD project, the recrystallization and deformation mechanisms that govern the flow of ice were studied along the length of the North Greenland Eemian Ice Drilling (NEEM) ice core in northwest Greenland. Two methods were used during this study: (i) cryogenic electron backscatter diffraction (cryo-EBSD) in combination with (polarized) light microscopy and (ii) flow law modelling using two different flow laws for ice constrained by the actual temperature and grain size data from the NEEM ice core. The NEEM ice core was divided up into three depth intervals originating from different climatic stages that differ strongly in terms of impurity content, microstructure, deformation mode and temperature: the Holocene ice (0-1419 m of depth), the glacial ice (1419-2207 m of depth) and the Eemian-glacial facies (2207-2540 m of depth).

Microstructures indicate that the Holocene ice deforms by the easy slip system (crystallographic basal slip) accommodated by the harder slip systems (non-basal slip), also known as dislocation creep, and by recovery via strain induced boundary migration (SIBM), which removes dislocations and stress concentrations and allows further deformation to occur. The amount of non-basal slip that is activated is controlled by the extent of SIBM. The dominant recrystallization mechanisms in the Holocene ice are SIBM, bulging recrystallization and grain dissection in total leading to dynamic grain growth, with a contribution from normal grain growth in the upper 250 m. The strain rate variability with depth in the Holocene ice, estimated by flow law modelling, is low.

In contrast, the strain rate variability is relatively high in the glacial ice as a result of variability in grain boundary sliding (GBS) with depth that accommodates basal slip (GBS-limited creep). Grain boundary sliding in the glacial ice is particularly strong in fine grained sub-horizontal bands which contain many aligned grain boundaries. Subgrain boundaries (SGBs) form ahead of the aligned grain boundaries in these fine grained sub-horizontal bands and when a misorientation angle of 5.0° - 6.0° is reached, the SGB has rotated into a sliding boundary. Rotation recrystallization is more prominent, while SIBM is less important in the glacial ice compared to the Holocene ice.

The ice in the Eemian-glacial facies, which is affected by premelting along the grain boundaries, alternates between relatively fine grained glacial ice with a single maximum crystallographic preferred orientation (CPO) and very coarse grained Eemian ice with a partial girdle CPO. Due to the difference in grain size and CPO, it is argued that the glacial ice in the Eemian-glacial facies deforms almost entirely by GBS-limited creep in simple shear and at high strain rates, while the Eemian ice in the Eemian-glacial facies deforms at much lower strain rates in coaxial deformation with a roughly equal contribution of GBS-limited creep and dislocation creep to bulk strain rate. The large difference in

microstructure, and consequently viscosity, between impurity-rich glacial ice and impurity-depleted interglacial ice in the premelting layer ($262\text{K} < T < 273\text{K}$) of polar ice sheets can have important consequences for ice dynamics close to the bedrock, which provides the major contribution of the horizontal movement of ice towards the oceans.

Glen's flow law (Glen, 1955; Paterson, 1994), which is independent of grain size, predicts a higher strain rate along the NEEM ice core than the grain size sensitive composite flow law of Goldsby and Kohlstedt (1997, 2001) for which the flow law parameters of the dislocation creep mechanism were modified during this PhD project. Only a grain size sensitive flow law can predict the variability in strain rate resulting from a variability in grain size with depth, which is expected to be large in the NEEM ice core.

Chapter 1

Introduction

1.1 Summary of thesis

As a consequence of anthropogenic global warming, the Greenland and Antarctic ice sheets are expected to lose mass in the coming decades and centuries, resulting in global mean sea level (GMSL) rise. Despite extensive research, the projections of future GMSL rise are still highly uncertain, varying from a few decimetres to more than two meters by 2100 (e.g. IPCC, 2014; DeConto and Pollard, 2016; Kopp et al. 2017). One of the uncertainties in GMSL predictions is the flow of ice in polar ice sheets (Vaughan and Arthern, 2007). Near the margins of the ice sheets, ice moves mainly by sliding over the bedrock (e.g. Zwally et al., 2002; Vaughan and Arthern, 2007; Krabbendam, 2016), while in the central part of the ice sheets flow is mainly controlled by internal deformation of the ice (e.g. Duval et al., 1983; Schulson and Duval, 2009; Faria et al., 2014a).

When modelling the evolution of polar ice sheets, the deformation of ice is often described in simple terms using Glen's flow law (section 1.2.7) (Glen, 1955; Paterson, 1994), which was derived at relatively high stresses and assumes that ice deforms by a single deformation mechanism, that is dislocation creep. However, ice microstructure studies have shown that, at the low stresses that occur in polar ice sheets, ice can deform by other deformation mechanisms such as a grain size sensitive mechanism (Goldsby and Kohlstedt, 1997, 2001; Cuffey et al., 2000) and basal slip accommodated by grain boundary migration (Pimienta and Duval, 1987; Duval et al., 2000; Montagnat and Duval., 2000). The question which deformation mechanism is active as a function of depth in polar ice sheets is still a topic of debate (e.g. Duval and Montagnat, 2002; Goldsby and Kohlstedt, 2002; Faria et al., 2014a). Each deformation mechanism responds differently to changes in boundary conditions such as temperature, deformation mode, grain size and driving stress and consequently each deformation mechanism requires its own flow law (Alley, 1992). The use of Glen's flow law to describe the flow of ice in polar ice sheets has proved to be inaccurate (Thorsteinsson et al., 1999; Huybrechts, 2007). Therefore, a full description of the microphysical processes that are active in polar ice sheets is required to improve or replace the ice flow laws that are used to model the evolution of polar ice sheets. The aim of this PhD project is to study the dominant recrystallization and deformation mechanisms in polar ice sheets and the effect these mechanisms may have on ice sheet flow laws and ice sheet dynamics.

Naturally deformed polar ice from the North Greenland Eemian Ice Drilling (NEEM) ice core in northwest Greenland was used to study ice recrystallization and deformation mechanisms. Two different methods were used in this PhD project to study ice recrystallization and deformation mechanisms in the NEEM ice core: (i) microstructural studies using cryogenic electron backscatter diffraction (cryo-EBSD) combined with (polarized) light microscopy (LM) techniques and (ii) flow law modelling using two different ice flow laws constrained with NEEM temperature and grain size data.

Cryo-EBSD provides full crystallographic information (c- and a-axes) at high resolution (micron scale). The method of Weikusat et al. (2011a) was used for preparing,

transporting and mapping of ice core sections in a scanning electron microscope (SEM) equipped with a cryo-stage and an EBSD detector (Appendix A and B). EBSD samples were prepared from ice core sections at different depths along the length of the NEEM ice core. The EBSD microstructures that were obtained were analyzed in terms of active recrystallization and deformation mechanisms and subgrain boundaries (SGBs) were analyzed in terms of possible slip system activity.

Flow law modelling, using Glen's flow law (Glen, 1955; Paterson, 1994) and the composite flow law of Goldsby and Kohlstedt (1997, 2001), was performed to study the strain rate predicted by the different flow laws and the effect of grain size on strain rate in the NEEM ice core. The grain size sensitive mechanism in the Goldsby and Kohlstedt (2001) flow law was applied using a mean grain size as well as a full grain size distribution (Freeman and Ferguson, 1986; Heilbronner and Bruhn, 1998; Ter Heege et al., 2004). The grain size distribution enabled the application of two different model end members: a micro-scale constant stress model, where each grain deforms by the same stress, and a micro-scale constant strain rate model, by which each grain deforms by the same strain rate but supports a different stress. In the lowest part of the NEEM ice core, where temperatures are just below the pressure-melting point, the grain size data were combined with crystallographic preferred orientation (CPO) data (Eichler et al., 2013) to study the effect of high temperatures and grain size on strain rate and CPO development.

The results of flow law modelling were combined with the results obtained by cryo-EBSD studies and previous work on ice microstructures in the NEEM ice core to infer which recrystallization and deformation mechanisms are active and at what depth these occur in the NEEM ice core. In what follows, a brief overview is given of the relevant background information regarding ice sheet dynamics, ice recrystallization and deformation mechanisms, the NEEM ice core and the methods used in this PhD project.

1.2 General Background

1.2.1 Ice sheets and sea level rise

GMSL rise in the coming decades and centuries will have a serious impact on coastal areas worldwide, including many densely populated metropolitan areas bordering the sea. Therefore, it is of high importance to accurately predict GMSL rise in order for governments to take appropriate precautions. According to the Intergovernmental Panel on Climate Change (IPCC), GMSL has risen by 0.19 m between 1901 and 2010 (IPCC, 2014). However, it is expected that, as a result of intensified anthropogenic global warming, GMSL rise will accelerate considerably in the next decades and centuries. The IPCC stated in their latest report (IPCC, 2014) that GMSL is expected to rise between 0.26 and 0.55 m for the lowest greenhouse gas emission scenario (RCP2.6) and between 0.45 and 0.82 m for the highest emission scenario (RCP8.5) by the year 2100. However, more recent studies, that include the complex dynamical response of the west Antarctic ice sheet, have shown that the polar ice sheets are likely to be much more vulnerable to global warming than previously thought (e.g. DeConto and Pollard, 2016; Hansen et al., 2016; Kopp et al.,

2017). It is therefore argued that GMSL level projections of the IPCC report have to be revised upward, since the studies used in the IPCC report did not include the full range of physical processes that are incorporated in the latest ice sheet models.

There are three main contributors to GMSL rise: i) ocean thermal expansion, ii) melting of non-polar glaciers and ice caps and iii) melting of the polar ice sheets. Although i) and ii) have been identified as the dominant contributor to GMSL rise during the twentieth century (IPCC, 2014), it is expected that the contribution of melting of the polar ice sheets to GMSL rise will increase considerably in the next decades and centuries. Furthermore, the potential GMSL rise from polar ice sheets is much larger than from non-polar glaciers and ice caps. GMSL will rise by about 0.5 meter if non-polar glaciers and ice caps are melted completely, whereas the potential GMSL rise of the Greenland and Antarctic ice sheet is about 7 and 61 meters, respectively (Church et al., 2013). The IPCC identified the contribution from polar ice sheets to GMSL rise as one of the key uncertainties in projections of global and regional climate change (IPCC, 2014).

The main components of the mass balance of an ice sheet are precipitation on the surface, solid water discharge via calving into the ocean and release of meltwater by runoff (Alley et al., 2005). Locally, sublimation or wind erosion can also be an important component in the mass balance of the Antarctic ice sheet (Bintanja, 2009). The melting of ice and calving of icebergs is mostly limited to a narrow margin at the edge of the ice sheet, which often meets with the ocean. Therefore, the transport of ice from the interior of the ice sheet to the margins of the ice sheet determines the volume of ice available for melting and calving. This transport depends on two mechanisms: sliding of the ice over the bedrock (e.g. Zwally et al., 2002; Vaughan and Arthern, 2007; Thoma et al., 2010; Wolovick et al., 2016) and the internal deformation of the ice sheet as a whole (e.g. Duval et al., 1983; Montagnat and Duval, 2000; Schulson and Duval, 2009; Faria et al., 2014a). Whereas sliding of ice over the bedrock is mostly limited to the margins of the ice sheet and ice streams (e.g. Krabbendam, 2016; Bons et al., 2018), internal deformation is the dominant mechanism in the interior of the ice sheet. In order to understand and describe the internal deformation of ice under different boundary conditions like stress, temperature and deformation mode, a full understanding of the microphysical processes in polar ice is required.

1.2.2 Ice in polar ice sheets

The ice in polar ice sheets and glaciers is formed by the compaction of snow at the surface. During each snow accumulation event the older snow layers experience a pressure increase which leads to sintering of the snow crystals with trapped air. This compacted snow layer is called firn. Gradually, the ice crystals in the firn layer grow and the porosity decreases. When a density of about 830 kg m^{-3} is reached, the air pores in the ice are no longer connected and form isolated bubbles (Cuffey and Paterson, 2010). The depth of this pore close-off varies between 50 and 150 m below the surface and typically takes several centuries to occur (Cuffey and Paterson, 2010). With increasing depth, the increase in overburden pressure causes the air bubbles to shrink. At a certain depth, the air bubble

pressure reaches a point where pressure-temperature conditions for the phase transition from air bubbles into clathrate hydrates is reached (e.g. Kipfstuhl et al., 2001). Below this depth, a transition zone exists where air bubbles and clathrate hydrates coexist. This depth range varies for different ice cores, but generally starts at 400-900 m and ends at 1200-1600 m of depth (e.g. Faria et al., 2014b). The transition zone is also known as the ‘brittle zone’ since the ice from this depth tends to crack when it is retrieved from the ice core after drilling (Gow, 1971).

The Greenland and Antarctic ice sheets consist of layers of snow that have been thinned and sintered into ice due to the overburden pressure in the upper part of the ice sheets. The ice in polar ice sheets can be hundreds of thousands of years old spanning multiple glacial cycles (e.g. EPICA community members, 2004). The temperature of the ice during deposition can be estimated using the oxygen stable isotope values ($\delta^{18}\text{O}_{\text{ice}}$) of H_2O , which give the ratio of ^{18}O over ^{16}O of the ice relative to a standard known ratio of ^{18}O over ^{16}O . Oxygen stable isotope values are a proxy for condensation temperature at the time of deposition (Dansgaard, 1964). Generally speaking, ice deposited during warm interglacial periods (high $\delta^{18}\text{O}_{\text{ice}}$ values) contains a lower concentration of impurities than ice deposited during the cold glacial periods (low $\delta^{18}\text{O}_{\text{ice}}$ values) (Dansgaard, 1964; Paterson, 1991).

The temperature of the ice in the upper part of the ice sheet is equal to the yearly average temperature at the surface of the ice sheet, which ranges from just below the melting point at the edges of the ice sheet to about -60°C in the coldest parts of the Antarctic ice sheet (e.g. Faria et al., 2014b). The temperature fluctuations caused by the different seasons and weather patterns penetrate only the upper couple of meters of the ice sheet. At a certain depth, which strongly depends on the location and the length of the ice core, the temperature starts to increase due to geothermal heat coming from the bedrock. The geothermal heat flux generally has a strength of about $50\text{-}100\text{ mW m}^{-2}$ (Rogozhina et al., 2016). Locally, heating caused by friction due to rapidly flowing ice (Krabbendam, 2016) or refreezing of meltwater coming from the surface that drained into the interior of the ice sheet (e.g. Zwally et al., 2002; Van de Wal et al., 2008; Catania and Neumann, 2010) can be important sources of heat near the bedrock as well. The temperature of the ice near the bedrock can reach pressure-melting point (e.g. Faria et al., 2014b), depending on the strength of the different heat sources.

The grain size in polar ice sheets depends on factors such as impurity content, stress, strain and strain rate (e.g. Paterson, 1991; Jacka and Li, 1994; Durand et al., 2006; Faria et al., 2014a, b). Many polar ice cores, where the grain size is measured along kilometres of ice core, have shown that the grain size varies considerably with depth (Faria et al., 2014b). The mean grain area increases linearly with depth from sub-millimetre size in the upper part of the ice sheet until a steady grain area of about ten to a few tens of mm^2 is reached at a couple of hundred meters of depth. Below this depth, the grain size varies strongly with impurity content. Even though the exact mechanisms are still unclear (Eichler et al., 2017), it is well accepted that impurities influence grain size as negative correlations between grain size and impurity content have been found in many different polar ice cores (Gow and Williamson, 1976; Lipenkov et al., 1989; Thorsteinsson et al., 1995; Gow et al.,

1997; Azuma et al., 1999, 2000; Durand et al., 2009; Weikusat et al., 2017). In general, ice deposited during interglacial periods has a relatively low impurity content and a relatively large grain size, whereas the ice deposited during glacial periods has a high impurity content and a relatively fine grain size. Near the bottom of the ice sheet, where temperatures are often high, grain boundary mobility increases and often grain areas reach many hundreds of mm^2 (e.g. Gow and Williams, 1976; Gow and Engelhardt, 2000; NEEM community members, 2013; Weikusat et al., 2017).

The flow patterns of ice in polar ice sheets is complex. Figure 1.1 shows a highly idealized cross section of a polar ice sheet showing the ice flow from the accumulation zone, where mass is gained by precipitation, to the ablation zone, where mass is lost by (subglacial) melting, calving and other processes. The shape and weight of the ice sheet induce stress by which the ice starts to deform plastically and flows towards the ablation zone near the edges of the ice sheet. The flow lines show that ice in the upper part of the ice sheet the ice deforms mainly by vertical compression and extension in the (sub)horizontal plane. Deeper down in the ice sheet, the ice increasingly starts to deform by simple shear parallel to the surface slope.

The shear stress in an ice sheet depends on the ice thickness and the surface slope and can be estimated using the shallow ice approximation (e.g. Hutter, 1983; Greve and Blatter, 2009) according to:

$$\tau = -\rho_{\text{ice}} z_{\text{ice}} g \frac{\partial h}{\partial x}, \quad (1.1)$$

where τ is the shear stress (Pa), ρ_{ice} is the density of ice (kg m^{-3}), z_{ice} is the ice thickness (m), g is the gravitational constant and $\frac{\partial h}{\partial x}$ is the surface slope in the direction of flow. The shear stress at ice domes and ice divides is less than 0.05 MPa, but shear stresses reach values of about 0.20-0.30 MPa in ice streams and outlet glaciers (Sergienko et al., 2014). In the lowest hundreds of meters of the polar ice sheets, the flow becomes more irregular caused by the increase in temperature, topographic constraints of the bedrock and sliding of

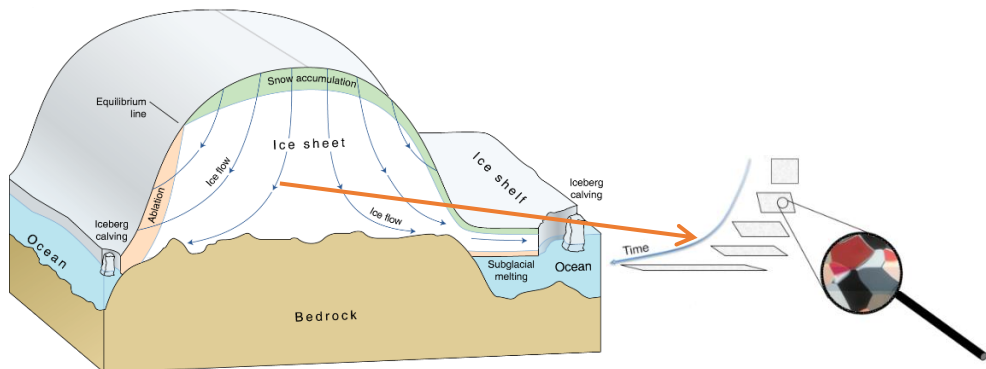


Figure 1.1: A cross section of a highly idealized ice sheet resting on the bedrock, showing the accumulation (green) and ablation (orange) zones, the equilibrium line separating the accumulation and ablation zone, the flow of ice in the ice sheet (flow lines), iceberg calving into the ocean, subglacial melting and on the right the deformation modes of the ice inside the ice sheet. Figure taken from <http://lima.nasa.gov/antarctica/>

the ice over the bedrock (e.g. Weertman, 1957; Vaughan and Arthern, 2007; Krabbendam, 2016).

1.2.3 The ice single crystal

The ice crystal lattice and its mechanical properties are central to the understanding of natural ice deformation. Although many different phases of ice have been identified so far (e.g. Schulson and Duval, 2009), hexagonal ice (I_h) is the only phase that is stable at pressure-temperature conditions on Earth's surface (from now on the term 'ice' refers to hexagonal ice, I_h , unless stated otherwise). The water molecule in the ice crystal lattice consists of one oxygen atom and two hydrogen atoms. The hydrogen atoms are bonded to the oxygen atom by covalent bonds. The two free electrons in the outer shell of the oxygen atom form relatively weak hydrogen bonds with the hydrogen atoms of other water molecules (Figure 1.2). Each oxygen atom is surrounded by four other oxygen atoms, two by a covalent bond and two by a hydrogen bond, to form a tetrahedron which is the essential unit of each lattice point in the ice crystal. These tetrahedrons organize themselves in a series of parallel planes, known as the basal plane (0001). The axis normal to the basal plane is known as the c-axis, [0001], and is the optical axis of the ice crystal. There are three identical axes on the basal plane which intersect at a 60° angle. These axes are known as the a-axes $\langle 1\bar{2}10 \rangle$.

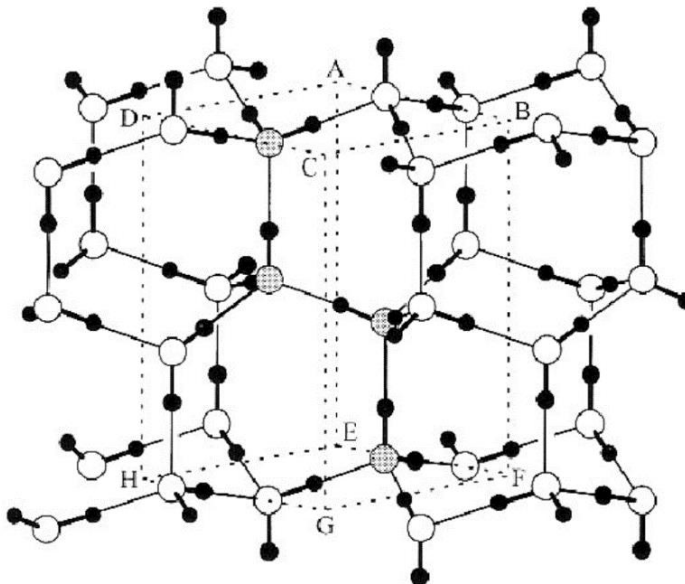


Figure 1.2: Crystal ice structure (I_h) with oxygen atoms (white) and hydrogen atoms (black) spheres. Covalent bonds are represented by a thick short black line and hydrogen bonds are represented by a long thin black line. The unit cell, containing four oxygen atoms, is indicated by the eight letters ABCDEFGH. Figure taken from Petrenko and Whitworth (1999).

Plastic deformation at low shear stresses in crystals occurs by the movement of dislocations through the crystal lattice. Dislocations are line defects which have two end members: edge dislocations and screw dislocations. Edge dislocations form extra half planes in a crystal (Figure 1.3a) and are defined by the Burgers vector being perpendicular to the dislocation line. Screw dislocations produce a rotation in the crystal (Figure 1.3b) and are defined by the Burgers vector being parallel to the dislocation line. More complex dislocations exist as a combination of edge and screw dislocations. Dislocations can move through the lattice, which produces slip of two parts of the lattice relative to each other, which results in deformation of the crystal.

In principle, dislocations can move by glide on any of the geometric planes in a crystal lattice and thereby plastically deform the crystal (Hirth and Lothe, 1982; Weertman and Weertman, 1992). However, the stress required to activate glide of dislocations along a certain geometric plane can vary strongly. In the case of ice, glide of dislocations along the basal plane (basal slip, Figure 1.4a) is at least 60 times easier to activate than glide of dislocations along one of the non-basal planes (Figure 1.4b-e) (Duval et al., 1983). The preferred glide of dislocations on different crystallographic planes is known as plastic anisotropy and this effect is very strong in the ice single crystal. Therefore, ice is considered as a good analogue for rock-forming minerals with strong plastic anisotropy deforming at high temperature ($T/T_{\text{melt}} > 0.85$) in the Earth's crust and mantle, such as quartz, feldspar, pyroxene, mica and olivine (e.g. Hobbs, 1985; Drury and Urai, 1990; Hirth and Kohlstedt, 1995; Neumann, 2000; Ji et al., 2002). Dislocations start to glide along crystallographic planes when the stress is equal or larger than the critical resolved shear stress. Each type of dislocation can move in a limited number of slip directions on a certain set of slip planes. The slip direction and slip plane together are known as a slip system. Dislocations tend to pile up at structures that form a barrier to glide such as dislocation walls, SGBs and grain boundaries.

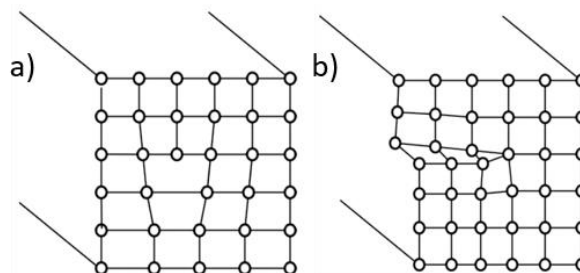


Figure 1.3: Cross section of (a) an edge dislocation and (b) a screw dislocation. For simplicity a cubic lattice is shown.

1.2.4 Recovery, recrystallization and grain growth in ice

Crystalline defects, like point defects, dislocations, SGBs and grain boundaries, store energy in the crystal lattice. The stored strain energy can be reduced by processes known as

recovery, recrystallization and grain growth. Recovery is the set of processes that decreases the total length of dislocations and rearrangement of dislocations into subgrain boundaries (Passchier and Trouw, 2005; Appendix C). Recrystallization is the reworking of the material with a change in grain size, shape, and orientation within the same mineral (Drury and Urai, 1990; Appendix C). The process of normal grain growth is the increase in crystal size that tends to lower the internal interfacial energy of a grain aggregate (e.g. Passchier and Trouw, 2005). The activity of these processes varies with depth in polar ice sheets, which leads to different ice microstructures with depth.

Dislocations and other crystalline defects form in response to a differential stress and store strain energy in the crystal lattice. The total length of dislocations per unit volume in a polycrystal is known as the dislocation density. Recovery can reduce the stored strain energy produced by thermomechanical processes. Recovery during deformation is known as dynamic recovery, while the term static recovery is used for recovery after deformation (Appendix C). As a result of recovery, dislocations organize into SGBs. The formation of SGBs by recovery of dislocations is known as polygonization (Appendix C). If a SGB is formed by polygonization (Section 1.2.6) and information on the rotation axis and the trace orientation in the host grain (trace) is known, the type of dislocations and slip systems involved in the formation of the SGB can be inferred (e.g. Trepied et al., 1980; Neumann, 2000; Weikusat et al., 2011a).

In addition to recovery, the stored strain energy caused by deformation can further be reduced by recrystallization. When recrystallization occurs during deformation, the term dynamic recrystallization is used, while it is termed static recrystallization after deformation (Appendix C). The critical energy required to initiate recrystallization in ice is low compared to ceramics and minerals, which is due to the high plastic anisotropy of the

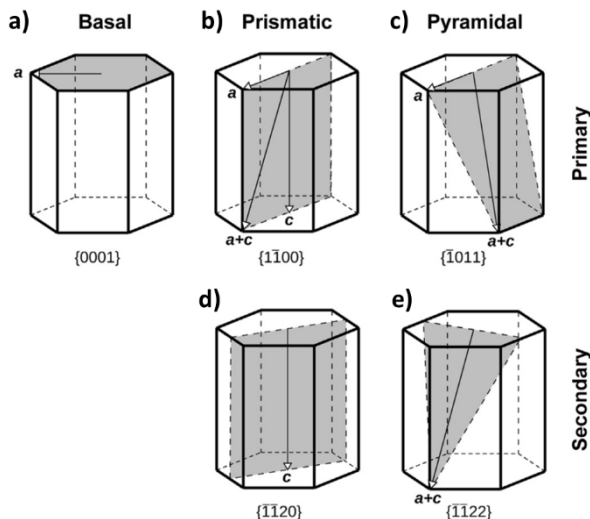


Figure 1.4: The possible slip systems in ice (Figure after Hondoh, 2000).

ice crystal that leads to large variations in stored strain energy between hard and softly oriented grains (Schulson and Duval, 2009). The recrystallization mechanisms that operate in ice are similar to those in rocks and metals and are described in the next paragraphs.

Rotation recrystallization (sometimes called ‘polygonization’ in the glaciology literature; Appendix C) is a process responsible for creating new grain boundaries. Dislocations, that are formed as a result of deformation, recover into SGBs (polygonization). If dislocations continue to be added to the SGB, the misorientation angle of the SGB continues to increase until it can no longer be qualified as being part of the same grain. The misorientation angle at which this transition occurs is about 10° - 15° for most materials (e.g. de Meer et al., 2002; Humphreys and Hatherly, 2004). However, studies on boundary energy and sublimation behaviour have shown that this SGB to grain boundary threshold could be much lower for ice at about 5° (Weikusat et al., 2011b; Montagnat et al., 2015). The process of grain subdivision and rotation recrystallization are seen as fundamental mechanisms of strain accommodation in natural ice (e.g. Alley, 1992; De La Chapelle et al., 1998; Weikusat et al., 2009). Rotation recrystallization in ice can be detected by studying a population of grain boundary misorientations (Alley et al., 1995; Obbard et al., 2006). If rotation recrystallization is active, then nearest-neighbour grains (correlated boundaries) have statistically more grain boundaries with a low misorientation angle compared to randomly selected grains (uncorrelated boundaries) in the polycrystal. The depth where the grain area increase ends in polar ice cores, often at couple of hundred metres of depth (Faria et al., 2014b; Section 1.2.2), has often been ascribed to the onset of rotation recrystallization (e.g. Alley, 1992; Montagnat and Duval, 2000). However, more recent studies have called this into question by showing evidence of rotation recrystallization at much shallower depths in polar ice cores (Mathiesen et al., 2004; Durand et al., 2008).

Migration recrystallization, or strain induced grain boundary migration (SIBM), is the migration of a grain boundary of a grain into another grain (Humphreys and Hatherly, 2004). The driving force of SIBM is the reduction in lattice energy stored in point defects, dislocation walls and SGBs. Grain boundaries tend to migrate into areas of high dislocation density, leaving a crystal behind with a low dislocation density. Two types of migration recrystallization are recognized: bulging recrystallization and migration recrystallization. Bulging recrystallization involves the creation of a new grain by the separation of the bulge from the host grain by the formation of a new grain boundary or by migration of a grain boundary (Stipp et al., 2002; Appendix C). Migration recrystallization is the migration of a grain boundary, often through entire crystals, and sweeps the area clean of dislocations and SGBs (Passchier and Trouw, 2005). Migration recrystallization is active at all depths in polar ice sheets, although its activity varies with depth (Kipfstuhl et al., 2006, 2009; Faria et al., 2014a).

Normal grain growth is the mechanism that is driven by the reduction of free surface energy associated with grain boundary area within a polycrystal (e.g. Humphreys and Hatherly, 2004). Normal grain growth is most pronounced in the upper part of the ice sheet and is characterized by a linear increase of grain area with time (Gow, 1969). The

grain size increase in the upper hundreds of meters of an ice sheet (e.g. Faria et al., 2014b) and the so-called foam-like grain boundary microstructure is often ascribed to normal grain growth (e.g. Alley et al., 1986; De la Chapelle et al., 1998), although more recent studies have shown that rotation and migration recrystallization are also active in the upper part of the ice sheet as well (Mathiesen et al., 2004; Kipfstuhl et al., 2006, 2009; Durand et al., 2008).

The contribution of each of these recrystallization mechanisms varies strongly with depth and location in the ice sheet and depends on the deformation mode, impurity content, temperature and stress. The various competing recovery, recrystallization and grain growth mechanisms contribute to the evolution of microstructure of polar ice during deformation. The microstructure in its turn determines the flow properties of polar ice under different boundary conditions. In order to describe the flow of ice mathematically, glaciologists have been developing and improving ice flow laws for decades (e.g. Glen, 1955; Nye, 1957; Barnes et al, 1971; Homer and Glen, 1978; Goldsby and Kohlstedt, 2001).

In this Chapter and throughout the remainder of this thesis, the most appropriate terminology has been used to describe microstructures and mechanisms. The material science terminology was used for basic dislocation structures and processes. To describe ice microstructures and microstructural processes a combination of the geological and glaciological terminology was used (Appendix C).

1.2.5 The creep of polycrystalline ice

Many deformation tests on ice have been performed in the last decades to calibrate ice flow laws and study ice deformation mechanisms under different boundary conditions (e.g. Glen, 1955; Barnes et al., 1971; Duval and Castelnau, 1995; Treverrow et al., 2012). Most of these deformation tests were performed with synthetically produced polycrystalline, initially isotropic (no preferred c-axes orientation) ice under constant stress or constant strain rate in uniaxial compression. A typical stress-strain rate plot obtained during a constant stress deformation tests at constant temperature is shown in Figure 1.5. The stress-strain rate plots that are obtained during ice deformation experiments are similar to deformation experiments on rocks and other minerals (e.g. Hobbs et al., 1976; Poirier, 1985). The elastic response of the material (not shown in Figure 1.5) is followed by primary creep (sometimes called transient creep), where deformation is mainly produced by the easy slip system (e.g. Andrade, 1910; Poirier, 1985): for ice this is the basal slip system (e.g. Montagnat et al., 2009; Schulson and Duval, 2009; Figure 1.4a). The strain rate during primary creep quickly decelerates due to work hardening, which generally involves an increase in dislocation and subgrain density (e.g. Hobbs et al., 1976; Duval et al., 1983; Humphreys and Hatherly, 2004; Hamann et al., 2007) as well as pile ups of dislocations at the grain boundaries. Work hardening leads to the activation of the hard slip system (non-basal slip for ice, Figure 1.4b-e).

A minimum in strain rate, $\dot{\epsilon}_{\min}$, is reached as the ice moves into the secondary creep regime at about 1% strain. During secondary creep, work hardening is

counterbalanced by softening caused by the onset of dynamic recovery and recrystallization processes (section 1.2.4) (e.g. Jacka, 1984; Montagnat et al., 2009; Schulson and Duval, 2009). The strain rate acceleration after secondary creep is accompanied by the formation of a CPO and by the occurrence of dynamic recrystallization. At high creep strains, greater than about 10%, the strain rate can develop a stable strain rate, $\dot{\epsilon}_{\text{ter}}$, (Budd and Jacka, 1989; Treverrow et al., 2012). This strain rate is generally relevant to ice sheet dynamics in the deeper parts of glacial ice (e.g. Alley, 1992). A stable strain rate can develop at lower strains, depending on a number of factors, such as an initial CPO (Figure 1.5). Due to the very long time scales involved, tertiary creep is hardly ever attained in laboratory experiments.

The term “steady state creep” is applied to an unchanging strain rate, which occurs in some materials in secondary creep. Sometimes, the term “steady state (tertiary) creep” is used to describe stable strain rates that can occur in ice during the tertiary creep regime (e.g. Schulson and Duval, 2009; Treverrow et al., 2012; Figure 1.5). In this thesis, both terms will be used where appropriate.

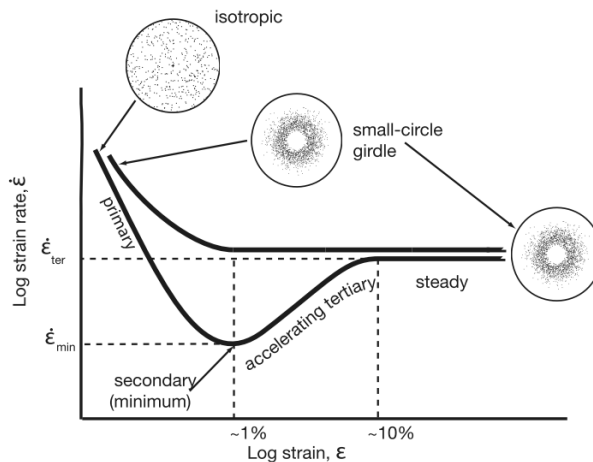


Figure 1.5: Typical log strain rate versus log strain creep curve showing the strain required to reach the different stages of creep under constant stress in unconfined vertical compression tests. For initially isotropic polycrystalline ice, the strain rate decelerates going through secondary (minimum) creep before accelerating to tertiary (steady state) creep. When starting with polycrystalline ice with a compatible fabric for unconfined compression, tertiary (steady state) creep is followed immediately after primary (decelerating) creep. Figure taken from Treverrow et al. (2012).

1.2.6 Subgrain boundaries in ice

SGBs are two dimensional planes in the lattice around which the lattice is slightly rotated. Means and Ree (1988) and Drury and Pennock (2007) showed that there are many different ways a SGB can form. In-situ deformation tests on the rock-analogue octachloropropane (OCP) allowed Means and Ree (1988) to identify seven (I-VII) different types of SGBs (Figure 1.6). Type I and II are formed by polygonization and glide polygonization, respectively. For these two types of SGBs the rotation axis and trace are determined by the

crystallography of the host grain. Means and Ree's type III and IV are produced by misorientation reduction and grain coalescence, respectively. The impingement of migrating SGBs and growth of SGBs behind migration grain boundaries were qualified as type V and VI, respectively. The last type of SGB (type VII) develops in grains without an orientation gradient by static recovery. SGB type III-VII are not controlled by the glide of geometrically necessary dislocations in the host grain.

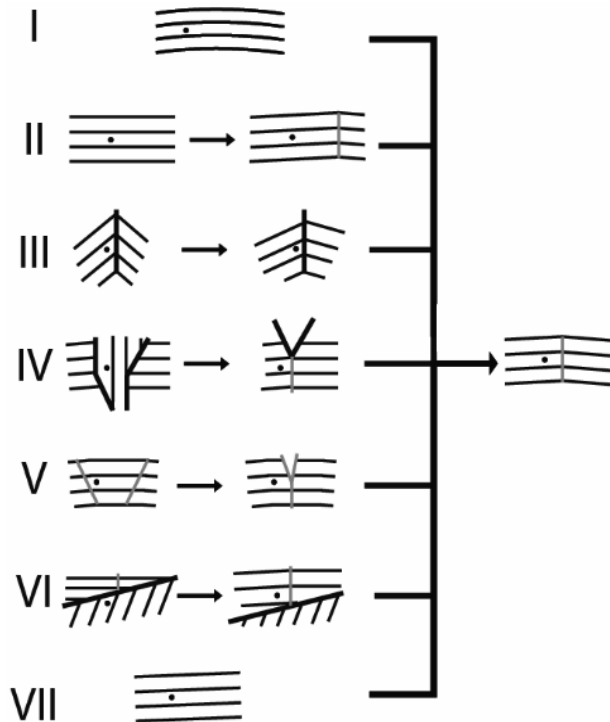


Figure 1.6: Schematic representation of the seven types of subgrain boundary development. Thick black lines are grain boundaries, grey lines are subgrain boundaries, and thin black lines represent the basal planes in the ice crystal. The black dot represents a marker particle. Figure after Means and Ree (1988).

1.2.7 Ice flow laws and deformation mechanisms

The most commonly used flow law in ice sheet models is Glen's flow law (Glen, 1955; Paterson, 1994). Glen's flow law was defined on the basis of results of uniaxial compression experiments on artificial (originally) isotropic polycrystalline ice. Several tests at various stresses and temperatures were performed (Glen, 1952, 1953, 1955) and a power law of the form:

$$\dot{\epsilon} = A \sigma^n e^{-\frac{Q}{RT}}, \quad (1.2)$$

was derived, where $\dot{\epsilon}$ is the strain rate (s^{-1}), σ is the axial stress (MPa), n is the stress exponent, Q is the activation energy ($J \text{ mol}^{-1}$), R is the gas constant ($J \text{ K}^{-1} \text{ mol}^{-1}$), T is the

absolute temperature (K) and A is a material parameter depending on grain size, impurity content, anisotropy, etc. Glen's flow law is characterized by a stress exponent of $n \sim 3$ and can, strictly speaking, only be applied between 0.5% and 2% strain in secondary creep (Budd and Jacka, 1989), since Glen's flow law was calibrated during secondary creep. Furthermore, Glen's flow law was derived at stress levels of 0.1-1.0 MPa (Glen, 1955), which is up to an order of magnitude higher than the stress levels experienced by ice in polar ice sheets (e.g. Sergienko et al., 2014). Extrapolation of Glen's flow law down to stress levels relevant for ice sheet dynamics causes a considerable underestimation of the strain rate (e.g. Thorsteinsson et al., 1999; Huybrechts, 2007).

Glen's flow law assumes that ice is deforming only by a combination of basal slip and non-basal slip (Schulson and Duval, 2009; Knight, 2009), also known as dislocation creep. In this deformation mechanism, basal slip is the dominant slip system and non-basal slip is the accommodating mechanism that is activated in regions of high stress and strain incompatibility. Dislocation creep is assumed to be independent of grain size and it is the dominant deformation mechanism at high stress (e.g. Duval et al., 1983, Schulson and Duval, 2009). However, there has been ample evidence from borehole closure and tilt data (Doake and Wolff, 1985; Dahl-Jensen and Gundestrup, 1987) and ice deformation tests (Mellor and Testa, 1969; Pimienta and Duval, 1987; Duval and Castelnau, 1995; Goldsby and Kohlstedt, 1997, 2001) that ice at low stress deforms by a different mechanism than dislocation creep. This low stress deformation mechanism is characterized by a stress exponent of 2 instead of 3 used for Glen's flow law.

One of two other mechanisms that are often proposed to accommodate basal slip in polar ice is grain boundary sliding (GBS) (Ignat and Frost, 1987; Durham et al., 1997, 2010; Goldsby and Kohlstedt, 1997, 2001). GBS is the displacement of grains relative to each other and is particularly effective at high temperatures and low strain rates (e.g. Langdon, 2006). A grain size sensitive mechanism like GBS could explain the negative correlation between grain size and borehole tilt that is often found in polar ice cores (e.g. Fisher and Koerner, 1986; Dahl-Jensen and Gundestrup, 1987; Paterson, 1991; Thorsteinsson et al., 1999; Cuffey et al., 2000). Goldsby and Kohlstedt (1997, 2001) performed a series of deformation experiments on very fine grained ice (grain size 3-200 μm) to explore the grain size sensitivity of ice deformation and its relevance for polar ice sheets. They found two different deformation mechanisms in ice: dislocation creep and basal slip accommodated by GBS. For basal slip accommodated by GBS it is assumed that basal slip is the main strain producing mechanism with GBS as the slower, rate-controlling mechanism. The flow law for dislocation creep and basal slip accommodated by GBS is given as:

$$\dot{\epsilon} = A_{\text{disl}} \sigma^{n_{\text{disl}}} e^{-\frac{Q_{\text{disl}}}{RT}} + A_{\text{GBS}} \sigma^{n_{\text{GBS}}} d^{-p} e^{-\frac{Q_{\text{GBS}}}{RT}} \quad (1.3)$$

where $\dot{\epsilon}$ is the strain rate (s^{-1}), A is a material parameter, σ is the axial stress (MPa), n is the stress exponent, Q is the activation energy (J mol^{-1}), R is the gas constant ($\text{J K}^{-1} \text{mol}^{-1}$), T is the absolute temperature (K), d is the grain size (m) and p is the grain size exponent. The

subscript ‘disl’ refers to dislocation creep and ‘GBS’ refers to basal slip accommodated by GBS.

One of the other possible mechanisms that has often been proposed is basal slip with recovery by SIBM associated with grain growth and rotation recrystallization (Pimienta and Duval, 1987; Duval et al., 2000; Montagnat and Duval, 2000; Schulson and Duval, 2009). These processes can remove crystallographic defects in a grain that have been produced by basal slip, which allows further deformation to occur. Duval et al. (2000) proposed that creep involving accommodation of basal slip by rotation recrystallization and grain boundary migration is characterized by a stress exponent of 2. Both rotation recrystallization and grain boundary migration have been shown to be active in all parts of the ice sheet, although the relative activity of these mechanisms varies strongly with depth (Mathiesen et al., 2004; Kipfstuhl et al., 2006, 2009; Durand et al., 2008).

Diffusion creep has often been identified as an important (accommodating) mechanism in the deformation of polycrystalline materials (e.g. Ashby and Verrall, 1973; Frost and Ashby, 1982). However, it is generally accepted that diffusion creep is irrelevant for deformation in polar ice sheets as this mechanism is expected to be important at very small grains ($\ll 1$ mm), low temperature and very low equivalent stresses (Goldsby and Kohlstedt, 2001; Durham et al., 2010).

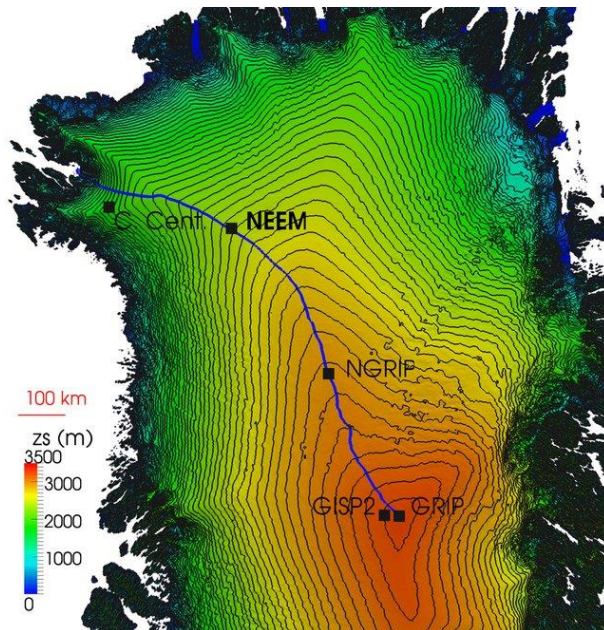


Figure 1.7: Greenland ice sheet surface elevation and the location of several drilling sites for ice core retrieval. Contour lines are every 50 meters. The blue line shows a flow line running along an ice ridge where several ice cores were drilled: Greenland Ice Core Project (GRIP), Greenland Ice Sheet Project 2 (GISP2), North Greenland Ice-core Project (NGRIP), North Greenland Eemian Ice Drilling (NEEM) and Camp Century Ice Core Project (C. Cent). Figure taken from Montagnat et al. (2014).

1.2.8 The NEEM ice core

The 2540 m long NEEM ice core was drilled during the field seasons of 2008 to 2012 in the north western part (77.45°N, 51.06°W) of the Greenland ice sheet (Figure 1.7). The ice core was drilled next to an ice ridge dipping towards the northwest resulting in a slightly divergent ice flow with the main flow component parallel to the ridge. The horizontal flow velocity at the surface is about 6 m per year (NEEM community members, 2013), with an average surface accumulation of about 22 cm per year (ice equivalent) (Rasmussen et al., 2013). The mean annual surface temperature is -29°C. The brittle zone in the NEEM ice core starts at about 600 m of depth and continues until 1160 m of depth (Binder, 2014). The main purpose of the ice core drilling was to extract a Greenlandic ice core with the complete stratigraphic record of the Eemian interglacial (130,000-150,000 years bp). However, only part of the Eemian interglacial ice could be recovered due to severe folding and several stratigraphic disruptions below 2200 m of depth (NEEM community members, 2013).

Figure 1.8 provides an overview of the available data that are relevant for recrystallization and deformation mechanisms in the NEEM ice core. The upper 1419 m of the NEEM ice core consist of ice that was deposited during the current interglacial, the Holocene (0-11,700 years bp). Below, the ice from the last glacial period (11,700-115,000 years bp) can be found to a depth of 2207 m. The Eemian ice is found below the glacial ice and extends until the ice-bedrock interface at 2540 m of depth.

The CPO in the Holocene ice is described by a weak girdle that strengthens with depth (Figure 1.8a). At the Holocene-glacial interface at 1419 m of depth, the c-axes clustering strengthens and the weak girdle CPO develops into a single maximum. The single maximum CPO in the glacial ice weakens at the glacial-Eemian interface and varies strongly with depth until the ice-bedrock interface at 2540 m of depth.

The mean grain area in the NEEM ice core shows a linear increase from the surface of the ice sheet, where the mean grain area is sub-millimetre size, to roughly 5 mm² at a depth of about 400 m (Figure 1.8b). From 400 m of depth to the Holocene-glacial interface, the mean grain size remains relatively stable, although the variation of mean grain size with depth is high. At the Holocene-glacial interface the mean grain size decreases rapidly and remains small for the remainder of the glacial ice. The mean grain size at the glacial-Eemian interface increases rapidly. The mean grain size variation with depth in the Eemian ice is very high, ranging from about 10 mm² to many hundreds of mm².

The temperature in the upper 1200 m of depth is equal to the yearly average temperature at the NEEM drill site of -29°C (Figure 1.8c). Below, the temperature steadily increases reaching an in-situ temperature of -3.4°C at the ice-bedrock interface at 2540 m of depth. The in-situ temperature at the ice-bedrock interface is only about one degree °C below the estimated pressure-melting temperature (Sheldon et al., 2014).

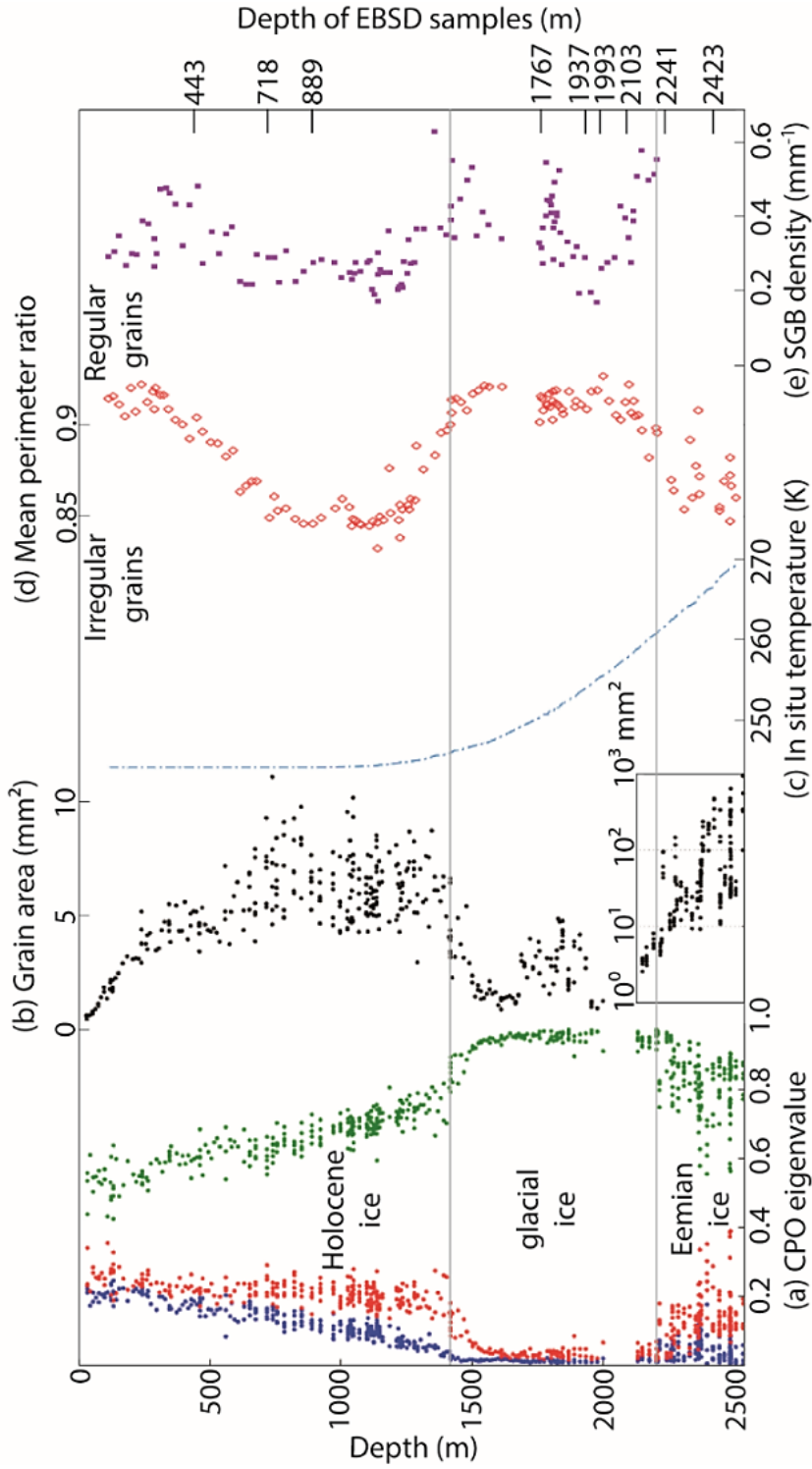


Figure 1.8: Compilation of microstructure and borehole data of the NEMM ice core. (a) Orientation tensor eigenvalue data from light microscopy studies (blue, green, red) (Eichler et al., 2013). (b) Mean grain area (black dots) (Eichler et al., 2013). (c) The in-situ temperature (broken blue line) (Sheldon et al., 2014). (d) Mean perimeter ratio of the grains (red diamonds) (Binder, 2014). (e) Mean SGB density (purple dots) (Binder, 2014). The horizontal grey lines separate the different depth intervals. The depth of the EBSD samples that were prepared and mapped during this PhD project is given on the right

The mean perimeter ratio (Figure 1.8d) is a measure of the irregularity of the grains (Uthus et al., 2005; Hamann et al., 2007; Binder, 2014), where low values indicate irregular grains. The mean perimeter ratio decreases from just below the surface to a minimum value at about 1200 m of depth. Bubble relaxation features in the brittle zone (600 m to 1160 m of depth) that are produced after the retrieval of the ice core from the borehole may influence the lowest values of the grain perimeter ratio (Binder, 2014). In the glacial ice, the grains are relatively regular with a mean perimeter ratio of >0.9 . In the Eemian ice, the grains become more irregular again, although variability with depth is very high until the ice-bedrock interface at 2540 m of depth.

The measured SGB density (Figure 1.8e) shows a relatively high variability throughout the length of the NEEM ice core. However, a minimum in SGB density can be identified in the Holocene ice between about 600 and 1400 m of depth. In the glacial ice, the SGB density is relatively high between at about 1800 and 2200 meters of depth and relatively low in between 1900 and about 2100 m of depth. No data on mean SGB density in the Eemian ice are available. Due to the difficulty with automatic extraction of SGBs from LM images, typically about half the SGBs are automatically detected (Binder, 2014). Therefore, the data in Figure 1.8e should be treated with care and be interpreted in terms of relative differences in SGB density instead of absolute SGB densities.

1.2.9 Cryogenic EBSD

EBSD on ice was developed about a decade ago with Iliescu et al. (2004) being the first to take EBSD patterns from a sample of polycrystalline ice. Some years later, the first EBSD maps were published by Piazzolo et al. (2008). Weikusat et al. (2011a) developed a method to transfer ice samples into the SEM chamber and stabilize the surface of small samples so that EBSD maps can be correlated directly with LM images. Later, Prior et al. (2015) developed the transfer methods for large samples and protocols for EBSD on very fine-grained ice.

During the cryo-EBSD studies of this thesis the methods of Weikusat et al. (2011a) were used. The protocol for EBSD sample preparation at the Alfred Wegener Institute (AWI) in Bremerhaven (Germany) and the protocol for cryo-EBSD at Utrecht University (the Netherlands) is provided in Appendix A and B, respectively. Using these methods and protocols, EBSD samples of about 8 x 8 mm were prepared from ice core sections of the NEEM ice core in the cold lab (-25°C) at the AWI and were transported to Utrecht University. The EBSD samples were mapped with two different SEMs: the FEI Nova Nanolab, which was later replaced by the FEI Helios Nanolab G3 UC. Both SEMs were equipped with the same EBSD detector (Oxford Instruments HKL Technology, Abingdon, UK) and cryo-stage (Quorum Technologies Ltd. Ringmer, UK). For a detailed description of the EBSD sample preparation, transport, transfer into the SEM and EBSD work the reader is referred to Weikusat et al. (2011a) and Appendix A and B of this thesis.

1.2.10 Flow law modelling

Flow law modelling was performed using two different flow laws: Glen's flow law (Glen, 1955; Paterson, 1994) and the composite flow law of Goldsby and Kohlstedt (1997, 2001). The model was written in plain C++ code using open source libraries and software packages. The results were analyzed and plotted using MATLAB (www.mathworks.com). The two different flow laws were constrained with actual borehole temperature data from the NEEM ice core (Sheldon et al., 2014). The equivalent stress at the NEEM site was estimated using the shallow ice approximation (e.g. Hutter, 1983; Greve and Blatter, 2009; Equation 1.1) and constraints on strain rates in the upper part of the NEEM ice core.

The flow law of Goldsby and Kohlstedt (1997, 2001) was constrained with grain size data from Binder et al. (2013). The grain size was determined for each ice core section (90 x 55 mm) and described using a mean grain size and a full grain size distribution (Freeman and Ferguson, 1986; Heilbronner and Bruhn, 1998; Ter Heege et al., 2004). The grain size distribution allowed for the use of two theoretical end members to describe the deformation of ice: a micro-scale constant stress model, where each grain deforms by the same stress, and a micro-scale constant strain rate model, where each grain deforms by the same strain rate but supports a different stress (Freeman and Ferguson, 1986; Ter Heege et al., 2004). The different model end members were used to study the effect of grain size variation on strain rate and the dependence of the dominant deformation mechanism on grain size variations in the NEEM ice core.

1.3 Scope and outline of the thesis

Chapter 1 provides an introduction to the thesis.

Chapter 2 investigates two ice core sections using cryo-EBSD in combination with LM measurements, one from an Antarctic ice core (EPICA-DML ice core at 656 m of depth) and one from a Greenland ice core (NEEM ice core at 718 m of depth). Both ice core sections are from the upper part of the ice core consisting of Holocene ice and deformed predominantly by vertical compression. The study was performed to collect comparable statistics of SGBs at roughly equivalent depths from two different polar ice cores. The rotation axis and trace orientation in the boundary plane (trace) of each SGBs was categorized and interpreted in terms of possible slip system activity. The results of slip system activity in the two polar ice core sections are presented and discussed in the light of rate-controlling processes of polar ice deformation.

Chapter 3 investigates slip system activity of SGBs along the entire NEEM ice core using cryo-EBSD in combination with LM measurements. Each SGB was categorized in terms of its misorientation angle, rotation axis and trace. The rotation axis and trace of each SGB were used to infer the active slip system and dislocations that were most likely involved in the formation of the SGB. The results of slip system activity with depth were used to

discuss the possible deformation and recrystallization mechanisms that may be active in the NEEM ice core.

Chapter 4 investigates the role of grain size on strain rate in the upper 2207 m of the NEEM ice core using the composite flow law of Goldsby and Kohlstedt (1997, 2001). The grain size data were available (Binder et al., 2013) and described using a mean grain size and a full grain size distribution. The methods of Heilbronner and Bruhn (1998) were used to convert the grain size data from 2D sectional circles to 3D volume fractions in order to correct for the over-representation of small grains in a LM image compared to the bulk volume. The two model end members, the micro-scale constant stress and the micro-scale constant strain rate model, were applied using the grain size distribution. The two model end members were used to study the effect of grain size variation on the bulk strain rate and its effect on the dominant deformation mechanism. The results obtained using the different descriptions of grain size and model end members were evaluated and compared to the results obtained using Glen's flow law.

Chapter 5 investigates the role of grain size on strain rate in the lowest 540 m of the NEEM ice core. Similar to Chapter 4, Glen's flow law and the composite flow law of Goldsby and Kohlstedt (1997, 2001) were applied using actual temperature and grain size data of the NEEM ice core. Due to the large grain size in some layers it was not possible to derive a grain size distribution and only a mean grain size was used as model input. The rheology in this part of the NEEM ice core is likely affected by premelting along the grain boundaries due to the high temperature of the ice. The grain size in this part of the NEEM ice core varies strongly with depth as a result of several stratigraphic disruptions (NEEM community members, 2013). The influence of grain size variations, which coincides with changes in strength and type of CPO (Eichler et al., 2013), on deformation mechanisms and strain rates are discussed and the results using the composite flow law and Glen's flow law for the lowest 540 m of the NEEM ice core are compared.

Chapter 6 investigates the dominant recrystallization and deformation mechanisms along the length of the NEEM ice core. Data obtained by (polarized) LM imaging (Eichler et al., 2013; Binder, 2014) were combined with all data and results obtained from cryo-EBSD studies of SGBs on NEEM ice core samples (Chapter 2 and 3) and flow law modelling (Chapter 4 and 5). Information provided by the cryo-EBSD dataset of the NEEM ice core include lattice bending within grains, a-axes alignment and microstructural analysis of EBSD maps. The recrystallization and deformation mechanisms in the Holocene ice (0-1419 m of depth), glacial ice (1419-2207 m of depth) and the Eemian ice (2207-2540 m of depth) in the NEEM ice core are discussed based on the results from the combined datasets.

Chapter 7 Summarizes the main conclusions of this thesis and offers suggestions for further research.

References

- Alley, R. B. (1992) Flow-law hypotheses for ice-sheet modeling. *Journal of Glaciology*, 38, 129, 245-256, doi: 10.1017/S002214300003658.
- Alley, R. B., Clark, P. U., Huybrechts, P., Joughin, I. (2005) Ice-Sheet and Sea-Level Changes. *Science*, 310, 456, doi:10.1126/science.1114613.
- Alley, R. B., Gow, A. J., Meese, D. A. (1995) Mapping c-axis fabrics to study physical processes in ice. *Journal of Glaciology*, 41, 137, 197-203, doi: 10.1017/S0022143000017895.
- Alley, R. B., Perepezko, J. H., Bentley, C. R. (1986) Grain growth in polar ice: I. Theory. *Journal of Glaciology*, 32, 112, 415-424, doi: 10.1017/S0022143000012120.
- Andrade, E. (1910) On the viscous behaviour of metals. *Proceeding of the Royal Society A: Mathematical, Physical and Engineering Sciences*, 84, 1-12.
- Ashby, M., Verrall, R. (1973) Diffusion-accommodated flow and Superplasticity. *Acta Metallurgica*, 21, 2, 149-163, doi: 10.1016/0001-6160(73)90057-6.
- Azuma, N., Wang, Y., Mori, K., Narita, H., Hondoh, T., Shoji, H., Watanabe, O. (1999) Textures and fabrics in Dome F (Antarctica) ice core. *Annals of Glaciology*, 29, 163-168, doi:10.3189/172756499781821148.
- Azuma, N., Wang, Y., Yoshida, Y., Narita, H., Hondoh, T., Shoji, H., Watanabe, O. (2000) Crystallographic analysis of the Dome Fuji ice core. in: *Physics of Ice Core Records*, edited by Hondoh, T., pp. 45-61, Hokkaido University Press, Sapporo.
- Barnes, P., Tabor, D., and Walker, J. C. F. (1971) The friction and creep of polycrystalline ice. *Proceedings of the Royal Society London A.*, 324, 1557, 127-155.
- Binder, T. (2014) Measurements of grain boundary networks in deep polar ice cores – A digital image processing approach. PhD thesis, University of Heidelberg, Germany.
- Binder, T., Weikusat, I., Freitag, J., Garbe, C. S., Wagenbach, D., Kipfstuhl, S. (2013) Microstructure through an ice sheet. *Materials Science Forum*, 753, 481-484, doi: 10.4028/www.scientific.net/MSF.753.481.
- Bintanja, R. (2009) *Glacier Science and environmental change* (eds. by P. G. Knight). pp. 174-176. Blackwell, Oxford.
- Bons, P. D., Kleiner, T., Llorens, M.-G., Prior, D. J., Sachau, T., Weikusat, I., Jansen, D. (2018) Greenland Ice Sheet: Higher Nonlinearity of Ice Flow Significantly Reduces Estimated Basal Motion. *Geophysical Research Letters*, 45, doi: 10.1029/2018GL078356.
- Budd, W. F., Jacka, T. H. (1989) A review of ice rheology for ice sheet modelling. *Cold Regions Science and Technology*, 16, 107-144, doi: 10.1016/0165-232X(89)90014-1.
- Catania, G. A., Neumann, T. A. (2010) Persistent englacial drainage features in the Greenland Ice Sheet. *Geophysical Research Letters*, 37, 2, 1-5, doi: 10.1029/2009GL041108.
- Church, J. et al. (2013). "Climate Change 2013: The Physical Science Basis. Contribution of Working Group I to the Fifth Assessment Report of the Intergovernmental Panel on Climate Change". Ed. by T. Stocker et al. Cambridge University Press, Cambridge, United Kingdom and New York, NY, USA. Chap. Sea Level Change (cit. on p. 1).

- Cuffey, K. M., Thorsteinsson, T., Waddington, E. D. (2000) A renewed argument for crystal size control of ice sheet strain rates. *Journal of Geophysical Research*, 105, B12, 27889-27894, doi: 10.1029/2000JB900270.
- Cuffey, K.M., Paterson, W.S.B. (2010) *The Physics of Glaciers*. 4th edn. Elsevier.
- Dahl-Jensen, D. Gundestrup, N. S. (1987) Constitutive properties of ice at Dye 3, Greenland. *The Physical Basis of Ice Sheet Modelling*, 170, 31-43.
- Dansgaard, W. (1964) Stable isotopes in precipitation, *Tellus*, 16, 4, 436-468, doi: 10.3402/tellusa.v16i4.8993.
- DeConto, R. M., Pollard, D. (2016) Contribution of Antarctica to past and future sea-level rise. *Nature*, 531, 591-597, doi: 10.1038/nature17145.
- De La Chapelle, S., Castelnau, O., Lipenkov, V., Duval, P. (1998) Dynamic recrystallization and texture development in ice as revealed by the study of deep ice cores in Antarctica and Greenland. *Journal of Geophysical Research*, 103, B3, 5091-5105, doi: 10.1029/97JB02621.
- De Meer, S., Drury, M. R., De Bresser, J. H. P., Pennock, G. M. (2002) Current issues and new developments in deformation mechanisms, rheology and tectonics. *Deformation mechanisms, Rheology and Tectonics: Current Status and Future Perspectives*. The Geology Society, London, Special Publication, pp 1-27.
- Doake, S. S. M., Wolff, E. W. (1985) Flow law for ice in polar ice sheets. *Nature*, 314, 6008, 255-257.
- Drury, M., Pennock, G. (2007) Subgrain Rotation Recrystallization in Minerals Materials. *Materials Science Forum*, 550, 94, 104, doi: 10.4028/www.scientific.net/MSF.550.95.
- Drury, M. R., Urai, J. L. (1990) Deformation-related recrystallization processes. *Tectonophysics*, 172, 235-253.
- Durand, G., Persson, a., Samyn, D., Svensson, A. (2008) Relation between neighbouring grains in the upper part of the NorthGRIP ice core – Implication for rotation recrystallization. *Earth and Planetary Science Letters*, 265, 3-4, 666-671, doi: 10.1016/j.epsl.2007.11.002.
- Durand, G., Svensson, A., Kipfstuhl, S., Persson, A., Gagliardini, O., Gillet, F., Sjolte, J., Montagnat, M., Dahl-Jensen, D. (2009) Evolution of the texture along the EPICA dome C ice core. 68, 91–106, Institute of Low Temperature Science, Hokkaido University, Sapporo Japan, Nepal.
- Durand, G., Weiss, J., Lipenkov, V., Barnola, J. M., Krinner, G., Parrenin, F., Delmonte, B., Ritz, C., Duval, P., Röthlisberger, R., Bigler, M. (2006) Effect of impurities on grain growth in cold ice sheets. *Journal of Geophysical Research*, 111, F01015, 1-18, doi: 10.1029/2005JF000320.
- Durham, W. B., Kirby, S. H., Stern, L. A. (1997) Creep of water ices at planetary conditions: A compilation. *Journal of Geophysical Research*, 102, E7, 16293-16302, doi: 10.1029/97JE00916.
- Durham, W. B., Prieto-Ballesteros, O., Goldsby, D. L., Kargel, J. S. (2010) Rheological and Thermal Properties of Icy Materials. *Space Science Reviews*, 153, 273-298, doi: 10.1007/s11214-009-9619-1.

- Duval, P., Arnaud, L., Brissaud, O., Montagnat, M., De La Chapelle, S. (2000) Deformation and recrystallization processes of ice from polar ice sheets. *Annals of Glaciology*, 30, 83-87, doi: 10.3189/172756400781820688.
- Duval, P., Ashby, M. F., Anderman, I. (1983) Rate-Controlling processes in the creep of polycrystalline ice. *Journal of Physical Chemistry*, 87, 21, 4066-4074, doi: 10.1021/j100244a014.
- Duval, P., Castelnau, O. (1995) Dynamic Recrystallization of Ice in Polar Ice Sheets. *Journal de Physique III*, 05, C3-197-C3-205, doi: 10.1051/jp4:1995317.
- Duval, P., Montagnat, M. (2002) Comment on "Superplastic deformation of ice: Experimental observations" by D. L. Goldsby and D. L. Kohlstedt. *Journal of Geophysical Research*, 107, B4, 1-2, doi: 10.1029/2001JB000946.
- Eichler, J., Kleitz, I., Bayer-Giraldi, Jansen, D., Kipfstuhl, S., Shigeyama, W., Weikusat, C., Weikusat, I. (2017) Location and distribution of micro-inclusions in the EDML and NEM ice cores using optical microscopy and in situ Raman spectroscopy. *The Cryosphere*, 11, 3, 1075-1090, doi: 10.5194/tc-11-1075-2017.
- Eichler, J., Weikusat, I., Kipfstuhl, S. (2013): Orientation-tensor eigenvalues along the NEM ice core. *PANGAEA*, <https://doi.org/10.1594/Pangaea.838059>.
- EPICA community members (2004) Eight glacial cycles from an Antarctic ice core. *Nature*, 429, 623-628, doi: 10.1038/nature02599.
- Faria, S. H., Weikusat, I., Azuma, N. (2014b) The Microstructure of Polar ice. Part I: Highlights from ice core research. *Journal of Structural Geology*, 61, 2-10, doi: 10.1016/j.jsg.2013.09.010.
- Faria, S. H., Weikusat, I., Azuma, N. (2014a) The microstructure of polar ice. Part II: State of the art. *Journal of Structural Geology*, 61, 21-49, doi: 10.1016/j.jsg.2013.11.003.
- Fisher, D. A., Koerner, R. M. (1986) On the special rheological properties of ancient microparticle-laden northern hemisphere ice as derived from bore-hole and core measurements. *Journal of Glaciology*, 32, 112, 501-510.
- Freeman, B., Ferguson, C. (1986) Deformation mechanism maps and micromechanics of rocks with distributed grain sizes. *Journal of Geophysical Research*, 91, B3, 3849-3860, doi: 10.1029/JB091iB03p03849.
- Frost, H. J., Ashby, M. F. (1982) *Deformation-Mechanism Maps: The Plasticity and Creep of Metals and Ceramics*. Pergamon Press, Oxford.
- Glen, J. W. (1952) Experiments on the deformation of ice. *Journal of Glaciology*, 2, 12, 111-114.
- Glen, J. W. (1953) Rate of flow of polycrystalline ice. *Nature*, 172, 721-722.
- Glen, J. W. (1955) The creep of polycrystalline ice. *Proceedings of the Royal Society A: Mathematical, Physical and Engineering Sciences*, 228, 1175, 519-538, doi: 10.1098/rspa.1955.0066.
- Goldsby, D. L., Kohlstedt, D. L. (1997) Grain boundary sliding in fine grained ice I. *Scripta Materialia*, 37, 9, 1399-1406.
- Goldsby, D. L., Kohlstedt, D. L. (2001) Superplastic deformation of ice: Experimental observations. *Journal of Geophysical Research*, 106, B6, 11017-11030, doi: 10.1029/2000JB900336.

- Goldsby, D. L., Kohlstedt, D. L. (2002) Reply to comment by P. Duval and M. Montagnat on “Superplastic deformation of ice: Experimental observations”. *Journal of Geophysical Research*, 107, B11, 1-5, doi: 10.1029/2002JB001842.
- Gow, A. J. (1969) On the rates of growth of grains and crystals in south polar firn. *Journal of Glaciology*, 8, 53, 241-252, doi: 10.3189/S0022143000031233.
- Gow, A. J. (1971) Relaxation of Ice in Deep Drill Cores from Antarctica. *Journal of Geophysical Research*, 76, 11, 2533-2541, doi: 10.1029/JB076i011p02533.
- Gow, A. J., Engelhardt, H. (2000) Preliminary analysis of ice cores from Siple Dome, West Antarctica. In Hondoh, T., ed. *Physics of ice core records*. Sapporo, Hokkaido University Press, 63–82.
- Gow, A. J., Williamson, T. (1976) Rheological implications of the internal structure and crystal fabrics of the West Antarctic ice sheet as revealed by deep core drilling at Byrd Station. *Geological Society of America Bulletin*, 87, 12, 1665-1677.
- Gow, A. J., Meese, D. A., Alley, R. B., Fitzpatrick, J. J., Anandakrishnan, S., Woods, G. A., Elder, B. C. (1997) Physical and structural properties of the Greenland Ice Sheet Project 2 ice core: A review. *Journal of Geophysical Research*, 102, C12, 26559-26575, doi: 10.1029/97JC00165.
- Greve, R., Blatter, H. (2009) *Dynamics of ice sheets and glaciers*. Springer Berlin/Heidelberg.
- Guillope, I., Poirier, J. P. (1979) Dynamic recrystallization during the creep of single-crystalline halite: an experimental study. *Journal of Geophysical Research*, 84, B10, 5557-5567, doi: 10.1029/JB084iB10p05557.
- Hamann, I., Weikusat, C., Azuma, N., Kipfstuhl, S. (2007) Evolution of ice crystal microstructure during creep experiments. *Journal of Glaciology*, 53, 182, 479-489.
- Hansen, J., Sato, M., Hearty, P., Ruedy, R., Kelley, M., Masson-Delmotte, V., Russell, G., Tselioudis, G., Cao, J., Rignot, E., Velicogna, I., Tormey, B., Donovan, B., Kandiano, E., Von Schuckmann, K., Kharecha, P., Legrande, A. N., Bauer, M., Lo, K.-W. (2016) Ice melt, sea level rise and superstorms: Evidence from paleoclimate data, climate modeling, and modern observations that 2°C global warming could be dangerous. *Atmospheric Chemistry and Physics*, 16, 6, 3761–3812. doi: 10.5194/acp-16-3761-2016.
- Heilbronner, R., Bruhn, D. (1998) The influence of three-dimensional grain size distributions on the rheology of polyphaser rocks. *Journal of structural Geology*, 20, 6, 695-705, doi: 10.1016/S0191-8141(98)00010-8.
- Hirth, G., Kohlstedt, D. (1995) Experimental constraints on the dynamics of the partially molten upper mantle: Deformation in the diffusion creep regime. *Journal of Geophysical Research*, 100, B2, 1981-2001, doi: 10.1029/94JB02128.
- Hirth, J. P., Lothe, J. (1982) *Theory of Dislocations*. 2nd ed. Krieger Publishing Company, Malabar, FL.
- Hobbs, B. E. (1985) *Preferred Orientation in Deformed Metals and Rocks*, Academic Press, Orlando.
- Homer, D. R., Glen, J. W. (1978) The creep activation energies of ice. *Journal of Glaciology*, 21, 85, 429-444.
- Hobbs, B. E., Means, W. D., Williams, P. F. (1976) *An outline of structural geology*. New York, Wiley, 571.

- Hondoh, T. (2000) Nature and behavior of dislocations in ice. *Physics of Ice Core Records*, 3-24.
- Homer, D. R., Glen, J. W. (1978) The creep activation energies of ice. *Journal of Glaciology*, 21, 85, 429-444.
- Humphreys, F. J. and Hatherly, M. (2004) *Recrystallization and Related Annealing Phenomena*, Elsevier, Oxford, UK.
- Hutter, K. (1983) *Theoretical glaciology; material science of ice and the mechanics of glaciers and ice sheets*. Reidel Publishing Co., Dordrecht, Terra Scientific Publishing Co, Tokyo.
- Huybrechts, P. (2007) Ice sheet modelling, *Encyclopedia of the Antarctic* (ed. by Riffenburgh, B.), pp 514-417. Routledge. New York and London.
- Ignat, M., Frost, H. J. (1987) Grain Boundary Sliding in Ice. *Le Journal de Physique Colloques*, 48, 9, C1-189-C1-195, doi: 10.1051/jphyscol:1987127.
- Iliescu, D., Baker, I., Chang, H. (2004) Determining the orientations of Ice Crystals Using Electron Backscatter Patterns. *Microscopy Research and Technique*, 63, 183-187, doi: 10.1002/jemt.20029.
- IPCC. (2014) *Climate change 2014: Synthesis report. contribution of working groups i, ii, iii to the fifth assessment report of the intergovernmental panel on climate change*, IPCC, Geneva, Switzerland, 151.
- Jacka T. H. (1984) The time and strain required for development of minimum strain rates in ice. *Cold Regions Science and Technology*, 8, 3, 261-268.
- Jacka, T. H., Li, J. (1994) The steady-state crystal size of deforming ice. *Annals of Glaciology*, 20, 13-18, doi: 10.3189/172756494794587230.
- Ji, S., Wang, Q., Xia, B. (2002) *Handbook of Seismic Properties of Minerals, Rocks and Ores*. Polytechnic International Press, Montreal, ISBN: -553-01032-X.
- Kipfstuhl, S., Faria, S. H., Azuma, N., Freitag, J., Hamann, I., Kaufmann, P., Miller, H., Weiler, K., Wilhelms, F. (2009) Evidence of dynamic recrystallization in polar firn. *Journal of Geophysical Research*, 114, B05204, doi: 10.1029/2008JB005583.
- Kipfstuhl, S., Hamann, I., Lambrecht, A., Freitag, J., Faria, S. H., Grigoriev, D., Azuma, N. (2006) Microstructure mapping: a new method for imaging deformation-induced microstructural features of ice on the grain scale. *Journal of Glaciology*, 52, 178, 398-406, doi: 10.3189/172756506781828647.
- Kipfstuhl, S., Pauer, F., Kuhs, W. F., Shoji, H. (2001) Air bubbles and clathrate hydrates in the transition zone of the NGRIP ice core. *Geophysical Research Letters*, 28, 4, 591-594, doi: 10.1029/1999GL006094.
- Knight, P. (2006) *Glacier Science and Environmental Change*. Blackwell, Oxford.
- Kopp, R. E., DeConto, R. M., Bader, D. A., Hay, C. C., Horton, R. M., Kulp, S., Oppenheimer, M., Pollard, D., Strauss, B. H. (2017) Evolving understanding of Antarctic ice-sheet physics and ambiguity in probabilistic sea-level projections. *Earth's Future*, 5, doi: 10.1002/2017EF000663.
- Krabbendam, M. (2016) Basal sliding of temperate basal ice on a rough, hard bed: pressure melting, creep mechanisms and implications for ice streaming. *The Cryosphere*, 10, 1915-1932, doi: 10.5194/tc-10-1915-2016.

- Langdon, L. (2006) Grain Boundary sliding revisited: Developments in sliding over four decades. *Journal of Materials Science*, 41, 3, 597-609, doi: 10.1007/s10853-006-6476-0.
- Lipenkov, V. Y., Barkov, N. I., Duval, P., Pimienta, P. (1989) Crystalline texture of the 2083 m ice core at Vostok station, Antarctica. *Journal of Glaciology*, 35, 121, 392–398.
- Mathiesen, J., Ferkinghoff-Borg, J., Jensen, M. H., Levinsen, M., Olesen, P., Dahl-Jensen, D., Svensson, A. (2004) Dynamics of crystal formation in the Greenland NorthGRIP ice core. *Journal of Glaciology*, 50, 170, 325-328, doi: 10.3189/172756504781829873.
- Means, W. D., Ree, J.H. (1988) Seven types of subgrain boundaries in octachloropropane. *Journal of Structural Geology*, 10, 7, 765-770, doi: 10.1016/0191-8141(88)90083-1.
- Mellor, M., Testa, R. (1969) Creep of ice under low stress. *Journal of Glaciology*, 8, 52, 147-152.
- Montagnat, M., Chauve, T., Barou, F., Tommasi, A., Beausir, B., Fressengaes, C. (2015) Analysis of Dynamic Recrystallization of Ice from EBSD Orientation Mapping. *Frontiers in Earth Science*, 3, 81, 1-13, doi: 10.3389/feart.2015.00081.
- Montagnat, M., Duval, P. (2000) Rate controlling processes in the creep of polar ice, influence of grain boundary migration associated with recrystallization. *Earth and Planetary Science Letter*, 183, 1-2, 179-186, doi: 10.1016/S0012-821X(00)00262-4.
- Montagnat, M., Durand, G., Duval, P. (2009) Recrystallization processes in granular ice. In Hondoh, T. ed. *Physics of ice core records II*. Hokkaido University Press, Sapporo (Supplement Issue of *Low Temperature Science*, 68).
- NEEM community members. (2013) Eemian interglacial reconstructed from a Greenland folded ice core. *Nature*, 493, 489-494, doi: 10.1038/nature11789.
- Neumann, B. (2000) Texture development of recrystallized quartz polycrystals unravelled by orientation and misorientation characteristics. *Journal of Structural Geology*, 22, 1695-1711, doi: 10.1016/S0191-8141(00)00060-2.
- Nye, J. F. (1957) the distribution of stress and velocity in glaciers and ice-sheets. *Proceedings of the Royal Society A: Mathematical, Physical and Engineering Sciences*, 239, 1216, 113-133, doi: 10.1098/rspa.1957.0026.
- Obbard, R., Baker, I., Sieg, K. (2006) Using electron backscatter diffraction patterns to examine recrystallization in polar ice sheets. *Journal of Glaciology*, 52, 179, 546-557, doi: 10.3189/172756506781828458.
- Rasmussen, S. O., Abbott, P.M., Blunier, T., Bourne, A. J., Brook, E., Buchardt, S. L., Buizert, C., Chappellaz, J., Clausen, H. B., Cook, E., Dahl-Jensen, D., Davies, S. M., Guillevic, M., Kipfstuhl, S., Laepple, T., Seierstad, I. K., Severinghaus, J. P., Steffensen, J. P., Stowasser, C., Svensson, A., Vallenga, P., Vinther, B. M., Wilhelms, F., Winstrup, M. (2013) A first chronology for the North Greenland Eemian Ice Drilling (NEEM) ice core. *Climate of the Past*, 9, 2713-2730, doi: 10.5194/cp-9-2713-2013.
- Rogozhina, I., Petrunin, A. G., Vaughan, A. P. M., Steinberger, B., Johnson, J., Kaban, M. K., Calov, R., Rickers, F., Thomas, M., Koulakov, I. (2016) Melting at the base of the Greenland ice sheet explained by Iceland hotspot history. *Nature Geosciences*, 9, 366-369, doi: 10.1038/NGEO2689.
- Paterson, W. S. B. (1991) Why ice-age ice is sometimes “soft”. *Cold Regions Science and Technology*, 20, 1, 75-98, doi: 10.1016/0165-232X(91)90058-O.

- Paterson, W. S. B. (1994) *The physics of glaciers*, Third edition. Oxford, Elsevier.
- Petrenko, V. F., Whitworth, R. W. (1999) *Physics of Ice*. Clarendon Press.
- Piazolo, S., Montagnat, M., Blackford, J. R. (2008) Sub-structure characterization of experimentally and naturally deformed ice using cryo-EBSD. *Journal of Microscopy*, 230, Pt 3, 509-519, doi: 10.1111/j.1365-2818-2008.02014.x.
- Pimienta, P., Duval, P. (1987) Rate controlling processes in the creep of polar glacier ice. *Journal de Physique*, 48, C1, 243-248, doi: 10.1051/jphyscol:1987134.
- Prior, D. J., Lilly, K., Seidemann, Vaughan, M., Becroft, L., Easingwood, R., Diebold, S., Obbard, R., Daghlian, C., Baker, I., Caswell, T., Golding, N., Goldsby, D., Durham, W. B., Piazolo, S., Wilson, C. J. L., Wilson, C. J. L. (2015) Making EBSD on water ice routine. *Journal of Microscopy*, 00, 0, 1-20, doi: 10.1111/jmi.12258.
- Passchier, C. W., Trouw, R. A. J. (2005) *Microtectonics*, Springer, Berlin.
- Poirier, J. P. (1985) *Creep of Crystals*. Cambridge University Press, Cambridge, 260 pp.
- Schulson, E. M., Duval, P. (2009) *Creep and Fracture of Ice*. Cambridge University Press.
- Sergienko, O. V., Creyts, T. T., Hindmarsh, R. C. A. (2014) Similarity of organized patterns in driving stress and basal stresses of Antarctic and Greenland ice sheets beneath extensive areas of basal sliding. *Geophysical Research Letter*, 41, 11, 3925-3932, doi: 10.1002/2014GL059976.
- Sheldon, S. G., Steffensen, J. P., Hansen, S. B., Popp, T. J., Johnsen, S. J. (2014) The investigation and experience of using ESTISOL™ 240 and COASOL™ for ice-core drilling. *Annals of Glaciology*, 55, 68, 219-232, doi: 10.3189/2014AoG68A036.
- Stipp, M., Stunitz, H., Heilbronner, R., Schmid, S. M. (2002) Dynamic recrystallization of quartz: correlation between natural and experimental conditions. *Geological Society, London, Special Publications*, 200, 1, 171-190.
- Ter Heege, J. H., De Bresser, J. H. P., Spiers, C. J. (2004) Composite flow laws for crystalline materials with log normally distributed grain size: theory and application to olivine. *Journal Structural Geology*, 26, 1693-1705, doi: 10.1016/j.jsg.2004.01.008.
- Thoma, M., Grosfeld, K., Mayer, C., Pattyn, F. (2010) Interaction between ice sheet dynamics and subglacial lake circulation: a coupled modelling approach. *The Cryosphere*, 4, 1, 1-12. doi: 10.5194/tc-4-1-2010.
- Thorsteinsson, T., Kipfstuhl, J., Eicken, H., Johnsen, S. J., Fuhrer, K. (1995) Crystal size variations in Eemian-age ice from the GRIP ice core, Central Greenland. *Earth and Planetary Science Letters*, 131, 3-4, 381-394, doi: 10.1016/0012-821X(95)00031-7.
- Thorsteinsson, T., Waddington, E.D., Taylor, K. C., Alley, R. B., Blankenship, D. D. (1999) Strain-rate enhancement at Dye 3, Greenland. *Journal of Glaciology*, 45, 150, 338-345, doi: 10.3189/002214399793377185.
- Trépiéd, L., Doukhan, J. C., Paquet, J. (1980) Subgrain Boundaries in Quartz: Theoretical Analysis and Microscopic Observations. *Physics and Chemistry of Minerals*, 5, 3, 201-218, doi: 10.1007/BF00348570.
- Treverrow, A., Budd, W. F., Jacka, T. H., Warner, R. C. (2012) The tertiary creep of polycrystalline ice: Experimental evidence for stress-dependent levels of strain-rate enhancement. *Journal of Glaciology*, 58, 208, 301-314, doi: 10.3189/2012JoG11J149.

- Urai, J. Means, W. D., Lister, G. (1986) Dynamic recrystallization of minerals. Geophysical Monograph Series, Geophysical Union, 36, 161-199, doi: 10.1029/GM036p0161.
- Uthus, L., Hoff, I., Horvli, I. (2005) Evaluation of grain shape characterization methods for unbound aggregates. Seventh International Conference on the Bearing Capacity of Road, Trondheim.
- Vaughan, D. G., Arthern, R. (2007) Why is it hard to predict the future of ice sheets? Science, 315, 1503-1504, doi: 10.1126/science.1141111.
- Van de Wal, R. S. W., Boot, W., Van den Broeke, M. R., Smeets, C. J. P. P., Reijmer, C. H., Donker, J. J. A., Oerlemans, J. (2008) Large and Rapid Melt-Induced Velocity Changes in the Ablation Zone of the Greenland Ice Sheet. Science, 321, 111-114, doi: 10.1126/science.1158540.
- Weertman, J. (1957) On the sliding law of glaciers. Journal of Glaciology, 3, 21, 33-38, doi: 10.3189/S0022143000024709.
- Weertman, J., Weertman, J. R. (1992) Elementary Dislocation Theory. Oxford University Press, New York.
- Weikusat, I., de Winter, D. A. M., Pennock, G. M., Hayles, M., Schneiderberg, C. T. W. M., Drury, M. R. (2011a) Cryogenic EBSD on ice: preserving a stable surface in a low pressure SEM. Journal of Microscopy, 242, 3, 295-310, doi: 10.1111/j.1365-2818.2010.03471. x.
- Weikusat, I., Jansen, D., Binder, T., Eichler, J., Faria, S. H., Wilhelms, F., Kipfstuhl, S., Sheldon, S., Miller, H., Dahl-Jensen, D., Kleiner, T. (2017) Physical analysis of an Antarctic ice core (EDML) – towards an integration of micro- and macrodynamics of polar ice. Philosophical Transactions A, 375, doi: 10.1098/rsta.2015.0347.
- Weikusat, I., Kipfstuhl, S., Faria, S. H., Azuma, N., Miyamoto, A. (2009) Subgrain boundaries and related microstructural features in EDML (Antarctica) deep ice core. Journal of Glaciology, 55, 191, 461-472.
- Weikusat, I., Miyamoto, A., Faria, S., Kipfstuhl, S., Azuma, N., Hondoh, T. (2011b) Subgrain boundaries in Antarctic ice quantified by X-ray Laue diffraction. Journal of Glaciology, 57, 201, 85-94, doi: 10.3189/002214311795306628.
- Wolovick, M. J., Creyts, T. T. (2016) Overturned folds in ice sheets: Insight from a kinematic model of travelling sticky patches and comparisons with observations. Journal of Geophysical Research: Earth Surface, 121, 5, 1065-1083, doi: 10.1002/2015JF003698.
- Zwally, H. J., Abdalati, W., Herring, T., Larson, K., Saba, J., Steffen, S. (2002) Surface Melt-Induced Acceleration of Greenland Ice-Sheet Flow. Science, 297, 218-223, doi: 10.1126/science.1072708.

EBSD analysis of subgrain boundaries and dislocation slip systems in Antarctic and Greenland ice

After:

Weikusat, I., Kuiper, E. N., Pennock, G. M., Kipfstuhl, S., Drury, M. R. (2017) EBSD analysis of subgrain boundaries and dislocation slip systems in Antarctic and Greenland ice. *Solid Earth*, 8, 5, 883-898, doi: 10.5194/se-8-883-2017.

Abstract

Ice has a very high plastic anisotropy with easy dislocation glide on basal planes, while glide on non-basal planes is much harder. Basal glide involves dislocations with Burgers vector $\mathbf{b}=(1/3)\langle 1\bar{2}10 \rangle$, while glide on non-basal planes can involve dislocations with $\mathbf{b}=(1/3)\langle 1\bar{2}10 \rangle$, $\mathbf{b}=[0001]$ and $\mathbf{b}=(1/3)\langle 11\bar{2}3 \rangle$. During natural ductile flow of polar ice sheets, most of the deformation is expected to occur by basal slip accommodated by other processes including non-basal slip and grain boundary processes. However, the importance of different accommodating processes is controversial. The recent application of micro-diffraction analysis methods to ice, such as X-ray Laue diffraction and electron backscatter diffraction (EBSD), has demonstrated that subgrain boundaries indicative of non-basal slip are present in naturally deformed ice, although so far the available data sets are limited. In this study, an analysis of a large number of subgrain boundaries in ice core samples from one depth level from two deep ice cores from Antarctica (EPICA-DML deep ice core at 656 m depth) and from Greenland (NEEM deep ice core at 718 m depth) is presented.

EBSD provides information for the characterization of subgrain boundary types and on the dislocations that are likely to be present along the boundary. EBSD analyses, in combination with light microscopy measurements, are presented and interpreted in terms of the dislocation slip systems. The most common subgrain boundaries are indicative of basal $\mathbf{b}=(1/3)\langle 1\bar{2}10 \rangle$ slip, with an almost equal occurrence of subgrain boundaries indicative of prism $\mathbf{b}=[0001]$ or $\mathbf{b}=(1/3)\langle 11\bar{2}3 \rangle$ slip on prism and/or pyramidal planes. A few subgrain boundaries are indicative of prism $\mathbf{b}=(1/3)\langle 1\bar{2}10 \rangle$ slip or slip of $\mathbf{b}=(1/3)\langle 1\bar{2}10 \rangle$ screw dislocations on the basal plane. In addition to these classical polygonization processes that involve recovery of dislocations into boundaries, alternative mechanisms are discussed for the formation of subgrain boundaries that are not related to the crystallography of the host grain.

The finding that subgrain boundaries indicative of non-basal slip are as frequent as those indicating basal slip is surprising. The evidence of frequent non-basal slip in naturally deformed polar ice core samples has important implications for discussions on ice about plasticity descriptions, rate-controlling processes which accommodate basal glide, and anisotropic ice flow descriptions of large ice masses with the wider perspective of sea level evolution.

2.1 Introduction

Ice, particularly the extensive amounts found in the polar ice sheets, impacts the global climate directly by changing the albedo and indirectly by supplying an enormous water reservoir that affects global mean sea level (GMSL) (Bindoff et al., 2007; IPCC, 2007, 2014; Lemke et al., 2007; Stocker et al., 2010). The discharge of material into the oceans is controlled by the melt excess over snow accumulation and the dynamic flow of ice (Hock, 2005). Fast discharge by ice streams of up to several hundreds of meters per year surface velocity (Joughin et al., 2015) includes rapid transportation of ice towards coasts by sliding over the bedrock due to various sub-glacial processes (Vaughan and Arthern, 2007; Hughes, 2009; Beem et al., 2010; Thoma et al., 2010; Wolovick and Creyts, 2016) and by the flow of material towards these rapid ice streams by internal deformation of the whole ice body. Internal deformation is therefore responsible for the required convergent flow geometries at the onset of ice streams (Bons et al., 2016), although at only a few centimetres to metres per year.

Ice sheet flow models (e.g. Huybrechts, 2007; Greve and Blatter, 2009) are based on Glen's flow law (Glen, 1955). This power law was derived from experimental deformation of small ice specimens at higher stresses (0.1 to 1 MPa) than the stress levels experienced by ice in polar ice sheets (Sergienko et al., 2014). Rate-limiting processes for different flow conditions are a matter of extensive discussion, and include contributions from various deformation mechanisms, such as dislocation creep and grain boundary sliding-limited basal slip. In addition, the flow properties are influenced by crystallographic preferred orientation (CPO), recrystallization and the occurrence of second phases (impurities, air or a liquid phase) (Alley, 1992; Goldsby and Kohlstedt, 1997, 2001; Duval and Montagnat, 2002; Alley et al., 2005; Song et al., 2008; Schulson and Duval, 2009; Steinbach et al., 2016; Eichler et al., 2017).

The main deformation process in the creep deformation of natural ice is presumed to be intra-crystalline dislocation glide in combination with climb recovery into subgrain boundary planes (e.g. Schulson and Duval, 2009; Faria et al., 2014a). This is supported by the occurrence of strong c-axis CPO and evidence of extensive dynamic recrystallization in natural ice (e.g. Duval and Montagnat, 2002; Kipfstuhl et al., 2009; Weikusat et al., 2009a; Faria et al., 2014a). Knowledge of dislocation activity and the types of dislocation involved, preferably along the length of an ice core, is therefore of importance for a complete understanding of ice deformation in ice sheets and glaciers.

Ice found on Earth is hexagonal, and dislocation activity along basal (0001) versus prismatic $\{h0\bar{1}0\}$ and pyramidal $\{h0\bar{1}l\}$ planes is highly anisotropic. Critical resolved shear stresses on non-basal planes require 60 to 100 times higher stresses than activating dislocation glide on basal planes (Duval et al., 1983; Ashby and Duval, 1985), so slip on basal planes is expected to dominate. Non-basal slip has been observed by X-ray topography in ice single crystals (e.g. Fukuda and Higashi, 1969; Fukuda et al., 1987; Higashi et al., 1988; Baker, 2003), although only as short segments that are not expected to contribute to the dominant macroscopic deformation (Shearwood and Withworth, 1991). To

date there is no direct evidence for slip on other non-basal planes in natural polycrystalline ice, in spite of the shortage of independent slip systems to deform ice only by basal slip (Hutchinson, 1977). Previous studies are mainly based on experimental deformation carried out under laboratory conditions on polycrystalline (Bryant and Mason, 1960; Barrette and Sinha, 1994; Wei and Dempsey, 1994; Breton et al., 2016; Chauve et al., 2017) and/or single crystal ice (Montagnat et al., 2001, 2003). This study presents the first step in an ongoing study using naturally deformed ice from a single depth level of two deep ice cores from the large ice sheets. The possible dislocation types are derived from an analysis of the subgrain boundaries (SGBs) present in the ice using light microscopy and electron backscatter electron diffraction (EBSD).

Microstructure mapping using light microscopy (LM) of etched surfaces (Figure 2.1), combined with automatic image processing tools, were developed to study ice core samples (Kipfstuhl et al., 2006; Binder et al., 2013a; Weikusat et al., 2017). Grain boundaries (GBs) and SGBs in ice are differentiated using LM images by the depth of thermally etched grooves (Mullins, 1957; Nishida and Narita, 1996; Arnaud et al., 1998; Barnes, 2003). SGBs have lower misorientation angles than GBs, so they form shallower etch grooves (Saylor and Rohrer, 1999), which have lower contrast than GBs in LM images and appear grey rather than black (Figure 2.1a). Sublimation behaviour changes due to boundary properties changes by intrinsic energies changes (e.g. Ketcham and Hobbs, 1969; Suzuki, 1970; Suzuki and Kuroiwa, 1972; Gottstein and Shvindlerman, 1999). In addition to contrast differences in the etched boundaries, the shape of the boundary was used to distinguish between SGBs and GBs: SGBs generally have straighter segments that are controlled by recovery of dislocations and locally tend to fade out, whereas GBs tend to be smoothly curved and are continuous.

X-ray Laue diffraction (Weikusat et al., 2011a) confirmed that the less deeply etched, straighter boundaries observed in LM (Weikusat et al., 2009b) all had low misorientation angles $<5^\circ$ and were SGBs. The SGBs in natural polar ice (Weikusat et al., 2009b) and in deformed artificial ice (Hamann et al., 2007; Weikusat et al., 2009a), can be grouped into certain types according to the alignment of their intersection line (trace) with the etched surface. The SGB trace can be described with respect to the c-axis, or basal plane from polarised LM. Four SGB types were identified (Figure 2.1c; Weikusat et al., 2009b): the N-type SGB has a trace that is predominantly normal to the basal plane, the P-type has a trace parallel to the basal plane, Z-type has an irregular zigzag trace with one orientation that is predominantly normal to the basal plane, and lastly, a SGB with no strong alignment to the basal plane, which is often curved. The N-type SGB is also called the "Nakaya"-type, after the first extensive description in 1958 by Nakaya of low misorientation angle boundaries in ice occurring "in the prism plane ... perpendicular to the gliding layers" (Nakaya, 1958). This type of SGB resembles the classical perception that glaciologists have of an ice grain undergoing recovery and polygonization of dislocations into a SGB (for example, Figure 2 in Alley et al., 1995). The N-type SGB is usually deeply etched and cuts across the whole, or a large part, of the grain. Several N-type SGBs can cluster together with one or two fainter, shorter sub-parallel SGBs. The P-type SGBs are

also straight and often occur in parallel swarms that typically do not cross a grain but fade out after a short distance. Z-type SGBs often appear in networks and intricate patterns that usually form short lengths that do not completely cross a grain. Z-type SGBs are typically less deeply etched and disappear towards the core of the grain. The curved SGB types are rarely observed, possibly because the surface orientation influences the sublimation (see method explanation in Weikusat et al., 2009b).

Based on analysis of LM mapping along an ice core, the P-type SGB is the most frequent of all subgrain boundary types at all depths of the EDML ice core, followed by Z-type, N-type and curved types (Weikusat et al., 2009b). X-ray Laue diffraction (Weikusat et al., 2011a) of approximately 240 shallow sublimation grooves revealed misorientation angles of less than 5° . Many of them (30-40%) were below the angular resolution of 0.5° for Laue, while the majority (50-60%) were below 3° . Only a few percent had misorientation angles between 3 and 5° . From those SGB found with misorientation angles $>0.5^\circ$ (165) analysis indicated that the formation of 45 of them involved significant activity of non-basal slip (Weikusat et al., 2011a). Although X-ray Laue diffraction is a very useful technique for determining the slip system of a boundary in materials with large grain size (e.g. natural ice), measurements and processing of Laue patterns are semi-automatic (Miyamoto et al., 2011) and thus time consuming. Only a limited number of boundaries could be measured. Identifying the proportion of non-basal dislocation activity is crucial for understanding the deformability of ice. Significant non-basal slip might cause a change in the deformation rate-controlling processes and lead to a change in the stress exponent from a value of 2 at low stresses towards 3 at higher stresses (Montagnat and Duval, 2000). To determine slip systems in a large number of SGBs, EBSD is needed.

Cryo-EBSD has been successfully used to study ice (Iliescu et al., 2004; Obbard et al., 2006). Maintaining a stable ice surface during EBSD assessment (Weikusat et al., 2011b; Prior et al., 2015) is essential for these studies to allow correlation between LM etched surfaces and also to differentiate between in-situ deformation occurring in the ice sheet and any relaxation effects that occur during the various sample preparation procedures (Weikusat et al., 2011b; appendix A and B). When a subgrain boundary is formed by the polygonization of geometrically necessary dislocations (Hirth and Lothe, 1982; Weertman and Weertman, 1992; Humphreys and Hatherly, 2004), the crystallography (boundary plane and rotation axis) of subgrain boundaries can be interpreted in terms of the active dislocation slip systems. EBSD provides full crystallographic information (Randle and Engler, 2000) from which slip systems can be derived (Trépiéd et al., 1980; Lloyd et al., 1997; Neumann, 2000; Prior et al., 2002; Piazzolo et al., 2008; Weikusat et al., 2011b; Montagnat et al., 2015), although SGB plane traces are best obtained from the corresponding LM images to avoid any artefacts (Weikusat et al., 2011b).

In this work, SGB types in two ice core samples from Antarctica and Greenland are assessed using LM and cryo-EBSD. A single depth in each ice core is assessed. The boundary types are described using the same terminology as that used in earlier LM studies. The slip systems from a significant number of boundaries in natural ice are inferred using

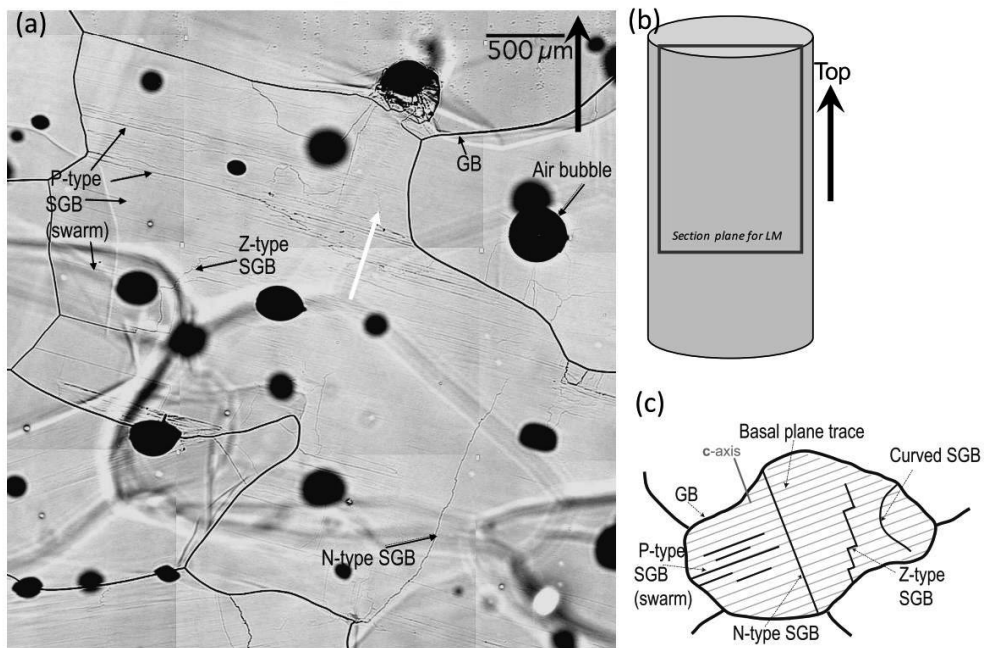


Figure 2.1: (a) Light microscopy (LM) image of the etched surface of EDML ice (694 m of depth). The small black arrow shows different SGB types. The white arrow shows the trace of the c-axis. The large dark features are air bubbles in the ice. Features beneath the surface are out of focus and indistinct. GB is grain boundary and SGB is subgrain boundary. (b) Schematic diagram showing the orientation of sample sections in the ice core. The large black arrows (a, b) point towards the upper surface of the ice sheet. (c) Schematic of the four types of SGBs described in the text. Figure after Weikusat et al. (2009b).

EBSD, so that the importance of non-basal slip activity that has been previously identified in a limited number of boundaries using combined X-ray and LM studies can be assessed.

2.2 Material and Methods

Samples from two polar ice cores were used for this study: NEEM (North Greenland Eemian ice drilling) and EDML (European project for ice coring in Antarctica - Dronning Maud land). Data was collected on a single, roughly equivalent depth for each core in order to obtain a first comparable statistic of SGB type.

The EDML samples were obtained from 656 m depth of the EPICA deep ice core, drilled between 2003 to 2006 at Kohnen station ($75^{\circ}00'S$, $0^{\circ}40'E$, 2892 m a.s.l.) in the Atlantic sector of east Antarctica (Orter et al., 2009; Ruth et al., 2007; Wilhelms et al., 2007; Wilhelms et al., 2014). The NEEM samples were obtained from 718 m depth and were drilled between 2008 and 2012 in northwest Greenland ($77^{\circ}27'N$, $51^{\circ}03'W$, 2484 m a.s.l.) (NEEM community members, 2013; Rasmussen et al., 2013). Both sample depths originated from snow deposited during the Holocene (Ruth et al., 2007, Rasmussen et al., 2013), and have comparably small impurity concentrations (e.g. Dansgaard et al., 1982;

EPICA community members, 2004, 2006; Kuramoto et al., 2011; Wegner et al., 2015). Both drill sites are located on ice ridges or ice divides with horizontal flow velocities at the surface of 0.8 m yr^{-1} for EDML (Wesche et al., 2007) and 6 m yr^{-1} for NEEM (personal comm. Christine Hvidberg, Okt. 2016). The divide flow at EDML is significantly more divergent compared to NEEM (Weikusat et al., 2017). This flow results in a stronger and clearer c-axes CPO, giving a vertical girdle in pole figures in the central part of the core, while in NEEM the c-axis CPO resembles an elongated single maximum (Montagnat et al., 2014). In order to compare similar flow conditions, the sampled depths for this study were selected to reflect the deformation regime expected at ice divides, that is, extension normal to the dividing ridge, with almost no deformation along the ridge, and with vertical compression (triaxial deformation state). The c-axis CPO was not strongly developed and similar for the depths selected: the eigenvalues of the second-order orientation tensor, which is typically used in glaciology, are $e_1=0.55$, $e_2=0.29$, $e_3=0.16$ for NEEM at 718 m depth, and $e_1=0.46$, $e_2=0.36$, $e_3=0.18$ for EDML at 656 m depth (Eichler et al., 2013, Weikusat et al., 2013, 2017; Montagnat et al., 2014).

Samples were transported at -25°C from Antarctica to Bremerhaven, and from Greenland to Bremerhaven via Copenhagen and subsequently stored at -30°C . Samples ($50 \times 100 \times 90 \text{ mm}$) were cut parallel to the long axis of the drill core (Figure 2.1b) using a band saw and polished in a -25°C cold laboratory in Bremerhaven according to standard procedures using a microtome (e.g. Pauer et al., 1999; Wang et al., 2002). LM microstructure mapping was performed at -20°C at the Alfred Wegener Institute (AWI) to obtain an overview of the microstructure using a Leica DMLM (Kipfstuhl et al., 2006) for high spatial resolution images (1 pixel edge $3.3\mu\text{m}$) and a large area scanning microscope (Krischke et al., 2015) with slightly lower spatial resolution (1 pixel edge $5\mu\text{m}$). The method was also applied on-site immediately after drilling (in 2003 for the EDML and in 2010 for the NEEM samples), which allowed the monitoring of any microstructural changes caused by pressure and temperature change during transportation and storage (Miyamoto et al., 2009; Weikusat et al., 2012) and to locate regions of interest for EBSD, particularly as the subgrain microstructures were heterogeneously distributed. The c-axes and CPO were measured in the depth ranges of the EBSD samples with an automated fabric analyser system of the Australian Russell-Head type (Peternell et al., 2010).

Typical SGB microstructures were identified in LM images and selected for cryo-EBSD analysis. Small specimen blocks (approximately $8 \times 8 \times 5 \text{ mm}$) were cut using a handsaw for EBSD studies (Appendix A). As SGBs in ice are mainly located close to GBs, triple junctions or grain necks (Weikusat et al., 2009b), EBSD mapped areas could be selected such that up to 15 SGBs could be measured in each map and up to 10 maps could cover almost the total area of the small block. The small blocks were again polished by microtoming and sublimation. A further high-resolution LM microstructure mapping step was performed. Polished specimens were stored in dry ice (solid carbon dioxide, -78.5°C) to reduce any further sublimation during transfer to Utrecht University (about 2 days to 3 weeks).

Data was collected using an FEI Nova Nanolab 600 scanning electron microscope (SEM), equipped with an EBSD detector (Oxford Instruments HKL Technology, Abingdon, U.K.), a cryo-preparation station and a cryo-stage (Quorum Technologies Ltd, Ringmer, U.K.). Samples transfer to the SEM involved a further short sublimation step of a few minutes under vacuum (Weikusat et al., 2011b; Appendix B). Typical measurement conditions for EBSD mapping were a working distance of 6-8 mm, -123 to -150°C sample stage temperature (-145 to -170°C cold trap temperature), 5×10^{-5} to 3×10^{-6} hPa chamber pressure, 10 or 20 kV accelerating voltage and 8.4 nA beam current. The sample surface was kept stable for 8–9 h under these conditions. Microstructures were imaged using secondary electrons. Channel 5 software (Oxford Instruments) was used to collect and analyse the EBSD data. Typical mapping rates were 0.15s per pixel and indexing rate 90%. EBSD data processing was performed using standard noise reduction and orientation filtering as described by (Weikusat et al., 2011b). Angular resolution was about 0.5° after orientation averaging. For EDML (656 m of depth) four individual samples were mapped with EBSD; for NEEM (718 m of depth) ten individual samples were mapped.

Each individual SGB was imaged using LM and relocated in the SEM before EBSD mapping. The pixels across boundaries in an EBSD map were selected manually and saved as subsets of the map, so that a narrow range of orientations from the boundary were analyzed, which avoided any orientation changes occurring away from the subgrain boundary. An upper misorientation angle of 5° was taken for all SGBs (Weikusat et al., 2011b). Neighbour pixel misorientation angles between 0.5 and 5° were plotted in an inverse pole figure (IPF) for each subset to determine the rotation axes of the SGBs. The trace of the SGB was determined from the LM image and compared to the EBSD orientation information to avoid any artefacts caused by charging or poor sample alignment with respect to the tilt axis (Weikusat et al., 2011b).

2.3 Results

The general appearance of the microstructures in the depth range of the two samples analyzed in this study are shown in Figure 2.2. Grains sizes range from a few millimetres to a few centimetres. Grain shapes are roughly equiaxed, interlocking and have curved boundaries. Several island grains are present. Changes in colour show lattice rotations within some grains.

2.3.1 Subgrain boundary types

Typical LM images for the EDML and NEEM samples are shown in Figures 2.3a and 2.4a respectively. The stripy contrast in Figure 2.3a (an artefact of automatic image processing) is aligned to the ice core axis, as in Figure 2.1. Two SGB types are labelled in Figure 2.3a: a P-type boundary, with a trace parallel to the basal plane and an N-type boundary, with a trace that is predominantly perpendicular to the basal plane.

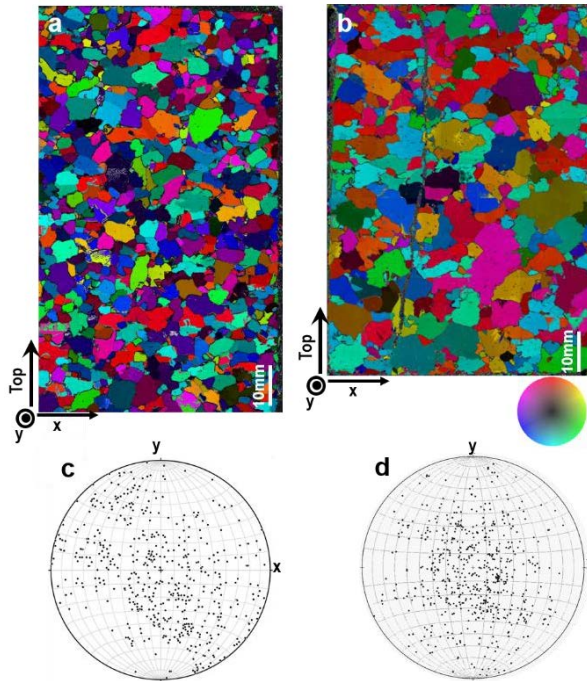


Figure 2.2: General appearance of the c-axes microstructure of (a) EDML microstructures at 656 m of depth and (b) NEEM at 718 m of depth. The orientation of the c-axes is shown by the coloured disc (the central grey colour indicates a c-axis that is perpendicular to the plane of the image). Panels (c) and (d) show pole figures (equal area, horizontal plane, upper hemisphere projection) of the c-axes for individual grains (one point per grain), 525 grains in the EDML sample and 601 grains in the NEEM sample.

2.3.2 Misorientation angle range used for subgrain boundaries using EBSD

Approximately 230 individual SGBs were measured in the EDML samples and about 180 in the NEEM samples using EBSD. More SGBs (ca. 30% for EDML and 20% for NEEM) were identified in LM images than in EBSD maps. Red arrows show three such boundaries in an LM images (Figure 2.3a and 2.4a) that were absent in the corresponding EBSD maps (Figure 2.3b and 2.4b) of the same area. The boundaries are likely SGBs with misorientation angles that were below the angular detection limit of $\sim 0.5^\circ$ found using the EBSD mapping conditions.

2.3.3 Analysis of subgrain boundary types

The same morphological SGB types (N-, P-, Z-type and curved) identified in LM images were observed in EBSD mapped microstructures. The different SGB types were analyzed using LM images and EBSD mapped data (Figures 2.3 and 2.4): the trace of the boundary and the rotation axes, \mathbf{R} , were used to determine the slip systems.

2.3.3.1 Subgrain boundary traces

Small rotation differences were observed between many EBSD images and the LM images (see Figures 2.3a and b). The orientations of the SGB traces were therefore made using the LM images, combined with EBSD orientation data (Figures 2.3c and 2.4c).

2.3.3.2 Subgrain boundary rotation axes

Twelve SGB subsets used to determine rotation axes are highlighted in both Figure 2.3 for the EDML ice core sample and in Figure 2.4 for the NEEM ice core sample. The axes are displayed in inverse pole figures (Figures 2.3d and 2.4d). The rotation axes are spread over a large portion of the IPF. Nevertheless, some rotation axes cluster around certain poles.

The following types of rotation axes, \mathbf{R} , found in the two samples are summarised below.

1. \mathbf{R} is in the basal plane (0001) with a general direction $\langle hki0 \rangle$ (Figure 2.3d, SGBs 1,5,6,7 and Figure 2.4d SGBs 6,11,12). Two special cases of this type of rotation axes occur, in which \mathbf{R} is either parallel to the prism plane normal, $\langle 10\bar{1}0 \rangle$ (Figure 2.3d, SGB 2, 3 and Figure 2.4d, SGBs 5, 8), or parallel to the a-axis $\langle 1\bar{2}10 \rangle$ (Figure 2.3d, SGB 4, 10 and Figure 2.4d, SGBs 2, 7, 9).
2. \mathbf{R} is parallel to the c-axis, [0001] (Figure 2.3d, SGB 8 and Figure 2.4d, SGB 3).
3. \mathbf{R} is parallel to the pyramidal plane normal, $\langle h0\bar{1}l \rangle$ (Figure 2.3d, SGB 9 and Figure 2.4d, SGB 4).
4. \mathbf{R} is not parallel to a specific orientation but dispersed (Figure 2.3d, SGBs 10, 11, 12 and Figure 2.4d, SGB 1).

2.3.3.3 Combination of subgrain boundary traces and rotation axes

In order to make a comparison with SGB statistics used in LM studies, similar arrangements of the SGB plane with respect to the basal plane were chosen. These arrangements are shown in Figure 2.5, which is an extended version of that given by Weikusat et al. (2011a, b). A SGB boundary plane that is perpendicular to the basal plane (N-type) is shown in Figures 2.5a and 2.5b and a SGB plane that is parallel to the basal plane (P-type) is shown in Figures 2.5c and 2.5d. For each of these arrangements, simple end member arrangements are chosen for the rotation axes (dots in Figure 2.5e) with only one end member \mathbf{R} lying in the basal plane (shaded in Figure 2.5e). In Figures 2.5a and 2.5d, \mathbf{R} is in the basal plane (perpendicular to the c-axis) and in Figure 2.5b and 2.5c \mathbf{R} is parallel to the c-axis. A shorthand notation is introduced to describe these four types of boundary, N[a], N[c] P[c] and P[a] (Table 2.1). N[a] describes a SGB trace normal to the basal plane (N-type) with rotation axis in the basal plane, (e.g. $\langle 1\bar{2}10 \rangle$, or $\langle 10\bar{1}0 \rangle$ or $\langle hki0 \rangle$), this is a tilt SGB (Figure 2.5a). N[c] is also a tilt SGB of N-type but with a rotation axis parallel to the c-axis (Figure 2.5b). P[c] has a SGB parallel to the basal plane (P-type) with rotation axis [c] and is a twist type of boundary (Figure 2.5c). P[a] is also a tilt boundary with the boundary parallel to the basal plane and a rotation axis in the basal plane, (e.g. $\langle 1\bar{2}10 \rangle$, or $\langle 10\bar{1}0 \rangle$ or $\langle hki0 \rangle$). A compilation of the complete data set of

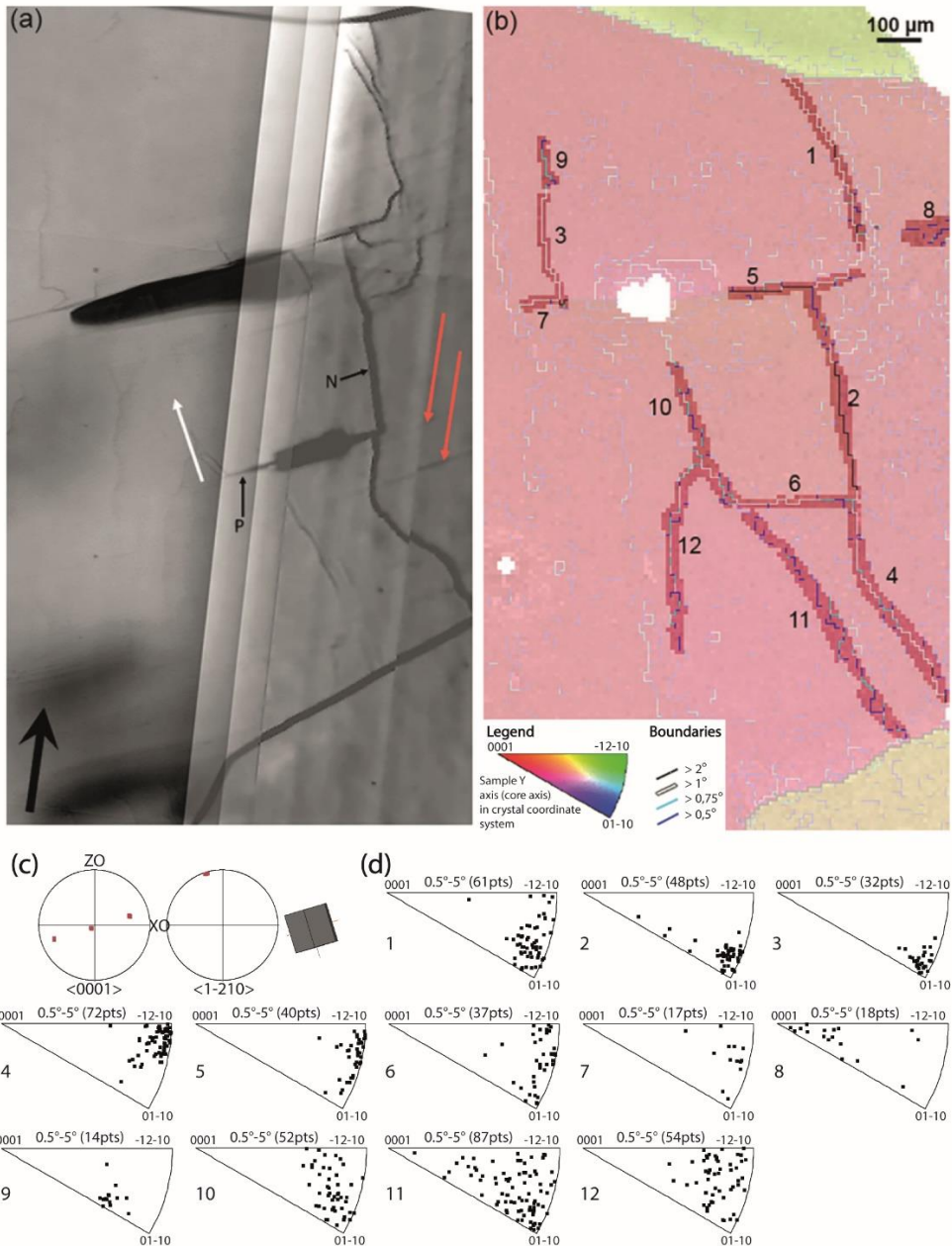


Figure 2.3: Microstructures used for the analysis of SGB types and slip systems: EDML sample (656 m of depth). (a) LM image of a map of sublimation-etched surface. The black arrow points to the top of the ice core. The white arrow indicates the orientation of the c-axis. A P-type boundary and an N-type boundary are labelled as examples. The red arrows show SGBs in LM that are not observed in the corresponding EBSD map. (b) EBSD map of the same area showing subsets of SGBs labelled 1–12. (c) Pole figure (equal area, upper hemisphere projection) of the central grain in the EBSD map showing the c- and a-axes and a schematic of the crystal orientation. (d) Inverse pole figures showing the rotation axes (equal area, upper hemisphere projection) of neighbouring pixels across the SGBs 1–12.

combined information from rotation axes and SGB trace alignments is given in Table 2.2. The number frequency of SGBs is shown in terms of the rotation axes and the orientation of the SGB plane trace with respect to the basal plane trace.

The majority of SGBs could be allocated to certain classes with a well-defined trace orientation and rotation axis. The most common SGB types have \mathbf{R} in the basal plane, with roughly an equal proportion of P and N plane traces, and \mathbf{R} normal to the basal plane. SGBs of the P[a] type are shown in Figure 2.3 for SGBs 5 and 7 and in Figure 2.4 for SGBs 7, 9 and 11. SGBs of the N[a] type are shown in Figure 2.3 for SGB 1-4 and in Figure 2.4 for SGBs 2, 5, 6, 8 and 10. SGB 8 in Figure 2.3 and SGB 3 in Figure 2.4 are examples of a P-type SGB with a rotation axis [0001] (P[c] type). SGBs with this rotation axis are rare in both ice cores, particularly the NEEM core (Table 2.2). SGB 3 in Figure 2.4 is another example of a SGB with $\mathbf{R}=[0001]$, however combined with a N-type SGB trace (N[c]). SGB 9 (Figure 2.3) and the left half of SGB 4 (Figure 2.4) are examples of a very rare N-type with $\mathbf{R} \langle \text{hki}0 \rangle$. SGB 10 and 11 (Figure 2.3) show N-type trace with \mathbf{R} dispersed: there is a slightly higher fraction of dispersed axes in EDML compared to NEEM.

The EBSD data are grouped (Table 2.2, rightmost 3 columns) into simplified statistics in order to make a direct comparison between EBSD and X-ray Laue diffraction data published for the EDML ice core (Table 2 in Weikusat et al., 2011a). Table 2.2 confirms the conclusion of the X-ray Laue study, which showed a dominance of SGB with a rotation axes in the basal plane.

2.4 Discussion

2.4.1 CPO and dislocation creep

The microstructure and CPO (Figure 2.2) suggest dislocation creep as the main deformation process with wide-spread formation of substructures. The CPOs in polar ice in general are consistent with glide of basal dislocations as the main mechanism accommodating deformation (Duval and Schulson, 2009; Faria et al., 2014a, b & references therein). The results presented here confirm that subgrain boundaries are very common in ice, such that the majority of all grains in all depths contain subgrains (Weikusat et al., 2009b), which reflects the high temperature deformation ($>0.8 T_m$) of natural ice.

2.4.2 Subgrain boundaries controlled by and geometrically related to host grain crystallography

Those SGBs with clustered rotation axes are described in terms of the host crystallography. The spread in orientation of these axes is consistent with errors expected from low angle misorientation boundaries (Prior et al., 1999). This study provides statistics of around 400 SGBs in Antarctic and Greenland ice. Analysis of LM and EBSD microstructures are described in the following paragraphs in terms of the possible slip involved in forming the observed SGB types. By means of the geometrical relation with the host crystal the SGB types are interpreted in terms of possible active dislocation slip systems. The term basal slip

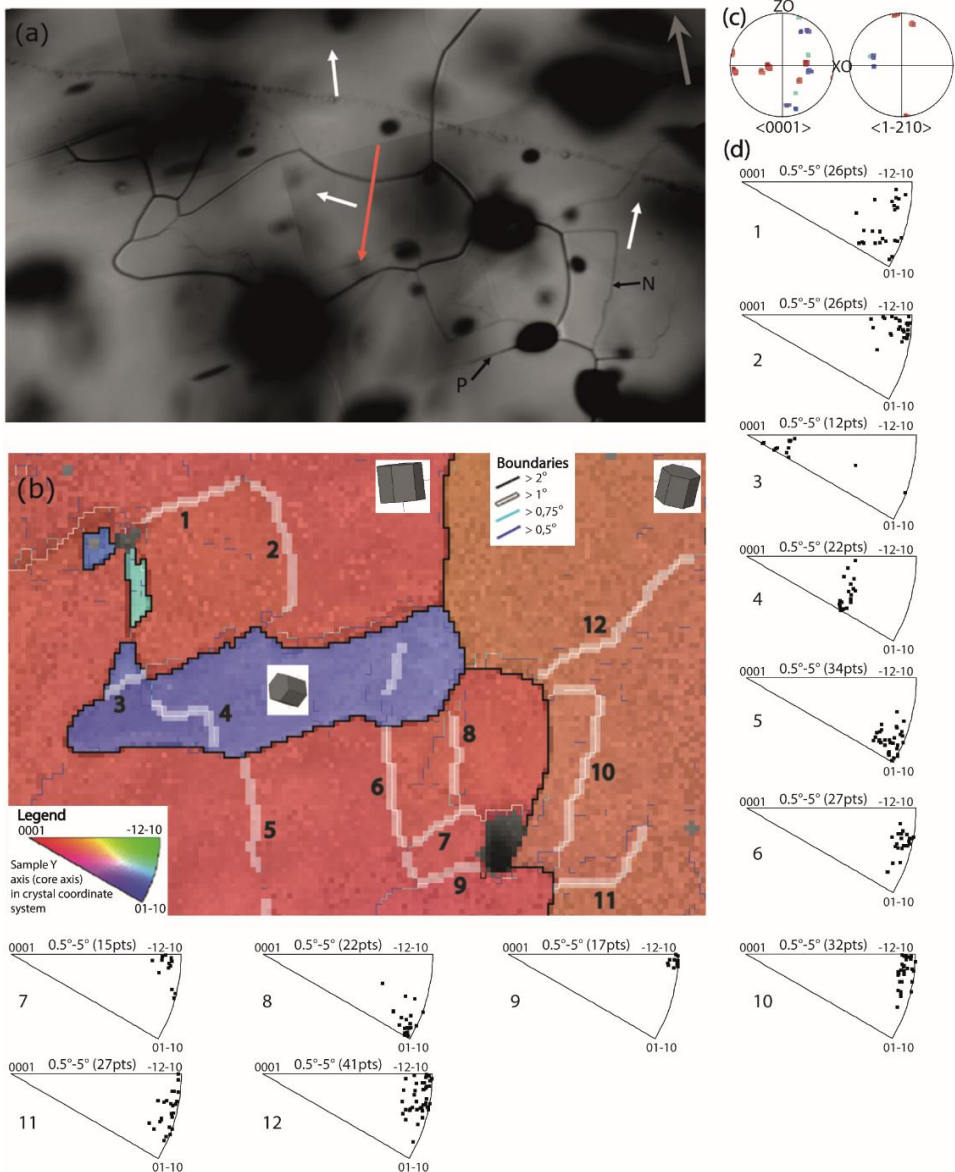


Figure 2.4: Microstructure analysis from the NEEM sample (718 m of depth). (a) LM microstructure map of sublimation-etched surface showing several GBs and SGBs. The vertical axis of the ice core is indicated by a dark grey arrow. The white arrows indicate the orientation of the c-axes. A P-type boundary and an N-type boundary are labelled as examples. The red arrow shows a SGB in the LM image that is not observed in the corresponding EBSD map. (b) The corresponding EBSD map showing SBG subsets labelled 1–12 and a schematic of the crystal orientation in the three grains shown. (c) Pole figure (equal area, upper hemisphere projection) of the three grains shown in the EBSD map showing the c- and a-axes with the colour coding as in panel (b). (d) Inverse pole figures showing the rotation axes (equal area, upper hemisphere projection) of the SGBs 1–12.

is used to describe dislocation glide on the basal plane and non-basal slip to describe dislocation glide on other glide planes.

- *N-type tilt boundaries with rotation axis in basal plane: N[a]*. A subgrain boundary normal to the basal plane (N- or Z-type) and a rotation axis, \mathbf{R} , in the basal plane with $\mathbf{R}=\langle hki \rangle$, can be produced by an array of edge dislocations, with $\mathbf{b}=(1/3)\langle 1\bar{2}10 \rangle$ ($\mathbf{b}=\langle \mathbf{a} \rangle$), gliding in the basal plane, where \mathbf{b} is the Burgers vector of the dislocation (Figure 2.5a). The observed N-type boundaries often have a general rotation axis orientation $\langle hki \rangle$ or are sub-parallel to $\langle 10\bar{1}0 \rangle$ or $\langle 1\bar{2}10 \rangle$, which can be explained by the glide and recovery of dislocations with Burgers vector of $[\mathbf{a}1]$ and $[\mathbf{a}2]$. The vast majority of all N-type SGBs (around 75 to 85%) have rotation axes in the basal plane and thus are potentially tilt boundaries made up by $\mathbf{b}=\langle \mathbf{a} \rangle$ edge dislocations that can glide on the basal plane (Table 2.2); that is, many N[a] boundaries are likely to be formed by polygonization of dislocations produced by basal slip.

If an N[a] boundary is a twist boundary or has a significant twist component of the misorientation, then non-basal dislocations should be present along the boundary (see interactive discussion). N[a] twist boundaries could possibly be made with i) one set of $\mathbf{b}=\langle \mathbf{a} \rangle$ dislocations and a second set of $\mathbf{b}=\langle \mathbf{c} \rangle$ dislocations or ii) with 2 sets of $\mathbf{b}=(1/3)\langle 11\bar{2}3 \rangle$ ($\mathbf{b}=\langle \mathbf{c}+\mathbf{a} \rangle$) dislocations. In the case of the N[a] boundaries it is not possible with 2D EBSD data to determine if the boundaries are pure tilt boundaries or if they have a twist component. Displaying the rotation axes and SGB normal in pole figures (in the sample reference frame) can be used to identify tilt and twist boundaries, however, in 2D-EBSD the dip of the SGB plane is not known. As N-type boundaries are commonly observed to be perpendicular to basal slip bands in transmitted light images (Weikusat et al., 2009b) and as basal slip is expected to be the dominant activated slip system (Hondoh 2000, 2009; Piazzolo et al., 2008), it is expected that the N[a] SGBs will be dominantly produced by basal slip.

- *N-type tilt boundaries with rotation axis parallel to c-axis: N[c]*. A subgrain boundary with a plane normal to the basal plane and with $\mathbf{R}=[0001]$ can be produced by an array of $\mathbf{b}=\langle \mathbf{a} \rangle$ edge dislocations slipping on a prismatic glide plane such as $\{10\bar{1}0\}$ or $\{1\bar{2}10\}$. Like the N[a] type SGB, these dislocations have Burgers vectors in the basal plane, but unlike the N[a] type SGB, the N[c] glide on non-basal planes (Figure 2.5b), that is, N[c] boundaries involve non-basal slip. N[c] SGBs were rarely observed and made up only a few percent of the N-type SGBs (Table 2.2).

- *P-type twist boundaries: P[c]*. A subgrain boundary accumulating dislocations parallel to the basal plane (P-type) and a resulting rotation around the c-axis $[0001]$ can be produced by two or three sets of basal screw dislocations (Figure 2.5c) with Burgers vectors $\mathbf{b}=\langle \mathbf{a} \rangle$ (Hondoh, 2000). Basal twist boundaries represent a minority (~2 to 8%) of all parallel SGBs (Table 2.2).

- *P-type tilt boundaries: P[a]*. A subgrain boundary parallel to the basal plane (P-type) and a rotation axis in the basal plane ($\langle 1\bar{2}10 \rangle$ or $\langle 10\bar{1}0 \rangle$) can be produced by an array of non-basal edge dislocations with $\mathbf{b}=[0001]$ ($\mathbf{b}=\langle \mathbf{c} \rangle$) or $\mathbf{b}=\langle \mathbf{c}+\mathbf{a} \rangle$ (Figure 2.5d). An

array of $\mathbf{b}=[\mathbf{c}]$ edge dislocations with $\{10\bar{1}0\}$ glide plane has a rotation axis $\mathbf{R}=\langle 1\bar{2}10 \rangle$, while an array of $\mathbf{b}=[\mathbf{c}]$ edge dislocations with $\{1\bar{2}10\}$ glide plane has $\mathbf{R}=\langle 10\bar{1}0 \rangle$. Many boundaries have a general rotation axis $\langle hki0 \rangle$, suggesting that the glide planes of the $\mathbf{b}=[\mathbf{c}]$ dislocations can occur on a range of $\{hki0\}$ prismatic planes. Dislocation arrays of $\mathbf{b}=\langle \mathbf{c}+\mathbf{a} \rangle$ with two Burgers vectors, $\mathbf{b}_1=\mathbf{c}+\mathbf{a}_1$ and $\mathbf{b}_2=\mathbf{c}+\mathbf{a}_2$, could also produce this type of SGB. The $\langle \mathbf{c}+\mathbf{a} \rangle$ dislocations may glide on prism or pyramidal planes. Most of the P-type boundaries (~ 72 to 90%) are tilt boundaries with non-basal dislocations (Table 2.2).

A main result of this study is that a very high fraction of SGBs (N[c] & P[a]) in polar ice (ca. 30-40% of all SGB) can be inferred to consist of non-basal dislocations and could therefore be formed by non-basal slip. Although somewhat unexpected with respect to the macroscopic behaviour of ice, this result is in accordance with earlier X-ray work on

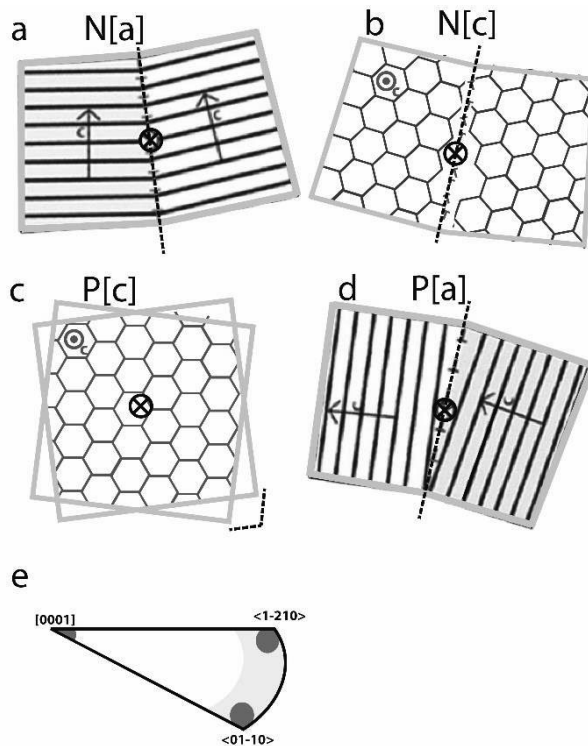


Figure 2.5: Schematic diagram showing some SGB types (modified from Weikusat et al., 2011b). Four end member types of boundaries are shown. The rotation axes, \mathbf{R} , are marked as circles with an X inside; the parallel lines and hexagons represent the basal plane and are perpendicular to the c-axis, shown by arrows or as a grey circle with a dot inside. The dashed lines denote the SGB plane trace; in panel (c) the SGB plane is in the plane of the paper. Panels (a) and (b) show SGBs with the boundary plane perpendicular to the basal plane, which are N-type SGBs. Panels (c) and (d) show subgrain boundary planes parallel to the basal plane, which are P-type SGBs. \mathbf{R} is perpendicular to the c-axis in (a) and (d) and is parallel to the c-axis in (b) and (c). (e) A simplified inverse pole figure of the rotation axes parallel and perpendicular to the c-axis (dark grey circles). Possible slip systems for these SGB configurations are described in the text.

a limited number of measurements in polar ice (Weikusat et al., 2011a). This is in agreement with recent finding of Chauve et al. (2017) who found up to 35% non-basal slip in experimentally deformed artificial ice. The activation of non-basal slip suggests that locally within grains stresses were high enough to activate the harder slip systems. In common with many materials, natural ice often has a weakly developed core and mantle substructure (Gifkins, 1976; Faria et al., 2014a) with more SGBs occur near the grain boundaries. The development of non-basal SGBs in the grain mantle is consistent with the stress concentration near grain boundaries and triple points, as has been found for hexagonal metals (Ion et al., 1982; Drury et al., 1985). In magnesium non-basal slip only occurs in the grain mantles at temperatures less than $T < 0.6 T_m$ (Ion et al., 1982), while at higher temperatures non-basal slip is activated throughout the grains (Ion et al., 1982; Drury et al., 1985).

Table 2.1: Summary and terminology of slip systems interpreted from analyses of LM and EBSD. **R** is the rotation axis of the subgrain boundary, **** is the Burgers vector for slip. “Prim” is for primary and “Sec” is for secondary. “Prism” stands for prismatic and “Pyr” stands for pyramidal.

SGB geometry			Slip system			Frequency	Examples	
Name	Trace	Rotation axis <R>	Slip plane	Burgers vector 	Tilt/ Twist	% of all SGB	EDML (Fig 3)	NEEM (Fig 4)
N[a]	N-type	$\langle 1\bar{2}10 \rangle$ or $\langle hki0 \rangle$	Basal	$\langle 1\bar{2}10 \rangle$	Tilt	27-41	SGBs 1,2,3,4	SGBs 2, 5, 6, 8, 10
N[c]	N-type	[0001]	Prism	$\langle 1\bar{2}10 \rangle$	Tilt	1	-	SGB 3
P[c]	P-type	[0001]	Basal	$\langle 1\bar{2}10 \rangle$	Twist	1-3	SGB 8	-
P[a]	P-type	$\langle 1\bar{2}10 \rangle$	Prim Prism {1-100}	[0001] or $\langle 11\bar{2}3 \rangle$	Tilt	5-7		SGB 7, 9
P[a]	P-type	$\langle 10\bar{1}0 \rangle$	Sec Prism {1-210}	[0001] or $\langle 11\bar{2}3 \rangle$	Tilt	6-10		-
P[a]	P-type	$\langle 1\bar{2}10 \rangle$ or $\langle hki0 \rangle$	Prism/ Pyr	$\langle 11\bar{2}3 \rangle$	Tilt	29-37	SGB 5, 6, 7	SGB 1, 11

Table 2.2: Summary of the EBSD data statistics for the EDML and the NEEM samples. The columns show the SGB rotation axes, **R**, and rows show the alignment of the SGB traces with respect to the basal plane shown in Figure 2.5. *n* is the number of SGBs and * signifies dispersed rotation axes. The outermost three columns give simplified statistics of the same data set for comparison with X-ray Laue diffraction (Weikusat et al. 2011a).

	Rotation axis	[0001]	$\langle 1\bar{2}10 \rangle$	$\langle 10\bar{1}0 \rangle$	$\langle hki0 \rangle$	$\langle h0i\bar{l} \rangle$	*		[0001]	in basal plane	*
SGB trace with basal plane	EDML (total $n_{>0.5}=227$)										
	N-type	3	11	21	30	2	16		3 _{N[c]}	62 _{N[a]}	18
	P-type	7	12 _{P[a]prim}}	14 _{P[a]sec}}	40	2	16		7 _{P[c]}	66 _{P[a]}	18
	other	7	10	5	15	0	16		7	30	16
	NEEM (total $n_{>0.5}=181$)										
	N-type	2	20	23	33	0	13		2 _{N[c]}	76 _{N[a]}	13
	P-type	2	13 _{P[a]prim}}	19 _{P[a]sec}}	36	0	5		2 _{P[c]}	68 _{P[a]}	5
	other	0	1	3	3	0	8		0	7	8

2.4.3 Implications on the origin of non-basal dislocations from extended dislocations

For the ice core samples from EDML and NEEM, the common N[a] type SGBs (Table 2.2) are made of basal dislocations (basal $\langle a \rangle$ slip), while the equally common P[a] boundaries consist of non-basal $\mathbf{b}=[c]$ or $\langle c+a \rangle$ dislocations (prism [c] slip).

Hondoh (2000, 2009) proposed that P[a] boundaries could be formed by local slip of $\langle c+a \rangle$ screw dislocations in grains that were shortened parallel to the c-axis. According to Hondoh (2009) the strain produced by non-basal slip is rather limited and in the case of $\langle c+a \rangle$ pyramidal slip (Muguruma et al., 1966), limited strain can result in the formation of a P-type tilt wall made up of immobile [c] dislocations. In contrast, only a small proportion of the dislocations involved in basal slip are likely to become organized into dislocation walls. Analogous to the explanation by Hondoh (2009) it is here proposed that the local slip of the $\langle c+a \rangle$ screws formed an immobile edge dislocation dipole (Figure 2.6a). The dipole dislocations can dissociate into two dislocations, one with $\mathbf{b}=\langle a \rangle$ glides away, leaving

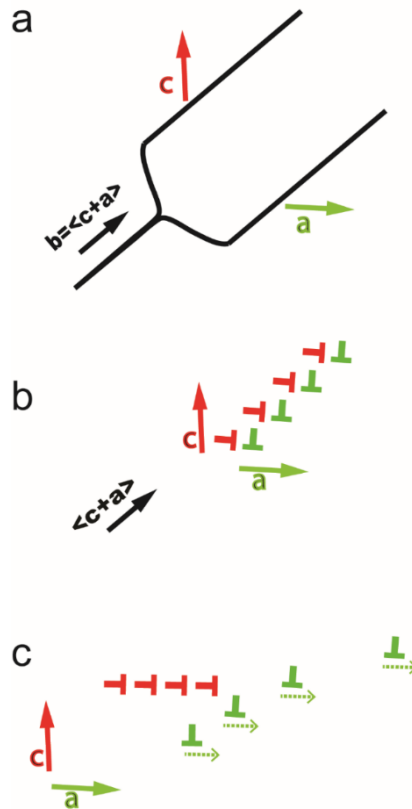


Figure 2.6: Schematic drawing of the dissociation of screw dislocation $\mathbf{b}=\langle c+a \rangle$ as one possibility to form a P[a] subgrain boundary; (a) $\langle c+a \rangle$ screw dislocation extending into an edge dislocation dipole (after Hondoh, 2006). (b) Dissociation into $\mathbf{b}=[c]$ and $\langle a \rangle$ dislocations. (c) $\mathbf{b}=\langle a \rangle$ dislocations glide away and $\mathbf{b}=[c]$ dislocations left behind to form P-type SGB.

behind a $\mathbf{b}=[\mathbf{c}]$ dislocation (Figure 2.6b). By repeating this process, an array of $\mathbf{b}=[\mathbf{c}]$ dislocations in the basal plane is formed (Figure 2.6c). shortening parallel to the c-axis can be accommodated by local non-basal slip and by climb of the $\mathbf{b}=[\mathbf{c}]$ dislocations.

The other type of SGB that indicates non-basal slip activity is the $N[\mathbf{c}]$ type (prism $\langle \mathbf{a} \rangle$ slip), which occur but are uncommon in the ice core samples (Table 2.2). Hondoh (2000, 2009) suggested that the $\mathbf{b}=\langle \mathbf{a} \rangle$ dislocations gliding on the prismatic planes could also move on to the basal plane, producing very irregular slip planes. The geometry of slip lines produced by prism $\langle \mathbf{a} \rangle$ slip on single crystals is similar to the Z-type SGBs (Weikusat et al., 2009b); thus some Z-boundaries may be non-basal slip bands rather than subgrains. This activation of non-basal slip has been directly observed in ice single crystals using X-ray topography (Higashi, 1988). Stress concentrations produced at grain boundaries or free crystal surfaces can result in the activation of non-basal dislocations (Levi et al., 1965; Shearwood and Whitworth, 1991; Wei and Dempsey, 1994). These studies show that strain accommodated by non-basal slip is limited, as the non-basal dislocations only glide on small portions of the slip plane, leaving behind a high density of immobile dislocations. As deformation in ice sheets occurs at very low stress and slow strain rates, the occurrence of recovery could make non-basal slip easier (Faria et al., 2014a), although it should be noted that non-basal slip systems have a higher stress exponent than basal slip, so that the strength difference between the slip systems will increase with decreasing stress.

Many studies assume that all subgrains form by polygonization of geometrically necessary dislocations (Ashby, 1970; Ashby and Duval, 1985). However, in-situ deformation experiments on rock analogues (Means and Ree, 1988) and observations in some rock-forming minerals (Drury and Pennock, 2007) have shown that subgrains may originate in several ways. Means and Ree (1988) recognised seven types (I to VII) of subgrain boundary in octachloropropane (OCP) deformed at 0.7 to 0.8 Tm. Two of these seven types are controlled by the host grain crystallography as they form from classical polygonization (I) and from glide polygonization (II). The SGB types discussed above ($N[\mathbf{a}]$, $N[\mathbf{c}]$, $P[\mathbf{c}]$, $P[\mathbf{a}]$) are all related to the host grain crystallography and can thus be considered as Means and Ree type I or II. The crystallography of Means and Ree type I SGBs are determined by the geometrically necessary dislocations that accommodated the lattice bending in the grain leading to polygonization. Means and Ree (1988) suggested that their type II SGBs formed by glide polygonization and thus also reflect the active slip systems in the grain. This process is similar to kinking, which has been observed in ice on the crystal scale in experimentally deformed samples (Wilson et al., 1986), but also on the polycrystal scale (Jansen et al., 2016) in depth regimes below those of the samples used in this study where the CPO is very strong. Type II, however, will experience some modification of the SGB crystallography, as these are mobile tilt boundaries and a boundary migrating through a bent lattice will collect all types of dislocations. This could explain parts of the dispersion of the rotation axes observed (Figure 2.3d and 2.4d). Means and Ree (1988) found that two thirds of the SGBs in their OCP experiment were type I and II boundaries related to the crystallography of the lattice and thus influenced by the active slip systems. Here it is also inferred that about two-thirds of SGBs are crystallographically

controlled; the remaining one third of SGBs do not have a relationship to the crystallography of the host grain.

2.4.4 Subgrain boundaries without connection to host grain crystallography

The geometry of approximately 20-30% of all measured SGB cannot be related to the host crystal orientation, so either the SGB trace cannot be determined because it is curved or at an arbitrary angle to the basal plane, or that the rotation axis of the misorientation is dispersed (Table 2.2). These SGBs could be formed by processes similar to that described by Means and Ree for type III to VII, which are: misorientation reduction by grain rotation or coalescence (III, IV), misorientation geometry resulting from combining two boundaries by impingement (V), misorientation grown from an existing boundary (VI) and statistically evolving boundaries from optically strain-free grains (VII).

The crystallography of type III and IV SGBs should have no simple relationship to the active slip systems, because these low angle boundaries are formed by reduction of the misorientation angle between grain boundaries (III) or by coalescence of migrating grain boundaries (IV). A particular rotation axis is not expected for these boundaries, although the occurrence of a strong CPO will tend to produce preferred rotation axes (Mainprice et al., 1993). At deeper depth levels in polar ice, where a characteristically strong CPO development with ice sheet depth is generally observed (Faria et al., 2014b; Fitzpatrick et al., 2014; Montagnat et al., 2014; Jansen et al., 2016; Weikusat et al., 2017 and references therein), it is suggested that type III SGBs might occur. SGBs that develop from GBs may be recognisable as such because they are part of the grain boundary network. In order to evaluate this, other methods such as the statistical evaluation of grain boundary networks (Binder et al., 2013b) are needed as larger grain populations have to be taken into account. However, in the sample studied here, and for most other deep ice microstructures (Faria et al., 2014b), the vast majority of SGB are microstructures that occur inside grains and are not low angle SGBs that form part of a GB network. Type IV SGB originating from grain coalescence might also be created by the mechanism of grain dissection (Steinbach et al., 2017).

The Means and Ree type V SGB involves impingement of two migrating SGBs that develop a combined misorientation angle that is the sum of the two SGBs. If the boundaries are formed by the same slip system, then only the angle will be changed. Impingement of boundaries formed by different slip systems will produce a new misorientation that combines the dislocation content of the two boundaries. Such SGB can be described as mixed boundaries composed of a mix of dislocations. A possible candidate of a SGB involving impingement of two migrating SGBs might be SGB 1 in Figure 2.4, which shows two separate orientation clusters of rotation axes.

The type VI SGBs increase in length and grow behind a migrating grain boundary, so their length does not reflect slip system activity; however, such boundaries would grow from boundaries initially produced by dislocation glide deformation, so the boundary misorientations should be related to the active slip systems. Given the extensive grain boundary migration that occurs at all levels in ice cores (Montagnat and Duval, 2004;

Weikusat et al., 2009a), it is likely that many SGBs may have been extended by growth behind migrating boundaries. This is conceivable in particular with the common observation that only a part of SGBs crosses grains completely, while many others fade out towards the centre of a grain (Hamann et al., 2007; Weikusat et al., 2009b), such as SGB 9 in Figure 2.3 and SGB 11 in Figure 2.4. As Means and Ree-type VI originate from mobile grain boundaries, this process may produce SGBs showing curved shapes, as observed for many SGB in the trace class “other” (Table 2.2; SGB 4 and 12 in Figure 2.3). There is a tendency for some SGBs to be more deeply etched near grain boundaries (Weikusat et al., 2009b, 2011a; Faria et al., 2014a), and SGB appear to pin the migrating grain boundaries; for example, SGB 9 in Figure 2.4. This type of SGB occurs in experimentally deformed ice (Hamann et al., 2007) that has undergone significant grain growth during deformation. These microstructures suggest that the P- and N-type boundaries in ice could be partly extended by growth behind migrating boundaries, such as the Means and Ree-type VI SGB.

2.4.5 Implications of SGB type and creep rate-control

Recent numerical simulations of ice deformation (Llorens et al., 2016a, b; Steinbach et al., 2016, 2017; Richeton et al., 2017) employ full-field modelling approaches taking into account the anisotropic crystal plasticity of ice. The evidence presented here for the activation of non-basal slip systems in natural ice deformed at low stress, supports the approach used in the full-field modelling. Llorens et al. (2016a, b) investigated the development of microstructure, subgrain formation and slip system activity during pure and simple shear deformation. In the simulations, non-basal slip was 20 times harder than basal slip. The simulations showed that in pure shear, the activity of non-basal slip increased with strain, related to the development of a strong CPO, which made basal slip more difficult. Even at low strains, 20% of the slip activity was accommodated by non-basal slip in the simulations. The microstructures produced in the simulations show heterogeneous activity of basal and non-basal slip systems, with different slip activity in different parts of grains resulting in formation of SGBs with a non-basal dislocation content (Llorens et al., 2017). The simulations show that a significant fraction of non-basal subgrains can be formed with a relatively small activity of the harder non-basal slip systems.

The microstructures, subgrain development and CPOs indicate that dislocation creep is an important mechanism in polar ice sheets. Most of the strain produced by dislocation creep should occur by glide on the easy basal $\langle a \rangle$ slip system. However, basal slip only provides two of the four independent slip systems needed to accommodate heterogeneous deformation in hexagonal systems (Hutchinson, 1977), so either harder non-basal slip systems or other deformation mechanisms must be activated. These accommodating deformation mechanisms are likely to be the slowest processes, so they will usually be the rate-controlling processes for deformation. Suggested accommodating deformation processes are dislocation climb of basal $\langle a \rangle$ dislocations, cross-slip or climb of non-basal dislocations and grain boundary sensitive mechanisms such as grain boundary sliding or diffusion. Grain size sensitive mechanisms, particularly grain boundary sliding, have been observed for fine grained artificial ice (Goldsby and Kohlstedt, 1997, 2001), but

are controversial for natural ice (Duval and Montagnat, 2002; Goldsby and Kohlstedt, 2002). The climb of dislocations gliding on the basal plane are processes related to recovery, which is rather active in ice, as ice on Earth is a hot material close to its pressure-melting point (homologous temperature $T_{\text{hom}} > 0.85 T_m$). Related to this, grain boundary migration, which in most cases is not a deformation mechanism, has been suggested to accommodate basal dislocation creep in ice via relaxation of the internal stress concentrations at grain boundaries (Montagnat and Duval, 2000). For grain boundary sliding or grain boundary migration as the rate-controlling accommodation processes the activation of non-basal slip systems would not be expected. The evidence of non-basal dislocations being mobile in glide and climb or cross-slip to form subgrain boundaries in polar ice, as presented here, suggests the possibility that non-basal dislocation slip could be the rate-controlling deformation process in natural ice, at least in the Holocene age samples investigated.

2.5 Conclusions

An analysis is presented of SGB and the dislocation slip systems they indicate for 400 individual boundaries in Antarctic and Greenlandic deep ice cores (656 m and 718 m depth). This study confirms the frequent occurrence of SGB in natural ice.

The analyses of the SGB traces with respect to the crystal orientation and the rotation axis associated with the boundary revealed (1) subgrain boundaries that can be related to slip system activity by their geometric relation to the host crystal orientations (ca. 70-80%) and (2) subgrain boundaries that cannot be easily related to slip system activity (ca. 20-30%).

The slip systems interpreted from the subgrain boundary measurements show that basal $\langle a \rangle$ slip is the most common slip system indicated by the subgrain boundaries. However, there is an almost equal occurrence of subgrain boundaries indicating $\langle c \rangle$ and/or $\langle c+a \rangle$ slip on non-basal planes. Far less frequent are subgrain boundaries indicating slip of $\langle a \rangle$ screw dislocations on basal planes and slip of $\langle a \rangle$ edge dislocations on prism planes.

Other possible means of producing subgrain boundaries in ice that cannot easily be related to slip system activity are discussed. SGB originating from misorientation reduction of grain boundaries are likely to arise from the generally strong CPO that develops in deeper parts of EDML and NEEM natural ice. Subgrain boundary growth behind migrating grain boundaries is another possible SGB formation processes.

A main result of this study is that a very high fraction of SGBs in polar ice (ca. 30-40% of all SGB) consist of non-basal dislocations and could therefore be formed by non-basal slip. We conclude from the relatively high frequency of SGBs consisting of non-basal dislocations that limited non-basal slip was active at these depths in EDML and NEEM natural ice. This finding is consistent with current crystal plasticity descriptions for ice as employed in full-field modelling approaches, which assume the significant activation of non-basal slip systems. The occurrence of non-basal slip in natural samples implies that activation of the harder slip systems is involved in the low stress deformation mechanisms

of ice. Thus, available models which propose that basal slip is accommodated only by grain boundary processes, such as sliding or migration, need to be modified. Further work is needed to understand the exact role of non-basal slip and grain boundary processes in the low stress deformation of ice, which is important for ice flow descriptions for different flow conditions of ice with respect to large scale ice modelling and its constitutive ice flow description.

References

- Alley, R., Gow, A., Meese, D. (1995) Mapping c-axis fabrics to study physical processes in ice. *Journal of Glaciology*, 41, 137, 197-203.
- Alley, R. B. (1992) Flow-law hypotheses for ice-sheet modeling. *Journal of Glaciology*, 38, 129, 245-256.
- Alley, R. B., Clark, P. U., Huybrechts, P., Joughin, I. (2005) Ice-Sheet and Sea-Level changes. *Science*, 310, 456-460, doi: 10.1126/science.1114613.
- Arnaud, L., Gay, M., Barnola, J.-M., Duval, P. (1998) Imaging firn and bubbly ice in coaxial reflected light: a new technique for the characterization of these porous media. *Journal of Glaciology*, 44, 147, 326-332, doi: 10.3189/S0022143000002653.
- Ashby, M. F. (1970) The deformation of plastically non-homogenous materials. *The Philosophical Magazine*, 21, 399-424, doi: 10.1080/14786437008238426.
- Ashby, M. F., Duval, P. (1985) The creep of polycrystalline ice. *Cold Regions Science and Technology*, 11, 285-300.
- Baker, I. (2003) Imaging dislocations in ice. *Microscopy Research and Technique*, 62, 70-82, doi 10.1080/14786437008238426.
- Barnes, P. R. F. (2003) Comment on "Grain boundary ridge on sintered bonds between ice crystals". *Journal of Applied Physics*, 90, 5782-5785, doi: 10.1063/1.1410889.
- Barrette, P. D., Sinha, N. K. (1994) Lattice misfit as revealed by dislocation etch pits in a deformed ice crystal. *Journal of Materials Science Letters*, 13, 1478-1481.
- Beem, L. H., Jezek, K. C., Van Der Veen, C. J. (2010) Basal melt rates beneath Whillans ice stream, west Antarctica. *Journal of Glaciology*, 56, 198, 647-654, doi: 10.3189/002214310793146241.
- Binder, T., Garbe, C. S., Wagenbach, D., Freitag, J., Kipfstuhl, S. (2013a) Extraction and parameterization of grain boundary networks, using a dedicated method of automatic image analysis. *Journal of Microscopy*, 250, 2, 130-141, doi: 10.1111/jmi.12029.
- Binder, T., Weikusat, I., Freitag, J., Garbe, C. S., Wagenbach, D., Kipfstuhl, S. (2013b) Microstructure through an ice sheet. *Materials Science Forum*, 753, 481-484, doi: 10.4028/www.scientific.net/MSF.753.481.
- Bindoff, N. L., Willebrand, J., Artale, V., Cazenave, A., Gregory, J., Gulev, S., Hanawa, K., Quere, C. K., Levitus, S., Nojiri, Y., Shum, C., Talley, L., Unnikrishnan, A. (2007) *Climate Change 2007: The Physical Science Basis. Contribution of Working Group I to the Fourth Assessment Report of the Intergovernmental Panel on Climate Change*. Cambridge University Press, Cambridge, United Kingdom and New York, NY, USA, Ch. Observations: Oceanic Climate Change and Sea Level, pp. 385-432. URL www.ipcc.ch.

- Bons, P. D., Jansen, D., Mundel, F., Bauer, C. C., Binder, T., Eisen, O., Jessell, M. W., Llorens, M.-G., Steinbach, F., Steinhage, F., Weikusat, I. (2016) Converging flow and anisotropy cause largescale folding in Greenland's ice sheet. *Nature Communications*, 7, 11427, doi: 10.1038/ncomms11427.
- Breton, D. J., Baker, I., Cole, D. M. (2016) Microstructural evolution of polycrystalline ice during confined creep testing. *Cold Regions Science and Technology*, 127, 25-36, doi: 10.1016/j.coldregions.2016.03.009.
- Bryant, G. W., Mason, B. J. (1960) Etch pits and dislocations in ice crystals. *Philosophical Magazine: Structure and Properties of Condensed Matter*, 5, 8, 1221-1227, doi: 10.1080/14786436008238334.
- Chauve, T., Montagnat, M., Piazzolo, S., Journaux, B., Wheeler, J., Barou, F., Mainprice, D., Tommasi, F. (2017) Non-basal dislocations should be accounted for in simulating ice mass flow. *Earth and Planetary Science Letters*, 473, 247-255, doi: 10.1016/j.epsl.2017.06.020.
- Dansgaard, W., Clausen, H. B., Gundestrup, N., Hammer, C. U., Johnsen, S. F., Kristinsdottir, P. M., Reeh, N. (1982) A New Greenland Deep Ice Core. *Science*, American Association for the Advancement of Science, 218, 4579, 1273-1277, doi: 10.1126/science.218.4579.
- Drury, M. R., Humphreys, F. J., White, S. H. (1985) Large strain deformation studies using polycrystalline magnesium as a rock analogue. Part II: dynamic recrystallization mechanisms at high temperatures. *Physics of the Earth and Planetary Interiors*, 40, 3, 208-222, doi: 10.1016/0031-9201(85)90131-1.
- Drury, M. R., Pennock, G. M. (2007) Subgrain Rotation Recrystallization in Minerals. *Materials Science Forum*, 550, 95-104, doi: 10.4028/www.scientific.net/MSF.550.95.
- Duval, P., Ashby, M. F., Anderman, I., (1983) Rate-controlling processes in the creep of polycrystalline ice. *Journal of Physical Chemistry*, 87, 21, 4066-4074, doi: 10.1021/j100244a014.
- Duval, P., Montagnat, M. (2002) Comment on "Superplastic deformation of ice: Experimental observations" by D. L. Goldsby and D. L. Kohlstedt. *Journal of Geophysical Research*, 107, B4, 1-2, doi: 10.1029/2001JB000946.
- Eichler, J., Kleitz, I., Bayer-Giraldi, M., Jansen, D., Kipfstuhl, S., Shigeyama, W., Weikusat, C., Weikusat, I. (2017) Location and distribution of micro-inclusions in the EDML and NEEM ice cores using optical microscopy and in situ Raman spectroscopy. *The Cryosphere*, 11, 3, 1075-1090, doi: 10.5194/tc-11-1075-2017.
- Eichler, J., Weikusat, I., Kipfstuhl, S. (2013): Orientation-tensor eigenvalues along the NEEM ice core. *PANGAEA*, <https://doi.org/10.1594/Pangaea.838059>.
- EPICA community members (2004) Eight glacial cycles from an Antarctic ice core. *Nature*, 429, 623-628, doi: 10.1038/nature02599.
- EPICA community members (2006) One-to-one coupling of glacial climate variability in Greenland and Antarctica. *Nature*, 444, 195-198, doi: 10.1038/nature05301.
- Faria, S. H., Weikusat, I., Azuma, N. (2014b) The microstructure of polar ice. Part I: Highlights from ice core research. *Journal of Structural Geology*, 61, 2-20, doi: 10.1016/j.jsg.2013.09.010.
- Faria, S. H., Weikusat, I., Azuma, N. (2014a) The microstructure of polar ice. Part II: State of the art. *Journal of Structural Geology*, 61, 21-49, doi: 10.1016/j.jsg.2013.11.003.

Fitzpatrick, J. J., Voigt, D. E., Fegyveresi, J. M., Stevens, N. T., Spencer, M. K., Cole-dai, J., Alley, R. B., Jardine, G. E., Cravens, E. D., Wilen, L. A., Fudge, T. J., McConnell, J. R. (2014) Physical properties of the WAIS Divide ice core. *Journal of Glaciology*, 60, 224, 1181-1198, doi: 10.3189/2013JoG14j100.

Fukuda, A., Higashi, A. (1969) X-ray diffraction topographic studies of dislocations in natural large ice single crystals. *Japanese Journal of Applied Physics*, 8, 8, 993-999, doi: 10.1143/JJAP.8.993.

Fukuda, A., Hondoh, T., Higashi, A. (1987) Dislocation Mechanisms of Plastic Deformation of Ice. *Journal de Physique Colloques*, 48, C1, 163-173, doi: 10.1051/jphyscol:1987124.

Gifkins, R. C. (1976) Grain Boundary Sliding and its Accommodation During Creep and Superplasticity. *Metallurgical Transactions A*, 7, 1225-1232.

Glen, J. W. (1955) The creep of polycrystalline ice. *Proceedings of the Royal Society A: Mathematical, Physical and Engineering Sciences*, 228, 1175, 519-538, doi: 10.1098/rspa.1955.0066.

Goldsby, D. L., Kohlstedt, D. L. (1997) Grain boundary sliding in fine grained ice I. *Scripta Materialia*, 37, 9, 1399-1406.

Goldsby, D. L., Kohlstedt, D. L. (2001) Superplastic deformation of ice: Experimental observations. *Journal of Geophysical Research*, 106, B6, 11017-11030, doi: 10.1029/2000JB900336.

Goldsby, D. L., Kohlstedt, D. L. (2002) Reply to comment by P. Duval and M. Montagnat on "Superplastic deformation of ice: Experimental observations". *Journal of Geophysical Research*, 107, B11, 1-5, doi: 10.1029/2002JB001842.

Gottstein, G., Shvindlerman, L. S. (1999) Grain boundary migration in metals: thermodynamics, kinetics, applications. Boca Raton, FL, CRC Press.

Greve, R., Blatter, H. (2009) Dynamics of ice sheets and glaciers. [Hutter, K. (Ed.)] Springer Berlin/Heidelberg, 287 pages.

Hamann, I., Weikusat, C., Azuma, N., Kipfstuhl, S. (2007) Evolution of ice crystal microstructures during creep experiments. *Journal of Glaciology*, 53, 182, 479-489, doi: 10.3189/002214307783258341.

Higashi, A., Fukuda, A., Shoji, H., Oguro, M., Hondoh, T., Goto-Azuma, K. (1988) Lattice defects in ice crystals. Hokkaido University Press, Sapporo, Japan, 156 pages.

Hirth, J. P., Lothe, J. (1982) Theory of Dislocations. Krieger Publishing Company, 857 pages.

Hock, R. (2005) Glacier melt: a review of processes and their modelling. *Progress in Physical Geography* 29, 3, 362-391, doi: 10.1191/0309133305pp453ra.

Hondoh, T. (2000) Nature and behavior of dislocations in ice. *Physics of Ice Core Records*, 3-24.

Hondoh, T. (2006) Anisotropy of ice plasticity and dislocations in ice: anomalous properties of hexagonal ice Ih associated with cubic structure Ic, *Low temperature Science*, 64, 141-156.

Hondoh, T. (2009) An overview of microphysical processes in ice sheets: Towards nanoglaciology. In: Hondoh, T. (Ed.), *Physics of Ice Core Records II*. Vol 68. Supplement

Issue of low Temperature Science, Vol 68. URL
<http://eprint.lib.hokudai.ac.jp/handle/2115/45402>

Hondoh, T. (2015) Dislocation mechanism for transformation between cubic ice Ic and hexagonal ice Ih. *Philosophical Magazine*, 95, 32, 3590-3620. doi: 10.1080/14786435.2015.1091109.

Hughes, T. (2009) Modeling ice sheets from the bottom up. *Quaternary Science Reviews* 28, 19-20, 1831–1849, doi: 10.1016/j.quascirev.2009.06.004.

Humphreys, F. J., Hatherly, M. (2004) *Recrystallization and Related Annealing Phenomena*. Elsevier, 574 pages.

Hutchinson, J. W. (1977) Creep and plasticity of hexagonal polycrystals as related to single crystal slip. *Metallurgical Transactions A.*, 8, 9, 1465-1469.

Huybrechts, P. (2007) Ice sheet modelling, *Encyclopedia of the Antarctic* (ed. by Riffenburgh, B.), pp 514-417. Routledge. New York and London.

Iliescu, D., Baker, I., Chang, H. (2004) Determining the Orientations of ice Crystals Using Electron Backscatter Diffraction Patterns. *Microscopy Research and Technique*, 63, 183-187, doi: 10.1002/jemt.20029.

Ion, S. E., Humphreys, F. S., White, S. H. (1982) Dynamic recrystallisation and the development of microstructure during the high temperature deformation of magnesium. *Acta Metallurgica*, 30, 10, 1909-1919, doi: 10.1016/0001-6160(82)90031-1.

IPCC (2007) *Climate Change 2007: The Physical Science Basis. Contribution of Working Group I to the Fourth Assessment Report of the Intergovernmental Panel on Climate Change*. Cambridge University Press, Cambridge, United Kingdom and New York, NY, USA, Ch. Summary for Policymakers, Solomon, S. and Qin D. and Manning M. and Chen Z. and Marquis M. and Averyt K. B. and Tignor M. and Miller H. L., editors. URL www.ipcc.ch.

IPCC (2014) *Climate change 2014: Synthesis report. contribution of working groups i, ii and iii to the fifth assessment report of the intergovernmental panel on climate change*. [Core Writing Team, Pachauri P. K. and Meyer L. A. (eds.)]. IPCC, Geneva, Switzerland, 151. URL www.ipcc.ch.

Jansen, D., Llorens, M.-G., Westhoff, J., Steinbach, F., Kipfstuhl, S., Bons, P. D., Griera, A., Weikusat, I. (2016) Small-scale disturbances in the stratigraphy of the NEEM ice core: observations and numerical model simulations. *The Cryosphere*, 10, 359-370, doi: 10.5194/tc-10-359-2016.

Joughin, I., Smith, B., Howat, I., Scambos T. (2015) *MEaSURES Greenland Ice Velocity Map from InSAR Data, Version 2*. Boulder, Colorado, USA: NASA DAAC at the National Snow and Ice Data Center, doi:10.5067/OC7B04ZM9G6Q.

Ketcham, W. M., Hobbs, P. V. (1969) An experimental determination of the surface energies of ice. *Philosophical Magazine*, 19, 162, 1161-1173, doi: 10.1080/14786436908228641.

Kipfstuhl, S., Faria, S. H., Azuma, N., Freitag, J., Hamann, I., Kaufmann, P., Miller, H., Weiler, K., Wilhelms, F. (2009) Evidence of dynamic recrystallization in polar firn. *Journal of Geophysical Research*, 114, 5, 1-10, doi: 10.1029/2008JB005583.

Kipfstuhl, S., Hamann, I., Lambrecht, A., Freitag, J., Faria, S., Grigoriev, D., Azuma, N. (2006) Microstructure mapping: a new method for imaging deformation induced

microstructural features of ice on the grain scale. *Journal of Glaciology*, 52, 178, 398-406, doi: 10.3189/172756506781828647.

Krischke, A., Oechsner, U., Kipfstuhl, S. (2015) Rapid Microstructure Analysis of Polar Ice Cores. *Optik & Photonik*, 10, 2, 32-35, doi: 10.1002/opph.201500016.

Kuramoto, T., Goto-Azuma, K., Hirabayashi, M., Miyake, T., Motoyama, H., Dahl-Jensen, D., Steffensen, J. P. (2011) Seasonal variations of snow chemistry at NEEM, Greenland. *Annals of Glaciology*, 52, 58, 193-200, doi: 10.3189/172756411797252365.

Lemke, P., Ren, J., Alley, R., Allison, I., Carrasco, J., Flato, G., Fujii, Y., Kaser, G., Mote, P., Thomas, R., Zhang, T. (2007) *Climate Change 2007: The Physical Science Basis. Contribution of Working Group I to the Fourth Assessment Report of the Intergovernmental Panel on Climate Change*. Cambridge University Press, Cambridge, United Kingdom and New York, NY, USA, Ch. Observations: Changes in Snow, Ice and Frozen Ground, pp. 337-383. URL www.ipcc.ch.

Levi, L., DeAchaval, E. M., Suraski, E. (1965) Experimental study of non-basal dislocations in ice crystals. *Journal of Glaciology*, 5, 41, 691-699, doi: <https://doi.org/10.3189/S0022143000018682>.

Lloyd, G. E., Farmer, A. B., Mainprice, D. (1997) Misorientation analysis and the formation and orientation of subgrain and grain boundaries. *Tectonophysics*, 279, 1-4, 55-78, doi 10.1016/S0040-1951(97)00115-7.

Llorens, M-G., Griera, A., Bons, P. D., Lebensohn, R. A., Evans, L. A., Jansen, D., Weikusat, I. (2016a) Full-field predictions of ice dynamic recrystallization under simple shear conditions. *Earth and Planetary Science Letters*, 450, 233-242, doi: 10.1016/j.1016/j.epsl.2016.06.045.

Llorens, M-G., Griera, A., Bons, P. D., Roessiger, J., Lebensohn, R., Evans, L., Weikusat, I. (2016b) Dynamic recrystallization of ice aggregates during co-axial viscoplastic deformation: a numerical approach. *Journal of Glaciology*, 62, 232, 359-377, doi: 10.1017/jpg.2016.28.

Llorens, G-M., Griera, A., Steinbach, F., Bons, P. D., Gomez-Rivas, E., Jansen, D., Roessiger, J., Lebensohn, R. A., Weikusat, I. (2017) Dynamic recrystallization during deformation of polycrystalline ice: insights from numerical simulations. *Philosophical transactions A*, 375, doi: 10.1098/rsta.2015.0346.

Mainprice, D., Lloyd, G. E., Casey, M. (1993) Individual orientation measurements in quartz polycrystals: advantages and limitations for texture and petrophysical property determinations. *Journal of Structural Geology*, 15, 9-10, 1169-1187, doi: 10.1016/0191-8141(93)90162-4.

Means, W. D., Ree, J. H. (1988) Seven types of subgrain boundaries in octachloropropane. *Journal of Structural Geology*, 10, 7, 765-770, doi: 10.1016/0191-8141(88)90083-1.

Miyamoto, A., Saito, T., Hondoh, T. (2009) Visual observation of volume relaxation under different storage temperatures in the dome fuji ice core, Antarctica. In: Hondoh, T. (Ed.) *Physics of Ice Core Records II*. Vol. 2 of PICR. Supplement Issue of *Low Temperature Science*, 68, 73-79.

Miyamoto, A., Weikusat, I., Hondoh, T. (2011) Complete determination of ice crystal orientation and microstructure investigation on ice core samples enabled by a new x-ray laue diffraction method. *Journal of Glaciology*, 57, 201, 103-110, doi: 10.3189/002214311795306754.

- Montagnat, M., Duval, P. (2000) Rate controlling processes in the creep of polar ice, influence of grain boundary migration associated with recrystallization. *Earth and Planetary Science Letter*, 183, 1-2, 179-186, doi: 10.1016/S0012-821X(00)00262-4.
- Montagnat, M., Duval, P., Bastie, P., Hamelin, B., Brissaud, O., de Angelis, M., Petit, J.-R., Lipenkov, V. Y. (2001) High crystalline quality of large single crystals of subglacial ice above Lake Vostok (Antarctica) revealed by hard X-ray diffraction. *Earth and Planetary Sciences*, 333, 8, 419-425, doi: 10.1016/S1251-8050(01)01667-6.
- Montagnat, M., Duval, P., Bastie, P., Hamelin, B., Lipenkov, V. Y. (2003) Lattice distortion in ice crystals from the Vostok core (Antarctica) revealed by hard X-ray diffraction; implication in the deformation of ice at low stresses. *Earth and Planetary Science Letters*, 214, 1-2, 369-378, doi: 10.1016/S0012-821X(03)00364-9.
- Montagnat, M., Duval, P. (2004) Dislocations in Ice and Deformation Mechanisms: from Single Crystals to Polar Ice. *Defect and Diffusion Forum*, 229, 43-54.
- Montagnat, M., Azuma, N., Dahl-Jensen, D., Eichler, J., Fujita, S., Gillet-Chaulet, F., Kipfstuhl, S., Samyn, D., Svenson, A., Weikusat, I. (2014) Fabric along the NEEM ice core, Greenland, and its comparison with GRIP and NGRIP ice cores. *The Cryosphere*, 8, 1129-1138, doi: 10.5194/tc-8-1129-2014.
- Montagnat, M., Chauve, T., Barou, F., Tommasi, A., Beausir, B., Fressengeas, C. (2015) Analysis of Dynamic Recrystallization of Ice from EBSD Orientation Mapping. *Frontiers in Earth Science*, 3, 81, 1-13, doi: 10.3389/feart.2015.00081.
- Muguruma, J., Mae, S., Higashi, A. (1966) Void formation by non-basal glide in ice single crystals. *Philosophical Magazine*, 13, 123, 625-629, doi: 10.1080/14786436608212656.
- Mullins, W. W. (1957) Theory of thermal grooving. *Journal of Applied Physics*, 28, 3, 333-339, doi: 10.1063/1.1722742.
- Nakaya, U. (1958) Mechanical properties of single crystal of ice. Part I. Geometry of deformation. US Army Snow Ice and Permafrost Research Establishment, Research Report 28.
- NEEM community members. (2013) Eemian interglacial reconstructed from a Greenland folded ice core. *Nature*, 493, 489-494, doi: 10.1038/nature11789.
- Neumann, B. (2000) Texture development of recrystallized quartz polycrystals unravelled by orientation and misorientation characteristics. *Journal of Structural Geology*, 22, 1695-1711, doi: 10.1016/S0191-8141(00)00060-2.
- Nishida, K., Narita, H. (1996) Three-dimensional observations of ice crystal characteristics in polar ice sheets. *Journal of Geophysical Research*, 101, D16, 21,311-21,317, doi: 10.1029/96JD01770.
- Obbard, R., Baker, I., Sieg, K. (2006) Using electron backscatter diffraction patterns to examine recrystallization in polar ice sheets. *Journal of Glaciology*, 52, 179, 546-557, doi: 10.3189/172756506781828458.
- Oerter, H., Drücker, C., Kipfstuhl, S., Wilhelms, F. (2009) Kohnen station - the drilling camp for the EPICA deep ice core in Dronning Maud land. *Polarforschung* 78, 1, 1-23.
- Pauer, F., Kipfstuhl, S., Kuhs, W. F., Shoji, H. (1999) Air hydrates crystals from the GRIP deep ice core, Greenland: a number- size- and shape-distribution study. *Journal of Glaciology*, 45, 149, 22-30.

- Peternell, M., Russell-Head D. S., Wilson C. J.L. (2010) A technique for recording polycrystalline structure and orientation during in situ deformation cycles of rock analogues using an automated fabric analyser. *Journal of Microscopy*, 242, 2, 181–188, doi: 10.1111/j.1365-2818.2010.03456.x.
- Piazolo, S., Montagnat, M., Blackford, J. R. (2008) Sub-structure characterization of experimentally and naturally deformed ice using cryo-EBSD. *Journal of Microscopy*, 230, Pt 3, 509-519, doi: 10.1111/j.1365-2818-2008.02014.x.
- Prior, D. J., Boyle, A. P., Brenker, F., Cheadle, M. C., Day, A., Lopez, G., Peruzzo, L., Potts, G. J., Reddy, S., Spiess, R., Timms, N. E., Trimby, P., Wheeler, J., Zetterström, L. (1999) The application of electron backscatter diffraction and orientation contrast imaging in the SEM to textural problems in rocks. *American Mineralogist*, 84, 11-12, 1741-1759, doi: 10.2138/am-1999-11-1204.
- Prior, D. J., Wheeler, J., Peruzzo, L., Spiess, R., Storey, C. (2002) Some garnet microstructures: an illustration of the potential of orientation maps and misorientation analysis in microstructural studies. *Journal of Structural Geology*, 24, 6-7, 999-1011, doi: 10.1016/S0191-8141(01)00087-6.
- Prior, D. J., Lilly, K., Seidemann, M., Vaughan, M., Becroft, L., Easingwood, R., Diebold, S., Obbard, R., Daghlian, C., Baker, I., Caswell, T., Golding, N., Goldsby, D., Durham, W. B., Piazolo, S., Wilson, C. J. L. (2015) Making EBSD on water ice routine. *Journal of Microscopy*, 259, 00, 1-20, doi: 10.1111/jmi.12258.
- Randle, V., Engler, O. (2000) *Introduction to texture analysis: Macrotexture, Microtexture and Orientation Mapping*. Taylor & Francis, 388.
- Rasmussen, S. O., Abbott, P.M., Blunier, T., Bourne, A. J., Brook, E., Buchardt, S. L., Buizert, C., Chappellaz, J., Clausen, H. B., Cook, E., Dahl-Jensen, D., Davies, S. M., Guillevic, M., Kipfstuhl, S., Laepple, T., Seierstad, I. K., Severinghaus, J. P., Steffensen, J. P., Stowasser, C., Svensson, A., Vallelonga, P., Vinther, B. M., Wilhelms, F., Winstrup, M. (2013) A first chronology for the North Greenland Eemian Ice Drilling (NEEM) ice core. *Climate of the Past*, 9, 2713-2730, doi: 10.5194/cp-9-2713-2013.
- Richeton, T., Le, L., Chauve, T., Bernacki, M., Berbenni, S., Montagnat, M. (2017) Modelling the transport of geometrically necessary dislocations on slip systems: application to single- and multi-crystals of ice. *Modelling and Simulation in Materials Science and Engineering*, 25, 2, 025010, doi: 10.1088/1361-651X/aa5341.
- Ruth, U., Barnola, J. M., Beer, J., Bigler, M., Blunier, T., Castellano, E., Fischer, H., Fundel, F., Huybrechts, P., Kaufmann, P., Kipfstuhl, S., Lambrecht, A., Morganti, A., Oerter, H., Parrenin, F., Rybak, O., Severi, M., Udisti, R., Wilhelms, F., Wolff, E. (2007) “EDML1”: A chronology for the EPICA deep ice core from Dronning Maud Land, Antarctica, over the last 150 000 years. *Climate of the Past*, 3, 475-484, doi: 10.5194/cp-3-475-2007.
- Saylor, D. M., Rohrer, G. S. (1999) Measuring the Influence of Grain- Boundary Misorientation on Thermal Groove Geometry in Ceramic Polycrystals. *Journal of the American Ceramic Society*, 82, 1529-1536, doi: 10.1111/j.1151-2916.1999.tb01951.x.
- Schulson, E. M., Duval, P. (2009) *Creep and Fracture of Ice*. Cambridge University Press.
- Shearwood, C., Whitworth, R. W. (1991) The velocity of dislocations in ice. *Philosophical Magazine A*, 64, 2, 289-302, doi: 10.1080/01418619108221186.
- Sergienko, O. V., Creyts, T. T., Hindmarsh, R. C. A. (2014) Similarity of organized patterns in driving stress and basal stresses of Antarctic and Greenland ice sheets beneath

- extensive areas of basal sliding. *Geophysical Research Letter*, 41, 11, 3925-3932, doi: 10.1002/2014GL059976.
- Song, M., Baker, I., Cole, D. M. (2008) The effect of particles on creep rate and microstructures of granular ice. *Journal of Glaciology*, 54, 186, 533-537, doi: 10.3189/002214308785836959.
- Steinbach, F., Bons, P. D., Griera, A., Jansen, D., Llorens, M-G, Roessiger, J., Weikusat, I. (2016) Strain localization and dynamic recrystallization in the ice-air aggregate: a numerical study. *The Cryosphere*, 10, 6, 3071-3089, doi: 10.5194/tc-10-3071-2016.
- Steinbach, F., Kuiper, E. N., Eichler, J., Bons, P. D., Drury, M. R., Griera, A., Pennock, G. M., Weikusat, I. (2017) The relevance of grain dissection for grain size reduction in polar ice: insights from numerical models and ice core microstructure analysis. *Frontiers in Earth Science*, 5, 66, 1-19, doi: 10.3389/feart.2017.00066.
- Stocker, T., Dahe, Q., Plattner, G.-K., Tignor, M., Allen, S., Midgley, P. (2010) Workshop report of the intergovernmental panel on climate change workshop on sea level rise and ice sheet instabilities. www.ipcc-wg1.unibe.ch/meetings/slr/slr.html.
- Suzuki, S. (1970) Grain Coarsening of Microcrystals of Ice (III). *Low Temperature Science, Series A*, 28, 47-61.
- Suzuki, S. Kuroiwa, D. (1972) Grain-boundary energy and grain-boundary groove angles in ice. *Journal of Glaciology*, 11, 62, 265-277.
- Thoma, M., Grosfeld, K., Mayer, C., Pattyn, F. (2010) Interaction between ice sheet dynamics and subglacial lake circulation: a coupled modelling approach. *The Cryosphere*, 4, 1, 1-12, doi: 10.5194/tc-4-1-2010.
- Trépiéd, L., Doukhan, J. C., Paquet, J. (1980) Subgrain Boundaries in Quartz: Theoretical Analysis and Microscopic Observations. *Physics and Chemistry of Minerals*, 5, 3, 201-218, doi: 10.1007/BF00348570.
- Vaughan, D. G., Arthern, R. (2007) Why is it hard to predict the future of ice sheets? *Science*, 315, 1503-1504, doi: 10.1126/science.1141111.
- Wang, Y., Thorsteinsson, T., Kipfstuhl, S., Miller, H., Dahl-Jensen, D., Shoji, H. (2002) A vertical girdle fabric in the NorthGRIP deep ice core, North Greenland. *Annals of Glaciology*, 35, 515-520, doi: 10.3189/172756402781817301.
- Weertman, J., Weertman, J. R. (1992) *Elementary Dislocation Theory*. Oxford University Press, New York.
- Wegner, A., Fischer, H., Delmonte, B., Petit, J.-R., Erhardt, T., Ruth, U., Svensson, A., Vinther, B., Miller, H. (2015) The role of seasonality of mineral dust concentration and size on glacial/interglacial dust changes in the EPICA Dronning Maud Land ice core. *Journal of Geophysical Research: Atmospheres*, 120, 19, 9916-993, doi: 10.1002/2015JD023608.
- Wei, Y., Dempsey, J. P. (1994) The motion of non-basal dislocations in ice crystals. *Philosophical Magazine A*, 69, 1, 1-10, doi: 10.1080/01418619408242205.
- Weikusat, C., Freitag, J., Kipfstuhl, S. (2012) Raman spectroscopy of gaseous inclusions in EDML ice core: first results - microbubbles. *Journal of Glaciology* 58, 210, 761-766, doi: 10.3189/2012JoG11J222.
- Weikusat, I., de Winter, D. A. M., Pennock, G. M., Hayles, M., Schneiderberg, C. T. W. M., Drury, M. R. (2011b) Cryogenic EBSD on ice: preserving a stable surface in a low

pressure SEM. *Journal of Microscopy*, 242, 3, 295-310, doi: 10.1111/j.1365-2818.2010.03471.x.

Weikusat, I., Kipfstuhl, S., Azuma, N., Faria, S. H., Miyamoto, A. (2009a) Deformation microstructures in an Antarctic Ice Core (EDML) and in Experimentally Deformed Artificial Ice. In: Hondoh, T. (Ed.), *Physics of Ice Core Records II*. Vol. 2 of PICR. Supplement Issue of *Low Temperature Science*, Vol. 68, pp. 115-123. URL <http://eprints.lib.hokudai.ac.jp/dspace/handle/2115/45402>.

Weikusat, I., Kipfstuhl, S., Faria, S. H., Azuma, N., Miyamoto, A. (2009b) Subgrain boundaries and related microstructural features in EDML (Antarctica) deep ice core. *Journal of Glaciology*, 55, 191, 461-472, doi: 10.3189/002214309788816614.

Weikusat, I., Miyamoto, A., Faria, S. H., Kipfstuhl, S., Azuma, N., Hondoh, T. (2011a) Subgrain boundaries in Antarctic ice quantified by X-ray Laue diffraction, 57, 201, 85-94, doi: 10.3189/002214311795306628.

Weikusat, I., Jansen, D., Binder, T., Eichler, J., Faria, S. H., Wilhelms, F., Kipfstuhl, S., Sheldon, S., Miller, H., Dahl-Jensen, D., Kleiner, T. (2017) Physical analysis of an Antarctic ice core (EDML) – towards an integration of micro- and macrodynamics of polar ice. *Philosophical Transactions A*, 375, doi: 10.1098/rsta.2015.0347.

Weikusat, I., Lambrecht, A., Kipfstuhl, S. (2013) Eigenvalues of crystal orientation tensors for c-axes distributions of vertical thin sections from the EDML ice core. doi:10.1594/PANGAEA.807142.

Wesche, C., Eisen, O., Oerter, H., Schulte, D., Steinhage, D. (2007) Surface topography and ice flow in the vicinity of the EDML deep-drilling site, Antarctica. *Journal of Glaciology*, 53, 182, 442-448, doi: 10.3189/002214307783258512.

Wilhelms, F., Sheldon, S. G., Hamann, I., Kipfstuhl (2007) Implications for and findings from deep ice core drillings – An example: The ultimate tensile strength of ice at high strain rates. *Physics and Chemistry of Ice (The proceedings of the International Conference on the Physics and Chemistry of Ice held at Bremerhaven, Germany on 23-28 July 2006)*. The Royal Society of Chemistry Special Publication, 311, 635-639.

Wilhelms, F., Miller, H., Gerasimoff, M. D., Drücker, C., Frenzel, A., Fritzsche, D., Grobe, H., Hansen, S. B., Hilmarsson, S. Æ., Hoffmann, G., Hörnby, K., Jaeschke, A., Jakobsdóttir, S. S., Juckschat, P., Karsten, A., Karsten, L., Kaufmann, P. R., Karlin, T., Kohlberg, E., Kleffel, G., Lambrecht, A., Lambrecht, A., Lawer, G., Schärmeli, I., Schmitt, J., Sheldon, S. G., Takata, M., Trenke, M., Twarloh, B., Valero-Delgado, F. & Wilhelms-Dick, D. (2014) The EPICA Dronning Maud Land deep drilling operation. *Annals of Glaciology*, 55, 68, 355-366, doi: 10.3189/2014AoG68A189.

Wilson, C., Burg, J., Mitchell, J. (1986) The origin of kinks in polycrystalline ice. *Tectonophysics*, 127, 1-2, 27-48, doi: 10.1016/0040-1951(86)90077-6.

Wolovick, M. J., Creyts, T. T. (2016) Overtaken folds in ice sheets: Insights from a kinematic model of traveling sticky patches and comparisons with observations *Journal of Geophysical Research: Earth Surface*, 121, 5, 1065-1083, doi: 10.1002/2015JF003698.

Variation in non-basal slip activity controlled by strain induced boundary migration in the NEEM deep ice core, Greenland

After:

Kuiper, E. N., Pennock, G. M., Kilian, R., de Bresser, J. H. P., Weikusat, I., Drury, M. R.
Variation in non-basal slip activity controlled by strain induced migration in the NEEM
deep ice core, Greenland. *Manuscript in preparation.*

Abstract

A study of subgrain boundaries (SGBs) has been carried out in order to study ice slip systems and recrystallization mechanisms that are active at different depths in natural ice samples. The samples were taken from the North Greenland Eemian ice drilling (NEEM) deep ice core. The SGBs were analyzed using cryogenic electron backscatter diffraction (cryo-EBSD) in combination with light microscope (LM) imaging. Nine depth levels were investigated: three from the Holocene ice (0-1419 m of depth), four from the glacial ice (1419-2207 m of depth) and two from the Eemian ice (2207-2540 m of depth). In total, more than 1000 SGBs were mapped using cryo-EBSD and the SGBs were categorized based on misorientation angle, rotation axis and the orientation of the boundary plane.

The boundary plane trace and the rotation axis were used to analyse the most likely slip system of each SGB. The analyses show that SGBs that can be formed by an array of edge dislocations with Burgers vector $\mathbf{b}=(1/3)\langle 1\bar{2}10 \rangle$ gliding on the basal plane are the most common in the Holocene, glacial (both about 40%) and Eemian ice (60%). A small percentage of the SGBs are indicative of prism $\mathbf{b}=(1/3)\langle 1\bar{2}10 \rangle$ slip or slip of $\mathbf{b}=(1/3)\langle 1\bar{2}10 \rangle$ screw dislocations on the basal plane. However, about 30-35% of SGBs in the Holocene and glacial ice and 15% of SGBs in the Eemian ice are indicative of $\mathbf{b}=[0001]$ or $\mathbf{b}=(1/3)\langle 11\bar{2}3 \rangle$ slip gliding on prism and/or pyramidal planes and could therefore be formed by glide of dislocations on non-basal planes. The presence of SGBs that are indicative of slip in the $[0001]$ or $\langle 11\bar{2}3 \rangle$ directions along the ice core length shows that non-basal slip is activated at all depths in the NEEM ice core.

The misorientation angle of the SGBs, which were all less than 6.5° , were arbitrarily divided into three ranges, 0.5° - 2.0° , 2.0° - 4.0° and 4.0° - 6.5° . The highest percentage of SGBs in the range 0.5° - 2.0° was found in the Eemian ice, followed by the Holocene ice and the glacial ice. This higher percentage of these lower angle misorientations can be explained by strain induced boundary migration (SIBM), which consumes SGBs before higher misorientations can develop, being more extensive in the Holocene and especially in the Eemian ice.

Two regions of the NEEM ice core, in the deeper part of the Holocene ice and in the Eemian ice, contained fewer SGBs that were formed by non-basal slip compared to the rest of the ice core. The microstructures in these regions indicate considerable activity of SIBM, which in the Eemian ice is probably further enhanced by premelting along the grain boundaries. The results indicate that SIBM controls the amount of non-basal slip that is activated by reducing the build-up of strain incompatibilities which activate non-basal slip.

About 20% of the SGBs along the length of the NEEM ice core could not easily be related to a known slip system. Of these not-classified SGBs, only 1% in the Holocene ice had a misorientation angle in the range 4.0° - 6.5° , while this was 36% for the glacial ice. Two different explanations are provided for this difference. (i) Boundary sliding along these newly formed boundaries (4.0° - 6.5°) in the glacial ice results in a 'general' rotation axis and (ii) activation of multiple slip systems with different rotation axes contribute to the formation of the SGB and leads to a 'general' rotation axis.

3.1 Introduction

The Greenland and Antarctic ice sheets form the largest fresh water reservoir on Earth. Together, these ice sheets contain enough water to increase global mean sea level (GMSL) by about 70 meters (Alley et al., 2005; Church et al., 2013). The future contribution of the Antarctic and Greenland ice sheet to sea level rise remains one of the key uncertainties in understanding the climate system (IPCC, 2014). The main components of the mass balance of an ice sheet consist of precipitation on the one hand and melting and calving of ice on the other hand. The amount of ice available for melting and calving, which occurs mainly near the margins of an ice sheet, depends on the flow of ice from the interior towards the edges of the ice sheet (e.g. Trusel et al., 2015). The flow of ice is controlled by two processes: sliding of the ice over the bedrock (e.g. Vaughan and Arthern, 2007) and internal deformation of the ice sheet as a whole (Duval et al., 2000; Faria et al., 2014). Whereas sliding over the bedrock is the dominant process in most ice streams and margins of the ice sheet (e.g. Krabbendam, 2016), internal deformation of the ice is the dominant mechanism in the interior of the ice sheet (e.g. Duval et al., 1983; Schulson and Duval, 2009; Faria et al., 2014).

The dominant deformation mechanisms of ice that are responsible for flow in ice sheets has been the topic of many studies during the last decades (e.g. Duval et al., 1983; Alley, 1992; Faria et al., 2014 and references therein). Ice has a hexagonal crystal structure and has a strong mechanical anisotropy (e.g. Hondoh, 2000; 2009; 2015) with slip of dislocations along the basal plane being 60 to 100 times easier than slip of dislocations along one of the non-basal planes, such as the prism or pyramidal planes (Duval et al., 1983; Ashby and Duval, 1985, Figure 1.4b-e). A high mechanical anisotropy in materials leads to stress concentrations when polycrystals are deformed, with stress concentrations predominantly located at grain boundaries and triple junctions (Gifkins, 1976, 1994; Hobbs, 1985; Hirth and Kohlstedt, 1995; Neumann, 2000; Ji et al., 2002; Grennerat et al., 2012; Faria et al., 2014; Piazzolo et al., 2015). Whether the build-up of internal stresses due to strain incompatibilities between grains in ice are accommodated by grain boundary sliding (Gifkins, 1976; Goldsby and Kohlstedt, 1997, 2001), accommodated by non-basal slip (e.g. Schulson and Duval, 2009; Faria et al., 2014) or removed by strain induced boundary migration (SIBM) (Pimienta and Duval, 1987; Montagnat and Duval, 2000; Duval et al., 2000; Schulson and Duval, 2009) remains a topic of debate. The study of ice microstructures and slip systems in ice is one of the methods to determine which accommodating mechanism for basal slip is active during the deformation of polar ice.

One of the techniques that can be used to study ice microstructures is cryogenic electron backscatter diffraction (cryo-EBSD). Most previous studies on polycrystalline ice using cryo-EBSD have been performed on artificial ice (Iliescu et al., 2004; Piazzolo et al., 2015; Prior et al., 2012, 2015; Montagnat et al., 2015; Breton et al., 2016), while only a small number of studies using cryo-EBSD were performed on natural ice (Obbard et al., 2006, 2007; Weikusat et al., 2017). Cryo-EBSD studies on artificial ice have greatly increased the understanding of deformation mechanisms at different temperatures, stresses

and grain sizes. However, microstructural studies on natural glacier and polar ice are invaluable due to the large differences in strain rate, anisotropy, stress and grain size between natural ice deformation and the artificial ice used in most experimental deformation tests. By studying ice microstructural features in ice core samples, such as subgrain boundaries (SGBs), grain size and grain shape, and comparing these with ice microstructure models (e.g. Montagnat et al., 2014a; Llorens et al., 2016a, 2016b, 2017; Steinbach, 2016; Richeton et al., 2017) and ice deformation tests (e.g. Glen, 1955; Hamann et al., 2007; Piazzolo et al., 2015; Breton et al., 2016; Chauve et al., 2017), a better understanding of natural ice deformation can be obtained. This knowledge can be used to improve ice flow laws that are used in ice sheet models, which in turn will improve predictions in GMSL rise.

One of the microstructural features that can be used to study which deformation mechanisms operate in ice are SGBs. SGBs are often formed during recovery when many dislocations polygonize into a dislocation wall (Hirth and Lothe, 1982; Weertman and Weertman, 1992; Humphreys and Hatherly, 2004). SGBs and grain boundaries (GBs) can be observed using light microscopy (LM) images after the surface of the ice sample has been thermally etched (Kipfstuhl et al., 2006). GBs generally form deeper and wider etch grooves than SGBs, in part because of the higher misorientation angle of GBs (Saylor and Rohrer, 1999; Gottstein and Shvindlerman, 1999), that provides a very useful guide for differentiating between the two (Kipfstuhl et al., 2006). These LM images can be used to index grain boundary networks in polar ice by advanced image processing tools (Binder et al., 2013a). In this way, estimates can be made of the driving forces for SIBM (Binder et al., 2013b; Binder, 2014). However, in order to analyse a SGB in terms of slip system activity in the host grain, full crystallographic information (c- and a-axes) is required. This information can be used to derive the rotation axis of a SGB which, in combination with the trace orientation of a SGB provided by the LM image, can be used to analyse the SGB in terms of the active dislocation slip system if the SGB is formed by polygonization of geometrically necessary dislocations (Hirth and Lothe, 1982; Weertman and Weertman, 1992; Humphreys and Hatherly, 2004). Polarized LM techniques alone are not sufficient for this analysis since they only provide information about the c-axis orientation. X-ray Laue diffraction is one of the techniques that can provide the full crystallographic information (Miyamoto et al., 2005, 2011; Weikusat et al., 2011a). Although X-ray Laue diffraction has proven to be a valuable tool in determining the rotation axes of SGBs, the processing of the technique is semi-automatic and therefore too labour intensive to derive large data sets of SGBs along the length of an ice core. Therefore, the faster cryo-EBSD technique is the preferred method for making a full crystallographic analysis of a large number of SGBs in polycrystalline ice.

Knowledge of the trace and the rotation axis of a SGB can be used to determine the most likely glide planes and type of dislocations that define the active slip systems (Trepied et al., 1980; Lloyd et al., 1997; Neumann, 2000; Prior et al., 2002; Piazzolo et al., 2008; Weikusat et al., 2011b, 2017; Montagnat et al., 2015). EBSD data provides the rotation axes of a SGB and the trace is determined from the LM image, which is free of any

distortion that can occur in EBSD maps caused by charging or by any misalignment in mounting the EBSD sample at high tilts. EBSD provides information about boundary misorientation angles greater than about 0.5° .

In a first study of SGB types in naturally deformed ice, Weikusat et al. (2017) (Chapter 2) collected LM and EBSD data from single, equivalent depths from the EDML (EPICA-DML, Antarctica) and the NEEM (North Greenland Eemian Ice Drilling) ice cores. SGBs that were formed by glide of dislocations with Burgers vector $\mathbf{b}=(1/3)\langle 1\bar{2}10\rangle$ ($\mathbf{b}=\langle \mathbf{a}\rangle$) on the basal plane were most abundant in both ice core sections, with an almost equal occurrence of SGBs that were indicative of $\mathbf{b}=[0001]$ ($\mathbf{b}=\langle \mathbf{c}\rangle$) or $\mathbf{b}=(1/3)\langle 11\bar{2}3\rangle$ ($\mathbf{b}=\mathbf{a}+\mathbf{c}$) slip on the prism or the pyramidal planes. The relatively high occurrence of SGBs formed by non-basal slip, meaning dislocation glide on the prism or pyramidal plane (Figure 1.4b-e), was a surprising finding and formed the motivation to perform a more extensive study of slip systems of SGBs using cryo-EBSD along the length of a polar ice core. The evolution of SGBs formed by basal and non-basal slip with depth was of particular interest as this provides an indication for which mechanism is accommodating basal slip at what depth. The NEEM ice core was chosen as a sufficient number of ice core sections were readily available.

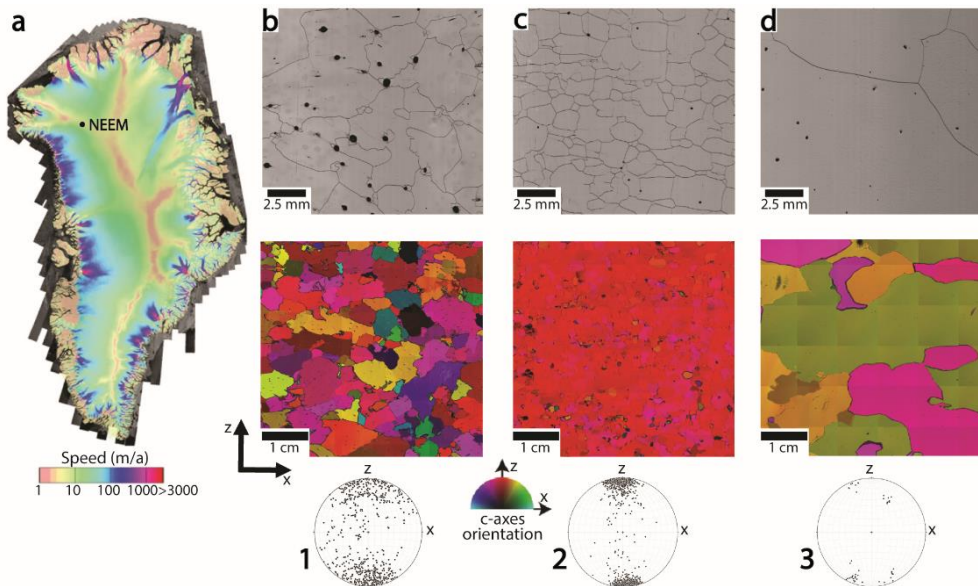


Figure 3.1: (a) The measured surface velocity of the Greenland ice sheet taken from Joughin et al. (2018) with the NEEM ice core drilling location with general appearances of the grain boundary network in reflective light microscopy (LM) images and the c-axes microstructure in (b) the Holocene ice at 889 m of depth, (c) the glacial ice at 1955 m of depth and (d) the Eemian ice at 2263 m of depth. Colors indicate the azimuth of the c-axes relative to the z-axis (parallel to the vertical ice core axis). The pole figures (equal area) projected onto the vertical plane show the c-axes for individual grains (one point per grain) of the three ice core sections in b-d.

In this study, EBSD analyses of SGBs in the NEEM ice core is presented. The approach of this study was similar to Weikusat et al. (2017) (Chapter 2). The ice in the NEEM ice core was divided into three different depth intervals as shown in Figure 3.1. The three depth intervals differ considerably in crystallographic preferred orientation (CPO), grain size, grain shape, deformation mode and rheology and coincide with different climate stages: the Holocene ice (0-1419 m of depth), the glacial ice (1419-2207 m of depth) and the Eemian ice (2207-2540 m of depth) (NEEM community members, 2013; Montagnat et al., 2014b; Figure 1.8). In total, over a thousand SGBs were mapped using cryo-EBSD at nine different ice core depth levels along the length of the NEEM ice core. The data were categorized in terms of the misorientation angles, boundary traces and rotation axes.

3.2 Background

The NEEM deep ice core (77.45°N, 51.06°W; 2484 m above sea level; ice core length 2540 m) was drilled in northwest Greenland during the field seasons of 2008 to 2012 (NEEM community members, 2013; Rasmussen et al., 2013). The NEEM ice core is located next to a ridge running roughly northwest-southeast (Montagnat et al., 2014b) and the flow of the ice at the surface is mainly parallel to this ridge with a small component of divergent flow normal to the ridge. The c-axis orientation in the NEEM ice core presents a gradual strengthening of the weak c-axes alignment in the uppermost part of the ice core to a strong single maximum c-axes alignment in the deeper, fine grained glacial ice. At the deeper glacial-Eemian interface the CPO develops into a partial girdle (Chapter 5), which coincides with a strong increase in grain size (Eichler et al., 2013; Montagnat et al., 2014b; Chapter 5). In the Holocene and in parts of the Eemian ice (Figure 1.8a; Chapter 5), a weak girdle CPO develops. The strong single maximum CPO that develops deeper in the ice core in the glacial ice indicates predominantly simple shear (Alley, 1988).

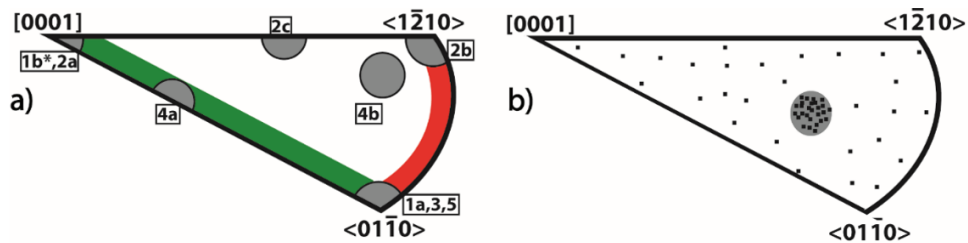
The trace of the SGBs in the host crystals were derived using LM images in combination with EBSD maps. The trace of each SGB was divided into four different categories: (i) the N-type, where the trace of the SGB is sub-normal to the basal plane, (ii) the P-type, where the trace of the SGB is sub-parallel to the basal plane, (iii) the curved boundary trace or the boundary trace that is oblique with respect to the basal plane and (iv) the Z-type, where the trace has an irregular and zig-zag shape. For Z-type SGBs, the sections parallel to the c-axis are often the longest and dominate the SGB. Z-type SGBs were therefore included in the N-type SGBs. The reader is referred to Weikusat et al. (2009a, 2009b, 2011a, 2011b, 2017) for a more elaborate description of the different types of SGBs.

The rotation axis of the SGBs, \mathbf{R} , can be categorized into several types (Weikusat et al., 2017; Chapter 2): (i) \mathbf{R} is in the basal plane (0001) with a direction $\langle hki0 \rangle$, (ii) \mathbf{R} is sub-parallel to the prism plane normal, $\langle 10\bar{1}0 \rangle$, (iii) \mathbf{R} is sub-parallel to the a-axis, $\langle 1\bar{2}10 \rangle$, (iv) \mathbf{R} is parallel to the c-axis, [0001], (v) \mathbf{R} is sub-parallel to a pyramidal plane normal, $\langle h0\bar{1}l \rangle$ and (vi) \mathbf{R} is general or dispersed. Here, ‘general’ means that \mathbf{R} is not parallel to a direction corresponding to a known slip system and ‘dispersed’ means that \mathbf{R} is

widely dispersed so that the rotation axes were spread out over a wide angle with no clear clustering around the rotation axes of known slip systems. An overview of the location of the rotation axes in the inverse pole figure (IPF) and known slip systems in ice (Hondoh, 2000) that were classified in this study are given in Figure 3.2. A spread of orientation in rotation axes is expected for low angle misorientation boundaries (Prior et al., 1999; Bate et al., 2005).

Previous work on SGBs in ice using X-ray Laue diffraction (Miyamoto et al., 2005, 2011; Weikusat et al., 2011a) and EBSD (Weikusat et al., 2011b, 2017) have shown that most SGBs can be classified in terms of four basic types of SGBs:

- N[c]: N-type tilt boundaries with the rotation axis parallel to the c-axis (Figure 3.2 number 2a; Figure 2.5b). These SGBs can be produced by an array of edge dislocations with Burgers vector $\mathbf{b}=(1/3)\langle 1\bar{2}10 \rangle$ gliding on a non-basal plane.



Number	Slip system according to Hondoh (2000)	Symmetrical tilt SGB plane	Rotation axis	Terminology according to Weikusat et al. (2017)
1a	$\langle 11\bar{2}0 \rangle / (0001)$	$\{11\bar{2}0\}$ - N	$\langle 10\bar{1}0 \rangle$	N[a]
1b*	$\langle 11\bar{2}0 \rangle / (0001)$	$\{0001\}$ - P	$[0001]$	P[c]
2a	$\langle 11\bar{2}0 \rangle / \{10\bar{1}0\}$	$\{11\bar{2}0\}$ - N	$[0001]$	N[c]
2b	$\langle 0001 \rangle / \{10\bar{1}0\}$	$\{0001\}$ - P	$\langle 11\bar{2}0 \rangle$	P[a]
2c	$\langle 11\bar{2}3 \rangle / \{10\bar{1}0\}$	$\{11\bar{2}5\}$ - other	$\langle 5\bar{1}0\ 5\ 6 \rangle$	
3	$\langle 0001 \rangle / \{11\bar{2}0\}$	$\{0001\}$ - P	$\langle 10\bar{1}0 \rangle$	P[a]
4a	$\langle 11\bar{2}0 \rangle / \{10\bar{1}1\}$	$\{11\bar{2}0\}$ - N	$\langle 1\bar{1}02 \rangle$	
4b	$\langle 11\bar{2}3 \rangle / \{10\bar{1}1\}$	$\{11\bar{2}5\}$ - other	$\langle 5\ 8\ \bar{1}3\ 3 \rangle$	
5	$\langle 11\bar{2}3 \rangle / \{11\bar{2}2\}$	$\{11\bar{2}5\}$ - other	$\langle 10\bar{1}0 \rangle$	

Figure 3.2: Simplified inverse pole figures (IPF) (equal area, upper hemisphere projection) showing a) the rotation axis of known slip systems (grey circles) with the general direction in the basal plane (red area) and one type of pyramidal rotation axes of the form $\langle h0\bar{l} \rangle$ (green area) and b) an example of a general rotation axis highlighted by the grey circle and a dispersed rotation axis spread out in the IPF. The table shows the known slip systems in ice with the symmetrical tilt SGB plane, rotation axis and the terminology according to Weikusat et al. (2017). The only type of twist boundary that was identified in this study was added to the table and is indicated by an asterisk (*). The rotation axes of the different slip systems are indicated in a). In the third column the SGB planes that are normal (N) and parallel (P) to the basal plane are indicated. Data courtesy of G. M. Pennock (Utrecht University) and R. Kilian (Basel University).

- P[c]: P-type tilt boundaries with the rotation axis parallel to the c-axis (Figure 3.2 number 1b; Figure 2.5c). These SGBs can be produced by sets of screw dislocations with Burgers vector $\mathbf{b}=(1/3)\langle 1\bar{2}10 \rangle$ gliding on the basal plane.

- P[a]: P-type tilt boundary with the rotation axis parallel to the basal plane (Figure 3.2 number 2b and 3; Figure 2.5d). This type of SGB can be produced by an array of edge dislocations with Burgers vector $\mathbf{b}=[0001]$ or $\mathbf{b}=(1/3)\langle 11\bar{2}3 \rangle$ gliding on one of the non-basal planes.

- N[a]: N-type boundaries with the rotation axis within the basal plane can be a tilt or a twist boundary (Figure 3.2 number 1a; Figure 2.5a). The rotation axis can have an orientation $\langle hki0 \rangle$ or be sub-parallel to $\langle 10\bar{1}0 \rangle$ or $\langle 1\bar{2}10 \rangle$ axes. In the case of basal tilt boundaries, the SGBs consist of $\mathbf{b}=(1/3)\langle 1\bar{2}10 \rangle$ dislocations gliding on the basal plane. In the case of twist boundaries, the SGBs consist of $\mathbf{b}=(1/3)\langle 1\bar{2}10 \rangle$ and $\mathbf{b}=[0001]$ or $\mathbf{b}=(1/3)\langle 11\bar{2}3 \rangle$ dislocations.

In this Chapter, similar to Weikusat et al. (2009b, 2011b, 2017) and Chapter 2, N[a] and P[c] boundaries were classified as basal slip, while N[c] and P[a] boundaries were classified as non-basal slip.

3.3 Materials and methods

Nine samples from the NEEM deep ice core were used in this study: three ice core samples from the Holocene ice at depths of 443 m, 718 m and 889 m, four ice core samples from the glacial ice at depths of 1767 m, 1937 m, 1993 m and 2103 m and two ice core samples from the Eemian ice at depths of 2241 m and 2423 m. The EBSD dataset of the ice core sample at a depth of 718 m was also used for the study of Weikusat et al. (2017) presented in Chapter 2. All nine ice core samples in this study were mapped using cryo-EBSD between July 2014 and August 2016 using the techniques described by Weikusat et al. (2011b). Ice core samples were transported at -25°C from the NEEM drilling site in Greenland to the Alfred Wegener Institute (AWI) in Bremerhaven, Germany. Samples (90 x 55 mm) were cut parallel to the long axis of the ice core using a band saw in the cold lab at -20°C (Weikusat et al., 2017). Subsequently, the samples were polished following the procedures using a microtome (e.g. Pauer et al., 1999). LM microstructure mapping was performed on each ice core section (Kipfstuhl et al., 2006).

After LM mapping of the ice core section, the most interesting areas were selected based on microstructural features like GB and SGB density, slip bands and bulging of GBs. SGBs associated with plate-like inclusions (Nedelcu et al., 2009) and air bubbles were excluded from the analyses, as these SGBs probably formed during storage of the ice core sections (Binder, 2014) or during EBSD sample transport and storage. SGBs were differentiated from GBs by the lighter etch depth and by the continuity of the trace in the host crystal.

A total of 10-15 samples, approximately 8 x 8 x 5 mm, were cut using a handsaw from the selected regions of interest for each ice core section. Each individual small section

was microtomed a second time and the LM mapping procedure repeated. These LM images, made 2 and 21 days prior to the EBSD mapping, were used to determine the SGB trace and to check if any artefacts appeared during transport or sample transfer into the scanning electron microscope (SEM).

All EBSD samples were packed into small metal boxes and wrapped into two plastic bags to prevent condensation and sublimation during transport. Dry ice (solid carbon dioxide, -78.5°C) was used during the transport of the EBSD samples from the AWI in Bremerhaven to Utrecht University in the Netherlands where they were stored in a -20°C storage room. Often, the dry ice did not fully sublime for several days to a week so that the EBSD samples were at dry ice temperature for most of the time during storage at Utrecht University.

All EBSD data, except for the ice core section selected at a depth of 443 m, were collected on a FEI Nova Nanolab equipped with an EBSD detector (Oxford Instruments HKL Technology, Abingdon, UK) and a cryo-stage (Quorum Technologies Ltd. Ringmer, UK). The EBSD patterns were acquired, processed and indexed using the Channel 5 software of OI-HKL Technology. The EBSD patterns of the ice core section taken at a depth of 443 m were collected on a FEI Helios Nanolab G3 UC, which was equipped with

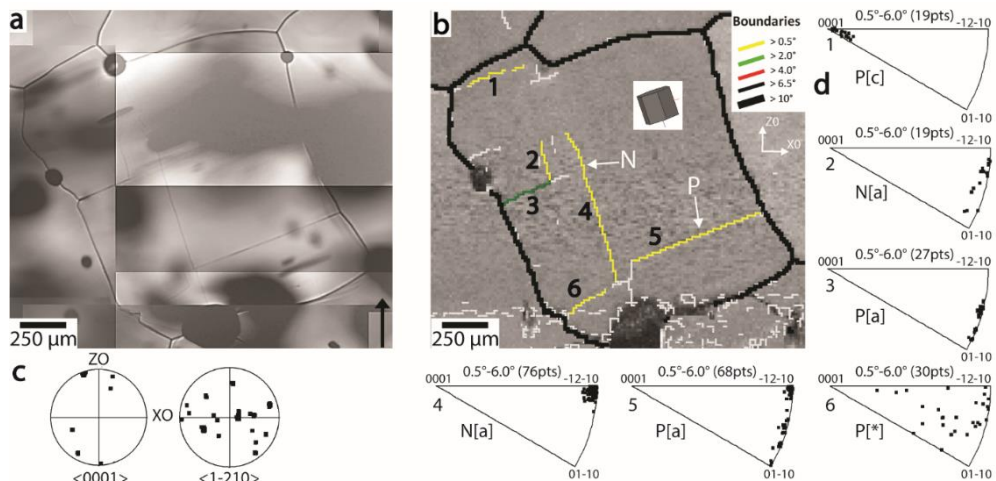


Figure 3.3: Light microscopy (LM) and corresponding EBSD data for one of the studied areas in the Holocene ice at a depth of 443 m. (a) Transmitted LM image showing several GBs as deeper etched (darker) lines and less deeply etched lines for SGBs. Black regions are air bubbles. The black arrow in (a) points to the top of the ice core. (b) The corresponding EBSD map (band contrast) showing six SGBs subsets labelled 1-6: the misorientation angle of each of the SGBs is shown in the legend. White boundaries are boundaries with a misorientation angle $>0.5^{\circ}$ and were not included in the data set. A schematic showing a hexagonal crystal shows the crystal orientation of the grain that contains the highlighted SGBs. An example of a SGB parallel (P) and one normal (N) to the basal plane are indicated with white arrows. (c) Pole figure (equal area, upper hemisphere projection) of the [c] and $\langle a \rangle$ axis of the grains for the complete EBSD map. (d) Inverse pole figures (equal area, upper hemisphere projection) showing the rotation axes in crystal coordinates of SGBs 1-6. The classification of the SGBs is indicated next to the IPFs.

White boundaries are boundaries with a misorientation angle $>0.5^{\circ}$ and were not included in the data set. A schematic showing a hexagonal crystal shows the crystal orientation of the grain that contains the highlighted SGBs. An example of a SGB parallel (P) and one normal (N) to the basal plane are indicated with white arrows. (c) Pole figure (equal area, upper hemisphere projection) of the [c] and $\langle a \rangle$ axis of the grains for the complete EBSD map. (d) Inverse pole figures (equal area, upper hemisphere projection) showing the rotation axes in crystal coordinates of SGBs 1-6. The classification of the SGBs is indicated next to the IPFs.

the same EBSD detector and cryo-stage. The EBSD patterns of this ice core section were processed and indexed using the AZTEC software (Oxford Instruments, High Wycombe, UK). Typical SEM conditions were a working distance of 6-12 mm, a sample stage temperature of -100°C to -150°C, a cold trap temperature of -120°C to -170°C, an accelerating voltage of 7.5-20 kV, a beam current of 2.1-8.4 nA and a chamber pressure of 10^{-5} - 10^{-7} hPa. EBSD collection conditions were typically a frame averaging of 1-2, pattern binning of 1x1 to 4x4 and a step size of 5-20 μm . Mapping rates were typically 8-30 pixels per second and the indexing rate was better than 80% for the majority of the maps, partly by re-indexing the saved EBSD patterns. Using these conditions, subgrain boundaries with misorientation angles of 0.5° could be reliably detected after orientation averaging (Humphreys et al., 2001). The EBSD maps were analyzed using the Channel 5 software (Oxford Instruments). Pixels across individual SGBs were manually selected and were saved as a subset.

Most SGBs originate at the GBs or ‘mantle’ of the grains (e.g. Gifkins 1976; Weikusat et al., 2009b; Faria et al., 2014) and their misorientation angle becomes lower towards the core of the grain. Therefore, a cut-off angle would be needed to define the length of SGBs that have a relatively high misorientation angle near the GB and fade out in the core of the grain. Since the thermal etching of SGBs with misorientation angles $<0.5^\circ$ is obvious in the LM images and the EBSD method is unable to detect these low misorientation angles, analyses in terms of SGB length was omitted in this study. Not all SGBs that were observed in the EBSD maps were included in the data set. All white boundaries in Figure 3.3-3.6 have a misorientation angle $>0.5^\circ$, but were not included in the data set. In many cases, the white boundaries are noise. Some white boundaries were excluded from the data set because they were affected by air bubbles or plate-like inclusions, such as the white boundaries near the air bubble in the centre of Figure 3.4b or part of SGB 6 in Figure 3.5. Boundary 8 in Figure 3.4 was also excluded from the data set as this boundary is part of the grain boundary network, has a curved trace and the thickness of the etch groove in the LM image suggests that this is a low-angle grain boundary instead of a SGB.

The allocation of the rotation axis of a SGBs to one of the different types of rotation axes was performed manually following the approach of Weikusat et al., (2011b). Spread is observed in \mathbf{R} of many SGBs that cluster around the rotation axis of a known slip system. For orientation averaged data a typical spread of \mathbf{R} is about 15-20 degrees for subgrain misorientations in the range of 0.5 to 1 degree (Weikusat et al., 2011b, their Figure 13). This spread mainly occurs because of the low misorientation angle of the SGB (Prior et al., 1999) and is inversely dependent on misorientation angle of the SGB (Bate et al., 2005). Nevertheless, the clustering of \mathbf{R} around a known direction is usually sufficient to classify the rotation axis.

The EBSD analysis does not provide information about the 3D orientation of the SGB plane and therefore it was not possible to distinguish between different types of N[a] boundaries. In the interpretation it is assumed that most N[a] boundaries are tilt walls made by basal slip, as is expected from Hondoh (2000, 2009) and Piazzolo et al. (2008). Also, the

observation of N-type SGBs with slip bands in natural ice (Weikusat et al., 2009b) is consistent with tilt boundaries and not with twist boundaries.

As the grain size of the Eemian ice core samples, 5 mm to many centimetres in diameter (Chapter 5), were much larger than both the Holocene ice, 2.5 to 5 mm and the glacial ice, 1.5 to 3.5 mm, (Eichler et al., 2013; Montagnat et al., 2014b) fewer SGBs per sample could be sampled. Furthermore, the SGB density is much lower in the Eemian ice (Montagnat et al., 2014b) and heterogeneously distributed (Weikusat et al., 2009b). A z-test (Wonnacott and Wonnacott, 1990) was used to determine whether the results of different data sets with different sample sizes was statistically significant. The outcome (p-value) of these z-tests gives the probability of the results occurring by chance. For example: $p=0.26$

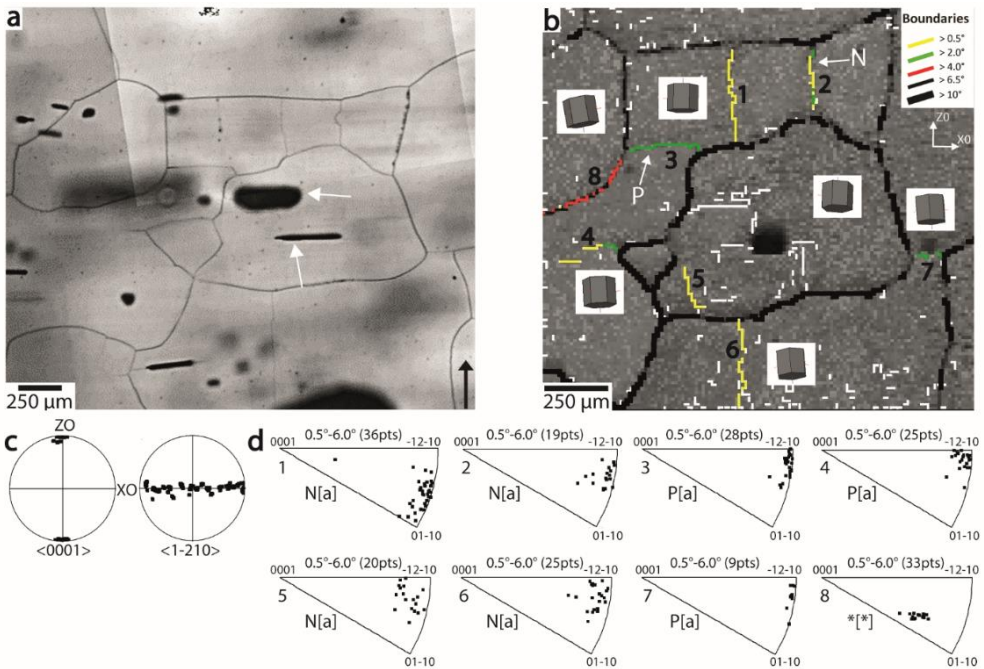


Figure 3.4: Light microscopy and corresponding EBSD data for one of the studied areas in the glacial ice at a depth of 2103 m. (a) Transmitted LM image showing several GBs as deeper etched (darker) lines and less deeply etched lines for SGBs. A plate-like inclusion (lower white arrow) and an air bubble (upper white arrow) are shown in the LM image. The black arrow in (a) points to the top of the ice core. (b) The corresponding EBSD map (band contrast) showing eight boundary subsets labelled 1-8: the misorientation angle of each of the boundaries is shown in the legend. Boundary 8 is not included in the data set as it is part of the grain boundary network and has a deep and wide etch groove. White boundaries are boundaries with a misorientation angle $>0.5^\circ$ and were not included in the data set. Several schematics of a hexagonal crystal show the crystal orientations of different grains in the EBSD map. An example of a SGB parallel (P) and one normal (N) to the basal plane are indicated with white arrows. (c) Pole figure (equal area, upper hemisphere projection) of the [c] and <a> axes of the grains of the complete EBSD map. (d) Inverse pole figures (equal area, upper hemisphere projection) showing the rotation axes in crystal coordinates of boundaries 1-8. The classification of the SGBs is indicated next to the IPFs.

means that there is a 26% chance that the two populations are the same, but their difference is a result of chance and there is a 74% chance that the populations differ.

3.4 Results

3.4.1 Overview of microstructures

The location of the NEEM ice core and examples of microstructures typical for the three depth intervals are shown in Figure 3.1. The Holocene ice contains relatively coarse and interlocking grains (Binder, 2014) with a relatively weak CPO (Eichler et al., 2013). The grain size in the glacial ice is much finer with a more regular grain shape and the CPO showing a strong single maximum. The grains in the Eemian ice can grow to many centimetres with a strongly bulging grain boundary network and often have a multi maxima or partial girdle type of CPO (Chapter 5). In Figures 3.3-3.6, examples are given of LM images and the corresponding EBSD maps for the three depth intervals. The SGBs in each EBSD map are highlighted and coloured according for the ranges of different misorientation angles (Section 3.4.2.1). White boundaries have a misorientation angle $>0.5^\circ$, but were excluded from the data set. A compilation of the complete data set of SGB trace alignment, rotation axes and misorientation angles for each of the three depth intervals is given in Table 3.1.

3.4.2 EBSD mapped microstructures

In general, EBSD mapping of the samples was successful for the Holocene and glacial ice but collecting data from the Eemian ice samples was problematic. A large number of the Eemian EBSD samples cracked, causing EBSD sample loss and severe charging during EBSD mapping. Combined with the larger grain size, heterogeneity and low density of SGBs in the Eemian ice, far fewer SGB data was collected compared to the Holocene and glacial ice.

Figures 3.3-3.6 show representative microstructures (LM images and EBSD maps) of samples from the Holocene, glacial and Eemian ice. All SGBs that were observed in the LM images and EBSD maps emanated from a grain boundary or triple junctions. About 20% of the SGB that were identified in the LM images were not detected in the EBSD maps. Some SGBs were obscured by damage or contamination of the surface in the EBSD sample. In some cases, the misorientation angle of a SGB was lower than the detection limit of about 0.5° . For example, the LM image in Figure 3.5a shows a SGB indicated by a red arrow, which was observed in secondary electron images, but was not detected in the EBSD map because the misorientation angle was $<0.5^\circ$. These missing SGBs were both N- and P-type SGBs, so there is no bias to a particular type of boundary in the measured types of SGBs shown in Table 3.1 and Figure 3.7. Most SGBs (compare the LM images and EBSD microstructures in Figures 3.3-3.6) remained stable during transport and storage at Utrecht University. However, some of the GBs migrated a small amount in the 2-21 day interval between LM imaging at Bremerhaven and EBSD mapping at Utrecht University. In Figure 3.4 for example, the grain between SGB 4 and SGB 5 shrunk and the grain boundary

marked by a white arrow in Figure 3.6b migrated during storage, leaving behind SGB 6. Sometimes, the EBSD mapped microstructure differed from the LM image, as in Figure 3.5 where the shape of the GBs differs. This distortion arises because of misalignment of the EBSD sample on the SEM sample holder. Other distortions of EBSD maps arose because of charging, which occurred most often in the Eemian ice due to cracking of the samples during the SEM transfer procedure (Weikusat et al., 2011b; Appendix B). Air bubbles and clathrates hydrates often changed in shape or size during storage of the EBSD samples, such as the plate-like inclusion and air bubbles indicated by the white arrows in Figure 3.5a.

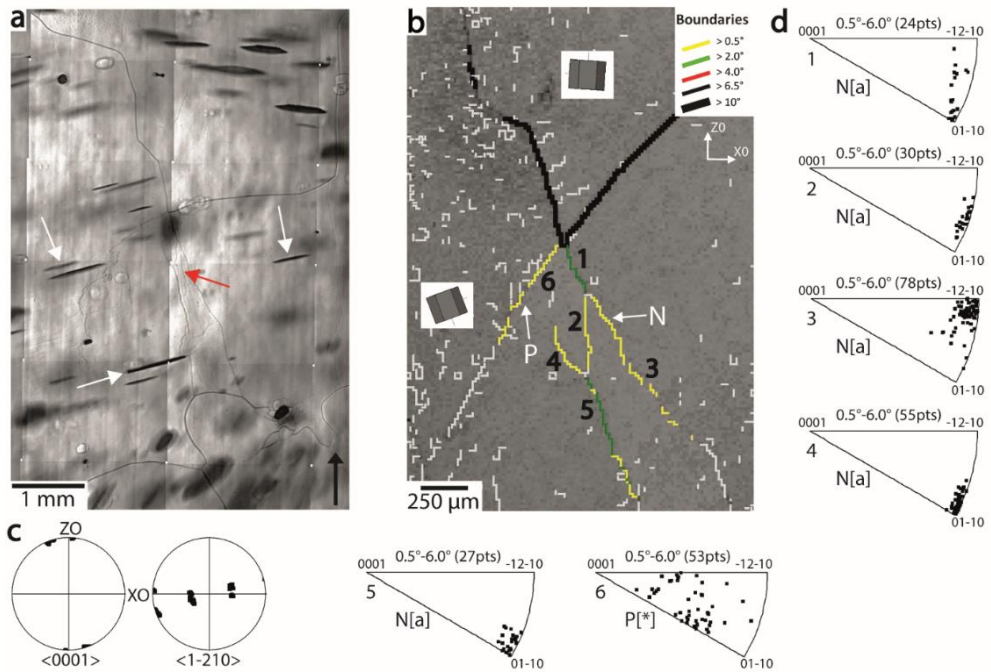


Figure 3.5: LM microscopy and corresponding EBSD data for one of the studied areas in the Eemian ice at a depth of 2241 m. (a) Transmitted LM image showing several GBs as deeper etched (darker) lines and several less deeply etched lines for SGBs. Plate-like inclusions are indicated by white arrows in the LM image. The red arrow indicates a SGB identified in the LM image, but that was not detected using EBSD because the misorientation angle was $< 0.5^\circ$. The black arrow in (a) points to the top of the ice core. (b) The corresponding EBSD map (band contrast) showing the location of six SGB subsets labelled 1-6: the misorientation angle of each of the SGBs is given in the legend. The EBSD map is distorted relative to the LM image due to a misalignment of the EBSD sample on the SEM sample holder. White boundaries are boundaries with a misorientation angle $> 0.5^\circ$ and were not included in the data set. Schematics of the hexagonal crystals show the crystal orientations of the grains. SGBs parallel (P) and normal (N) to the basal plane are indicated with white arrows. Part of SGB 6 was excluded from the dataset (the white coloured part), because this part is likely affected by the plate-like inclusion next to SGB 6. (c) Pole figure (equal area, upper hemisphere projection) of the [c] and $\langle a \rangle$ axes of the grains of the complete EBSD map. (d) Inverse pole figures (equal area, upper hemisphere projection) showing the rotation axes in crystal coordinates of SGBs 1-6. The classification of the SGBs is indicated next to the IPFs.

These inclusions tend to produce SGBs (Figure 3.4b) or influence the orientation of SGBs (Figure 3.5 SGB 6): these SGBs, produced or deviated by a bubble or plate-like inclusion, were not included in the SGB data set.

A total of 1024 SGBs were analyzed using EBSD during this study: 475 in the Holocene ice, 502 in the glacial ice and 47 in the Eemian ice. The classification of the SGBs in Figure 3.3-3.6 is indicated next to the inverse pole figures (IPFs). Table 3.1 shows a summary of the number frequency of these SGB. The data for all depths are grouped together for a comparison of the different types of SGB in the three depth intervals of the NEEM ice core. All SGBs are categorized by misorientation angle, rotation axis, trace with the basal plane and types of SGB for each of the three depth intervals (Figure 3.7a-d). The glide planes as inferred from the types of SGBs (Figure 3.7d) are shown in Figure 3.7e. A summary of the slip system as a function of misorientation angle for the Holocene ice and glacial ice is given in Figure 3.7f. A detailed description of each of these SGB categories is given below.

3.4.2.1 SGB misorientation angles

The misorientation angles of all SGBs were less than 6.5° . The misorientation angles of SGBs were arbitrarily divided into three ranges of about 2° (0.5° to 2.0° , 2.0° to 4.0° and 4.0° to 6.5°). Most SGBs have misorientations in the range 0.5° to 2.0° (Figure 3.7a). The Holocene ice shows a different SGB misorientation angle distribution than the glacial ice. The Holocene ice contains 18% more 0.5° to 2.0° SGBs than the glacial ice, whereas there are 5% more 2.0° to 4.0° SGBs in the glacial ice than in the Holocene ice. 4.0° to 6.5° SGBs are found more frequent in the glacial ice (17%) than in the Holocene ice (3%). Over 90% of the SGBs found in the Eemian ice were 0.5° to 2.0° SGBs, the remaining SGBs in the Eemian ice were all in the range 2.0° to 4.0° .

3.4.2.2 SGB rotation axes

The rotation axes, \mathbf{R} , are displayed in IPFs. Most SGBs have a rotation axis in the basal plane (0001) with a direction $\langle hki \rangle$ (Figure 3.3d SGBs 2, 3, 5; Figure 3.4d SGB 1, 2, 3, 5, 6, 7; Figure 3.5d SGB 1, 2; Figure 3.6d SGB 5). Two special directions in the basal plane occur where the clustering of \mathbf{R} is parallel to the a-axis $\langle 1\bar{2}10 \rangle$ (Figure 3.3d SGB 4; Figure 3.4d SGB 4; Figure 3.5d SGB 3) or \mathbf{R} parallel to the prism plane normal $\langle 10\bar{1}0 \rangle$ (Figure 3.5d SGB 4, 5). Other crystallographic directions include \mathbf{R} parallel to the c-axis [0001] (Figure 3.3d SGB 1; Figure 3.6d SGB 1, 2, 3), \mathbf{R} is parallel to a pyramidal plane normal $\langle h0\bar{1} \rangle$ (not present in Figures 3.3-3.6), \mathbf{R} is widely dispersed (Figure 3.3d SGB 6, Figure 3.5d SGB 6; Figure 3.6d SGB 6) and \mathbf{R} has a general rotation axis (Figure 3.4d SGB 8; Figure 3.6d SGB 4). The rotation axes of the SGBs in Figure 3.3-3.6 are indicated next to the IPFs. An asterisk, *, was used for rotation axes that were widely dispersed or for general rotation axes.

The rotation axes of the SGBs show a similar trend for all three depth intervals (Figure 3.7b). The majority (>75%) of the SGBs have a rotation axis in the basal plane. Table 3.1 shows that for all three depth intervals, the most frequently found rotation axis is parallel to $\langle hki0 \rangle$ followed by $\langle 1\bar{2}10 \rangle$ and $\langle 10\bar{1}0 \rangle$ directions. There are more SGBs with a rotation axis within the basal plane in the Holocene ice (85%) than in the glacial ice (75%) (Figure 3.7b) (z-test, $p < 0.001$). For all three layers, Holocene, glacial and Eemian, a small percentage (10-15%) of the SGBs have a rotation axis classified as 'other', which means that the rotation axis was either dispersed, had a general rotation axis or was parallel to $\langle h0\bar{1}l \rangle$ (shown in Table 3.1). A small percentage of SGBs (<10%) has a rotation axis parallel to the c-axis. In the glacial ice, about 10% of the SGBs have a rotation axis parallel to the c-axis, while this is only 3% for the Holocene ice (z-test, $p < 0.001$). Unlike the misorientation angle distribution, the ice in the Eemian shows the same trend in rotation axes as the Holocene and glacial ice.

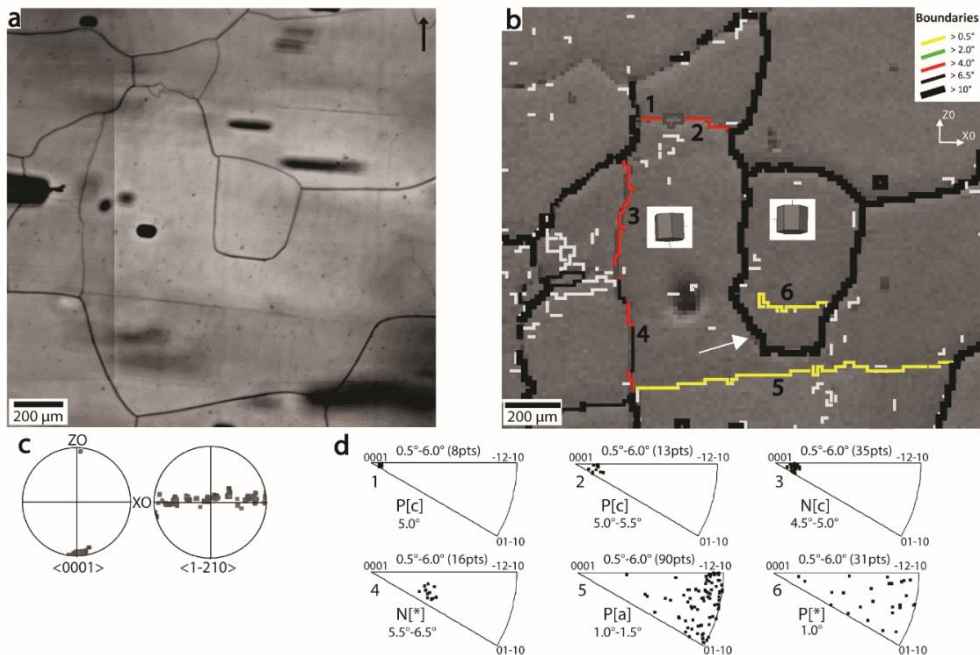


Figure 3.6: Light microscopy and corresponding EBSD data for one of the studied areas in the glacial ice at a depth of 2103 m showing high angle (4.0° - 6.5°) SGBs with a general rotation axis. (a) Transmitted LM image showing several GBs as deeper etched (darker) lines and less deeply etched lines for SGBs with misorientations less than 4.0° . The black arrow points to the top of the ice core. (b) The corresponding EBSD map (band contrast) showing six SGB subsets labelled 1-6: the misorientation angle range of each of the SGBs is shown in the legend. White boundaries are boundaries with a misorientation angle $>0.5^\circ$ and were not included in the data set. Schematics of the hexagonal crystal shows the crystal orientation of the grain. The white arrow shows a grain boundary that migrated during EBSD sample storage. (c) Pole figure (equal area, upper hemisphere projection) of the [c] and $\langle a \rangle$ axes of the grains of the complete EBSD map. (d) Inverse pole figures (equal area, upper hemisphere projection) showing the rotation axes in crystal coordinates and the misorientation angles of SGBs 1-6. The classification of the SGBs is indicated next to the IPFs.

Table 3.1: Summary of the SGB data in the NEEM ice core for the Holocene ice (depth range down to 1419 m), glacial ice (depth range of 1419-2207 m) and Eemian ice (depth range of 2207-2540 m). The total number of SGBs measured, n , is given for misorientation angle $>0.5^\circ$. The first column defines the three types of SGB trace, where N-type has a SGB trace normal to the basal plane, P type has a SGB trace parallel to the basal plane and oblique has a SGB trace neither parallel nor normal to the basal plane. The misorientation angle range of the SGBs is subdivided into 0.5° - 2.0° , 2.0° - 4.0° and 4.0° - 6.5° ranges in the second column. The next six columns show different rotation axes, respectively: $[0001]$ ($[c]$); $\langle 1\bar{2}10 \rangle$ ($\langle a \rangle$); $\langle 10\bar{1}0 \rangle$ (prism plane normal); basal plane $\langle hki0 \rangle$ (general direction in basal plane); $\langle h0\bar{l}l \rangle$ (pyramidal type plane normal); * refers to a SGB rotation axis that was not-classified in terms of one of the preceding 5 columns. The outer four columns give simplified statistics where the column 'in basal plane' combines the $\langle 1\bar{2}10 \rangle$, $\langle 10\bar{1}0 \rangle$ and $\langle hki0 \rangle$ rotation axes and the column 'other' combines the $\langle h0\bar{l}l \rangle$ (pyramidal type plane normal) rotation axis and the * type. The rotation axes of these columns are also shown in Figure 3.7b. High angle SGBs (4.0° - 6.5°) in the glacial ice that could not be classified are indicated by #.

Holocene ice (total $n>0.5^\circ = 475$)											
		Rotation axes									
trace with basal plane	misorientation angle	$[0001]$	$\langle 1\bar{2}10 \rangle$	$\langle 10\bar{1}0 \rangle$	$\langle hki0 \rangle$	$\langle h0\bar{l}l \rangle$	*	$\langle 0001 \rangle$	in basal plane	other	total
N-type	0.5° - 2.0°	4	47	40	77	1	15	4	164	16	233
	2.0° - 4.0°	0	8	20	15	0	0	0	43	0	
	4.0° - 6.5°	0	2	2	2	0	0	0	6	0	
P-type	0.5° - 2.0°	7	26	18	69	0	18	7	113	18	183
	2.0° - 4.0°	2	12	8	14	0	2	2	34	2	
	4.0° - 6.5°	0	2	3	2	0	0	0	7	0	
oblique	0.5° - 2.0°	1	8	4	19	0	14	1	31	14	59
	2.0° - 4.0°	0	2	4	4	1	1	0	10	2	
	4.0° - 6.5°	0	0	0	0	0	1	0	0	1	
total		14	107	99	202	2	51	14	408	53	

glacial ice (total $n>0.5^\circ = 502$)											
		Rotation axes									
trace with basal plane	misorientation angle	$[0001]$	$\langle 1\bar{2}10 \rangle$	$\langle 10\bar{1}0 \rangle$	$\langle hki0 \rangle$	$\langle h0\bar{l}l \rangle$	*	$\langle 0001 \rangle$	in basal plane	other	total
N-type	0.5° - 2.0°	2	37	27	64	0	12	2	128	12	225
	2.0° - 4.0°	1	14	18	22	0	1	1	54	1	
	4.0° - 6.5°	6	2	6	5	4	4	6	13	8 [#]	
P-type	0.5° - 2.0°	16	29	17	53	0	10	16	99	10	212
	2.0° - 4.0°	7	13	7	21	1	5	7	41	6	
	4.0° - 6.5°	8	4	9	4	2	6	8	17	8 [#]	
oblique	0.5° - 2.0°	2	7	3	4	0	15	2	14	15	65
	2.0° - 4.0°	2	2	4	2	0	1	2	8	1	
	4.0° - 6.5°	4	0	2	2	0	15	4 [#]	4 [#]	15 [#]	
total		49	107	93	177	7	69	49	377	76	

Eemian ice (total $n>0.5^\circ = 47$)											
		Rotation axes									
trace with basal plane	misorientation angle	$[0001]$	$\langle 1\bar{2}10 \rangle$	$\langle 10\bar{1}0 \rangle$	$\langle hki0 \rangle$	$\langle h0\bar{l}l \rangle$	*	$\langle 0001 \rangle$	in basal plane	other	total
N-type	0.5° - 2.0°	2	6	4	14	1	1	2	24	2	32
	2.0° - 4.0°	0	3	1	0	0	0	0	4	0	
	4.0° - 6.5°	0	0	0	0	0	0	0	0	0	
P-type	0.5° - 2.0°	1	2	2	1	1	2	1	5	3	9
	2.0° - 4.0°	0	0	0	0	0	0	0	0	0	
	4.0° - 6.5°	0	0	0	0	0	0	0	0	0	
oblique	0.5° - 2.0°	0	0	2	1	0	3	0	3	3	6
	2.0° - 4.0°	0	0	0	0	0	0	0	0	0	
	4.0° - 6.5°	0	0	0	0	0	0	0	0	0	
total		3	11	9	16	2	6	3	36	8	

3.4.2.3 SGB trace

The most abundant type of SGB trace are N-type boundaries (Figure 3.3 SGB 2, 4; Figure 3.4 SGB 1, 2, 5, 6; Figure 3.5 SGB 1, 2, 3, 4, 5; Figure 3.6 SGB 3, 4) with a slightly lower percentage of P-type boundaries (Figure 3.3 SGB 1, 3, 5, 6; Figure 3.4 SGB 3, 4, 7; Figure 3.5 SGB 6; Figure 3.6 SGB 1, 2, 5, 6). Relatively rare are SGBs that are neither parallel nor normal to the basal plane. The trace of the SGBs in Figure 3.3-3.6 is indicated next to the IPFs. An asterisk, *, was used for a trace that was irregular or oblique to the basal plane. The Holocene ice and the glacial ice have roughly the same percentage of SGBs normal to the basal plane (N-type), SGBs parallel to the basal plane (P-type) and SGBs that were neither parallel nor normal to the basal plane (other boundaries) (Figure 3.7c). However, the Eemian ice contains far more SGBs with an orientation normal to the basal plane (68%) than the Holocene and the glacial ice (both about 40%) (z-test, $p < 0.001$).

3.4.2.4 Analysis of SGB types

All four types of SGBs (Section 3.2) were identified in NEEM ice core as can be seen by the classification of the SGBs in Figure 3.3-3.6 next to the IPFs. These results are summarized in Figure 3.7d. SGBs with a trace normal to the basal plane and with a rotation axis in the basal plane, N[a] type boundaries, (Figure 3.3 SGB 2, 4; Figure 3.4 SGB 1, 2, 5, 6; Figure 3.5 SGB 1, 2, 3, 4, 5) are the most common in all three depth intervals, followed by SGBs parallel to the basal plane with a rotation axis in the basal plane, P[a] type boundaries, (Figure 3.3 SGB 3, 5; Figure 3.4 SGB 3, 4, 7). All three depth intervals show a low percentage of SGBs parallel or normal to the basal plane with the c-axis as rotation axis (P[c] and N[c] boundaries, respectively). Per depth interval, an average of 20-25% of SGBs were not-classified (Figure 3.7d) either because of the rotation axis was classified as 'other' (Section 3.4.2.2) and/or the SGBs had an oblique or irregular trace (* types of SGB). These not-classified SGBs, including the SGBs with a rotation axis parallel to $\langle h0\bar{1}l \rangle$, are therefore inconsistent with a known slip system. Figure 3.7e gives an overview of the likely slip systems of the SGBs, where 'basal slip' is dislocation glide on the basal plane (N[a] and P[c]) and 'non-basal slip' is dislocation glide on one of the non-basal planes (N[c] and P[a]), such as the prism or pyramidal planes. The percentage of SGBs that were not-classified as basal or non-basal slip is roughly the same for all three depth intervals (Figure 3.7e). However, a higher percentage of SGBs formed by basal slip is found in the Eemian ice (62%) than in the Holocene ice and glacial ice (47% and 45%, respectively) (z-test, $p = 0.017$).

Table 3.2 shows the slip system activity when excluding not-classified SGBs with the mean grain size for the ice core sections mapped with EBSD in the Holocene, glacial and Eemian ice. The slip system activity is given for each of the individual ice core section in the fifth column and for the three depth intervals as a whole in the last column. In the Holocene ice, there is a trend of an increasing percentage of SGBs indicative of basal slip with increasing depth. To check the significance of this trend, the basal/non-basal slip ratio of the ice core sections at 718 and 889 m of depth were compared to the ice core section at 443 m of depth using a z-test. The p-values indicate that there is a small chance (16.4%)

that the basal/non-basal slip ratio in the ice core section at 443 and 718 m of depth are the same, but the difference is explained by chance. For the ice core section at 889 m of depth, this chance is <0.1%. In the glacial ice there is no clear trend of basal/non-basal slip ratio with depth or with grain size.

3.4.2.5 Combination of possible slip system and misorientation angle

Figure 3.7f shows a comparison of the slip systems (Figure 3.7e) in the Holocene and the glacial ice for each of the three ranges of misorientation angle (Figure 3.7a). The Eemian ice was not included in this comparison as there were too few SGBs in this depth interval to subdivide the results further. The percentage of SGBs produced by basal or non-basal slip is almost the same for each of the three misorientation angle ranges: for instance, in the Holocene ice, the percentages for basal slip and non-basal slip are respectively 77% and 74% for the 0.5° to 2.0° range. For those SGBs in the Holocene ice that were not-classified, the trend in misorientation angle shows roughly a similar trend to the SGBs analyzed with basal and non-basal slip, that is, the contribution of all types of SGB decreases with increasing misorientation angle. However, there are more SGBs that were not-classified (84%) compared to SGBs classified as basal (74%) and non-basal (77%) slip at low misorientation angles (0.5°-2.0°). Only 1% of SGBs that were not-classified had a misorientation angle in the higher angle range 4.0°-6.5° in the Holocene ice. For the glacial ice, the SGBs that are not-classified with a known slip system show a very different misorientation angle distribution compared to the Holocene ice. Less than half (48%) of these SGBs are made up of 0.5°-2.0° SGBs, while 36% have higher misorientation angles in the range 4.0°-6.5°, which is a higher percentage than the SGBs classified as basal and non-basal with 9 and 14%, respectively.

Figure 3.6 shows an example of a not-classified high angle SGB in the glacial ice (SGB 4). SGB 1 and 2, which are parallel to the basal plane, are separated by a tiny subgrain. The rotation axes of SGBs 1 and 2 are almost parallel to the c-axis. SGBs 3 and 4, both roughly normal to the basal plane, are connected, but show a change in direction and rotation axis next to the air bubble on the left side of the boundary. SGB 3 has a rotation axis that is, similar to the rotation axis of SGB 1 and 2, slightly tilted relative to the c-axis, while the lower part (SGB 4) has a rotation axis between $[0001]$ and $\langle 10\bar{1}0 \rangle$. This rotation axis is close to the rotation axis for pyramidal slip (Figure 3.2 number 4a), but the clustering is relatively weak and the rotation axis deviated significantly relative to the pyramidal rotation axis.

3.5 Discussion

3.5.1 General discussion of SGB statistics

During this study, SGBs in the NEEM ice core were analyzed on the basis of their misorientation angle, rotation axis and trace in the host grain. SGBs likely produced by basal and non-basal slip have a similar range of SGB misorientation angles (Figure 3.7f). This shows that there is no preferred misorientation angle for SGB that have likely been

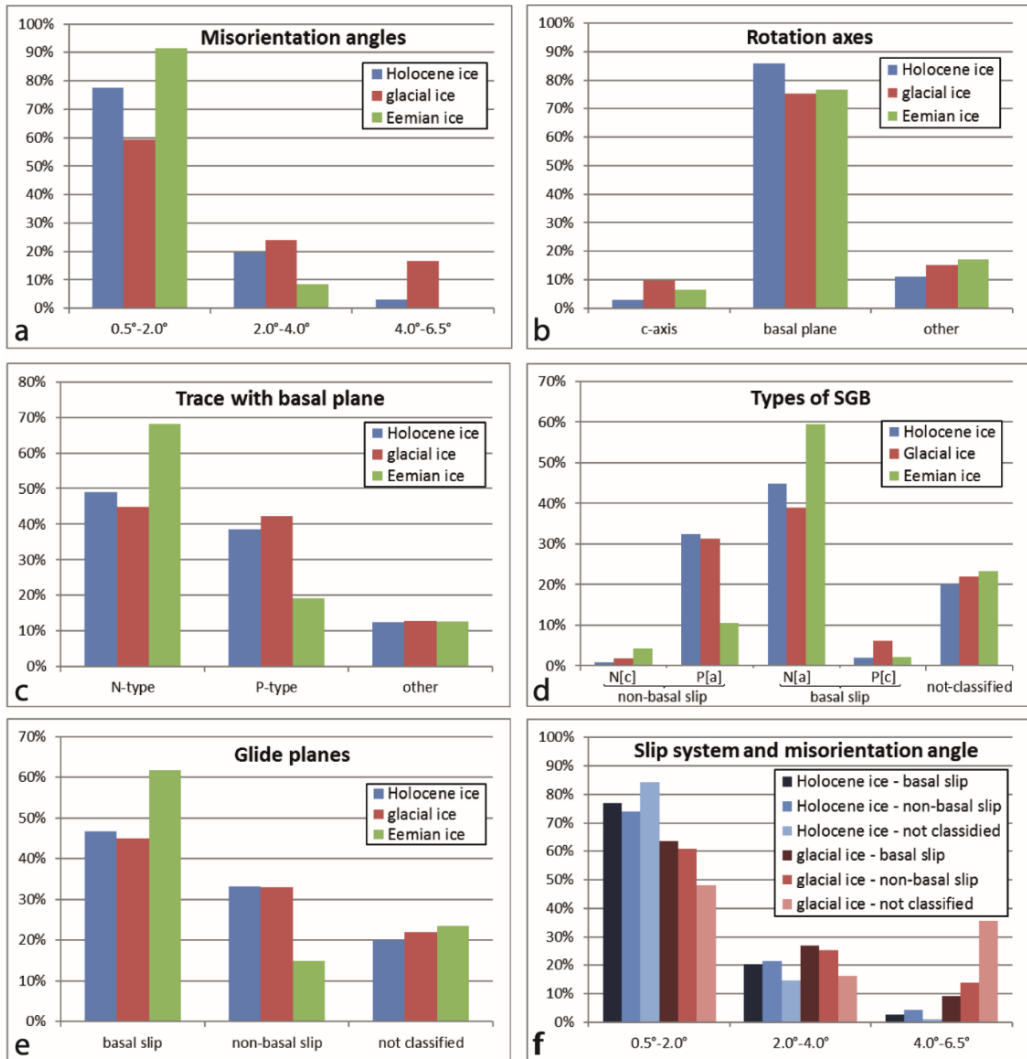


Figure 3.7: Overview of SGB data, showing the number of SGBs, expressed as a percentage of the total number of SGBs analyzed (n in Table 3.1) for each ice depth interval: n=475 in the Holocene, n=502 in the glacial and n=47 in the Eemian. The percent frequency of the SGBs is plotted for (a) the three misorientation angle ranges, (b) the rotation axes types shown in Table 3.1, (c) the trace with respect to the basal plane in the host grain also given in Table 3.1, (d) the types of SGBs based on the rotation axis and trace of the SGB where ‘not-classified’ means that the SGB was not consistent with one of the four basic types of SGBs (Section 3.2), (e) the likely slip systems as analyzed from (d) with the ‘not-classified’ boundaries being similar to (d) and (f) the frequency of the active slip system of the SGBs is shown as a function of the misorientation angle for the Holocene and glacial ice only.

formed by basal slip or non-basal slip. Therefore, it can also be argued that, because there is no preferred misorientation angle $>0.5^\circ$ for basal and non-basal slip SGBs, that excluding SGBs $<0.5^\circ$ did not influence the ratios in basal and non-basal slip of the SGBs, as the excluded SGBs ($<0.5^\circ$) will very likely have a similar distribution of glide planes as presented for SGB $>0.5^\circ$ shown in Figure 3.7e. Clearly, not including SGBs with misorientation angles $<0.5^\circ$ does affect the misorientation angle distribution. The real percentage of SGBs with a misorientation angle $<2.0^\circ$ is higher than the percentage of low angle SGBs (0.5° - 2.0°) that is reported here.

Weikusat et al. (2017) (Chapter 2) found that ca. 30-40% of SGBs in a single depth in Holocene ice from the EDML and the NEEM ice core probably consisted of non-basal dislocations and could have been formed by non-basal slip. This study confirms these results and shows that ca. 30-35% of all SGBs in the Holocene and glacial ice of the NEEM ice core are likely produced by non-basal slip. Only 15% of the SGBs in the Eemian ice are likely formed by non-basal slip. This shows that non-basal slip is activated in all three depth intervals in the NEEM ice core and the ratio of basal/non-basal slip is roughly similar in the Holocene and glacial ice. Based on the significant number of SGBs indicative of non-basal slip at the single depths in the NEEM and EDML ice core, Weikusat et al. (2017) concluded that grain boundary processes such as SIBM and GBS were not the only processes that accommodated basal slip. Adding to Weikusat et al. (2017), it is concluded that nowhere along the NEEM ice core deformation occurred only via basal slip accommodated by recovery via SIBM (Pimienta and Duval, 1987; Montagnat and Duval, 2000; Duval et al., 2000) or basal slip accommodated by grain boundary sliding (Goldsby and Kohlstedt, 1997; 2001).

3.5.1.1 Subgrain boundary misorientation angles

Low angle SGBs (0.5° - 2.0°) are most common in all three depth intervals in the NEEM ice core (Figure 3.7a). The Eemian ice contains the highest percentage of low angle SGBs, followed by the Holocene ice and the glacial ice (Figure 3.7a). These results indicate that either dislocations are less mobile in the Eemian and Holocene ice compared to the glacial ice and therefore organize less often in SGBs or that SGBs are removed before they develop into higher angles. Impurities in the ice lattice are expected to suppress SGB formation by slowing down or preventing dislocations to glide or climb (e.g. Glen, 1968; Thorsteinsson et al., 1997). However, the glacial ice contains a higher impurity content than the Holocene and Eemian ice (e.g. NEEM community members, 2013; Eichler et al., 2017) and it is therefore unlikely that the difference in misorientation angle distribution between the glacial and the Eemian ice can be explained by the difference in impurity content which is expected to inhibit dislocations glide or climb. SGB density in the upper 2250 m of the NEEM ice core varies between 0.2 and 0.6 per mm (Binder, 2014) and the SGB density is on average slightly higher in the glacial ice than in the Holocene ice, although variability in SGB density is high throughout all depths. The ice core samples that were used during this study are spread out relatively evenly along the length of the NEEM ice core (Figure 1.8) and it is therefore unlikely that the EBSD samples represent the upper or lower end of the

SGB density in the NEEM ice core. Therefore, it is concluded that it is unlikely that the difference in misorientation angle distribution between the depth intervals is caused by a difference in ease of SGB formation.

Another explanation for the difference in misorientation angle distribution is that the low angle SGBs in the Holocene and Eemian ice are consumed by strain induced boundary migration (SIBM) before being able to develop into high angle SGBs. A strong effect of grain boundary migration on the development of subgrain misorientations was shown in experimentally deformed NaCl polycrystals by Trimby et al. (2000) and Pennock et al. (2006). The coarse grain size in the Holocene and especially the Eemian ice (NEEM community members, 2013; Binder, 2014; Figure 1.8b) could explain this misorientation angle distribution as it is generally believed that SIBM increases grain size (e.g. Alley, 1992; Duval and Castelnau, 1995). Additional evidence for enhanced SIBM in the Holocene ice was provided by Binder (2014), who showed that the mean curvature of the grain boundaries is higher in the Holocene ice than in the glacial ice. Strong curvature of grain boundaries is an indicator of active SIBM (e.g. Kipfstuhl et al., 2006, 2009).

No SGBs with a misorientation angle $>6.5^\circ$ was found during this study. No high angle SGBs (4.0° - 6.5°) were found in the Eemian ice and only a very small fraction (3%) of the SGBs in the Holocene ice have a high misorientation angle. On the contrary, 17% of SGBs in the glacial ice have higher angle SGBs. The overall curvature of the GBs in glacial ice is lower compared to the Holocene ice (Binder, 2014; Figure 8d), which indicates less extensive SIBM. It is often assumed that migrating boundaries can be pinned by impurities (e.g. Fisher and Koerner, 1986; Durand et al., 2006) and by SGBs (Weikusat et al., 2009b; Binder, 2014). However, recently Eichler et al. (2017) showed that the efficiency of pinning of migrating boundaries by micro inclusions can be questioned. Even though the exact mechanisms are still debated (Eichler et al., 2017), there is a consensus that some impurity effect is modulating grain size as negative correlations between impurity content and average grain sizes have been found in many different ice cores (Gow and Williamson, 1976; Gow et al., 1997; Lipenkov et al., 1989; Thorsteinsson et al., 1995; Azuma et al., 1999, 2000; Durand et al., 2009). Therefore, the difference in impurity content between the Holocene and the glacial ice can explain the difference in SIBM as described above and hence the difference in misorientation angle distribution between the three depth intervals by consuming low angle SGBs before they develop into high angle SGBs. Furthermore, the difference in activity of SIBM between the Holocene and glacial ice could also explain the difference in grain size between the two depth intervals and could thereby possibly influence the activity of grain boundary processes like diffusion creep and grain boundary sliding (e.g. Baker, 1978; Goldsby and Kohlstedt, 1997, 2001).

Just like other Greenlandic ice cores (Thorsteinsson et al., 1997; De La Chapelle et al., 1998; Duval et al., 2000), a strong increase in grain size and the development of a partial girdle or multi maxima CPO is observed in the lower part of NEEM ice core (Eichler et al., 2013; Montagnat et al., 2014b; Chapter 5). This microstructure is produced by the rapid migration of grain boundaries between newly formed (dislocation free) grains and deformed grains (SIBM-N, Faria et al., 2014, appendix C) and is an enhanced form of

SIBM (Faria et al., 2014; Chapter 5). Enhanced SIBM results in large and interlocking grains and clears many grains of dislocations before SGBs can form. Therefore, enhanced SIBM likely causes the low concentration of SGBs in the Eemian ice and the high percentage of low angle misorientation SGBs in the Eemian ice.

3.5.1.2 Rotation axes

Along the entire length of the NEEM ice core, >75% of all SGBs have their rotation axis in the basal plane (Figure 3.7b). The percentage is higher in the Holocene ice (about 85%) than in the glacial and Eemian ice (both about 75%). The z-test result of $p < 0.001$ shows that this is a significant difference. This result can be explained very well by the observation of CPO development in the NEEM ice core, where the increase in the c-axes eigenvalue is strongest in the Holocene ice (Eichler et al., 2013; Montagnat et al., 2014b). In order to produce a vertical single maximum CPO (Figure 1.8a), the c-axes of the grains need to rotate towards the vertical. In case of non-uniform deformation, which is virtually guaranteed in ice due to its high mechanical anisotropy, rotation of the c-axis leads to curvature of the basal plane. When the geometrically necessary dislocations that accommodate this curvature polygonize into a SGB, they will form a SGB with a rotation axis in the basal plane. When basal slip is involved, this will lead to the formation of N[a] tilt SGBs, while non-basal slip will produce P[a] tilt SGBs. The percentage of N[a] boundaries is higher in the Holocene than in the glacial ice (45% versus 39%), whereas the difference in P[a] SGBs is only 1% (Figure 3.7d). In both the Holocene and the glacial ice, a small percentage of SGBs had a rotation axis in the basal plane with the trace of the SGB being oblique and therefore these SGBs did not fit with the known slip systems for ice (Figure 3.2).

Table 3.2: Summary of the number of analyzed slip systems per ice core sections for the Holocene, glacial and Eemian ice. SGBs that could not easily be analyzed in terms of active slip system were excluded. Different depth intervals and the average grain area for each depth are also given. The data for the average grain area per ice core section in column 4 were taken from (Binder et al., 2013a). The final columns show the percentages of SGBs analyzed in terms of basal and non-basal slip per ice core section at a particular depth (column 5) and per depth interval (column 6). The deepest sample in the Eemian ice (at 2423 m depth) was excluded from the table due to insufficient data.

	depth (m)	nr of SGBs >0.5°	Mean grain size (mm)	(%) basal - non-basal slip	
				Ice core sections	Depth interval
Holocene ice	443	104	3.8	50-50	58-42
	718	152	4.1	54-46 (p=0.164)	
	889	124	3.9	71-29 (p<0.001)	
glacial ice	1767	79	2.5	57-43	57-43
	1937	84	2.7* (1934)	53-47	
	1993	101	1.8* (1999)	53-47	
	2103	128	2.3* (2099)	62-38	
Eemian ice	2241	36	5.6* (2243)	81-19	81-19

*No grain size measurement was taken from the actual ice core section. The grain size that is given was derived from LM images at the depth given in brackets (Binder et al., 2013a), which is close to the actual grain size of the ice core section used for EBSD sampling.

3.5.1.3 Slip system analysis

The number of SGB that were not-classified because the rotation axis of the SGB was classified as ‘other’ (10-15%, Figure 3.7b) and/or the trace was classified as ‘other’ (about 12%, Figure 3.7c) is remarkably similar for all three depth intervals. The percentage of SGBs likely formed by basal and non-basal slip in the Eemian ice is very different than for the Holocene and glacial ice (Figure 3.7e). Figure 3.7b and 3.7c show that this difference is not produced by a difference in rotation axes of the SGBs, but by a difference in the trace with respect to the basal plane.

When assuming that yearly precipitation of 22 cm (ice equivalent) (Rasmussen et al., 2013) remained constant at the NEEM drilling site during the Holocene, a total (vertical) strain for the EBSD sections in the Holocene can be estimated based on the observed NEEM annual layer thickness. The total estimated natural strain, calculated using $\epsilon = \ln(L_f/L_i)$ (where L_f and L_i are the final and initial annual layer thickness), for the ice core sections increases with depth with $\epsilon = 0.2$ at 443 m, $\epsilon = 0.35$ at 718 m and $\epsilon = 0.56$ at 889 m of depth. These results of SGB slip system analysis of the Holocene ice were compared with the relative slip system activity in modelling studies (Llorens et al., 2017) for the range 0.2 to 0.56 strain during coaxial deformation. Llorens et al. (2017) showed that relative slip system activity on the basal plane was 55-65% for the range of 0.2-0.56 of strain in coaxial deformation. The remaining 35-45% of the dislocations were gliding on the pyramidal or prism plane. When including only the SGBs that could be related to a known slip system (N[c], P[a], N[a] and P[c], Figure 3.7d, e), slip system analysis of the SGBs in the Holocene ice show that 58% of SGBs were likely formed by basal slip (N[a] and P[c] SGBs) and 42% of SGBs were likely formed by non-basal slip (N[c] and P[a] SGBs), which is also shown in Table 3.2. So, the slip system activity on the basal plane, as analyzed from SGBs in the Holocene ice, lies in the range of the values determined by the modelling studies of Llorens et al. (2017) (58% compared to 55-65%). Even though this is a comparison of slip system activity from modelling studies of Llorens et al. (2017) with slip system analysis of SGBs (and consequently only record the recovered dislocations), the results agree well. Another important difference to point out is that Llorens et al. (2017) assumed the basal slip system to be 20 times weaker than the pyramidal and prism ones, while experiments suggest that basal slip is >60 times weaker (Duval et al., 1983; Ashby and Duval, 1985). Furthermore, in this comparison it is also assumed that excluding SGBs that were not-classified (Figure 3.7e) in this study does not affect the percentages of SGB likely formed by basal and non-basal slip.

The total (equivalent) strain is hard to estimate for the glacial ice. However, it is safe to assume that the (equivalent) strain is >1.0, since the layer thinning rate at the top of the ice core ($3.2 \cdot 10^{-12} \text{s}^{-1}$; Gillet-Chaulet et al., 2011; Montagnat et al., 2014b) times the age of the ice exceeds unity. It is expected that simple shear was the dominant deformation mode in the more recent deformation history, as simple shear is the dominant deformation mode in the glacial ice (Dansgaard and Johnsen, 1969; Montagnat et al., 2014b). The microstructural modelling of Llorens et al. (2017) showed that, at strains of >1.0, the basal and non-basal slip systems contribute both roughly 50% to deformation in simple shear.

The results of slip system analysis of SGBs show that, when only including the SGBs that could be related to a known slip system (N[c], P[a], N[a] and P[c], Figure 3.7d, e), 57% of SGBs were produced by basal slip with the remainder of 43% being produced by non-basal slip (Table 3.2). Comparing basal slip activity of the model of Llorens et al. (2017) (50%) with basal slip system activity derived from slip system analysis of SGBs (57%), shows that there is a small difference. One of the possible explanations for this difference is that the model of Llorens et al. (2017) did not include the full range of recrystallization and/or deformation mechanisms that are active in the glacial ice of the NEEM ice core. The model includes rotation recrystallization, GBM and recovery but mechanisms that are not included in the model are diffusional creep and grain boundary sliding. Diffusional creep is an unlikely candidate to explain the difference in basal slip activity as diffusional creep is predicted to be the dominant deformation mechanism at low T, very small grain size ($\ll 1$ mm) and very low strain rates (Goldsby and Kohlstedt, 2001). Grain boundary sliding could be the possible missing mechanism. A strain rate enhancement by accommodation of grain boundary sliding in the glacial ice could explain the higher strain rates that are often observed in fine grained glacial ice in other ice cores (Fisher and Koerner, 1986; Dahl-Jensen et al., 1987; Paterson, 1991; Thorsteinsson et al., 1999).

Llorens et al. (2017) predicted that, under pure shear conditions, the contribution of basal slip to bulk strain rate would decrease with increasing strain. Uniaxial unconfined compression deformation tests have also shown that the contribution of basal slip decreases with increasing strain (Chauve et al., 2017). In the three Holocene ice core sections, the reverse trend is observed: the contribution of basal slip increases with depth, hence the contribution of basal slip increases with strain. The difference in trend of slip system activity with increasing strain could be a result of studying only three depths in the Holocene ice. However, the difference in contribution of basal slip from 50-54% at 443 and 889 m of depth to 71% at 889 m of depth is rather large and the results of the z-test ($P < 0.001$) showed that this difference is significant. The most likely explanation for this increase in basal slip activity with depth is the increase in SIBM in the same depth range as was shown by analysing the grain boundary curvature by Binder (2014). This way, higher rates of SIBM in parts of the Holocene ice clears the grains of strain incompatibilities which reduces the activation of non-basal slip that often originate from these strain incompatibilities. This mechanism of intracrystalline slip accommodated by recovery via SIBM, which removes dislocations and stress concentrations in grains and allows further deformation to occur, has been proposed before by Pimienta and Duval (1987), Montagnat and Duval (2000), Duval et al. (2000) and Duval and Schulson (2009).

The glacial ice shows less variability in basal/non-basal ratio (Table 3.2). Since the total strain is unknown and > 1.0 , it is not possible to compare the slip system activity against strain. A clear trend in slip system activity with grain size is also not very obvious. A further complication in comparing slip system activity with grain size is that during EBSD sample preparation (Appendix A), the regions with the smallest grains were selected in order to maximize the number of grains in the small (8 x 8 mm) EBSD samples.

Therefore, the average grain size for the 90 x 55 mm ice core section is likely not representative for the grain size in the EBSD samples.

The ratio of SGBs likely produced by basal slip versus non-basal slip, when not-classified SGBs are excluded (Table 3.2), is very different for the Eemian ice (81% versus 19%, respectively) than the Holocene and glacial ice (57% versus 43%, respectively). Rates of SIBM in the warm Eemian ice are thought to be much higher than in the colder Holocene and glacial ice (Duval and Castelnau, 1995; Schulson and Duval, 2009; Chapter 5). It is likely that the high rate of SIBM softens the ice in the Eemian which results in a lower contribution of non-basal slip to the total deformation. This explanation would also be consistent with the modelling studies of Llorens et al. (2017) who showed a smaller amount of non-basal slip is needed at low strains, which is similar to the material being reset by SIBM recrystallization. The deformation tests of Chauve et al. (2017) also agree with these results that a smaller amount of non-basal slip is activated at low strain. Another explanation for the low number of SGBs likely produced by non-basal slip in the Eemian ice is premelting along the grain boundaries (Chapter 5). Premelting along the GBs can increase the removal of strain incompatibilities by enhanced SIBM, which reduces the amount of non-basal slip that originates from strain incompatibilities. Microstructural studies and flow law modelling (Chapter 5) show that the Eemian ice in the NEEM ice core is likely affected by premelting. A lower contribution of non-basal slip due to premelting has been proposed by De La Chapelle et al. (1999) and Durham et al. (2010).

The results from slip system analysis for the Holocene and glacial ice are different from the results of Chauve et al. (2017) on artificially deformed ice. Chauve et al. (2017) performed cryo-EBSD studies on ice that was deformed at 0.5 MPa under torsion and uniaxial unconfined compression. These authors showed that 65% of the geometrically necessary dislocations (GNDs) were composed of $\langle a \rangle$ dislocations, 23% of the GNDs had a similar proportion of $\langle a \rangle$ and $[c]$ dislocations and in 12% the $[c]$ dislocation component was dominant at total shear strain >0.2 . The results presented here, although with a higher uncertainty due to the exclusion of not-classified SGBs (Figure 3.7d, e), show a lower contribution of basal slip and a higher contribution of non-basal slip to total strain in the glacial and Holocene ice. However, the basal/non-basal slip percentages for the Eemian ice (81% versus 19%, respectively; Table 3.2) agrees very well with the results from Chauve et al. (2017). In both cases, the ice was deforming at temperatures close to the melting point: -11°C to -6°C for the EBSD samples in the Eemian ice and a homologous temperature of about 0.98 (about -5.5°C) during the deformation tests of Chauve et al. (2017). These results suggest that slip system activity in the Eemian ice and the ice in the deformation tests of Chauve et al. (2017) could have been influenced by premelting along the grain boundaries, resulting in a higher ratio of basal/non-basal slip due to the effect of enhanced SIBM and/or grain boundary sliding caused by premelting along the GBs (Chapter 5). Likely, the ice during the deformation tests of Chauve et al. (2017) experienced a higher rate of GBM due to the higher driving stress (0.5 MPa) than the driving stress in the lower part of the NEEM ice core (0.07 MPa, Section 4.2.3).

3.5.2 Misorientation angle of not-classified SGBs

One of the most striking results of this study is the big difference between the Holocene and glacial ice in misorientation angles of SGBs which were not-classified in terms of slip system (Figure 3.7f). In total, 39 high angle SGBs (4.0° - 6.5°) in the glacial ice were not-classified as shown in Table 3.1 (indicated by #). 16 of these SGBs were not-classified because of a general rotation axis (8 N-type and 8 P-type), while a total of 8 high angle SGBs were not-classified due to an oblique trace of the SGB plane and 15 high angle SGBs were not-classified because the SGB had both an oblique trace and a general rotation axis. These results indicate that the formation and/or the behavior of high angle SGBs in the glacial ice is different than in the Holocene ice in both rotation axes and orientation of the SGB in the host grains.

Means and Ree (1988) described seven different ways that a SGB can be formed (type I-VII) (Section 1.2.6). Five of these types of SGBs (type III-VII) are not expected to have low index rotation axes or boundary planes. Type III & IV are produced by misorientation reduction and grain coalescence, respectively. As the single-maximum CPO in the glacial ice is much stronger than in the Holocene ice, these two types of SGBs are more likely to form in the glacial ice than in the Holocene ice (Mainprice et al., 1993). No particular rotation axis or trace can be expected for these two types of SGBs. However, the SGB dataset (Table 3.1) shows that 24 of the 39 not-classified high angle SGBs (4.0° - 6.5°) in the glacial ice do have either a rotation axis that could be classified (8) or a trace that could be classified (16), therefore it is unlikely that these particular SGBs were formed by misorientation reduction and grain coalescence (type III & IV). An example of a boundary that could have been formed by grain coalescence (type IV) is boundary 8 in Figure 3.4. Means and Ree's SGB type V & VI are formed by impingement of migrating SGBs and growth of a SGB behind migrating grain boundaries, respectively. Since SIBM rates are likely lower in the glacial ice than in the Holocene ice (Binder, 2014) and since SGBs are relatively immobile (Humphreys and Hatherly, 2004), it is unlikely that impingement of migrating SGBs or growth of SGBs behind migration grain boundaries (type V & VI) can explain the difference between the Holocene and glacial ice in not-classified high angle (4.0° - 6.5°) SGBs. An example of a SGB that could have been formed by growth behind a migrating grain boundary is SGB 6 in Figure 3.6. Type VII SGBs develop during static recovery in grains with no orientation gradient. Such grains are not common in the Holocene and glacial ice of the NEEM ice core (Figure 3.7). Therefore, it is unlikely that Means and Ree's SGB types III-VII can explain the difference in misorientation angles of not-classified SGBs between the Holocene ice and the glacial ice.

The results presented in Figure 3.7f indicate that in the glacial ice of the NEEM ice core the behavior or formation of high angle SGBs is different from high angle SGBs in the Holocene ice. Therefore, it is proposed that in the glacial ice the high angle SGBs are no longer controlled by the host grain in terms of trace and rotation axes. One explanation is that, at misorientation angles of 4.0° - 6.5° , newly formed subgrains in the glacial ice might behave like grains and rotate 'freely'. If sliding occurs along these higher angle boundaries, then this might explain the difference in high angle SGBs between the Holocene and glacial

ice. In this case the high angle SGB has become a low angle grain boundary. This process where the rotation axis changes at a certain misorientation angle from a crystallographic position expected from dislocation creep to a more ‘general’ rotation axis has been shown before (e.g. Fliervoet and White, 1995; Bestmann and Prior, 2003). Therefore, a general rotation axis for high angle SGBs or low angle grain boundaries may be used as a potential indicator for GBS in ice. The Holocene ice, where GBs are bulging and interlocking (Binder et al., 2014) which makes grain boundary sliding less likely, does not show this behavior in high angle SGBs. The glacial ice on the other hand has a much smaller grain size and relatively straight grain boundaries. If limited grain boundary sliding is occurring in the glacial ice and not in the Holocene ice, then grain boundary sliding could explain the difference in slip system activity between the SGB analysis and the modelling work of Llorens et al., (2017) as discussed in section 3.5.1.3. as well as the occurrence of more general rotation axes for the high angle subgrains or low angle grain boundaries. It should be noted, however, that Bestmann and Prior (2003) found that the development of a general rotation axis only occurred in calcite once a grain was completely surrounded by a high angle boundary. Many examples in the glacial ice as shown in Figure 3.6 are not completely surrounded by a 4.0° - 6.5° boundary so may not be able to rotate as independent domains as suggested by Bestmann and Prior (2003).

A different explanation for the difference in rotation axes of high angle not-classified SGBs in the Holocene and glacial ice could be that multiple slip systems are involved in the formation of the SGB. If two different slip systems, both with a different rotation axis, are active then the rotation axis will plot in between these two rotation axis, depending on the relative contribution of the two different slip systems. For example, SGB 4 in Figure 3.6 could have been formed by the activation of a slip system with a rotation axis $R_1=[0001]$ and a second slip system with a rotation axis $R_2=\langle 10\bar{1}0 \rangle$ or slip involving two pyramidal rotation axes. Altogether, GBS in the glacial ice is difficult to prove based on SGB analysis of this EBSD dataset. This topic will be discussed further in Chapter 6.

3.6 Conclusions

In this Chapter, an EBSD dataset of about 1000 SGBs at different depths along the NEEM deep ice core, which were studied using cryogenic EBSD in combination with LM imaging, is presented. About 20-25% of the SGBs per depth interval could not easily be classified in terms of known slip systems in ice based on rotation axis and/or SGB orientation in the host grain. SGBs indicative of edge dislocations with Burgers vector $\mathbf{b}=(1/3)\langle 1\bar{2}10 \rangle$ gliding on the basal plane (N[a] type) are most common along the length of the NEEM ice core, followed by SGBs indicative of dislocations with $\mathbf{b}=[0001]$ or $\mathbf{b}=(1/3)\langle 11\bar{2}3 \rangle$ gliding on prism and/or pyramidal planes (P[a] type). SGBs indicative of $\mathbf{b}=(1/3)\langle 1\bar{2}10 \rangle$ screw dislocations on the basal plane (N[c] type) or slip of $\mathbf{b}=(1/3)\langle 1\bar{2}10 \rangle$ along the prism plane (P[c] type) were relatively rare. The presence along the ice core length of SGBs indicative of slip in the $[0001]$ and $\langle 11\bar{2}3 \rangle$ directions shows that non-basal slip is activated at all depths in the NEEM ice core.

Over 75% of the SGBs in all depth intervals have a rotation axis in the basal plane. The Holocene ice has more SGBs with a rotation axis in the basal plane than the glacial ice, which likely results from the strong increase in CPO in this part of the ice core. In all depths studied, the low angle (0.5° - 2.0°) SGBs are most common, while high angle (4.0° - 6.5°) SGBs are almost absent in the Holocene and Eemian ice. The low percentage of high angle SGBs in the Eemian and Holocene ice is likely the result of SIBM, which consumes low angle SGBs before they can develop into high angle SGBs, being more extensive in the Holocene and Eemian ice than in the glacial ice.

The Holocene and glacial ice showed a similar percentage of SGBs indicative of basal and non-basal slip of about 46% and about 33%, respectively. The basal/non-basal activity in the Holocene ice agrees well with the modelling of Llorens et al. (2017), while for the glacial ice there is a small difference in slip system activity at the expected strain of >1.0 . A missing deformation mechanism in the modelling of Llorens et al. (2017), like grain boundary sliding, could explain this small difference in slip system activity. The Eemian ice contains more SGBs which were likely produced by basal slip (62%) than non-basal slip (15%). It is proposed that the low percentage of SGBs indicative of non-basal slip in the Eemian ice results from high rates of SIBM at this depth. In the Eemian ice, SIBM rates are very high due to the high temperature and likely the effect of premelting along the grain boundaries (Chapter 5). Further evidence for SIBM controlling the activation of non-basal slip was found in the Holocene ice, where the contribution of SGBs indicative of non-basal slip decreases with increasing SIBM.

Of the not-classified SGBs in the Holocene ice, only 1% had a high misorientation angle (4.0° - 6.5°), while this was 36% in the glacial ice. Two different explanations are proposed for this difference: 1) grain boundary sliding is an additional accommodating mechanism for basal slip in the glacial ice in the NEEM ice core. Sliding along newly formed boundaries (4.0° - 6.5°) that were formed by polygonization can result in the change of a rotation axis from being parallel to one of the crystallographic directions to a more general orientation after sliding initiated. 2) multiple slip systems are involved in the formation of these SGBs, each having a different rotation axis. The rotation axis of the SGB would therefore plot in a 'general' crystallographic orientation.

References

- Alley, R. B. (1988) Fabrics in Polar Ice Sheets: Development and Prediction. *Science*, 240, 4851, 493-495, doi: 10.1126/science.240.4851.493.
- Alley, R. B. (1992) Flow-law hypotheses for ice-sheet modeling. *Journal of Glaciology*, 38, 129, 245-256.
- Alley, R. B., Clark, P. U., Huybrechts, P., Joughin, I. (2005) Ice-Sheet and Sea-Level changes. *Science*, 310, 456-460, doi: 10.1126/science.1114613.
- Ashby, M. F., Duval, P. (1985) The creep of polycrystalline ice. *Cold Regions Science and Technology*, 11, 285-300.

Azuma, N., Wang, Y., Mori, K., Narita, H., Hondoh, T., Shoji, H., Watanabe, O. (1999) Textures and fabrics in Dome F (Antarctica) ice core. *Annals of Glaciology*, 29, 163–168, doi:10.3189/172756499781821148.

Azuma, N., Wang, Y., Yoshida, Y., Narita, H., Hondoh, T., Shoji, H., Watanabe, O. (2000) Crystallographic analysis of the Dome Fuji ice core. in: *Physics of Ice Core Records*, edited by Hondoh, T., pp. 45–61, Hokkaido University Press, Sapporo.

Baker, R. W. (1978) The influence of ice-crystal size on creep. *Journal of Glaciology*, 21, 85, 485-500.

Bate, P. S., Knutsen, R. D., Brough, I., Humphreys, F. J. (2005) The characterization of low-angle boundaries by EBSD. *Journal of Microscopy*, 220, 1, 36-46, doi: 10.1111/j.1365-2818.2005.01513.x.

Bestmann, M., Prior, D. J. (2003) Intragranular dynamic recrystallization in naturally deformed calcite marble: diffusion accommodated grain boundary sliding as a result of subgrain rotation recrystallization. *Journal of Structural Geology*, 25, 10, 1597-1613, doi: 10.1016/S0191-8141(03)00006-3.

Binder, T. (2014) Measurements of grain boundary networks in deep polar ice cores – A digital image processing approach. PhD dissertation, University of Heidelberg, Germany, 141 pages.

Binder, T., Weikusat, I., Freitag, J., Garbe, C. S., Wagenbach, D., Kipfstuhl, S. (2013a) Microstructure through an ice sheet. *Materials Science Forum*, 753, 481-484, doi: 10.4028/www.scientific.net/MSF.753.481.

Binder, T., Garbe, C. S., Wagenbach, D., Freitag, J., Kipfstuhl, S. (2013b) Extraction and parametrization of grain boundary networks in glacier ice, using a dedicated method of automatic image analysis. *Journal of Microscopy*, 250, 2, 130-141, doi: 10.1111/jmi.12029.

Breton, D. J., Baker, I., Cole, D. M. (2016) Microstructural evolution of polycrystalline ice during confined creep testing. *Cold Regions Science and Technology*, 127, 25-36, doi: 10.1016/j.coldregions.2016.03.009.

Chauve, T., Montagnat, M., Piazzolo, S., Journaux, B., Wheeler, J., Barou, F., Mainprice, D., Tommasi, F. (2017) Non-basal dislocations should be accounted for in simulating ice mass flow. *Earth and Planetary Science Letters*, 473, 247-255, doi: 10.1016/j.epsl.2017.06.020.

Church, J. et al. (2013). “Climate Change 2013: The Physical Science Basis. Contribution of Working Group I to the Fifth Assessment Report of the Intergovernmental Panel on Climate Change”. Ed. by T. Stocker et al. Cambridge University Press, Cambridge, United Kingdom and New York, NY, USA. Chap. Sea Level Change (cit. on p. 1).

Dahl-Jensen, D., Gundestrup, N. S. (1987) Constitutive properties of ice at Dye 3, Greenland. *The Physical Basis of Ice Sheet Modelling*, 170, 31-43.

Dansgaard, W., Johnsen S. J. (1969) A flow model and a time scale for the ice core from camp century, Greenland. *Journal of Glaciology*, 8, 53, 215-223, doi: 10.3189.S0022143000031208.

De La Chapelle, S., Castelnau, O., Lipenkov, V., Duval, P. (1998) Dynamic recrystallization and texture development in ice as revealed by the study of deep ice cores in Antarctica and Greenland. *Journal of Geophysical Research*, 103, B3, 5091-5105, doi: 10.1029/97JB02621.

De La Chapelle, S., Milsch, H., Castelnaud, O., Duval, P. (1999) Compressive creep of ice containing a liquid intergranular phase: rate-controlling processes in the dislocation creep regime. *Geophysical Research Letters*, 26, 2, 251-254, doi: 10.1029/1998GL900289.

Durand, G., Gagliardini, O., Thorsteinsson, T., Svensson, A., Kipfstuhl, S., Dahl-Jensen, D. (2006) Ice microstructure and fabric: an up-to-date approach for measuring textures. *Journal of Glaciology*, 52, 179, 619–630, doi: 10.3189/172756506781828377.

Durand, G., Svensson, A., Kipfstuhl, S., Persson, A., Gagliardini, O., Gillet, F., Sjolte, J., Montagnat, M., Dahl-Jensen, D. (2009) Evolution of the texture along the EPICA dome C ice core. 68, 91–106, Institute of Low Temperature Science, Hokkaido University, Sapporo Japan, Nepal.

Durham, W. B., Prieto-Ballesteros, O., Goldsby, D. L., Kargel, J. S. (2010) Rheological and Thermal Properties of Icy Materials, *Space Science Reviews*, 153, 273-298, doi: 10.1007/s11214-009-9619-1.

Duval, P., Ashby, M. F., Anderman, I. (1983) Rate-Controlling Processes in the Creep of Polycrystalline Ice. *Journal of Physical Chemistry*, 87, C1, 4066-4074, doi: 10.1021/j100244a014.

Duval, P., Arnaud, L., Brissaud, O., Montagnat, M., De La Chapelle, S. (2000) Deformation and recrystallization processes of ice from polar ice sheets. *Annals of Glaciology*, 30, 83-87, doi: 10.3189/172756400781820688.

Duval, P., Castelnaud, O. (1995) Dynamic Recrystallization of ice in Polar Ice Sheets. *Journal de Physique III*, 05, C3, 197-205, doi: 10.1051/jp4:1995317.

Eichler, J., Kleitz, I., Bayer-Giraldi, M., Jansen, D., Kipfstuhl, S., Shigeyama, W., Weikusat, C., Weikusat, I. (2017) Location and distribution of micro-inclusions in the EDML and NEEM ice cores using optical microscopy and in situ Raman spectroscopy. *The Cryosphere*, 11, 3, 1075-1090, doi: 10.5194/tc-11-1075-2017.

Eichler, J., Weikusat, I., Kipfstuhl, S. (2013): Orientation-tensor eigenvalues along the NEEM ice core. PANGAEA, <https://doi.org/10.1594/Pangaea.838059>.

Faria, S. H., Weikusat, I., Azuma, N. (2014) The microstructure of Polar Ice. Part II: State of the art. *Journal of Structural Geology* 61, 21-49, doi: 10.1016/j.jsg.2013.11.003.

Fisher, D. A., Koerner, R. M. (1986) On the Special Rheological Properties of Ancient Microparticle-Laden Northern Hemisphere Ice as Derived from Bore-Hole and Core Measurements. *Journal of Glaciology*, 32, 112, 501-510, doi: 10.1017/S0022143000012211.

Fliervoet, T. F., White, S. H. (1995) Quartz deformation in a very fine grained quartzofeldspathic mylonite: a lack of evidence for dominant grain boundary sliding deformation. *Journal of Structural Geology*, 17, 8, 1095-1109, doi: 10.1016/0191-8141(95)00007-Z.

Gifkins, R. C. (1976) Grain-Boundary Sliding and its accommodation During Creep and Superplasticity. *Metallurgical Transactions A*, 7, 1225-1232.

Gifkins, R. C. (1994) Grain-boundary participation in High-Temperature Deformation: An Historical Review. *Materials Characterization*, 32, 2, 59-77, doi: 10.1016/1044-5803(94)90093-0.

Gillet-Chaulet, F., Hindmarsh, R. C. A., Corr, H. F. J., King, E. C., Jenkins, A. (2011) In-situ quantification of ice rheology and direct measurement of the Raymond Effect at Summit, Greenland using a phase-sensitive radar. *Geophysical Research Letter*, 38, 24, 1-6, doi: 10.1029/2011GL049843.

- Glen, J. W. (1955) The creep of polycrystalline ice. *Proceedings of the Royal Society of London. Series A, Mathematical and Physical Sciences*, 228, 1175, 519-538.
- Glen, J. W. (1968) The Effect of Hydrogen Disorder Movement and Plastic Deformation of Ice. *Physik der Kondensierten Materie*, 7, 1, 43-51, doi: 10.1007/BF02422799.
- Goldsby, D. L., Kohlstedt, D. L. (1997) Grain boundary sliding in fine grained ice I. *Scripta Materialia*, 37, 9, 1399-1406.
- Goldsby, D. L., Kohlstedt, D. L. (2001) Superplastic deformation of ice: Experimental observations. *Journal of Geophysical Research*, 106, B6, 11017-11030, doi: 10.1029/2000JB900336.
- Gottstein, G., Shvindlerman, L. S. (1999) Grain boundary migration in metals, CRC Press, Taylor & Francis Group, Boca Raton, London, New York.
- Gow, A. J., Williamson, T. (1976) Rheological implications of the internal structure and crystal fabrics of the West Antarctic ice sheet as revealed by deep core drilling at Byrd Station. *Geological Society of America Bulletin*, 87, 12, 1665-1677.
- Gow, A. J., Meese, D. A., Alley, R. B., Fitzpatrick, J. J., Anandakrishnan, S., Woods, G. A., Elder, B. C. (1997) Physical and structural properties of the Greenland Ice Sheet Project 2 ice core: A review. *Journal of Geophysical Research*, 102, C12, 26559-26575, doi: 10.1029/97JC00165.
- Grennerat, F., Montagnat, M., Castelnau, O., Vacher, P., Moulinec, H., Suquet, P., Duval, P. (2012) Experimental characterization of the intragranular strain field in columnar ice during transient creep. *Acta Materialia*, 60, 8, 3655-3666, doi: 10.1016/j.actamat.2012.03.025.
- Hamann, I., Weikusat, C., Azuma, N., Kipfstuhl, S. (2007) Evolution of ice crystal microstructure during creep experiments. *Journal of Glaciology*, 53, 182, 479-489.
- Hirth, G., Kohlstedt, D. (1995) Experimental constraints on the dynamics of the partially molten upper mantle: Deformation in the diffusion creep regime. *Journal of Geophysical Research*, 100, B2, 1981-2001, doi: 10.1029/94JB02128.
- Hirth, J. P., Lothe, J. (1982) *Theory of Dislocations*. Krieger Publishing Company, 857 pages.
- Hobbs, B. E. (1985) *Preferred Orientation in Deformed Metals and Rocks*, Academic Press, Orlando.
- Hondoh, T. (2000) Nature and behavior of dislocations in ice. In Hondoh, T., ed. *Physics of ice core records*. Sapporo, Hokkaido University Press, 3-24.
- Hondoh, T. (2009) An overview of microphysical processes in ice sheets: Towards nanoglaciology. In: Hondoh, T. (Ed.), *Physics of Ice Core Records II*. Vol 68. Supplement Issue of *low Temperature Science*, Vol 68. URL <http://eprint.lib.hokudai.ac.jp/handle/2115/45402>
- Hondoh, T. (2015) Dislocation mechanism for transformation between cubic ice I_c and hexagonal ice I_h. *Philosophical Magazine*, 95, 32, 3590-3620, doi: 10.1080/14786435.2015.1091109.
- Humphreys, F. J., Bate P. S., Hurley, P. J. (2001) Orientation averaging of electron backscattered diffraction data. *Journal of Microscopy*, 201, 1, 50-58, doi: 10.1046/j.1365-2818.2001.00777.x.

- Humphreys, F. J., Hatherly, M. (2004) *Recrystallization and Related Annealing Phenomena*. Elsevier, 574 pages.
- Iliescu, D., Baker, I., Chang, H. (2004) Determining the Orientations of ice Crystals Using Electron Backscatter Diffraction Patterns. *Microscopy Research and Technique*, 63, 183-187, doi: 10.1002/jemt.20029.
- IPCC (2014) *Climate change 2014: Synthesis report. contribution of working groups i, ii and iii to the fifth assessment report of the intergovernmental panel on climate change*. [Core Writing Team, Pachauri P. K. and Meyer L. A. (eds.)]. IPCC, Geneva, Switzerland, 151. URL www.ipcc.ch.
- Ji, S., Wang, Q., Xia, B. (2002) *Handbook of Seismic Properties of Minerals, Rocks and Ores*. Polytechnic International Press, Montreal, ISBN: -553-01032-X.
- Joughin, I., Smith, B. E., Howat, I. M. (2018) A complete map of Greenland ice velocity derived from satellite data collected over 20 years. *Journal of Glaciology*, 64, 243, 1-11, doi: 10.1017/jog.2017.73.
- Kipfstuhl, S., Faria, S. H., Azuma, N., Freitag, J., Hamann, I., Kaufmann, P., Miller, H., Weiler, K., Wilhelms, F. (2009) Evidence of dynamic recrystallization in polar firn. *Journal of Geophysical Research: Solid Earth*, 114, 5, 1-10, doi: 10.1029/2008JB005583.
- Kipfstuhl, S., Hamann, I., Lambrecht, A., Freitag, J., Faria, S. H., Grigoriev, D., Azuma, N. (2006) Microstructure mapping: a new method for imaging deformation-induced microstructural features of ice on the grain scale. *Journal of Glaciology*, 52, 178, 298-406, doi: 10.3189/172756506781828647.
- Krabbendam, M. (2016) Sliding of temperate basal ice on a rough, hard bed: creep mechanisms, pressure melting, and implications for ice streaming. *The Cryosphere*, 10, 1915–1932, doi: 10.5194/tc-10-1915-2016.
- Lipenkov, V. Y., Barkov, N. I., Duval, P., Pimienta, P. (1989) Crystalline texture of the 2083 m ice core at Vostok station, Antarctica. *Journal of Glaciology*, 35, 121, 392–398.
- Llorens, M-G., Griera, A., Bons, P. D., Lebensohn, R. A., Evans, L. A., Jansen, D., Weikusat, I. (2016a) Full-field predictions of ice dynamic recrystallization under simple shear conditions. *Earth and Planetary Science Letters*, 450, 233-242, doi: 10.1016/j.epsl.2016.06.045.
- Llorens, M-G., Griera, A., Bons, P. D., Roessiger, J., Lebensohn, R., Evans, L., Weikusat, I. (2016b) Dynamic recrystallization of ice aggregates during co-axial viscoplastic deformation: a numerical approach. *Journal of Glaciology*, 62, 232, 359-377, doi: 10.1017/jpg.2016.28.
- Llorens, G-M., Griera, A., Steinbach, F., Bons, P. D., Gomez-Rivas, E., Jansen, D., Roessiger, J., Lebensohn, R. A., Weikusat, I. (2017) Dynamic recrystallization during deformation of polycrystalline ice: insights from numerical simulations. *Philosophical transactions A*, 375, doi: 10.1098/rsta.2015.0346.
- Lloyd, G. E., Farmer, A. B., Mainprice, D. (1997) Misorientation analysis and the formation and orientation of subgrain and grain boundaries. *Tectonophysics*, 279, 55-78, doi: 10.1016/S0040-1951(97)00115-7.
- Mainprice, D., Lloyd, G. E., Casey, M. (1993) Individual orientation measurements in quartz polycrystals – advantages and limitations for petrophysical property determinations. *Journal of Structural Geology*, 15, 9-10, 1169-1187, doi: 10.1016/0191-8141(93)90162-4.

Means, W. D., Ree, J.H. (1988) Seven types of subgrain boundaries in octachloropropane. *Journal of Structural Geology*, 10, 7, 765-770, doi: 10.1016/0191-8141(88)90083-1.

Miyamoto, A., Shoji, H., Hori, A., Hondoh, T., Clausen, H. B., Watanabe, O. (2005) Ice fabric evolution process understood from anisotropic distribution of *a*-axis orientation on the GRIP (Greenland) ice core. *Annals of Glaciology*, 42, 47-52, doi: 10.3189/172756405781812501.

Miyamoto, A., Weikusat, I., Hondoh, T. (2011) Instruments and Methods Complete determination of ice crystal orientation using Laue X-ray diffraction method. *Journal of Glaciology*, 57, 201, 103-110, doi: 10.3189/002214311795306754.

Montagnat, M., Azuma, N., Dahl-Jensen, D., Eichler, J., Fujita, S., Gillet-Chaulet, F., Kipfstuhl, S., Samyn, D., Svenson, A., Weikusat, I. (2014b) Fabric along the NEEM ice core, Greenland, and its comparison with GRIP and NGRIP ice cores. *The Cryosphere*, 8, 1129-1138, doi: 10.5194/tc-8-1129-2014.

Montagnat, M., Castelnau, O., Bons, P. D., Faria, S. H., Gagliardini, O., Gillet-Chaulet, F., Grennerat, F., Griera, A., Lebensohn, R. A., Moulinec, H., Roessiger, J., Suquet, P. (2014a) Multiscale modelling of ice deformation behavior. *Journal of Structural Geology*, 61, 78-108, doi: 10.1016/j.jsg.2013.05.002.

Montagnat, M., Chauve, T., Barou, F., Tommasi, A., Beausir, B., Fressengeas, C. (2015) Analysis of Dynamic Recrystallization of Ice from EBSD Orientation Mapping. *Frontiers in Earth Science*, 3, 81, 1-13, doi: 10.3389/feart.2015.00081.

Montagnat, M., Duval, P. (2000) Rate controlling processes in the creep of polar ice, influence of grain boundary migration associated with recrystallization. *Earth and Planetary Science Letters*, 183, 1-2, 179-186, doi: 10.1016/S0012-821X(00)00262-4.

Nedelcu, A. F., Faria, S. H., Kuhs, W. F. (2009) Raman spectra of plate-like inclusions in the EPICA-DML (Antarctica) ice core. *Journal of Glaciology*, 55, 189, 183-184, doi: 10.1039/b005411i.

NEEM community members. (2013) Eemian interglacial reconstructed from a Greenland folded ice core. *Nature*, 493, 489-494, doi: 10.1038/nature11789.

Neumann, B. (2000) Texture development of recrystallized quartz polycrystals unraveled by orientation and misorientation characteristics. *Journal of Structural Geology*, 22, 1695-1711, doi: 10.1016/S0191-8141(00)00060-2.

Obbard, R., Baker, I., Sieg, K. (2006) Using electron backscatter diffraction patterns to examine recrystallization in polar ice sheets. *Journal of glaciology*, 52, 179, 546-557.

Obbard, R., Baker, I. (2007) The microstructure of meteoric ice from Vostok, Antarctica. *Journal of Glaciology*, 53, 180, 41-62, doi: 10.3189/172756507781833901.

Paterson, W. S. B. (1991) Why ice-age ice is sometimes “soft”. *Cold Regions Science and Technology*, 20, 1, 75-98, doi: 10.1016/0165-232X(91)90058-O.

Pauer, F., Kipfstuhl, S., Kuhs, W. F., Shoji, H. (1999) Air hydrates crystals from the GRIP deep ice core, Greenland: a number- size- and shape-distribution study. *Journal of Glaciology*, 45, 149, 22-30.

Pennock, G. M., Drury, M. R., Spiers, C. J. (2006) Grain boundary populations in wet and dry NaCl. *Materials Science and Technology*, 22, 11, 1307-1315, doi: 10.1179/174328406X130975.

Piazolo, S., Montagnat, M., Blackford, J. R. (2008) Sub-structure characterization of experimentally and naturally deformed ice using cryo-EBSD. *Journal of Microscopy*, 230, Pt 3, 509-519, doi: 10.1111/j.1365-2818.2008.02014.x.

Piazolo, S., Montagnat, M., Grennerat, F., Moulinec, H., Wheeler, J. (2015) Effect of local stress heterogeneities on dislocation fields: Examples from transient creep in polycrystalline ice. *Acta Materialia*, 90, 303-309, doi: 10.1016/j.actamat.2015.02.046.

Pimienta, P., Duval, P. (1987) Rate controlling processes in the creep of polar glacier ice. *Journal de Physique Colloques*, 48, C1, 243-248, doi: 10.1051/jphyscol:1987134.

Prior, D. J., Boyle, A. P., Brenker, F., Cheadle, M. C., Day, A., Lopez, G., Peruzzo, L., Potts, G. J., Reddy, S., Spiess, R., Timms, N. E., Trimby, P., Wheeler, J., Zetterström, L. (1999) The application of electron backscatter diffraction and orientation contrast imaging in the SEM to textural problems in rocks. *American Mineralogist*, 84, 1741-1759, doi: 10.2138/am-1999-11-1204.

Prior, D. J., Diebold, S., Obbard, R., Daghlian, C., Goldsby, D. L., Durham, W. M., Baker, I. (2012) Insight into the phase transformations between Ih and ice II from electron backscattered diffraction data. *Scripta Materialia*, 66, 69-72, doi: 10.1016/j.scriptamat.2011.09.044.

Prior, D. J., Lilly, K., Seidemann, M., Vaughan, M., Becroft, L., Easingwood, R., Diebold, S., Obbard, R., Daghlian, C., Baker, I., Caswell, T., Golding, N., Goldsby, D., Durham, W. B., Piazolo, S., Wilson, C. J. L. (2015) Making EBSD on water ice routine. *Journal of Microscopy*, 259, 00, 1-20, doi: 10.1111/jmi.12258.

Prior, D. J., Wheeler, J., Peruzzo, L., Spiess, R., Storey, C. (2002) Some garnet microstructures: an illustration of the potential of orientation maps and misorientation analysis in microstructural studies. *Journal of Structural Geology*, 24, 6-7, 999-1011, doi: 10.1016/S0191-8141(01)00087-6.

Rasmussen, S. O., Abbott, P.M., Blunier, T., Bourne, A. J., Brook, E., Buchardt, S. L., Buizert, C., Chappellaz, J., Clausen, H. B., Cook, E., Dahl-Jensen, D., Davies, S. M., Guillevic, M., Kipfstuhl, S., Laepple, T., Seierstad, I. K., Severinghaus, J. P., Steffensen, J. P., Stowasser, C., Svensson, A., Vallelonga, P., Vinther, B. M., Wilhelms, F., Winstrup, M. (2013) A first chronology for the North Greenland Eemian Ice Drilling (NEEM) ice core. *Climate of the Past*, 9, 2713-2730, doi: 10.5194/cp-9-2713-2013.

Richeton, T., Le, L. T., Chauve, T., Bernacki, M., Berbenni, S., Montagnat, M. (2017) Modelling the transport of geometrically necessary dislocations on slip systems: application to single- and multi-crystals of ice. *Modelling and Simulation in Materials Science and Engineering*, 25, 2, 1-30, doi: 10.1088/1361-651X/aa5341.

Saylor, D. M., Rohrer, G. S. (1999) Measuring the influence of Grain-Boundary Misorientation on Thermal Groove Geometry in Ceramics. *Journal of the American Ceramic Society*, 82, 6, 1529-1536, doi: 10.1111/j.1151-2916.1999.tb01951.x.

Schulson, E. M., Duval, P. (2009) *Creep and Fracture of Ice*. Cambridge University Press.

Steinbach, F., Bons, P. D., Griera, A., Jansen, D., Llorens, M-G, Roessiger, J., Weikusat, I. (2016) Strain localization and dynamic recrystallization in the ice-air aggregate: a numerical study. *The Cryosphere*, 10, 6, 3071-3089, doi: 10.5194/tc-10-3071-2016.

Thorsteinsson, T., Kipfstuhl, J., Eicken, H., Johnsen, S. J., Fuhrer, K. (1995) Crystal size variations in Eemian-age ice from the GRIP ice core, Central Greenland. *Earth and Planetary Science Letters*, 131, 3-4, 381-394, doi: 10.1016/0012-821X(95)00031-7.

Thorsteinsson, T., Kipfstuhl, J., Miller, H. (1997) Textures and fabrics in the GRIP ice core. *Journal of Geophysical Research*, 102, C12, 26583-26599, doi: 10.1029/97JC00161.

Thorsteinsson, T., Waddington, E. D., Taylor, K. C., Alley, R. B., Blankenship, D. D. (1999) Strain-rate enhancement at Dye 3, Greenland. *Journal of Glaciology*, 45, 150, 338-345, doi: 10.3189/002214399793377185.

Trepied, L., Doukhan, J. C., Paquet, J. (1980) Subgrain boundaries in quartz theoretical analysis and microscopic observations. *Physics and Chemistry of Minerals*, 5, 3, 201-218, doi: 10.1007/BF00348570.

Trimby, P. W., Drury, M. R., Spiers, C. J. (2000) Misorientations across etched boundaries in deformed rocksalt: a study using electron backscatter diffraction. *Journal of Geology*, 22, 1, 81-89, doi: 10.1016/S0191-8141(99)00126-1.

Trusel, L., Frey, K. E., Das, S. B., Karnauskas, B., Kuipers Munneke, P., van Meijgaard, E., van den Broeke, M. R. (2015) Divergent trajectories of Antarctic surface melt under two twenty-first-century climate scenarios. *Nature Geoscience*, 8, 927-932, doi: 10.1038/NNGEO2563.

Vaughan, D., Arthern, R. (2007) Why is it so hard to predict the future of ice sheets? *Science*, 315, 1503-1504, doi: 10.1126/science.1141111.

Wonnacott, T. H., Wonnacott, R. J. (1990) *Introductory Statistics*. Wiley, 5th edition.

Weertman, J., Weertman, J. R. (1992) *Elementary Dislocation Theory*. Oxford University Press, UK, 231 pages.

Weikusat, I., de Winter, D. A. M., Pennock, G. M., Hayles, M., Schneiderberg, C. T. W. M., Drury, M. R. (2011b) Cryogenic EBSD on ice: preserving a stable surface in a low pressure SEM. *Journal of Microscopy*, 242, 3, 295-310, doi: 10.1111/j.1365-2818.2010.03471.x.

Weikusat, I., Kipfstuhl, S., Azuma, N., Faria, S. H., Miyamoto, A. (2009a) Deformation microstructures in an Antarctic Ice Core (EDML) and in Experimentally Deformed Artificial Ice. In: Hondoh, T. (Ed.), *Physics of Ice Core Records II*. Vol. 2 of PICR. Supplement Issue of *Low Temperature Science*, Vol. 68, pp. 115-123. URL <http://eprints.lib.hokudai.ac.jp/dspace/handle/2115/45402>.

Weikusat, I., Kipfstuhl, S., Faria, S. H., Azuma, N., Miyamoto, A. (2009b) Subgrain boundaries and related microstructural features in EDML (Antarctica) deep ice core. *Journal of Glaciology*, 55, 191, 461-472, doi: 10.3189/002214309788816614.

Weikusat, I., Kuiper, E. N., Pennock, G. M., Kipfstuhl, S., Drury, M. R. (2017) EBSD analysis of subgrain boundaries and dislocation slip systems in Antarctic and Greenland ice. *Solid Earth*, 8, 883-898, doi: 10.5194/se-8-883-2017.

Weikusat, I., Miyamoto, A., Faria, S. H., Kipfstuhl, S., Azuma, N., Hondoh, T. (2011a) Subgrain boundaries in Antarctic ice quantified by X-ray Laue diffraction. *Journal of Glaciology*, 57, 201, 85-94, doi: 10.3189/002214311795306628.

Using a composite flow law to investigate the role of grain size on the deformation of Holocene and glacial ice in the NEEM deep ice core, Greenland

After:

Kuiper, E. N., Weikusat, I., de Bresser, J. H. P., Jansen, D., Pennock, G. M., Drury, M. R. Using a composite flow law to model deformation in the NEEM deep ice core, Greenland: Part 1 the role of grain size and grain size distribution of Holocene and glacial ice.

Submitted to the Cryosphere.

Abstract

Many polar ice cores have shown that grain size varies considerably with depth in polar ice sheets, which can lead to changes in dominant deformation mechanism and strain rate with depth. In this study, the role of grain size on strain rate of ice deposited during the Holocene and glacial period in the North Greenland Eemian Ice Drilling (NEEM) deep ice core was investigated using the composite flow law developed by Goldsby and Kohlstedt (1997, 2001). This flow law describes the flow of ice by a combination of grain size insensitive (GSI) and grain size sensitive (GSS) deformation mechanisms. The grain size data employed in the composite flow law have been derived from 615 light microscope (LM) images and have been described by both a grain size distribution and a mean grain size, both derived from equivalent grain diameters and both evolve with depth. The grain size distribution was used to calculate the strain rate of the polycrystalline ice in two different ways: by assuming that each grain deforms by the same stress (micro-scale constant stress model) and by assuming that the same strain rate applies for each grain (micro-scale constant strain rate model).

For the analysis, NEEM temperature data and a modification of the composite flow law (Goldsby and Kohlstedt, 2001) were used. The modification of the composite flow law showed a major change occurring in the parameters for dislocation creep below the premelting temperature of 258K. The results show that GBS-limited creep (basal slip accommodated by grain boundary sliding) produces almost all of the deformation in the upper 2207 m of depth in the NEEM ice core, while dislocation creep (basal slip accommodated by non-basal slip) hardly contributes to bulk deformation. The difference in bulk strain rate using either the micro-scale constant stress or the micro-scale constant strain rate approach is relatively small. The micro-scale constant stress model predicts a slightly higher strain rate and a higher contribution of GBS-limited creep to the overall strain rate. This GSS deformation mechanism produces on average a four to five times higher strain rate in the fine grained glacial ice (1419-2207 m of depth) compared to the coarser grained Holocene ice (0-1419 m of depth). The glacial ice also shows a higher layer-to-layer variability in strain rate caused by the variation in grain size, with two peaks in the strain rate at about 1980 and 2100 m of depth. When comparing the results using the composite flow law to the results using Glen's flow law (Paterson, 1994), which assumes a dominant dislocation creep mechanism, Glen's flow law predicts a higher strain rate than the composite flow law throughout the upper 2207 m of depth in the NEEM ice core. However, Glen's flow law is unable to predict the layer-to-layer variability in strain rate that is predicted with the composite flow law. This layer-to-layer variability in strain rate in the finer grained parts of the ice sheet, which is only identified with the composite flow law, should be considered when modelling ice flow in ice sheets.

The overall microstructure in the glacial ice is consistent with dominant GBS-limited creep, while microstructures indicate that dislocation creep is important in the Holocene ice. Therefore, the results of the composite flow law approach using the modified flow law parameter showing that the GBS-limited creep strain rate is predicted to be about

an order of magnitude faster than the dislocation creep strain rate along the upper 2207 m of depth in the NEEM ice core is surprising. One of the explanations for this large difference could be that strain induced boundary migration (SIBM), which acts as a softening mechanism, was not active during the deformation experiments of Goldsby and Kohlstedt (1997, 2001), while SIBM is active in the naturally occurring polar ice material used in this study.

4.1 Introduction

Ice sheets regulate global mean sea level (GMSL) by storing large amounts of fresh water in the form of ice on land. As a consequence of increased anthropogenic global warming, the contribution of the Greenland and the Antarctic ice sheet to GMSL rise is likely to increase in the next centuries (IPCC, 2014). It is therefore important to improve the implementation of ice flow in ice sheet models that calculate the discharge of ice into the ocean, since the amount of water stored in ice sheets is enough to raise GMSL by about 70 m (Alley et al., 2005; Church et al., 2013). The mass balance of an ice sheet depends on the accumulation of snow on the surface, release of meltwater by runoff and the solid discharge via floating ice shelves and calving of icebergs into the ocean (e.g. Petrenko and Withworth, 1999; Marshall, 2006). In the coldest parts of Antarctica, sublimation and wind erosion can be important ablation mechanisms too (Bintanja, 2009). The amount of ice available for calving and melting depends on the flow of ice from the interior towards the margins of the ice sheet. This flow of ice is controlled by two processes: sliding of the ice over the bedrock, which includes various sub-glacial processes (Zwally et al., 2002; Vaughan and Arthern, 2007; Thoma et al., 2010; Wolovick and Creyts, 2016), and the internal deformation of the polycrystalline ice, which is governed by various mechanisms like dislocation creep, grain boundary migration (GBM) and grain boundary sliding (GBS) (e.g. Duval et al., 1983; Goldsby and Kohlstedt, 1997, 2001; Montagnat and Duval, 2000, 2004; Schulson and Duval, 2009; Faria et al., 2014a).

Due to the very high mechanical anisotropy of the hexagonal single ice crystal, it is 60 to 100 times easier to activate dislocation glide along the basal planes of the crystal lattice (basal slip) than to activate slip on other planes in the hexagonal structure of the ice lattice (e.g. Duval et al., 1983; Ashby and Duval, 1985; Figure 1.4). Dislocation glide using the basal slip system is therefore the dominant deformation mechanism in polycrystalline ice. However, the von Mises criterion (von Mises, 1928) states that a polycrystalline material undergoing creep at constant volume requires at least five independent slip systems to accommodate homogeneous deformation. Basal slip can only provide two of these independent slip systems (Hutchinson, 1977). Therefore, it is argued that other slip systems, notably the prismatic and pyramidal slip systems, are active too (Hondoh, 2000, 2009). The activation of slip systems other than basal glide is referred to as hard glide and is regarded to be rate-limiting under high stress conditions (Duval et al., 1983). Hard glide has been observed in natural (Weikusat et al., 2009a, b, 2011, 2017; Chapter 2 and 3) and in synthetic ice samples (Hondoh et al., 1990; Chauve et al., 2017). However, it has been suggested that at the low stress conditions in polar ice sheets, different mechanisms than hard glide could accommodate basal slip (Alley, 1992). For instance, strain induced boundary migration (SIBM) could remove local stress concentrations produced by basal slip and recrystallize the material (Pimienta and Duval, 1987; Montagnat and Duval, 2000; Duval et al., 2000). Basal slip can also be accommodated by GBS (Gifkins, 1976; Goldsby and Kohlstedt, 1997, 2001).

For large scale flow models, the deformation of the ice polycrystal is approximated in a homogenized way by continuum mechanics principles. Together with balance equations for mass, momentum and energy, continuum mechanics uses the relation between stress and strain rate given by a constitutive relation, also called the ‘flow law’. The most commonly used flow law in ice sheet models is Glen’s law (Glen, 1952, 1955; Paterson, 1994), which describes the flow of polycrystalline ice during deformation by a power law relating equivalent strain rate ($\dot{\epsilon}$) to equivalent stress (σ) according to

$$\dot{\epsilon} \propto \sigma^n, \quad (4.1)$$

where $n=3$ for Glen’s flow law. In this flow law, which is based on laboratory experiments, grain size insensitive (GSI) dislocation creep is assumed to be the dominant deformation mechanism. Variants of this type of strain rate-stress relation with different values for the stress exponent n have been used, ranging from $n=1.5$ to 4.0 , based on experiments at different conditions (Weertman, 1983). However, at the relatively low driving stresses of <0.3 MPa (equal to an equivalent stress of about 0.5 MPa using Equation 4.10) in terrestrial ice sheets (e.g. Sergienko et al., 2014), Glen’s flow law has proved to be inaccurate (e.g. Thorsteinsson et al., 1999; Huybrechts, 2007) and predicts strain rates that are too slow in both the deeper and the fine grained parts of the polar ice sheets. Laboratory experiments (Mellor and Testa, 1969a; Pimienta and Duval, 1987; Duval and Castelnau, 1995; Goldsby and Kohlstedt, 1997, 2001; De La Chapelle et al., 1999; Duval et al., 2000) and flow analysis of ice sheets (Dahl-Jensen and Gundestrup, 1987; Alley, 1992) have shown that under these low stress conditions, ice deformation is best described by a flow law with a stress exponent less than 3.0 . However, most polar ice cores are drilled at low stress locations like domes or ridges (e.g. Faria et al., 2014b), where the ice might deform by different deformation mechanisms, and therefore be described by a different stress exponent, than ice along the flanks or the margins of the ice sheet. The exact deformation mechanism of ice at these low driving stresses is still unclear.

During experiments with very fine grained ice (with a grain diameter between 3 μm and 90 μm), Goldsby and Kohlstedt (1997) found a transition from a GSI creep regime with a power law stress exponent of $n=4$ at high equivalent stress ($\sigma>3$ MPa) to a grain size sensitive (GSS) creep regime with $n=1.8$ and a grain size exponent of 1.4 at medium equivalent stress ($1-3$ MPa). At low equivalent stresses (<1 MPa) and with the finest grained samples, Goldsby and Kohlstedt found a third creep regime, again grain size independent, but with $n=2.4$. According to Goldsby and Kohlstedt, the GSI regime with $n=4$ is governed by dislocation creep using the easy slip systems in ice (basal slip; Figure 1.4a) accommodated by the hard slip systems (i.e. non-basal slip, Figure 1.4b-e). In the GSS regime with $n=1.8$, basal slip is thought to be accommodated by grain boundary sliding (GBS), while the opposite holds for the low stress GSI regime with $n=2.4$, where GBS is accommodated by basal slip. The accommodating mechanisms are rate-controlling. At even lower stresses a fourth creep regime, diffusion creep, is expected. This creep regime is expected to dominate the flow behavior of ice at very small grain sizes ($\ll 1$ mm), low temperature and very low equivalent stresses. This creep regime was not reached during the experiments of Goldsby and Kohlstedt (2001) and is assumed to be irrelevant for

terrestrial ice sheets (Goldsby and Kohlstedt, 2001; Durham et al., 2010). Therefore, diffusion creep will not be considered in the remainder of this Chapter.

Goldsby and Kohlstedt (2001), Goldsby (2006) and Durham et al. (2010) suggested that Glen's flow law actually represents a combination of deformation mechanisms at the stress range 0.1-1.0 MPa (Glen, 1952, 1955), rather than only one deformation mechanism, that is dislocation creep. This forms a possible explanation for a lack of accuracy found with Glen's flow law with fixed $n=3$ at very low stress (e.g. Peltier et al., 2000; Durham and Stern, 2001; Durham et al., 2010). For instance, Schulson and Duval (2009) claim that the $n=4$ regime applies to tertiary creep, which was the same stress exponent found in the high pressure experiments by Kirby et al. (1987). Analysis also indicates that a power law with a stress exponent of $n=4$ describes best the observed state of the northern part of the Greenland ice sheet (Bons et al., 2018). Other factors that are often linked to polar ice being softer than predicted by Glen's flow law at low stress are the anisotropy of ice, impurity content and the softening of ice caused by small grain size (e.g. Fisher and Koerner, 1986; Dahl-Jensen and Gundestrup, 1987; Paterson, 1991; Cuffey et al., 2000a). Attempts have been made to account for these softening factors by introducing a pre-exponential enhancement factor. When adjusted for anisotropy and grain size, this pre-exponential factor can be as high as 20 (Azuma, 1994). As an alternative to an artificial speed up of Glen's flow law, a flow law of different nature may be used (Peltier et al., 2000).

The different GSS and GSI creep regimes recognized by Goldsby and Kohlstedt (1997, 2001) have been moulded by these authors in the form of one composite flow law. The major advantage of such a composite flow law is that it explicitly denotes the components of the different creep mechanisms, rather than just describing bulk behaviour. This provides the opportunity to calculate the relative importance of the GSS and GSI deformation mechanisms over the range of temperatures, differential stresses and grain sizes found in ice sheets and compare their contribution to the total strain rate. This is not possible with the flow law developed by Baker (1981) for example, which adds a factor to the pre-existing Glen's flow law to account for the effect of grain size.

It is well known that grain size varies throughout both the Greenland and the Antarctic ice sheets (e.g. Gow et al., 1997; Faria et al., 2014b; Binder, 2014; Fitzpatrick et al., 2014). However, the effect of grain size on strain rate is usually not considered in ice sheet models that apply flow laws of the type of Glen's flow law. Furthermore, the grain size is always expressed as a single mean grain size. However, small grains in a distribution might contribute differently to the overall behaviour than large grains, with a given set of GSS and GSI mechanisms. Ter Heege et al. (2004) showed that using a mean grain size instead of a full grain size distribution in composite flow laws can lead to an over- or underestimate of the strain rates of natural rocks. In this Chapter, the composite flow law is used to investigate the role of grain size on strain rate down to 2207 m of depth in the NEEM deep ice core in northwest Greenland (77.45°N, 51.06°W, core length 2540 m) (NEEM community members, 2013) and the results are compared to results obtained with Glen's flow law. The grain size data are described using both a mean grain size and a grain

size distribution to evaluate the variation in grain size and the effect of grain size variation on strain rate in polar ice.

4.2 Methods

4.2.1 Study site and ice microstructure

The NEEM deep ice core was chosen because a comprehensive light microscope data set was available (Kipfstuhl, 2010) enabled by a fast line scan technique with microscopic resolution (LASM - Large Area Scanning Macroscope; Krischke et al., 2015). From these LM images the grain size distribution is available (Binder et al., 2013). The NEEM ice core was drilled between 2008 and 2012 and is located close to an ice ridge (NEEM community members, 2013). The flow at the NEEM ice core is mainly parallel to the ridge with a small divergent component perpendicular to the line of the ridge (Figure 1.7). The top 1419 m of the NEEM deep ice core consists of ice deposited during the Holocene (Holocene ice), which shows a steadily increasing crystallographic preferred orientation (CPO) towards a vertical c-axis single maximum with a tendency towards a girdle (Eichler et al., 2013; Montagnat et al., 2014; Figure 1.8a). The mean grain size increases from sub-millimetre size at the surface to 3-4 mm at about 400 m of depth, after which it remains approximately constant for the remainder of the Holocene ice (Montagnat et al., 2014; Figure 1.8b). At the transition from the Holocene ice to ice from the last glacial period (glacial ice), a sharp decrease in mean grain size to 1-2 mm is observed and the c-axis vertical clustering is further strengthened. At a depth of 2207 m, which is the transition from the glacial ice to the ice deposited during the Eemian period (Eemian-glacial facies, Chapter 5), the grain size increases sharply to tens of mm and the shape of the CPO varies strongly with depth (Figure 1.8a; Chapter 5).

The difference in microstructure between the Holocene ice and the glacial ice of the NEEM ice core is shown in Figure 4.1. The Holocene ice core section (Figure 4.1a) was taken from a depth of 921 m and contains coarse grains with an aspect ratio of about 1:1 and has a relatively irregular grain boundary structure (Figure 1.8d). The ice core section from the glacial ice (Figure 4.1b) is taken from a depth of 1977 m and is one of the finest grained ice core sections that was used in this study. The LM image shows very fine grained sub-horizontal bands with numerous quadruple junctions. The grains in these fine grained bands are flattened and have an aspect ratio of about 2:1. The fine grained sub-horizontal bands contain many grains with aligned grain boundaries. It is often thought that the dominant deformation mechanism in the Holocene ice is dislocation creep (e.g. De La Chapelle et al., 1998; Weikusat et al., 2017), while the microstructures in the glacial ice suggest that GSS mechanisms may be important (e.g. Goldsby and Kohlstedt, 2002; Faria et al., 2014a).

In this study, 615 LM images of the Holocene and glacial ice were used to determine the grain size evolution with depth in the NEEM ice core. These LM images were made of sections that were cut parallel to the long (vertical) axis of the ice core (Kipfstuhl et al., 2006). Each LM image is about 90 mm long and about 55 mm wide and

was digitally analyzed using the Ice-image software (www.ice-image.org) (Binder et al., 2013; Binder, 2014), which automatically detects the grain area of each grain in the cut sample surface by counting the pixels enclosed by grain boundaries. A lower cut-off grain size diameter of 0.3 mm was used to exclude the small features that are produced as results of sample relaxation around air bubbles and segmentation by the analysis software (Figure 4.2).

4.2.2 The composite flow law

The composite flow law as proposed by Goldsby and Kohlstedt (2001) is formulated as follows:

$$\dot{\epsilon} = \dot{\epsilon}_{\text{disl}} + \left(\frac{1}{\dot{\epsilon}_{\text{basal}}} + \frac{1}{\dot{\epsilon}_{\text{GBS}}} \right)^{-1} + \dot{\epsilon}_{\text{diff}}, \quad (4.2)$$

where $\dot{\epsilon}$ is the strain rate and the subscripts refer to basal slip accommodated by non-basal slip or dislocation creep (disl), grain boundary sliding accommodated by basal or easy slip (basal), basal slip accommodated by grain boundary sliding (GBS) and diffusion creep (diff). Each of these creep mechanisms can be described by a power law relation of the form:

$$\dot{\epsilon} = A \sigma^n d^{-p} \exp\left(-\frac{Q + PV^*}{RT}\right), \quad (4.3)$$

where A is a material parameter, σ is the differential stress (MPa), n is the stress exponent, d is the grain size diameter (m), p is the grain size exponent, Q is the activation energy for the creep mechanism at stake (J mol^{-1}), P is the hydrostatic pressure (MPa), V^* the activation volume ($\text{m}^3 \text{mol}^{-1}$), R is the gas constant ($\text{J K}^{-1} \text{mol}^{-1}$), and T the absolute

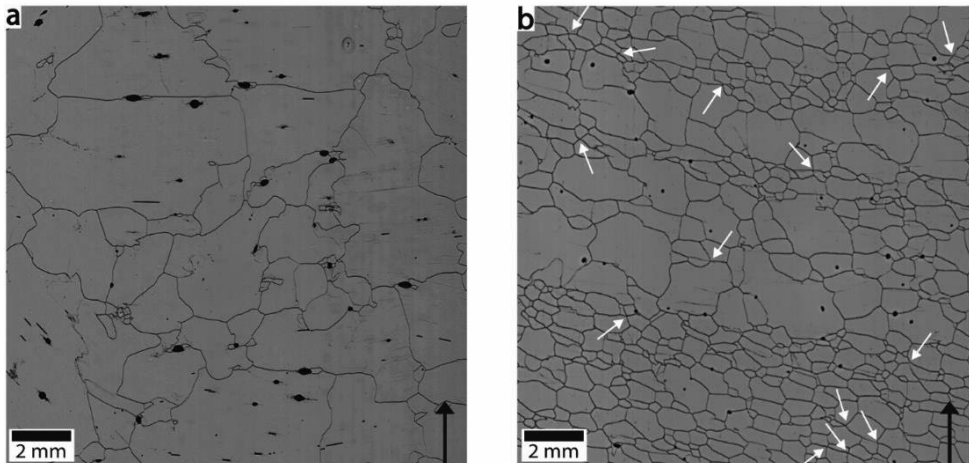


Figure 4.1: Part of two reflective LM images of ice core sections at (a) 921 m of depth in the Holocene ice and (b) of 1977 m depth in the glacial ice of the NEEM ice core. The black arrows indicate the top of the ice core. The Holocene ice core section contains relatively coarse grains with an irregular grain boundary network. The glacial ice core section contains layers with coarse and relatively fine grains that are distributed in sub-horizontal bands. The fine grained sub-horizontal bands have many aligned grain boundaries and quadruple junctions which are indicated by white arrows. Images taken from the PANGAEA database (doi: 10.1594/PANGAEA.743296).

temperature (K). The effect of PV^* is assumed to be very small (Durham and Stern, 2001) and is ignored for the remainder of this study.

As explained by Durham and Stern (2001), grain boundary sliding and dislocation slip are sequential processes where the slowest mechanism determines the overall strain rate, i.e. is rate-limiting. Under the temperatures, grain sizes and stresses that occur in natural ice on Earth, basal slip will always give faster strain rates than grain boundary sliding and non-basal slip (Goldsby and Kohlstedt, 2001; Goldsby, 2006). This makes, according to Goldsby and Kohlstedt (2001), either gbs or non-basal slip the accommodating (rate-limiting) mechanism for deformation of ice sheets. Therefore, basal slip-limited creep (grain boundary sliding accommodated by basal slip) is not considered in the remainder of this Chapter, as this deformation mechanism is not relevant for polar ice sheets. Hence, the composite flow law simplifies to:

$$\dot{\epsilon} = \dot{\epsilon}_{dist} + \dot{\epsilon}_{GBS}, \quad (4.4)$$

where $\dot{\epsilon}_{GBS}$ stands for GBS-limited creep (basal slip accommodated by grain boundary sliding). The power law relationship of Equation (4.3) also corresponds to the type of flow equation of Glen's law (Glen, 1955; Paterson, 1994). Both the composite flow law and Glen's flow law were derived during uniaxial deformation tests in secondary creep (Glen, 1952, 1955; Goldsby and Kohlstedt, 1997, 2001).

Figure 4.3 shows the effect of grain size and stress on strain rate for Glen's flow law, GBS-limited creep and the dislocation creep mechanism of the composite flow law. The chosen uniform temperature of 243K is representative for the upper 1200 m at NEEM (Sheldon et al., 2014; Figure 1.8c). Glen's flow law and the dislocation creep mechanism are not dependent on grain size ($p=0$), but have a different slope to each other resulting from the different stress exponents. GBS-limited creep shows relatively fast strain rates at small grain sizes and low stresses. At higher stresses and larger grains, the dislocation creep mechanism is dominant over GBS-limited creep.

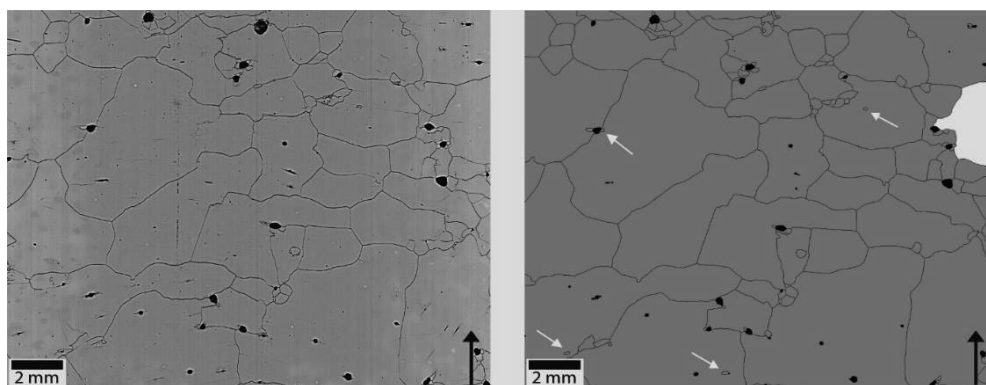


Figure 4.2: Part of a reflective LM image (left) and the segmented image (right) of an ice core section at 756 m depth. The black arrows indicate the top of the ice core. White arrows indicate examples of artifacts with a diameter <0.3 mm that were not included in the grain size data. The white grain in the upper right corner of the segmented image was excluded from the grain size data because the grain boundary was interrupted by the edge of the sample.

The smaller grains in a polycrystal can potentially deform by a different mechanism than the larger grains, since the smaller grains are more susceptible to GSS deformation mechanisms. In order to study the effect of the variation in grain size, a grain size distribution was used as well as a mean grain size in the flow law (Freeman and Ferguson, 1986; Heilbronner and Bruhn, 1998; Ter Heege et al., 2004). Similar to Freeman and Ferguson (1986) and Ter Heege et al. (2004), applying a grain size distribution into a composite flow law leads to application of two theoretical end members to describe the deformation of ice: the homogeneous stress, or micro-scale constant stress model, and the homogeneous strain rate, or micro-scale constant strain rate model.

The micro-scale constant stress model assumes that each grain experiences the same stress, which is equal to the bulk stress of the material. However, the strain rate produced by each grain is different. The driving stress and the bulk strain rate produced by this model can be expressed as follows:

$$\sigma_\sigma = \sigma_1 = \sigma_2 = \sigma_i, \quad (4.5)$$

$$\dot{\epsilon}_\sigma = v_1 \dot{\epsilon}_1 + v_2 \dot{\epsilon}_2 + \dots + v_n \dot{\epsilon}_n = \sum_{i=1}^n v_i \dot{\epsilon}_i, \quad (4.6)$$

where the bulk volume has been segmented into n grain size classes, and v_i stands for the volume fraction of grain size class i , and $\dot{\epsilon}_i$ stands for the strain rate of grain size class i .

The micro-scale constant strain rate model assumes that each grain deforms by the same strain rate, which is equal to the strain rate of the bulk material. The stress required to produce this strain rate is different for each grain size class. This end member assumes that the larger grains in the polycrystalline material support more stress than the smaller grains and can be describes as follows:

$$\dot{\epsilon}_\epsilon = \dot{\epsilon}_1 = \dot{\epsilon}_2 = \dot{\epsilon}_i, \quad (4.7)$$

$$\bar{\sigma}_\epsilon = v_1 \bar{\sigma}_1 + v_2 \bar{\sigma}_2 + \dots + v_n \bar{\sigma}_n = \sum_{i=1}^n v_i \bar{\sigma}_i, \quad (4.8)$$

where $\bar{\sigma}_i$ stands for the stress supported by grain size class i . An iterative approach is required to calculate the strain rate when the bulk stress is known.

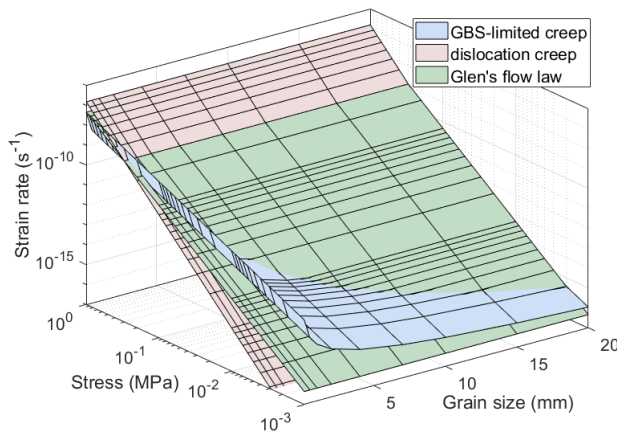


Figure 4.3: The effect of grain size and stress on strain rate plotted for Glen's flow, the dislocation creep mechanism and GBS-limited creep of the composite flow law at a constant temperature of 243K using the flow law parameters in Table 4.1.

4.2.3 Boundary conditions and input data

The temperature in the NEEM borehole reaches 269.8K at the bedrock interface, which is only 0.9K below the estimated pressure-melting point (Sheldon et al., 2014). At this temperature it is expected that the deformation of ice is affected by premelting (e.g. Mellor and Testa, 1969b; Barnes et al., 1971; Morgan, 1991; Goldsby and Kohlstedt, 2001; Chapter 5). To omit the effect of the different temperature thresholds given in Table 4.1 for Glen's flow law (263K), the GBS-limited mechanism (255K) and the dislocation creep mechanism (258K) of the composite flow law (Goldsby and Kohlstedt, 2001), the high temperature flow law parameters, and therefore the effect of premelting on strain rate, were not included in this Chapter. Since the effect of premelting is expected to start close to the glacial-Eemian interface (at $T > 262\text{K}$ see Chapter 5), all data below 2207 m of depth was excluded in this study.

The method of Heilbronner and Bruhn (1998) was used to convert 2D sectional areas to 3D volume fractions. This method uses an equivalent grain diameter that was determined for each grain and a 3D volume fraction was calculated with the assumption of a spherical grain. This method corrects for the over representation of small grains in an LM image compared to the bulk volume. The grain size distribution contains 80 grain size classes defined by steps of the equivalent diameter of 0.3 mm each, covering the full breath of the observed grain size distribution in the Holocene and glacial ice. The equivalent diameter of each grain in each ice core section was calculated and included in the corresponding grain size class. Figure 4.4 shows an example of the volume contribution of sectional circles and the corresponding volume contribution of spheres for an ice core section at 921 m of depth, part of which is shown in Figure 4.1a.

The mean grain size (right panel of Figure 4.7c) was determined by dividing the total area, as classified by the "grain" category in the Ice-image software, by the number of grains for each LM image. This way, the areas affected by bubbles, fracturing or frost are excluded from the mean grain size calculation. A mean equivalent diameter for each ice core section was calculated by assuming a circular grain. When using a mean grain size, there are no series of volume fractions (Equation 4.6, 4.8) so no application of the micro-scale constant stress model and the micro-scale constant strain rate model is required.

To calculate the strain rate using Glen's flow law and the composite flow law at the location of the NEEM ice core, information about the variation of stress with depth in

Table 4.1: Parameters for the simplified composite flow law and Glen's flow law relating grain size, temperature and stress to strain rate (Equation 4.3) taken from Goldsby and Kohlstedt (2001) and Glen's flow law (Paterson, 1994).

Creep regime	A (units)	n	Q (kJ mol ⁻¹)	p
Dislocation creep (T<258K)	$1.2 \cdot 10^6 \text{MPa}^{-4.0} \text{s}^{-1}$ *	4.0	60	0
GBS-limited creep (T<255K)	$3.9 \cdot 10^{-3} \text{MPa}^{-1.8} \text{m}^{1.4} \text{s}^{-1}$	1.8	49	1.4
Glen's flow law (T<263K)	$3.61 \cdot 10^5 \text{MPa}^{-3.0} \text{s}^{-1}$	3.0	60	0

*This value of A was updated from the original value (Goldsby, 2006).

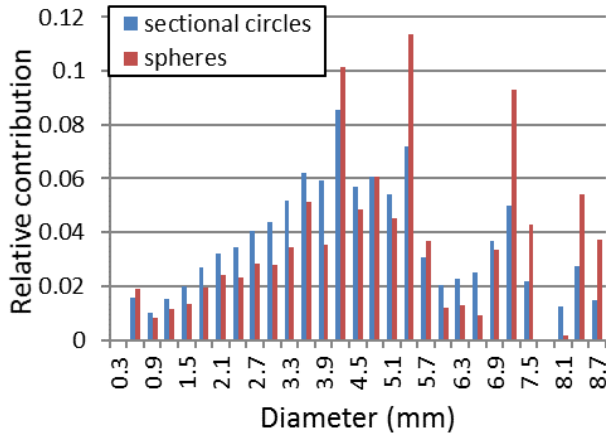


Figure 4.4: Relative contribution of each grain size class to the bulk volume of an ice core section at 921 m depth calculated for sectional circles (blue) and spherical grains (red) using the method of Heilbronner and Bruhn (1988).

the ice sheet is required. As stress itself cannot be measured, the stress has to be estimated based on theoretical considerations and constraints on strain rates in the NEEM ice core.

The shear stress in an ice sheet is driven by gravity and is determined by the surface slope of the ice sheet and the depth from the surface z_{ice} . The shear stress along an ice core can be estimated using the shallow ice approximation (e.g. Hutter, 1983; Greve and Blatter, 2009):

$$\tau = -\rho_{ice} z_{ice} g \frac{\partial h}{\partial x}, \quad (4.9)$$

where τ is the shear stress (Pa), ρ_{ice} is the density of ice (910 kg m^{-3}), z_{ice} is the ice thickness (m), g is the gravitational constant (9.81 m s^{-2}) and $\frac{\partial h}{\partial x}$ is the surface slope in the direction of flow. The surface slope at NEEM is about 1.8 m km^{-1} (Montagnat et al., 2014) and the ice core length is 2540 m (Rasmussen et al., 2013). Assuming a constant ice density, the shear stress increases linearly with depth reaching 0.041 MPa at the ice-bedrock interface at NEEM. Glen's flow law and the composite flow law were derived in uniaxial compression deformation tests. So in order to use the shear stress as input for the flow laws, the shear stress has to be converted to an equivalent stress σ_e using the following relationship (Paterson and Olgaard, 2000):

$$\sigma_e = \sqrt{3} \tau, \quad (4.10)$$

which results in an equivalent axial differential stress at the ice-bedrock interface at NEEM of 0.071 MPa as shown in Figure 4.5.

The upper part of the NEEM ice core is dominated by longitudinal stress, perpendicular to the plane of the divide, leading to thinning of the annual layers (Dansgaard and Johnsen, 1969; Montagnat et al., 2014). Longitudinal stresses can be calculated from the increase of the ice slope away from the divide, if the rheology of ice is assumed (Raymond, 1983; Dahl-Jensen, 1989a). In this study, the simple approach of assuming an

imposed stress-depth relationship will be taken to investigate how ice rheology is influenced by grain size, temperature and imposed stress. The layer thinning in the upper part of an ice core provides a constraint on the vertical strain rate, which in case of the NEEM ice core gives a value of about $3.2 \cdot 10^{-12} \text{ s}^{-1}$ (Gillet-Chaulet et al., 2011; Montagnat et al., 2014) in the Holocene ice. This strain rate can be used to estimate the equivalent stress in the upper part of the ice sheet using the composite flow law and Glen's flow law (Figure 4.5). A constant equivalent stress value of 0.07 MPa using the composite flow law, reproduced the rate of observed layer thinning, as shown in Figure 4.8. (Note that Figure 4.8 is based on the composite flow law with the modified flow law parameters, discussed in Section 4.3). For Glen's flow law the equivalent stress required to reproduce the observed layer thinning in the Holocene ice is lower at about 0.04 MPa. It was therefore decided to assume a constant equivalent stress of 0.07 MPa along the length of the NEEM ice core as input for Glen's flow law and the composite flow law. At the base of the ice sheet the vertical equivalent stress will tend to zero, with the decrease of vertical stress depending on the stress exponent in the flow law (Dansgaard and Johnson, 1969; Dahl-Jensen, 1989b).

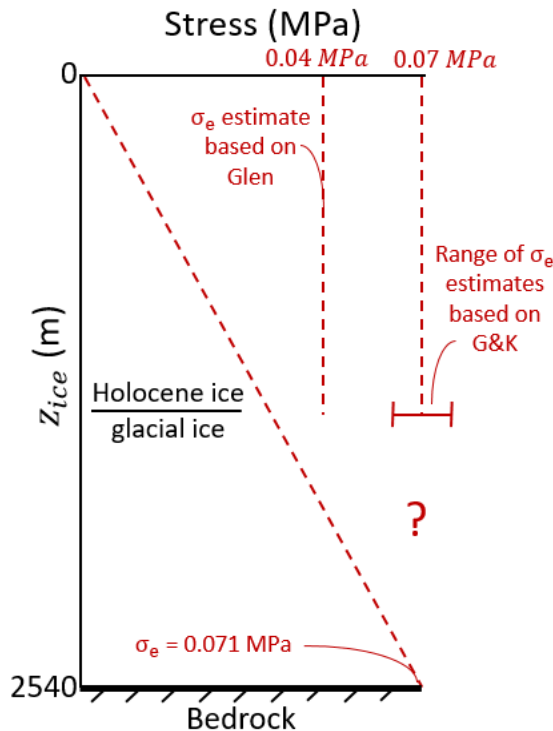


Figure 4.5: The equivalent shear stress (σ_e) with depth calculated using the shallow ice approximation (Equation 4.9) and the range of the estimated longitudinal stress based on the modified parameters of the composite flow law (G&K) of Table 4.2 and the best estimate for Glen's flow law constrained by the annual layer thinning in the Holocene ice of the NEEM ice core. There are no constraints on the annual layer thinning in the glacial and Eemian ice, which is indicated by the question mark.

The assumption of constant equivalent stress with depth is not realistic for ice sheets in general (e.g. Dahl-Jensen, 1989b). However, this assumption is a useful first approximation for the NEEM ice core where the equivalent stress, related to the shear stress in the lower part of the ice core, is by coincidence similar to the magnitude of equivalent stress related to the vertical stress in the upper part of the ice core. As this Chapter explores the effect of grain size, grain size distribution and different micro-scale models on the dominant deformation mechanism and the total strain rate, it is beyond the scope of this study to derive a stress-depth model for NEEM because this requires knowledge on the rheology, which is the property that is investigated here. When calculating strain rates, no distinction is made between simple shear and pure shear deformation.

4.3 Flow law parameters

The original flow law parameters for the simplified composite flow law (Goldsby and Kohlstedt, 2001) and Glen's flow law (Paterson, 1994) are given in Table 4.1. In order to apply the composite flow law of Goldsby and Kohlstedt (2001) to the NEEM ice core, a modification of the temperature regimes of the flow laws was required, as described in Chapter 5, which led to a check of the flow laws with the experimental data. A comparison of the calculated strain rate for dislocation creep with the experimental data points from Figure 6 of Goldsby and Kohlstedt (2001) was made. The calculated strain rates were based on the flow law parameters in Table 4.1 and using Equation (4.3). This comparison is shown in Figure 4.6a. The solid blue line shows the calculated strain rate for dislocation creep when the flow law parameters of Table 4.1 were used and forced with a stress of 6.3 MPa, which is the same stress as used in Figure 6 of Goldsby and Kohlstedt (2001). The calculated strain rate does not coincide with the three experimental data points for a temperature of $<258\text{K}$. The calculated strain rate is about 15 to 20 times higher than the experimental strain rates. An Arrhenius plot for GBS-limited creep (Figure 4.6b) was also calculated using a stress of 0.53 MPa and a uniform grain size of $73\ \mu\text{m}$, similar to Figure 4 of Goldsby and Kohlstedt (2001) and using the flow law parameters of Table 4.1. For this deformation mechanism, the calculated strain rate agrees well with the experimental data points at $T < 255\text{K}$ of Goldsby and Kohlstedt (2001).

To account for the discrepancy between the dislocation creep mechanism and the experimental data, the flow law parameters were modified (dashed blue line, Figure 4.6a). The modified flow law parameters that are proposed here are shown in Table 4.2. For GBS-limited creep, the flow law parameters remain the same as in Table 4.1. However, for dislocation creep, the material parameter A and the activation energy Q (Table 4.2) change significantly compared to the values given by Goldsby and Kohlstedt (2001) and Goldsby (2006) shown in Table 4.1. The temperature threshold for the onset of premelting for both dislocation creep and GBS-limited creep changed to 262K , which is discussed in Chapter 5. These modified flow law parameters show a better agreement with the experimental data points for dislocation creep at $T < 258$ (Figure 4.6a).

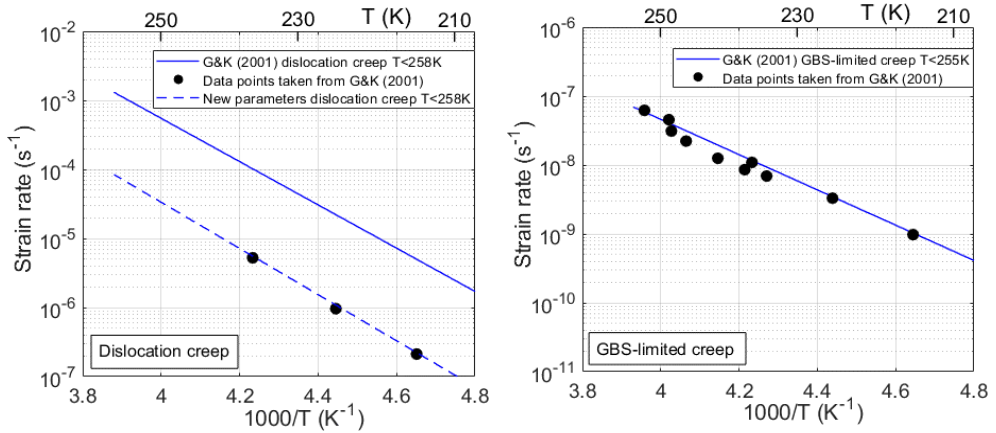


Figure 4.6: Arrhenius plot showing (a) the dislocation creep mechanism and (b) the GBS-limited creep mechanism below their temperature thresholds of 258K and 255K, respectively. A stress of 6.3 MPa was used to calculate the strain rates in (a) and a stress of 0.53 MPa and a uniform grain size of 73 μm was used for (b). The black dots are the experimental data points taken from Goldsby and Kohlstedt (2001). The solid lines represent the calculated strain rate using the original flow law parameters (Table 4.1). The dotted line is the calculated strain rates using the modified flow law parameters (Table 4.2).

Table 4.2: Modified flow law parameters for the composite flow law as derived from Figure 4.6.

Creep regime	A (units)	n	Q (kJ mol ⁻¹)	p
Dislocation creep (T < 262K)	$5.0 \cdot 10^5 \text{MPa}^{-4.0} \text{s}^{-1}$	4.0	64	0
GBS-accommodated basal slip (T < 262K)	$3.9 \cdot 10^{-3} \text{MPa}^{-1.8} \text{m}^{1.4} \text{s}^{-1}$	1.8	49	1.4

4.4 Results

Figure 4.7 shows plots of the equivalent strain rate as a function of depth for Glen’s flow law and the composite flow law with its two different deformation mechanisms and the three different model end members calculated using the original flow law parameters (Table 4.1). The contribution of GBS-limited creep to bulk strain rate is shown as well. The temperature input for all the models is shown in the right panel of Figure 4.7c. The results using the full grain size distribution with the micro-scale constant stress model (Figure 4.7a) and the micro-scale constant strain rate model with the grain size distribution (Figure 4.7b) are shown, as well as the results using the mean grain size model (Figure 4.7c) and the mean grain size evolution with depth (right panel of Figure 4.7c). All models show similarities, such as (i) a relatively constant strain rate between 400 m and 1400 m of depth, (ii) a strain rate increase below 1400 m of depth and (iii) a higher strain rate for Glen’s flow law compared to the composite flow law along the entire depth range down to 2207 m (that is, excluding the Eemian-glacial facies, Chapter 5) of the NEEM ice core. In all of the three model end members, the calculated strain rate for GBS-limited creep and the composite flow law both show a more variable strain rate below 1400 m. This depth coincides with the

transition from the coarse grained Holocene ice to the finer grained glacial ice and with an increase in temperature (Figure 4.7c, right panel). The peak values in strain rate in the glacial ice, indicated by the arrow in Figure 4.7a, predict strain rates that are comparable to the strain rate calculated using Glen's flow law. Two strain rate peaks occur at about 1980 m and 2100 m of depth and show a two to three-fold increase in strain rate compared to the mean strain rate in the glacial ice predicted by the composite flow law.

Throughout most of the Holocene ice (above 1419 m of depth), the dislocation creep (basal-slip accommodated by non-basal slip) mechanism predicts a slightly higher strain rate than the GBS-limited creep (basal-slip accommodated by grain boundary sliding) mechanism for each of the three models. The difference between the strain rates of GBS-limited creep and dislocation creep in the Holocene ice is smaller for the micro-scale constant stress model than for the micro-scale constant strain rate model and the mean grain size model. In the glacial ice, dislocation creep and GBS-limited creep have roughly the same strength for each of the three models, apart from the higher variability in strength of the GBS-limited creep with depth. Compared to the micro-scale constant stress model, the micro-scale constant strain rate model predicts slightly lower absolute strain rates from GBS-limited creep along the entire upper 2207 m of depth of the NEEM ice core (Figure 4.7a, b) and especially below 1419 m of depth where the strain rate is more variable. The average strain rate predicted by the composite flow law is 10% higher in the glacial ice and 8% higher in the Holocene ice when using the micro-scale constant stress model instead of the micro-scale constant strain rate model. Using a mean grain size produces a weaker variability in strain rate with depth than the two model end members using a grain size distribution (Figure 4.7c).

Figure 4.8 is similar to Figure 4.7, but shows the results for the NEEM ice core using the modified flow law parameters (Table 4.2). The trends are similar to those in Figure 4.7, with the main difference that dislocation creep hardly contributes to the overall strain rate for each of the three models. Using the modified flow law parameters (Figure 4.8a-c), the three models predict that almost all deformation in the upper 2207 m of depth in the NEEM ice core is produced by GBS-limited creep. The strain rate peaks in the glacial ice at a depth of about 1980 and 2100 m are slightly weaker than the peaks calculated with the original flow law constants (Table 4.1) in Figure 4.7. The average strain rate in the Holocene ice is about 60% higher using the micro-scale constant stress model compared to the micro-scale constant strain rate model. For the glacial ice, this difference between the two model end members is about 40%.

Figure 4.9a and 4.9b show the strain rate per grain size class and the contribution of the two deformation mechanisms (Equation 4.4) for an ice core section at 921 m of depth. Part of this ice core section is shown in Figure 4.1a. This ice core section is located in the middle of the Holocene ice and has a relatively high variation in grain size. Since dislocation creep is a GSI mechanism, the strain rate produced by this deformation mechanism is the same for each grain size class in the micro-scale constant stress model (Figure 4.9a). GBS-limited creep shows faster strain rates than dislocation creep and strongly decreases in strain rate with increasing grain size, which is consistent with the

inversely relationship to grain size given in Equation (4.3). The volume contribution of each grain size class (black bars in Figure 4.9a and 4.9b) is used in Equation (4.6) to calculate the bulk strain rate for this ice core section and in Equation (4.8) to iteratively calculate the stress supported by each grain size class.

The total strain rate produced by each grain size class is set to be the same for the micro-scale constant strain rate model shown in Figure 4.9b. The relative contribution of each deformation mechanism differs between grain size classes. GBS-limited creep is the dominant deformation mechanism for the smallest grains, whereas dislocation creep becomes increasingly more important for classes with larger grain sizes. However, even for the largest grains in this ice core section the strain rate produced by GBS-limited creep is still slightly larger than the strain rate produced by dislocation creep.

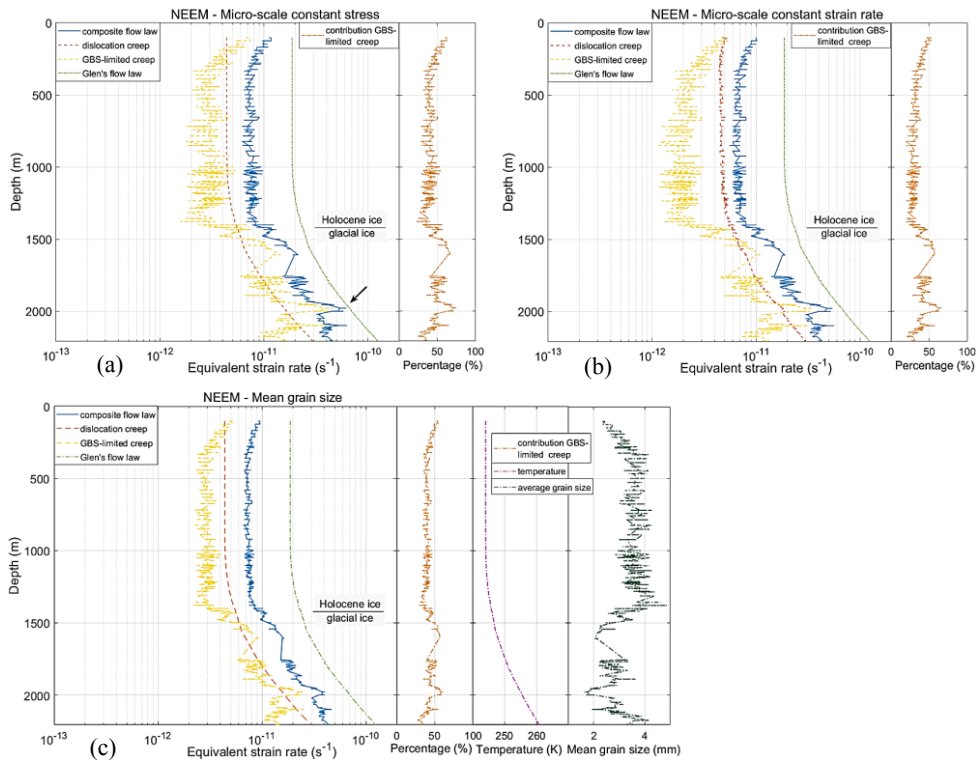


Figure 4.7: (a) Results for the Holocene and glacial ice for Glen’s flow law (light green, same in a, b, c) and the composite flow law (blue) using the flow law parameters in Table 4.1, which consist of dislocation creep (red) and GBS-limited creep (yellow), using (a) the micro-scale constant stress model with the grain size distribution with the arrow indicating the depth at which Glen’s flow law and the composite flow law have a similar strength, (b) the micro-scale constant strain rate model with the grain size distribution and (c) the composite flow law with the average grain size data. To show the influence of temperature and average grain size on calculated strain rates, these input parameters are added next to (c). The contribution of GBS-limited creep to bulk strain rate for all three model end members is shown. The temperature profile is used in all three figures (a, b, c), while the average grain size profile was only used for calculating the results shown in (c). A constant effective stress of 0.07 MPa was used for all figures.

The stress supported per grain size class for the micro-scale constant stress and micro-scale constant strain rate model for the composite flow law is shown in Figure 4.9c. The stress supported per grain size class using the micro-scale constant strain rate model is used in Equation (4.8) to iteratively calculate the stress in the bulk material of the ice core section. The smallest grain size classes support only a small amount of stress, since they are more sensitive to GBS-limited creep. As a consequence, the larger grains support more stress and activate a significant amount of dislocation creep.

To study the dominant deformation mechanism of the composite flow law at different stress levels as well as its comparison in strain rate to Glen's flow law, both flow laws were forced at different stress values, which roughly cover the range of equivalent stresses in the Greenland and Antarctic ice sheets (Sergienko et al., 2014). Figure 4.10a shows the calculated strain rate for dislocation creep and GBS-limited creep using the grain size distribution with the micro-scale constant stress model and the temperature profile of NEEM, forced with different constant stress values. At the lowest stress of 0.01 MPa, the strain rate produced by dislocation creep is about three orders of magnitude lower than the strain rate produced by GBS-limited creep. With increasing stress, the contribution of dislocation creep to the overall strain rate becomes bigger and at a stress of 0.25 MPa, dislocation creep and GBS-limited creep have roughly the same strength. The strain rate produced by the dislocation creep mechanism at 0.50 MPa is roughly five times higher than for GBS-limited creep. A similar graph showing the calculated strain rate for the composite flow law and Glen's flow law is shown in Figure 4.10b. At the lowest stress of 0.01 MPa the composite flow law predicts a slightly higher strain rate compared to Glen's flow law. However, with increasing stress, Glen's flow law predicts progressively higher strain rates than the composite flow law. At the highest stress of 0.50 MPa, the strain rate predicted by Glen's flow law is almost an order of magnitude higher than the strain rate predicted by the composite flow law.

4.5 Discussion

In the first part of the discussion, the results obtained using the original flow law parameters (Figure 4.7) and the modified flow law parameters (Figure 4.8) are discussed. Emphasis is given to the results obtained using the modified flow law parameters (Table 4.2), as these parameters show a better fit with the experimental data points than the original flow law parameters from Goldsby and Kohlstedt (2001) (Table 4.1). The modification is the most straightforward solution to account for the inconsistency between given parameters (Table 5 in Goldsby and Kohlstedt, 2001) and experimental results (Figure 6 in Goldsby and Kohlstedt, 2001). The modification of the flow law parameters results in dislocation creep being about 15 to 20 times slower compared to the original flow law parameters.

4.5.1 Comparison of micro-scale constant stress versus micro-scale constant strain rate model

The main difference between the micro-scale constant stress model and the micro-scale constant strain rate model is that the micro-scale constant stress model allows the smallest grains to deform more than an order of magnitude faster than the larger grains (Figure 4.9a), while this is not possible in the micro-scale constant strain rate model (Figure 4.9b). For the micro-scale constant strain rate model, the strain rate is set to be the same for each grain size class. GBS-limited creep and dislocation creep are therefore co-dependent, since the sum of the two deformation mechanisms has to add up to a certain strain rate (Equation 4.4). Consequently, since the strain rate produced by GBS-limited creep decreases with increasing grain size, the contribution of dislocation creep to bulk strain rate increases with

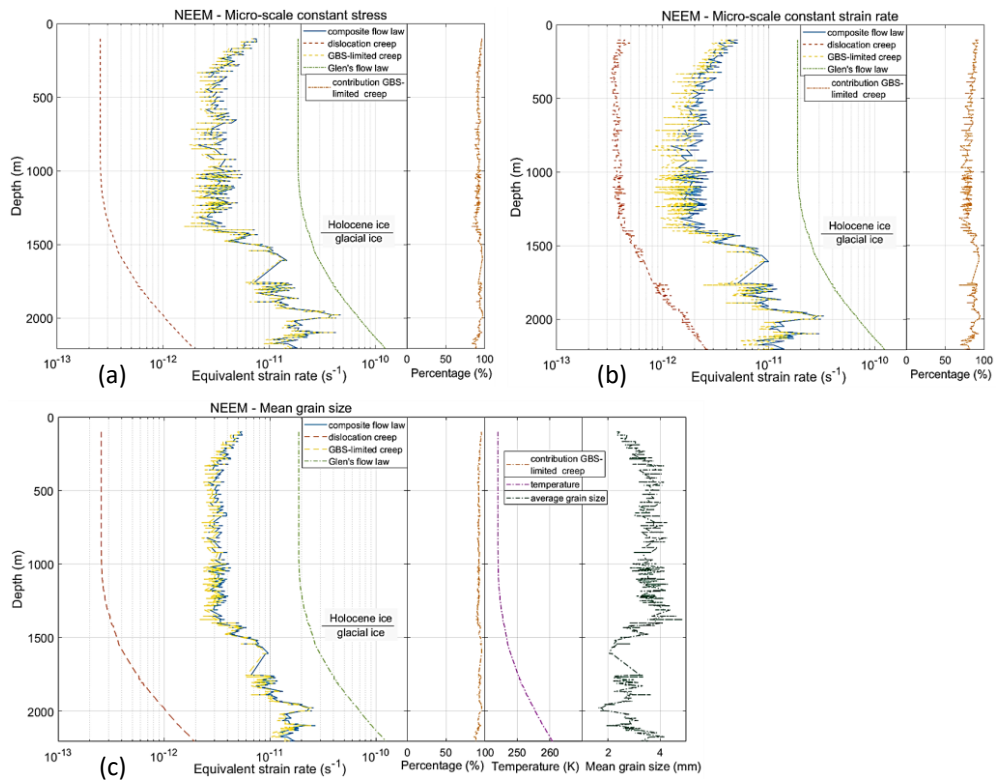


Figure 4.8: (a) Results for the Holocene and glacial ice for Glen’s flow law (light green, same in a, b, c) and the composite flow law (blue) using the flow law parameters in Table 4.2, which consist of dislocation creep (red) and GBS-limited creep (yellow), using (a) the micro-scale constant stress model with the grain size distribution, (b) the micro-scale constant strain rate model with the grain size distribution and (c) the composite flow law with the average grain size data. To show the influence of temperature and average grain size on calculated strain rates, these input parameters are added next to (c). The contribution of GBS-limited creep to bulk strain rate for all three model end members is shown. The temperature profile is used in all three figures (a, b, c), while the average grain size profile was only used for calculating the results shown in (c). A constant effective stress of 0.07 MPa was used for all figures.

grain size. This effect is shown in Figure 4.9b where the bulk strain rate is similar for each grain size class, but the contribution of dislocation creep to the bulk strain rate increases with increasing grain size. Due to this co-dependence of dislocation creep and GBS-limited creep in the micro-scale constant strain rate model, the strain rate produced by dislocation creep varies slightly with depth as is shown in Figure 4.7b and 4.8b.

For most ice core samples, the finest grain size classes contribute only slightly to the bulk volume of the material, as is also the case for the ice core section at 921 m of depth shown in Figure 4.9. For this particular ice core section, the smallest grain size classes (<0.9 mm) make up only 2.7% of the bulk volume. Therefore, the contribution of these smallest grain size classes to the bulk strain rate remains limited. Nevertheless, the average strain rate in the Holocene ice calculated using the micro-scale constant stress model and the modified flow law parameters (Table 4.2) is 60% higher than the average strain rate produced by the micro-scale constant strain rate model. In the glacial ice, where the grain sizes are finer and grain size distributions are more uniform, the difference in strain rates between the micro-scale constant stress and micro-scale constant strain rate model is 40%. However, these differences are remarkably small compared to results obtained for the two model end members in wet olivine (Ter Heege et al., 2004) and calcite mylonites (Herwegh et al., 2005). In wet olivine, the bulk strain rate could be up to an order of magnitude higher for the micro-scale constant stress model compared to the micro-scale constant strain rate model for samples with a high standard deviation in grain size distribution. This indicates that the grain size variation measured within each of the 90 x 55 mm ice core sections is not large enough to change the strain rate by an order of magnitude as observed for wet olivine.

By assuming that each grain deforms by the same amount in the micro-scale constant strain rate model, the strain heterogeneities that have often been observed in ice core microstructures (e.g. Obbard et al., 2006; Weikusat et al., 2009b; Faria et al., 2014a; Piaolo et al., 2015; Jansen et al., 2016) are ignored. Contrary to the micro-scale constant stress model, where the contribution of the finest grains is relatively large compared to their volume contribution, the micro-scale constant strain rate model likely overestimates the role of the larger grains on the bulk strain rate in the ice core section. Therefore, the two models represent the lower and upper limit of deformation behavior of a polycrystal with a distributed grain size (Ter Heege et al., 2004).

4.5.2 comparing grain size distribution model end members with the mean grain size model

The difference in calculated strain rate between using a grain size distribution with the micro-scale constant strain rate model and the mean grain size model is relatively small (Figure 4.8b and c). A single mean grain size eliminates the effect that smaller grains have on the bulk strain rate. However, the effect of the smaller grains on strain rate in the micro-scale constant strain rate model is also limited since all grain size classes deform by the same amount and thus the difference in bulk strain rate between the micro-scale constant strain rate model and mean grain size model is small. The much larger computational

expense of the micro-scale constant strain rate model and the small difference in calculated strain with the mean grain size model argues for using a mean grain size model over a micro-scale constant strain rate model when modelling GSS behaviour in polar ice sheets.

The difference in calculated strain rate between the micro-scale constant stress model and using a mean grain model size is larger than the difference between the micro-scale constant strain rate model and the mean grain size model. The strain rate peaks predicted in the layers at about 1980 m and 2100 m of depth are two to three times larger for the micro-scale constant stress model compared to the mean grain size model (Figure 4.8a, c). This difference is mainly caused by the effect that the finest grains have on the bulk strain rate in the micro-scale constant stress model (Figure 4.9a).

4.5.3 Stress sensitivities

Figure 4.10a shows that, at equivalent stresses below 0.25 MPa, the strain rate produced by GBS-limited creep is higher than the strain rate produced by dislocation creep, while at an equivalent stress of 0.50 MPa the strain rate produced by dislocation creep is higher than GBS-limited creep. The stress sensitivity of dislocation creep is controlled by a stress exponent of $n=4$, while the stress sensitivity of GBS-limited creep is controlled by $n=1.8$. Thus, if temperature and grain size remain constant, dislocation creep becomes

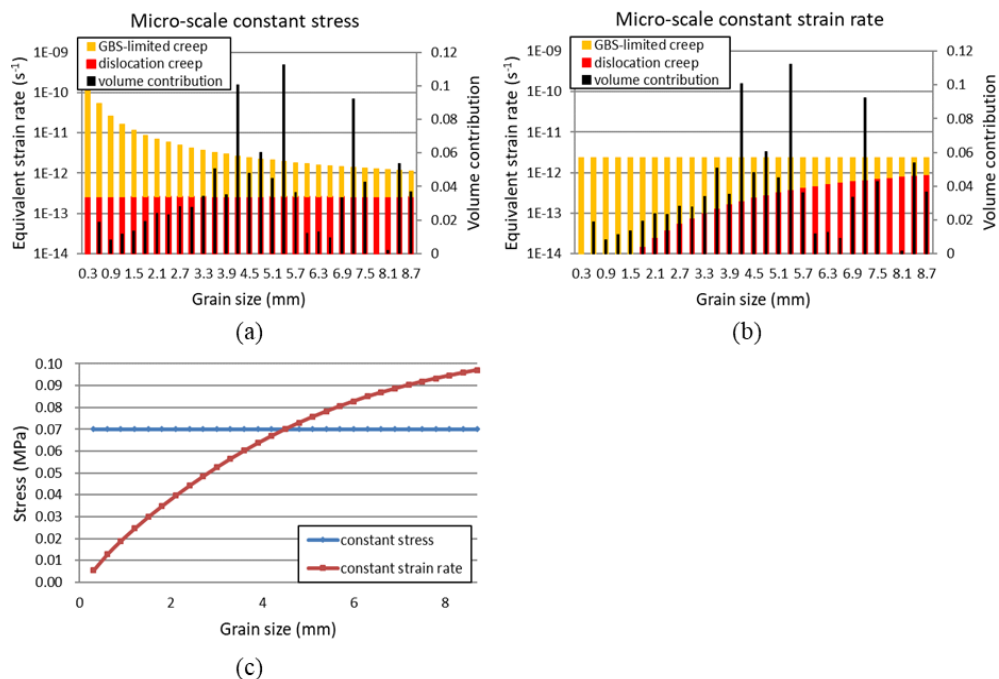


Figure 4.9: Grain size class versus log strain rate for an ice core section at 921 m depth for (a) the micro-scale constant stress model, (b) the micro-scale constant strain rate model and (c) the stress supported by each grain size class of the grain size distribution. The results were calculated using the flow law parameters in Table 4.2. The bulk strain rate for this ice core section using the micro-scale constant stress and micro-scale constant strain rate model following Equations (4.5) to (4.8) is $4.1 \cdot 10^{-12} s^{-1}$ and $2.4 \cdot 10^{-12} s^{-1}$, respectively.

progressively stronger relative to GBS-limited creep with increasing stress. However, with the temperature profile and grain size data from the upper 2207 m of depth in the NEEM ice core, an equivalent stress of about 0.25 MPa is required for dislocation creep to become as strong as GBS-limited creep. Such a high stress is not reached in the NEEM ice core as the best estimate gives an equivalent stress of 0.07 MPa. However, the driving stress progressively increases from the ice domes and divides towards the margins of the ice sheet, reaching a driving stress of about 0.30 MPa at the margins of the ice sheets (Sergienko et al., 2014). A driving stress of 0.30 MPa corresponds to an equivalent stress of about 0.50 MPa (Equation 4.10). Therefore, if the temperature and grain size along the NEEM ice core is comparable to the ice along the margins of the ice sheet, the dominant deformation mechanism could switch from GBS-limited creep near domes and divides to dislocation creep near the margins of the ice sheets.

Interestingly, the stress of 0.10–0.50 MPa is within the range of stresses (0.1–1.0 MPa) that was used during the deformation experiments of Glen (1952, 1955). The grain size reported of 1–2 mm by Glen (1952) is similar to the grain size in the glacial ice of the NEEM ice core (Figure 4.8c, right panel). The results in Figure 4.10a for 0.25 MPa show that the contribution of dislocation creep and GBS-limited creep to the total strain rate in the glacial ice is roughly equal. This result supports the hypothesis of Durham et al. (2001), Goldsby and Kohlstedt (2001, 2002) and Goldsby (2006) that the stress exponent of $n=3$ found by Glen (1952, 1955) is the result of collecting data at a transition regime between $n=4$ for dislocation creep and $n=1.8$ for GBS-limited creep.

Comparison of the results using the composite flow law with Glen's flow law at different equivalent stresses (Figure 4.10b) shows that at a stress of 0.01 MPa the composite flow law predicts a higher strain rate than Glen's flow law in most of the upper 2207 m of depth in the NEEM ice core. In the finest grained parts of the glacial ice, the composite flow law predicts a strain rate that is about five times faster than predicted by Glen's flow law at the low equivalent stress of 0.01 MPa. As the equivalent stress increases, Glen's flow law becomes progressively faster relative to the composite flow law. Since the dominant deformation mechanism of the composite flow law at low equivalent stress is GBS-limited creep (Figure 4.10a), the effective stress exponent will also be close to the stress exponent for GBS-limited creep ($n=1.8$). Glen's flow law, driven by a stress exponent of $n=3$, shows therefore a stronger increase in strain rate with increasing stress than the composite flow law. Consequently, at a driving stress of 0.25 MPa, Glen's flow law predicts a strain rate that is about an order of magnitude faster than the strain rate predicted by the composite flow law. As the contribution of dislocation creep in the composite flow law increases with increasing stress (Figure 4.10a), the sensitivity of the bulk strain rate to grain size variation decreases with increasing stress since dislocation creep is insensitive to grain size. This effect can be seen in Figure 4.10b where the strain rate peaks and the layer-to-layer variability predicted by the composite flow law become weaker with increasing stress.

4.5.4 Variability of predicted strain rates with depth

Levels of high borehole closure and borehole tilting have been observed in many polar ice cores and often coincide with high impurity content and small grain sizes (e.g. Fisher and Koerner, 1986; Paterson, 1994). These depth levels can be seen as layers with a different microstructure than the surrounding ice and therefore deform at a higher strain rate. Variations in borehole tilting with depth have been observed for the NEEM ice core (pers. comm. Dorth Dahl-Jensen, March 2016). The reason that small grain size and high impurity content coincide is still not well understood (Eichler et al., 2017). The results using the composite flow law suggest that prominent soft layers, i.e. layers with a high strain rate, could be present at two depths of about 1980 and 2100 m in the NEEM ice core. These soft layers are located in the lower part of the NEEM ice core, which is dominated by simple shear (Dansgaard and Johnson, 1969; Montagnat et al., 2014). The soft layers can therefore be seen as depths where a high rate of simple shear occurs, instead of layers with enhanced extrusion (Waddington, 2010). However, it is likely that not all soft layers that are caused by finer grains have been identified since the available sampling rate of 615 LM images along 2207 m of depth of the NEEM ice core leaves many depth intervals not studied. Glen's flow law is unable to predict soft layers related to grain size variations since the flow law is forced by stress and temperature only. The effects of anisotropy, grain size and/or impurity content on strain rate are often incorporated in the form of an enhancement factor (Azuma, 1994; Thorsteinsson et al., 1999). However, information about the softening effects, like grain size, are needed in order to incorporate the enhancement factor with the

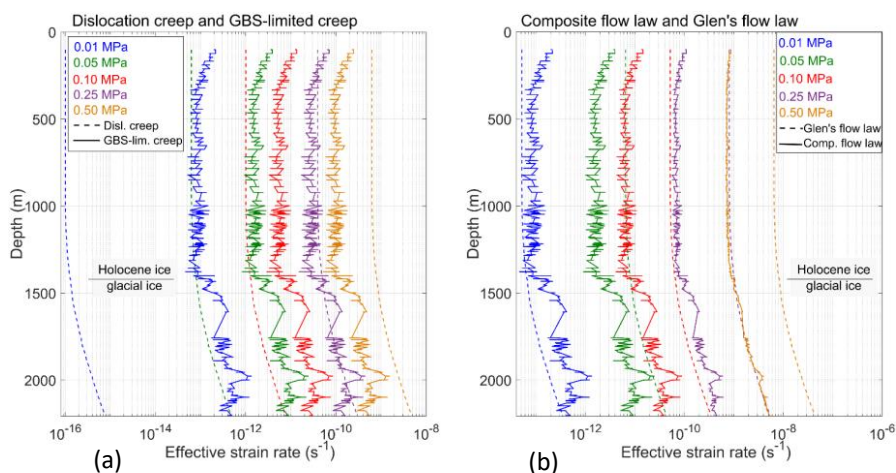


Figure 4.10: Stress sensitivity of the deformation mechanisms in the Holocene and glacial ice. (a) Strain rates predicted by the dislocation creep mechanism (dotted lines) and GBS-limited creep (continuous lines) at 0.01 MPa (blue), 0.05 MPa (green), 0.10 MPa (red), 0.25 MPa (purple) and 0.50 MPa (orange). For readability, only the results of the micro-scale constant stress model are shown. (b) Plot of Glen's flow law (dotted lines) and the composite flow law (continuous lines). For (a) and (b) the temperature profile and the grain size distribution of the NEEM ice core were used in combination with the flow law parameters in Table 4.2.

right value and at the right depth. This can only be achieved by a flow law that explicitly describes GSS deformation, such as the composite flow law of Goldsby and Kohlstedt (2001).

Another reason why soft layers might have been missed during this study is that by taking the grain size distribution of the 90 x 55 mm LM images, the fine grain size of shear bands or cloudy bands (Faria et al., 2010; 2014a) could have been averaged out. Often, these bands have a vertical thickness that is much thinner than the 90 mm height of the LM images (see examples in Figure 4.1b; Figure 4 in Faria et al., 2014b). Therefore, it is likely that many soft layers in the glacial ice of the NEEM ice core have not been identified in this study or have been averaged out over the 90 x 55 mm LM images.

4.5.5 Microstructural evidence and CPO development

The c-axis eigenvalues show a minor variability in the glacial ice of the NEEM ice core (Eichler et al., 2013; Montagnat et al., 2014; Figure 1.8a) where the layers of high strain rate are predicted. The strong development of CPO and the development of substructures with depth indicate that large amounts of strain are accommodated by basal slip of dislocations in the NEEM ice core. This may seem to be in disagreement with the conclusion that GBS-limited creep is the dominant deformation mechanism. However, grain boundary sliding is assumed to be the accommodating mechanism, with basal slip being the main strain producing mechanism. Several studies on other minerals, such as calcite (Schmid et al., 1987; Rutter et al., 1994) and olivine (Drury et al., 2011; Hansen et al., 2011, 2012) have shown that a CPO can develop in materials deforming by GSS deformation alone or in combination with GSI deformation. A modelling study of Zhang et al. (1994) showed that, if the amount of grain boundary sliding relative to intracrystalline slip is small, even stronger CPOs are developed compared to simulations where no grain boundary sliding was allowed. If indeed CPO in polar ice can be strengthened by a grain size sensitive deformation mechanism, then this could partly explain the sudden jump in CPO strengthening at the Holocene-glacial transition in the NEEM ice core (Eichler et al., 2013; Montagnat et al., 2014; Figure 1.8a). This jump in CPO coincides with the enhanced GBS-limited creep at the Holocene-glacial transition as shown in Figure 4.8. The high strain rates produced by GBS-limited creep at a depth of about 1980 and 2100 m also correspond with the highest c-axis eigenvalues in the NEEM ice core of >0.95 (Eichler et al., 2013; Montagnat et al., 2014). For example, the very fine grained ice core section at a depth of 1977 m, part of which is shown in Figure 4.1b, has a CPO with a first eigenvalue of 0.97.

For both the composite flow law and Glen's flow law, the influence of CPO on strain rate is not taken into account during this study, for example by a pre-exponential enhancement factor. In simple shear, a strong single maximum CPO produces less strain incompatibilities at grain boundaries by aligning the basal planes of the ice crystals in the direction of the flow. This means that less accommodation of basal slip is required by either non-basal slip or GBS per unit of strain, which causes the strain rate to increase compared to an isotropic ice sample. The strain rate enhancement caused by a well-developed CPO is

about 2.3 times stronger in simple shear than in pure shear (Budd and Jacka, 1989; Treverrow et al., 2012). Therefore, the difference in equivalent strain rate between the Holocene and the glacial ice is probably larger than shown in Figure 4.8, since the Holocene ice is predominantly deforming by pure shear, while the glacial ice is predominantly deforming by simple shear (Montagnat et al., 2014).

Both deformation mechanisms of the composite flow law assume basal slip to be the dominant strain producing mechanism and being accommodated by either grain boundary sliding or non-basal slip. It is therefore argued that both dislocation creep and GBS-limited creep are enhanced by a strong single maximum CPO as a strong alignment of the dominant slip system produces less strain incompatibilities at grain boundaries and/or triple junctions. Therefore, less accommodation of basal slip is required by GBS or non-basal slip or less removal of strain incompatibilities by SIBM. To what extent these two deformation mechanisms are enhanced by CPO remains the subject of further research.

The elongated aspect ratio found in sub-horizontal fine grained bands (Figure 4.1b) have a similar aspect ratio to grains reported by Goldsby and Kohlstedt (1997, Figure 6 therein) in the GBS-limited creep experiments. Also, similar to Goldsby and Kohlstedt (1997), aligned grain boundaries and numerous quadruple junctions were found (Figure 4.1b). These flattened grains, aligned grain boundaries and quadruple junctions were only found in the finest grained parts of the glacial ice, which could well indicate that these layers deform by a similar mechanism as in the GSS deformation experiments of Goldsby and Kohlstedt (1997, 2001).

4.5.6 Dominance of GBS-limited creep over dislocation creep

The results obtained using the original flow law parameters (Table 4.1) show that dislocation creep contributes more to bulk strain rate than GBS-limited creep in the Holocene ice, while in the glacial ice the dominant deformation mechanism depends on the grain size (Figure 4.7). The results using the modified flow law parameters (Table 4.2) suggest that ice deformation in the upper 2207 m of depth in the NEEM ice core is almost entirely produced by GBS-limited creep (Figure 4.8). However, there is evidence that significant non-basal slip is activated in the polar ice sheets (e.g. Weikusat et al., 2009a, b, 2011, 2017; Chapter 2 and 3). Goldsby (2006) compared the results of the composite flow law using the original flow law parameters (Table 4.1) to the grain size and strain rate variability with depth in the basal layer of the Meserve glacier, Antarctica (Cuffey et al., 2000b). It was found that the composite flow law overestimates the contribution of GBS-limited creep in the basal part of the Meserve glacier. The in-situ temperature (256K) and the estimated shear stress (0.05 MPa) in the basal layer of the Meserve glacier are fairly similar to the temperature and stress estimated for the glacial ice in the NEEM ice core (Figure 4.8c). With the modified flow law parameters for dislocation creep (Table 4.2), the calculated contribution of GBS-limited creep to total strain rate would be close to 100%, which is similar to the results with the NEEM ice core (Figure 4.8). Therefore, it is proposed that the composite flow law severely underestimates the strain rate produced by dislocation creep, as high stresses of about 0.25 MPa are required for dislocation creep to

become roughly as fast as GBS-limited creep in the NEEM ice core (Figure 4.10a). This while the large and interlocking grains in the Holocene ice of the NEEM ice core (Figure 4.1a) argue against GBS as the dominant accommodating mechanism for basal slip. The results using the original flow law parameters (Table 4.1), where dislocation creep is the dominant deformation mechanism in the Holocene ice (Figure 4.7), agrees well with the ice microstructures (Figure 4.1a). However, in order for dislocation creep to be as fast as GBS-limited creep in the Holocene ice with the modified flow law parameters (Table 4.2), a strain rate increase of about an order of magnitude for dislocation creep is needed.

The deformation experiments in the GSI and GSS regime of Goldsby and Kohlstedt (1997, 2001) were performed at low temperature in order to prevent grain growth during the deformation experiments. Significant grain growth during the deformation experiments would have complicated the derivation of the flow law parameters in the GSS creep regime. Goldsby and Kohlstedt (1997) stated that “grains in deformed samples were equiaxed with straight grain boundaries; irregular grain boundaries typical of dynamical recrystallization by grain boundary migration were not observed”. However, suppressing SIBM during the deformation experiments also meant that SIBM could not remove strain incompatibilities at grain boundaries and/or triple junctions. SIBM is considered an important softening mechanism in polar ice (e.g. Duval et al., 2000; Montagnat and Duval, 2000; 2004; Chapter 3). It is well established that SIBM is active at all depths in polar ice cores (e.g. Weikusat et al., 2009b), although the amount of SIBM varies strongly with depth (e.g. Duval and Castelnau, 1995; Kipfstuhl et al., 2009; Faria et al., 2014a). In the NEEM ice core, SIBM is probably less extensive in the finer grained glacial ice than in the coarser grained interglacial ice, which is supported by the lower grain boundary curvature in the glacial ice (Binder, 2014; Figure 1.8d). It is therefore proposed that SIBM is an important softening mechanism in the NEEM ice core (Chapter 3), while it was suppressed during the deformation experiments of Goldsby and Kohlstedt (1997, 2001). Therefore, the ice during the GSI deformation experiments of Goldsby and Kohlstedt (2001) was likely relatively hard as it was not softened by SIBM. This would have affected the flow law parameters that were derived from the results of these deformation experiments, potentially underestimating dislocation creep strain rates when using the composite flow law.

4.6 Conclusions

In order to study the effect of grain size and grain size variation with depth in polar ice sheets, the composite flow law of Goldsby and Kohlstedt (2001) was used with temperature and grain size data from the upper 2207 m of depth in the NEEM ice core. GSS deformation was described using a mean grain size and a grain size distribution in combination with two model end members: the micro-scale constant stress model and the micro-scale constant strain rate model. A modification of the flow law parameters for dislocation creep (GSI) in the composite flow law showed a better fit with the experimental data obtained during the deformation experiments of Goldsby and Kohlstedt (1997, 2001).

The results using the original flow law parameter showed that dislocation creep is the dominant deformation mechanism in the Holocene ice, while GBS-limited creep and dislocation creep have roughly the same strength in the glacial ice. The results using the modified flow law parameters show that GBS-limited creep produces almost all deformation in the upper 2207 m of depth in the NEEM ice core. The difference between the model end members is relatively small with the micro-scale constant stress model predicting higher strain rates than the micro-scale constant strain rate model and using a mean grain size. A strain rate increase, mainly resulting from a reduction in grain size, is observed below 1400 m of depth for all model end members. Two depths in the glacial ice with a higher strain rate, caused by enhanced GBS-limited creep, are identified at about 1980 m and 2100 m of depth. This variability in strain rate in the fine grained glacial ice could be important for ice sheet dynamics and can only be modelled using a GSS flow law.

At the grain size and temperature conditions of the NEEM ice core, GBS-limited creep is the dominant deformation mechanism over dislocation creep for equivalent stresses up to about 0.25 MPa. At higher stresses, which are only reached at the margins of the polar ice sheets, dislocation creep is dominant over GBS-limited creep. At low stresses of about 0.01 MPa, the composite flow law predicts a faster strain rate than Glen's flow law. However, the stress exponent of Glen's flow law is higher than the effective stress exponent for the composite flow law and therefore the strain rate increase with increasing stress is higher for Glen's flow law than for the composite flow law. At NEEM grain size and temperature conditions, Glen's flow law predicts a higher strain rate than the composite flow law at equivalent stresses higher than 0.05 MPa.

Dislocation creep with the modified flow law parameters in the composite flow law under NEEM temperatures, grain sizes and stresses is remarkably slow, both in absolute strain rate and compared to the strain rate predicted by GBS-limited creep. One possible explanation for this is that SIBM was not active during the experiments of Goldsby and Kohlstedt (1997, 2001), while SIBM is an important softening mechanism in polar ice.

References

- Alley, R. B. (1992) Flow-law hypothesis for ice-sheet modelling. *Journal of Glaciology*, 38, 129, 245-256.
- Alley, R. B., Clark, P. U., Huybrechts, P., Joughin, I. (2005) Ice-Sheet and Sea-Level changes. *Science*, 310, 456-460, doi: 10.1126/science.1114613.
- Ashby, M. F., Duval, P. (1985) The creep of polycrystalline ice. *Cold Regions Science and Technology*, 11, 285-300.
- Azuma, N. (1994) A flow law for anisotropic ice and its application to ice sheets. *Earth and Planetary Science Letters*, 128, 601-614, doi: 10.1016/0012-821X(94)90173-2.
- Baker, R. W. (1981) Textural and Crystal-Fabric Anisotropies and the Flow of Ice Masses. *Science, New Series*, 211, 4486, 1043-1044.
- Barnes, P., Tabor, D., Walker, J. C. F. (1971) The friction and creep of polycrystalline ice. *Proceedings Royal Society London A*, 324, 1557, 127-155.

- Binder, T., Weikusat, I., Freitag, J., Garbe, C. S., Wagenbach, D., Kipfstuhl, S. (2013) Microstructure through an ice sheet. *Materials Science Forum*, 753, 481-484, doi: 10.4028/www.scientific.net/MSF.753.481.
- Binder, T. (2014) Measurements of grain boundary networks in deep polar ice cores – A digital image processing approach. PhD thesis, University of Heidelberg, Germany.
- Bintanja, R. (2009) *Glacier Science and environmental change* (eds. by P. G. Knight). pp. 174-176. Blackwell, Oxford.
- Bons, P. D., Kleiner, T., Llorens, M.-G., Prior, D. J., Sachau, T., Weikusat, I., Jansen, D. (2018) Greenland Ice Sheet: Higher Nonlinearity of ice Flow Significantly Reduces Estimated Basal Motion. *Geophysical Research Letters*, 45, 1-7, doi: 10.1029/2018GL078356.
- Budd, W. F., Jacka, T. H. (1989) A review of ice rheology for ice sheet modelling. *Cold Regions Science and Technology*, 16, 107-144, doi: 10.1016/0165-232X(89)90014-1.
- Chauve, T., Montagnat, M., Piazzolo, S., Journaux, B., Wheeler, J., Barou, F., Mainprice, D., Tommasi, A. (2017) Non-basal dislocations should be accounted for in simulating ice mass flow. *Earth and Planetary Science Letters*, 473, 247-255, doi: 10.1016/j.epsl.2017.06.020.
- Church, J. et al. (2013). "Climate Change 2013: The Physical Science Basis. Contribution of Working Group I to the Fifth Assessment Report of the Intergovernmental Panel on Climate Change". Ed. by T. Stocker et al. Cambridge University Press, Cambridge, United Kingdom and New York, NY, USA. Chap. Sea Level Change (cit. on p. 1).
- Cuffey, K. M., Conway, H., Gades, A., Hallet, B., Raymond, C. F., Whitlow, S. (2000b) Deformation properties of subfreezing glacier ice: Role of crystal size, chemical impurities, and rock particles inferred from in situ measurements. *Journal of Geophysical Research*, 105, B12, 27895-27915, doi: 10.1029/2001JB900014.
- Cuffey, K. M., Thorsteinsson, T., Waddington, E. D. (2000a) A renewed argument for crystal size control of ice sheet strain rates. *Journal of Geophysical Research*, 105, B12, 27889-27894, doi: 10.1029/2000JB900270.
- Dahl-Jensen, D. (1989a) Two-dimensional thermo-mechanical modelling of flow and depth-age profiles near the ice divide in central Greenland. *Annals of Glaciology*, 12, 31-36.
- Dahl-Jensen, D. (1989b) Steady Thermomechanical flow along two-dimensional flow lines in large grounded ice sheets. *Journal of Geophysical research*, 94, B8, 10355-10362, doi: 10.1029/JB094iB08p10355.
- Dahl-Jensen, D., Gundestrup, N. S. (1987) Constitutive properties of ice at Dye 3. Greenland, *The Physical Basis of Ice Sheet Modelling*, 170, 31-40.
- Dansgaard, W., Johnsen, S. J. (1969) A flow model and a time scale for the ice core from camp century, Greenland. *Journal of Glaciology*, 8, 53, 215-223, doi: 10.3189/S0022143000031208.
- De la Chapelle, S., Milsch, H., Castelnau, O., Duval, P. (1999) Compressive creep of ice containing a liquid intergranular phase: rate-controlling processes in the dislocation creep regime. *Geophysical Research Letter*, 26, 2, 251-254, doi: 10.1029/1998GL900289.
- Drury, M. R., Avé Lallemant, H. G., Pennock, G. M., Palasse, L. N. (2011) Crystal preferred orientation in peridotite ultramylonites deformed by grain size sensitive creep,

- Étang de Lers, Pyrenees, France. *Journal Structural Geology*, 33, 12, 1776-1789, doi: 10.1016/j.jsg.2011.10.002.
- Durham, W. B., Prieto-Ballesteros, O., Goldsby, D. L., Kargel, J. S. (2010) Rheological and Thermal Properties of Icy Materials. *Space Science Reviews*, 153, 273-298, doi:10.1007/s11214-009-9619-1.
- Durham, W. B., Stern, L. A. (2001) Rheological Properties of Water Ice – Applications to satellites of the Outer Planets. *Annual Review of Earth and Planetary Science*, 29, 295-330.
- Duval, P., Arnaud, L., Brissaud, O., Montagnat, M., de la Chapelle S. (2000) Deformation and recrystallization processes of ice from polar ice sheets. *Annals of Glaciology*, 30, 83-87, doi: 10.3189/172756400781820688.
- Duval, P., Ashby, M. F., Anderman, I. (1983) Rate-controlling processes in the creep of polycrystalline ice. *Journal of Physical Chemistry*, 87, 21, 4066-4074, doi: 10.1021/j100244a014.
- Duval, P., Castelnau, O. (1995) Dynamic recrystallization of ice in polar ice sheets. *Journal de Physique III*, 05, C3, 197-205, doi: 10.1051/jp4:1995317.
- Eichler, J., Kleitz, I., Bayer-Giraldi, M., Jansen, D., Kipfstuhl, S., Shigeyama, W., Weikusat, C., Weikusat, I. (2017) Location and distribution of micro-inclusions in the EDML and NEEM ice cores using optical microscopy and in situ Raman spectroscopy. *The Cryosphere*, 11, 3, 1075-1090, doi: 10.5194/tc-11-1075-2017.
- Eichler, J., Weikusat, I., Kipfstuhl, S. (2013): Orientation-tensor eigenvalues along the NEEM ice core. *PANGAEA*, <https://doi.org/10.1594/Pangaea.838059>.
- Faria, S. H., Freitag, J., Kipfstuhl, S. (2010) Polar ice structure and the integrity of ice-core paleoclimate records. *Quaternary Science Reviews*, 29, 1-2, 338-351, doi: 10.1016/j.quascirev.2009.10.016.
- Faria, S. H., Weikusat, I., Azuma, N. (2014a) The microstructure of polar ice. Part II: State of the art. *Journal of Structural Geology*, 61, 21-49, doi: 10.1016/j.jsg.2013.11.003.
- Faria, S. H., Weikusat, I., Azuma, N. (2014b) The microstructure of polar ice. Part I: Highlights from ice core research. *Journal of Structural Geology*, 61, 2-20, doi: 10.1016/j.jsg.2013.09.010.
- Freeman, B., Ferguson, C. (1986) Deformation mechanism maps and micromechanics of rocks with distributed grain sizes. *Journal of Geophysical Research*, 91, B3, 3849-3860, doi: 10.1029/JB091iB03p03849.
- Fisher, D. A., Koerner, R. M. (1986) On the special rheological properties of ancient microparticle-laden northern hemisphere ice as derived from bore-hole and core measurements. *Journal of Glaciology*, 32, 112, 501-510.
- Fitzpatrick, J. J., Voigt, D. E., Fegyveresi, J. M., Stevens, N. T., Spencer, M. K., Cole-dai, J., Alley, R. B., Jardine, G. E., Cravens, E. D., Wilen, L. A., Fudge, T. J., McConnell, J. R. (2014) Physical properties of the WAIS Divide ice core. *Journal of Glaciology*, 60, 224, 1181-1198, doi: 10.3189/2013JoG14j100.
- Gifkins, R. C. (1976) Grain-Boundary Sliding and its accommodation During Creep and Superplasticity. *Metallurgical Transactions A*, 7, 1225-1232.
- Gillet-Chaulet, F., Hindmarsh, R. C. A., Corr, H. F. J., King, E. C., Jenkins, A. (2011) In-situ quantification of ice rheology and direct measurement of the Raymond Effect at

Summit, Greenland using a phase-sensitive radar. *Geophysical Research Letter*, 38, 24, 1-6, doi: 10.1029/2011GL049843.

Glen, J. W. (1952) Experiments on the deformation of ice. *Journal of Glaciology*, 2, 12, 111-114.

Glen, J. W. (1955) The creep of polycrystalline ice. *Proceedings of the Royal Society A: Mathematical, Physical and Engineering Sciences*, 228, 1175, 519-538, doi: 10.1098/rspa.1955.0066.

Goldsby, D. L., Kohlstedt, D. L. (1997) Grain boundary sliding in fine grained ice I. *Scripta Materialia*, 37, 9, 1399-1406.

Goldsby, D. L., Kohlstedt, D. L. (2001) Superplastic deformation of ice: Experimental observations. *Journal of Geophysical Research*, 106, B6, 11017-11030, doi: 10.1029/2000JB900336.

Goldsby, D. L., Kohlstedt, D. L. (2002) Reply to comment by P. Duval and M. Montagnat on "Superplastic deformation of ice: Experimental observations". *Journal of Geophysical Research*, 107, B11, 1-5, doi: 10.1029/2002JB001842.

Goldsby, D. L. (2006) Superplastic flow of ice relevant to glacier and ice-sheet mechanics. In Knight, P. G., editor, *Glacier Science and Environmental Change*. 308-314. Blackwell Publishing.

Gow, A. J., Meese, D. A., Alley, R. B., Fitzpatrick, J. J., Anandkrishnan, S., Woods, G. A., Elder, B. C. (1997) Physical and structural properties of the Greenland Ice Sheet Project 2 ice core: A review. *Journal of Geophysical Research*, 102, C12, 26559-26575, doi: 10.1029/97JC00165.

Greve, R., Blatter, H. (2009) *Dynamics of ice sheets and glaciers*. Springer Berlin/Heidelberg.

Hansen, L. N., Zimmerman, M. E., Kohlstedt, D. L. (2011) Grain boundary sliding in San Carlos olivine: Flow law parameters and crystallographic-preferred orientation. *Journal of Geophysical Research: Solid Earth*, 116, 8, 1-16, doi: 10.1029/2011JB008220.

Hansen, L. N., Zimmerman, M. E., Kohlstedt, D. L. (2012) The influence of microstructure on deformation of olivine in the grain-boundary sliding regime. *Journal of Geophysical Research: Solid Earth*, 117, 9, 1-17, doi: 10.1029/2012JB009305.

Heilbronner, R., Bruhn, D. (1998) The influence of three-dimensional grain size distributions on the rheology of polyphaser rocks. *Journal of structural Geology*, 20, 6, 695-705, doi: 10.1016/S0191-8141(98)00010-8.

Herwegh, M., Bresser, J. H. P., Ter Heege, J. H. (2005) Combining natural microstructures with composite flow laws: an improved approach for the extrapolation of lab data to nature. *Journal of Structural Geology*, 27, 503-521, doi: 10.1016/j.jsg.2004.10.010.

Hondoh, T., Iwamatsu, H., Mae, S. (1990) Dislocation mobility for nonbasal glide in ice measured by in-situ x-ray topography. *Philosophical Magazine A*, 62, 89-102, doi: 10.1018/01418619008244337.

Hondoh, T. (2000) Nature and behavior of dislocations in the ice. In: Hondoh, T. (Ed.), *Physics of Ice Core Records*, Hokkaido University Press, Sapporo, 3-24.

Hondoh, T. (2009) An Overview of Microphysical Processes in Ice Sheets: Towards Nanoglaciology, *Low Temperature Science Suppl. Issue*, 68.

- Hutchinson, J. W. (1977) Creep and Plasticity of Hexagonal Polycrystals as Related to Single Crystal Slip. *Metallurgical Transactions A*, 8, 9, 1465-1469, doi: 10.1007/BF02642860.
- Hutter, K. (1983) *Theoretical glaciology; material science of ice and the mechanics of glaciers and ice sheets*. Reidel Publishing Co., Dordrecht, Terra Scientific Publishing Co, Tokyo.
- Huybrechts, P. (2007) Ice sheet modelling, *Encyclopedia of the Antarctic* (ed. by Riffenburgh, B.), pp 514-417. Routledge. New York and London.
- IPCC. (2014) *Climate change 2014: Synthesis report. contribution of working groups i, ii, iii to the fifth assessment report of the intergovernmental panel on climate change*, IPCC, Geneva, Switzerland, 151.
- Jansen, D., Llorens, M.-G., Westhoff, J., Steinbach, F., Kipfstuhl, S., Bons, P. D., Griera, A., Weikusat, I. (2016) Small-scale disturbances in the stratigraphy of the NEEM ice core: observations and numerical simulations. *The Cryosphere*, 10, 359-370, doi: 10.5194/tc-10-359-2016.
- Kipfstuhl, S. (2010) Large area scan macroscope images from the NEEM ice core. Alfred Wegener Institute, Helmholtz Centre for Polar and Marine Research, Bremerhaven, Pangaea, <https://doi.pangaea.de/10.1594/PANGAEA.743296> (unpublished dataset).
- Kipfstuhl, S., Faria, S. H., Azuma, N., Freitag, J., Hamann, I., Kaufmann, P., Miller, H., Weiler, K., Wilhelms, F. (2009) Evidence of dynamic recrystallization in polar firn. *Journal of Geophysical Research*, 114, 5, 1-10, doi: 10.1029/2008JB005583.
- Kipfstuhl, S., Hamann, I., Lambrecht, A., Freitag, J., Faria, S. H., Grigoriev, D., Azuma, N. (2006) Microstructure mapping: a new method for imaging deformation induced microstructural features of ice on the grain scale, *Journal of Glaciology*, 52, 178, 398-406, doi: 10.3189/172756506781828647.
- Kirby, S., Durham, W., Beeman, M., Heard, H., Daley, M. (1987) Inelastic properties of ice I_h at low temperatures and high pressures. *Journal de Physique Colloques*, 48, C1, 227-232, doi: 10.1051/jphyscol:1987131.
- Krischke, A., Oechsner, U., Kipfstuhl, S. (2015) Rapid Microstructure Analysis of Polar Ice Cores. *Optik & Photonik*, 10, 2, 32-35, doi: 10.1002/opph.201500016.
- Marshall, S. J. (2006) Modelling glacier response to climate change. In Knight, P. G., editor, *Glacier Science and Environmental Change*. 163-173. Blackwell Publishing.
- Mellor, M., Testa, R. (1969a) Creep of ice under low stress. *Journal of Glaciology*, 8, 52, 147-152.
- Mellor, M., Testa, R. (1969b) Effect of temperature on the creep of ice. *Journal of Glaciology*, 8, 52, 131-145.
- Montagnat, M., Azuma, N., Dahl-Jensen, D., Eichler, J., Fujita, S., Gillet-Chaulet, F., Kipfstuhl, S., Samyn, D., Svenson, A., Weikusat, I. (2014) Fabric along the NEEM ice core, Greenland, and its comparison with GRIP and NGRIP ice core. *The Cryosphere*, 8, 1129-1138, doi: 10.5194/tc-8-1129-2014.
- Montagnat, M., Duval, P. (2000) Rate controlling processes in the creep of polar ice, influence of grain boundary migration associated with recrystallization. *Earth and Planetary Science Letter*, 183, 1-2, 179-186, doi: 10.1016/S0012-821X(00)00262-4.

Montagnat, M., Duval, P. (2004) Dislocations in ice and Deformation Mechanisms: from Single Crystals to Polar Ice. *Defect and Diffusion Forum*, 229, 43-54.

Morgan, V. I. (1991) High-Temperature ice creep tests. *Cold Regions Science and Technology*, 19, 295-300.

NEEM community members. (2013) Eemian interglacial reconstructed from a Greenland folded ice core. *Nature*, 493, 489-494, doi: 10.1038/nature11789.

Obbard, R., Baker, I, Sieg, S. (2006) Using electron backscatter diffraction patterns to examine recrystallization in polar ice sheets. *Journal of Glaciology*, 52, 179, 546-557.

Paterson, W. S. B. (1991) Why ice-age ice is sometimes “soft”. *Cold Regions Science and Technology*, 20, 1, 75-98, doi: 10.1016/0165-232X(91)90058-O.

Paterson, M. S., Olgaard, D. L. (2000) Rock deformation tests to large shear strains in torsion. *Journal of Structural Geology*, 22, 9, 1341-1358, doi: 10.1016/S0191-8141(00)00042-0.

Paterson, W. S. B. (1994) *The physics of glaciers*, Third edition. Oxford, Elsevier.

Peltier, W. R., Goldsby, D. L., Kohlstedt, D. L., Tarasov, L. (2000) Ice-age ice-sheet rheology: constraints from the Last Glacial Maximum form of the Laurentide ice sheet. *Annals of Glaciology*, 30, 163-176, doi: 10.3189/172756400781820859.

Petrenko, V. F., Withworth, R. W. (1999) *Physics of ice*. Oxford University Press, Oxford.

Piazolo, S., Montagnat, M., Grennerat, F., Moulinec, H., Wheeler, J. (2015) Effect of local stress heterogeneities on dislocation fields: Examples from transient creep in polycrystalline ice. *Acta Materialia*, 90, 303-309, doi: 10.1016/j.actamat.2015.02.046.

Pimienta, P., Duval, P. (1987) Rate controlling processes in the creep of polar glacier ice. *Journal de Physique Colloques*, 48, C1, 243-248, doi: 10.1051/jphyscol:1987134.

Rasmussen, S. O., Abbott, P. M., Blunier, T., Bourne, A. J., Brook, E., Buchardt, S. L., Buizert, C., Chappellaz, J., Clausen, H. B., Cook, E., Dahl-Jensen, D., Davies, S. M., Guillevic, M., Kipfstuhl, S., Laepple, T., Seierstad, I. K., Severinghaus, J. P., Steffensen, J. P., Stowasser, C., Svensson, A., Vallelonga, P., Vinther, B. M., Wilhelms, F., Winstrup, M. (2013) A first chronology for the North Greenland Eemian Ice Drilling (NEEM) ice core. *Climate of the Past*, 9, 2713-2730, doi: 10.5194/cp-9-2713-2013.

Raymond, C. F. (1983) Deformation in the vicinity of ice divides. *Journal of Glaciology*, 29, 103, 357-373.

Rutter, E. H., Casey, M., Burlini, L. (1994) Preferred crystallographic orientation development during the plastic and superplastic flow of calcite rocks. *Journal of Structural Geology*, 16, 10, 1431-1446, doi: 10.1016/0191-8141(94)90007-8.

Schmid, S. M., Pazonno, R., Bauer, S. (1987) Simple shear experiments on calcite rocks: Rheology and microfabric, *Journal of Structural Geology*, 9, 5-6, 747-778, doi: 10.1016/0191-8141(87)90157-X.

Schultson, E. M., Duval, P. (2009) *Creep and Fracture of Ice*. Cambridge University Press.

Sergienko, O. V., Creyts, T. T., Hindmarsh, R. C. A. (2014) Similarity of organized patterns in driving and basal stresses of Antarctic and Greenland ice sheets beneath extensive areas of basal sliding. *Geophysical Research Letter*, 41, 11, 3925-3932, doi: 10.1002/2014GL059976.

- Sheldon, S. G., Steffensen, J. P., Hansen, S. B., Popp, T. J., Johnson, S. J. (2014) The investigation and experience of using ESTISOL™ 240 and COASOL™ for ice-core drilling. *Annals of Glaciology*, 55, 68, 219-232, doi:10.3189/2014AoG68A036.
- Stern, L. A., Durham, W. B., Kirby, S. H. (1997) Grain-size-induced weakening of H₂O ice I and II and associated anisotropic recrystallization. *Journal of Geophysical Research*, 102, B3, 5313-5325.
- Ter Heege, J. H., De Bresser, J. H. P., Spiers, C. J. (2004) Composite flow laws for crystalline materials with log normally distributed grain size: theory and application to olivine. *Journal Structural Geology*, 26, 1693-1705, doi: 10.1016/j.jsg.2004.01.008.
- Thoma, M., Grosfeld, K., Mayer, C., Pattyn, F. (2010) Interaction between ice sheet dynamics and subglacial lake circulation: a coupled modelling approach. *The Cryosphere*, 4, 1, 1-12. doi: 10.5194/tc-4-1-2010.
- Thorsteinsson, T., Waddington, E.D., Taylor, K. C., Alley, R. B., Blankenship, D. D. (1999) Strain-rate enhancement at Dye 3, Greenland. *Journal of Glaciology*, 45, 150, 338-345, doi: 10.3189/002214399793377185.
- Treverrow, A., Budd, W. F., Jacka, T. H., Warner, R. C. (2012) The tertiary creep of polycrystalline ice: experimental evidence for stress-dependent levels of strain-rate enhancement. *Journal of Glaciology*, 58, 208, 301-314, doi: 10.3189/2012JoG11J149.
- Vaughan, D. G., Arthern, R. (2007) Why is it hard to predict the future of ice sheets? *Science*, 315, 1503-1504, doi: 10.1126/science.1141111.
- Von Mises, R. (1928) *Mechanik der Plastischen Formänderung von Kristallen*. *Zeitschrift für Angewandte Mathematik und Mechanik*, 8, 161-185.
- Waddington, E. D. (2010) Life, death and afterlife of the extrusion flow theory. *Journal of Glaciology*, 56, 200, 973-996, doi: 10.3189/002214311796406022.
- Weertman, J. (1983) Creep deformation of ice. *Annual Review of Earth and Planetary Sciences*, 11, 215-240.
- Weikusat, I., Kipfstuhl, S., Azuma, N., Faria, S. H., Miyamoto, A. (2009a) Deformation microstructures in an Antarctic ice core (EDML) and in experimentally deformed artificial ice. *Physics of Ice Core Records II*, 68, 115-123.
- Weikusat, I., Kipfstuhl, S., Faria, S. H., Azuma, N., Miyamoto, A. (2009b) Subgrain boundaries and related microstructural features in EDML (Antarctica) deep ice core. *Journal of Glaciology*, 55, 191, 461-472.
- Weikusat, I., Kuiper, E. N., Pennock, G. M., Kipfstuhl, S., Drury, M. R. (2017) EBSD analysis of subgrain boundaries and dislocation slip systems in Antarctic and Greenland ice. *Solid Earth*, 8, 883-898, doi: 10.5194/se-8-883-2017.
- Weikusat, I., Miyamoto, A., Faria, S. H., Kipfstuhl, S., Azuma, N., Hondoh, T. (2011) Subgrain boundaries in Antarctic ice quantified by X-ray Laue diffraction. *Journal of Glaciology*, 57, 201, 85-94, doi: 10.3189/002214311795306628.
- Wolovick, M. J., Creyts, T. T. (2016) Overtaken folds in ice sheets: Insight from a kinematic model of travelling sticky patches and comparisons with observations. *Journal of Geophysical Research: Earth Surface*, 121, 5, 1065-1083, doi: 10.1002/2015JF003698.
- Zhang, Y., Hobbs, B. E., Jessell, M. W. (1994) The effect of grain-boundary sliding on fabric development in polycrystalline aggregates. *Journal of Structural Geology*, 16, 9, 1315-1325, doi: 10.1016/0191-8141(94)90072-8.

Zwally, H. J., Abdalati, W., Herring, T., Larson, K., Saba, J., Steffen, S. (2002) Surface Melt-Induced Acceleration of Greenland Ice-Sheet Flow. *Science*, 297, 218-223, doi: 10.1126/science.1072708.

Using a composite flow law to investigate the role of grain size and premelting on ice deformation at high homologous temperature in the lower part of the NEEM ice core, Greenland.

After:

Kuiper, E. N., de Bresser, J. H. P., Drury, M. R., Eichler, J., Pennock, G. M., Weikusat, I. Using a composite flow law to model deformation in the NEEM deep ice core, Greenland: Part 2 the role of grain size and premelting on ice deformation at high homologous temperature. *Submitted to the Cryosphere.*

Abstract

Ice microstructure studies along many different polar ice cores have shown that in the lowest hundreds of meters of polar ice sheets, at temperatures close to the melting point, grains can become very coarse and have a strongly interlocking grain boundary structure with a multi maxima crystallographic preferred orientation (CPO). In some polar ice cores, like the North Greenland Eemian Ice Drilling (NEEM) ice core, these coarse grained impurity-depleted interglacial layers are alternated by much finer grained impurity-rich layers consisting of glacial ice with a single maximum CPO. The difference in grain size, grain shape and CPO between these layers can potentially have a large influence on the dominant deformation mechanism and strain rate. In this Chapter, Glen's flow law (Glen, 1955, Paterson, 1994) and the grain size sensitive (GSS) composite flow law of Goldsby and Kohlstedt (2001) were used to study the effects of grain size and premelting on strain rate in the lower part of the NEEM ice core. In addition, an analysis of ice microstructure and CPO in the different layers is compared with the predictions obtained from flow law calculations. The temperature threshold for the onset of premelting in polar ice sheets was evaluated and set at 262 K. The original composite flow law of Goldsby and Kohlstedt (2001) was modified to take this new premelting temperature threshold into account.

The results using temperature and grain size data from the NEEM ice core show that the effect of grain size variation on strain rate in the lower part of the NEEM ice core is large. In the fine grained glacial layers, the strain rate predicted by the modified composite flow law is about an order of magnitude higher than in the coarse grained interglacial layers. The modified composite flow law also predicts a difference in the dominant deformation mechanism between the fine and coarse grained layers with basal slip accommodated by grain boundary sliding (GBS-limited creep) producing virtually all strain in the fine grained layers, while GBS-limited creep and dislocation creep (basal slip accommodated by non-basal slip) contribute roughly equally to bulk strain rate in the coarse grained layers. The strain rate predicted by Glen's flow law, which is grain size independent, is not affected by the grain size variation and predicts a higher strain rate than the modified composite flow law in all of the lowest 540 m of depth in the NEEM ice core.

In the lower part of the NEEM ice core, changes in grain size correlate strongly with type and strength of CPO. The impurity-rich fine grained glacial layers have a strong single maximum CPO, while the impurity-depleted coarse grained interglacial layers have a partial girdle type of CPO. Deformation experiments have shown that the difference in CPO makes the fine grained glacial layers relatively soft in simple shear, whereas the coarse grained interglacial layers are softer in coaxial deformation. Therefore, strain partitioning is expected in the lower part of the NEEM ice core, with the fine grained layers mainly deforming by simple shear, while the coarse grained layers deform mainly by coaxial deformation or are relatively stagnant. The microstructural difference, and consequently the difference in viscosity, between glacial and interglacial ice at temperatures just below the melting point in polar ice sheets can have important consequences for ice dynamics close to the bedrock.

5.1 Introduction

As a consequence of anthropogenic global warming, it is expected that global mean sea level (GMSL) rise will accelerate in the next decades and centuries (e.g. IPCC, 2014; Kopp et al., 2017). To improve the predictions in GMSL rise, the flow of ice in polar ice sheet models should be accurately described, since it is expected that the melting of the polar ice sheets will contribute significantly to future GMSL rise (IPCC, 2014). Therefore, a full understanding and description of ice deformation mechanisms in polar ice sheets is required. Ice in the lower part of polar ice sheets is of particular interest. Generally, this ice is expected to deform much faster than the shallower ice, due to the well-developed crystallographic preferred orientation (CPO) and relatively high temperatures near the bedrock. However, stress and strain rates near the bedrock can vary considerably due to the influence of bedrock variations, slippery patches or subglacial lakes (e.g. Budd and Rowden-rich, 1985; Gudlaugsson et al., 2016). The high variation in deformation rates in the ice near the bedrock are often shown by borehole surveys (e.g. Gow and Williamson, 1976; Paterson, 1983; Thorsteinsson et al., 1999; Weikusat et al., 2017). The main source of heat of the ice near the bedrock is geothermal heat, which typically has a strength of 50-100 mW m⁻² (Rogozhina et al., 2016). Locally, other sources of heat can be important, like shear heating (e.g. Krabbendam, 2016) or latent heat released by refreezing of melt water coming from the surface that drained into the interior of the ice sheet (e.g. Zwally et al., 2002; Van de Wal et al., 2008; Catania and Neumann, 2010).

Ice deformation experiments have shown that the effect of temperature on the strain rate of ice can be described via a calibrated Arrhenius type flow law relating equivalent strain rate to equivalent stress and temperature (e.g. Glen, 1955; Homer and Glen, 1978; Morgan, 1991). However, at temperatures close to the melting point, the strain rate increase has been found to be higher than predicted by the extrapolation of lower temperature results using the Arrhenius relation, inferred to be due to the initiation of a new high temperature deformation mechanism or to the enhancement of the original one. To account for the latter, a higher activation energy is often used above a certain temperature threshold (e.g., Mellor and Testa, 1969; Barnes et al., 1971; Paterson, 1994; Goldsby and Kohlstedt, 2001). This higher activation energy, which is the result of a simple best-fit approach of temperature and strain rate using a Arrhenius type relation, lacks a good link with the controlling deformation mechanism, assumed to be intracrystalline dislocation motion. Therefore, its application is not well founded. In experiments on ice single crystals and bicrystals close to the melting point (Homer and Glen, 1978; Jones and Brunet, 1978), a strong strain rate increase has not been observed. This strongly suggests that the strain rate enhancement in natural ice close to the melting point is related to the occurrence of grain boundaries.

Premelting along grain boundaries has often been stated as being responsible for the high strain rates during ice deformation tests at high temperatures (e.g. Mellor and Testa, 1969; Dash et al., 1995, 2006; Wilson et al., 1996; Wilson and Zhang, 1996). Premelting is expected to initiate at surfaces or interfaces such as grain boundaries where

the crystallographic structure is disrupted and molecules can adopt water-like qualities at temperatures below the melting point (e.g. Orem and Adamson, 1969; Barnes et al., 1971; Dash et al., 1995, 2006; Döppenschmidt et al., 1998). High temperature deformation tests on polycrystalline ice have shown that a small liquid-like amorphous layer at the grain boundary increases grain boundary mobility by two to four orders of magnitudes (Duval and Castelnau, 1995; Schulson and Duval, 2009). Contrary to almost all other materials, grain boundary melting in ice at high cryostatic pressure is a thermodynamically favorable process as grain boundary melting causes a negative volume change of about 9% due to the low atomic packing factor of hexagonal ice (e.g. Schulson and Duval, 2009).

The different activation energy reflecting the onset of premelting is used widely at a temperature threshold of -10°C (263K) when applying Glen's flow law in ice sheet models (e.g. Paterson, 1994), but a higher temperature threshold of -8°C (285K) (Barnes et al., 1971) or lower temperature thresholds of -15°C (258K) to -18°C (255K) (Goldsby and Kohlstedt, 2001) should be considered. As temperature generally increases with depth in polar ice sheets, the temperature where premelting starts to affect ice rheology is important. A low premelting temperature would mean that a considerable larger portion of the ice is affected by premelting, hence will show strain rate enhancement over a larger range, compared to a higher temperature threshold.

At temperatures close to the melting point in the lower part of polar ice cores, a particular type of microstructure with very coarse grains and interlocking grain boundaries is often found (e.g. Gow and Williams, 1976; Gow and Engelhardt, 2000; NEEM community members, 2013; Weikusat et al., 2017). In the lower part of the North Greenland Eemian Ice Drilling (NEEM) ice core such regions of coarse, interlocking grains are alternated by regions of finer grains (NEEM community members, 2013). In case of the NEEM ice core, the alternated layers of fine and coarse grained ice are the results of stratigraphic disruptions and overturned folds, which consist of impurity-rich glacial ice from the penultimate glacial period and impurity-depleted Eemian interglacial ice (NEEM community members, 2013).

These coarse grained layers at the bottom of some polar ice cores typically possess CPOs that could be described as a multi maxima, although the exact type of CPO is often unclear due to the low number of grains measured in individual thin sections. The coarse grains and multi maxima CPO are thought to be the result of rapid strain induced boundary migration (SIBM) in combination with the nucleation of new grains (SIBM-N) (e.g. Alley, 1992; Duval and Castelnau, 1995; Durand et al., 2009; Faria et al., 2014). SIBM is the migration of grain boundaries driven by the difference in stored strain energy between neighbouring grains that result from lattice distortions such as dislocations (Humphreys and Hatherly, 2004). SIBM starts in firn (Kipfstuhl et al., 2006, 2009) and is assumed to increase grain size (e.g. Duval and Castelnau, 1995), although under certain conditions SIBM can also be a grain size reducing mechanism by grain dissection (Steinbach et al., 2017). The layers of alternating grain size in deeper NEEM samples allows for the study of the effect of premelting and grain size on strain rate and CPO development.

In this Chapter, the composite flow law of Goldsby and Kohlstedt (2001) was used to explore the effect of grain size on strain rate in the lower part of the NEEM ice core. The composite flow law describes the deformation of polycrystalline ice as a combination of grain size sensitive (GSS) and grain size insensitive (GSI) deformation mechanisms, where the dominant deformation mechanism depends on the temperature, stress and grain size. Compared to Chapter 4, the emphasis in this Chapter is on possible differences in the controlling deformation mechanism close to the melting point instead of ice at lower temperatures. The results from flow law calculations were combined with CPO data to study deformation mechanisms in the lower part of the NEEM ice core. The NEEM ice core was chosen because of the high density of reflective light microscopy (LM) images (Kipfstuhl, 2010; Binder et al., 2013) and the alternation of fine and coarse grained layers in the lower part of the ice core. These reflective LM images were used to determine the change in grain size with depth (Binder, 2014). Furthermore, the CPO data of the NEEM ice core (Eichler et al., 2013) were available. A critical assessment of the temperature threshold for the onset of premelting in polar ice sheets led to a modification of the composite flow law of Goldsby and Kohlstedt (2001). The NEEM ice core data were used to calculate the strain rate predicted by Glen's flow law (Glen, 1952, 1955; Paterson, 1994) and by the modified composite flow law of Goldsby and Kohlstedt (2001) in the lower part of the NEEM ice core. Possible deformation mechanisms are discussed.

5.2 Methods

5.2.1 The NEEM ice core and ice microstructure data

The NEEM ice core, located in the northwest of Greenland (77.45°N, 51.06°W), was drilled during the field seasons of 2008-2012 (NEEM community members, 2013; Rasmussen et al., 2013). The NEEM ice core is 2540 m long with ice deposited during the Holocene (Holocene ice) extending till a depth of 1419 m (Montagnat et al., 2014). Ice deposited during the last glacial period (glacial ice) lies below reaching a depth of 2207 m. The layering below the glacial ice is strongly disturbed and four stratigraphic disruptions were identified at 2209.6 m, 2262.2 m, 2364.5 m and 2432.2 m of depth by discontinuities in oxygen stable isotope values ($\delta^{18}\text{O}_{\text{ice}}$) of H_2O and methane (CH_4) (NEEM community members, 2013). These folded and overturned parts are from the interface between the glacial ice and the Eemian ice, which causes the coarse grained Eemian ice to be alternated with the finer grained glacial ice in the lowest 330 m of depth in the NEEM ice core. In the remainder of this Chapter, the ice from 2207 m of depth till the ice-bedrock interface at 2540 m of depth will be referred to as the 'Eemian-glacial facies'.

The lower part of the glacial ice of the NEEM ice core was included in this study to show the contrast in grain size, CPO and calculated strain rate between the glacial ice and the Eemian-glacial facies. Therefore, the available LM images, orientation images and CPO data below 2000 m of depth were included in this study. Calculations using the GSS composite flow law of Goldsby and Kohlstedt require grain size as an input variable. The grain size data in the lowest 540 m of the NEEM ice core were obtained using 224 large

area scanning microscope (LASM) images (Kipfstuhl, 2010) taken using reflective light microscopy (Krischke et al., 2015). This method uses thermal etching by sublimation to reveal (sub)grain boundaries as grooves on the surface of the ice core sample (e.g. Saylor and Rohrer, 1999) and has a resolution of 5 μm per pixel edge. Each LASM image is about 90 mm long by about 55 mm wide (Kipfstuhl et al., 2006) and was digitally analyzed using the Ice-image software (www.ice-image.org) (Binder et al., 2013; Binder, 2014). The software automatically detects the grain area of each grain by counting the pixels enclosed by grain boundaries. The total area classified as ‘grain’ by the Ice-image software was divided by the number of grains and a mean grain diameter was calculated assuming circular grains. Deriving a full grain size distribution, as was done in Chapter 4, was not possible in the Eemian-glacial facies because the number of grains in the LASM images (90 x 55 mm) of the coarse grained layers was too low. Grains with a diameter <0.3 mm were excluded from the data set as these grains are often artefacts caused by relaxation, especially around air bubbles after ice core retrieval (Figure 4.2). In some parts of the Eemian-glacial facies, the grains grow up to several centimetres and the grain boundaries are irregular with many grain boundary bulges. It is not possible to determine a mean grain size for these ice core sections by the Ice-image software as these grains often cross the edge of the LM images and are therefore not included in the grain size data (Binder, 2014, Figure 4.2). After visual inspection of the LASM images to check the grain size, the ice core sections containing very large grains were assigned a mean grain diameter of 30 mm, which was the estimated grain diameter based on the LASM images.

An automatic Fabric Analyzer (FA) was used to create high-resolution maps of the c-axes orientations. The method is based on the double-refracting properties of the hexagonal ice crystal. It offers a fast alternative for the measurement of crystal orientations, which are, however, limited only to the c-axes. The grains in each orientation image were plotted in a pole figure. For each orientation images the Woodcock parameter was calculated (Woodcock, 1977). The Woodcock parameter is often used in order to distinguish between cluster and girdle type of CPOs. A distribution with a Woodcock parameter >1 indicates a cluster, while a Woodcock parameter <1 indicates a girdle. Further computer-based analysis (Eichler et al., 2013) of the FA-CPO-maps enables the derivation of a variety of microstructural parameters, such as mean grain shape or size. These can be used as complementary values to the LASM analysis data. However, these microstructural parameters can differ significantly from the microstructural parameters obtained by the Ice-image software (www.ice-image.org) (Binder et al., 2013; Binder, 2014). For instance, the mean grain size derived from the orientation images in this study is systematically shifted towards lower values, which is mainly caused by the exclusion of grains with a grain diameter <0.3 mm in the LASM method as was described above. In the remainder of this Chapter, the grain size determined using the Ice-image software (Binder et al., 2013; Binder, 2014) will be used unless stated otherwise.

5.2.2 Flow laws and flow law parameters

One of the two flow laws that was used during this study is the composite flow law of Goldsby and Kohlstedt (2001). The composite flow law was derived during uniaxial deformation tests in secondary creep with very fine grained ice (Goldsby and Kohlstedt, 1997, 2001). The composite flow law combines different deformation mechanisms of ice explicitly, instead of presenting a series of individual flow laws. During their uniaxial deformation experiments on artificial fine grained ice in secondary creep, Goldsby and Kohlstedt (1997, 2001) found four different deformation regimes with the composite flow law formulated as follows:

$$\dot{\epsilon} = \dot{\epsilon}_{disl} + \left(\frac{1}{\dot{\epsilon}_{basal}} + \frac{1}{\dot{\epsilon}_{GBS}} \right)^{-1} + \dot{\epsilon}_{diff}, \quad (5.1)$$

where $\dot{\epsilon}$ is the strain rate and the subscripts refer to basal slip accommodated by non-basal slip or dislocation creep (disl), grain boundary sliding accommodated by basal slip (basal), basal slip accommodated by GBS (GBS) and diffusion creep (diff). Here, basal slip and grain boundary sliding are sequential processes acting together, where the slower mechanism determines the overall strain rate by accommodating the faster mechanism (Durham and Stern, 2001). In other words, $\dot{\epsilon}_{basal}$ is accommodated (i.e., rate-limited) by basal slip, while $\dot{\epsilon}_{GBS}$ is accommodated (rate-limited) by grain boundary sliding. Under stress, grain size and temperature conditions appropriate for terrestrial ice, diffusion creep and grain boundary sliding accommodated by basal slip are not relevant for ice deformation (Goldsby and Kohlstedt, 2001; Goldsby, 2006). Therefore, the composite flow law simplifies to:

$$\dot{\epsilon} = \dot{\epsilon}_{disl} + \dot{\epsilon}_{GBS}, \quad (5.2)$$

where now $\dot{\epsilon}_{GBS}$ refers to basal slip accommodated by GBS (GBS-limited creep). For both GBS-limited creep and dislocation creep it is assumed that basal slip is the main strain producing mechanism. In case of dislocation creep, basal slip is accommodated by non-basal slip, whereas for GBS-limited creep it is assumed that basal slip is accommodated by grain boundary sliding. The accommodating mechanism is the rate-controlling mechanism.

The strain rate produced by creep can be described by the following general flow law:

$$\dot{\epsilon} = A \sigma^n d^{-p} \exp\left(-\frac{Q}{RT}\right), \quad (5.3)$$

where $\dot{\epsilon}$ is the strain rate (s^{-1}), A is a material parameter, σ is the stress (MPa), n is the stress exponent (dimensionless), d is the grain size (m), p is the grain size exponent (dimensionless), Q is the activation energy ($J \text{ mol}^{-1}$), R the gas constant ($J \text{ K}^{-1} \text{ mol}^{-1}$) and T the absolute temperature (K) corrected for the change in pressure-melting point due to the cryostatic pressure. The value for p determines whether the creep is grain size insensitive ($p=0$) or grain size sensitive ($p \neq 0$). The mean grain diameter, as determined from LASM images with the Ice-image software, was used for the calculation of the strain rate produced by GBS-limited creep.

If the temperature is expressed in terms of the difference with the pressure-melting point, ice can, as a first order approximation, be considered incompressible (Rigsby, 1958; Doake and Wolff, 1985). The pressure-melting temperature was calculated according to:

$$T_m = -C \Delta P, \quad (5.4)$$

where T_m is the pressure-melting temperature ($^{\circ}\text{C}$), C is the pressure-melting constant for glacier ice ($9.8 \cdot 10^{-8} \text{ }^{\circ}\text{C Pa}^{-1}$; Lliboutry, 1976) and ΔP is the overburden pressure (Pa) which was calculated according to:

$$\Delta P = \rho_{ice} h_{ice} g, \quad (5.5)$$

where ρ_{ice} is the density of ice (910 kg m^{-3}), h_{ice} is the ice thickness (m) and g is the gravitational constant (9.81 m s^{-2}). The in-situ temperature (T) profile of the NEEM ice core was taken from Sheldon et al. (2014). In the remainder of this Chapter, T^* is used for the difference in temperature of the ice at a certain depth with respect to the pressure-melting point at that depth, which can be calculated according to:

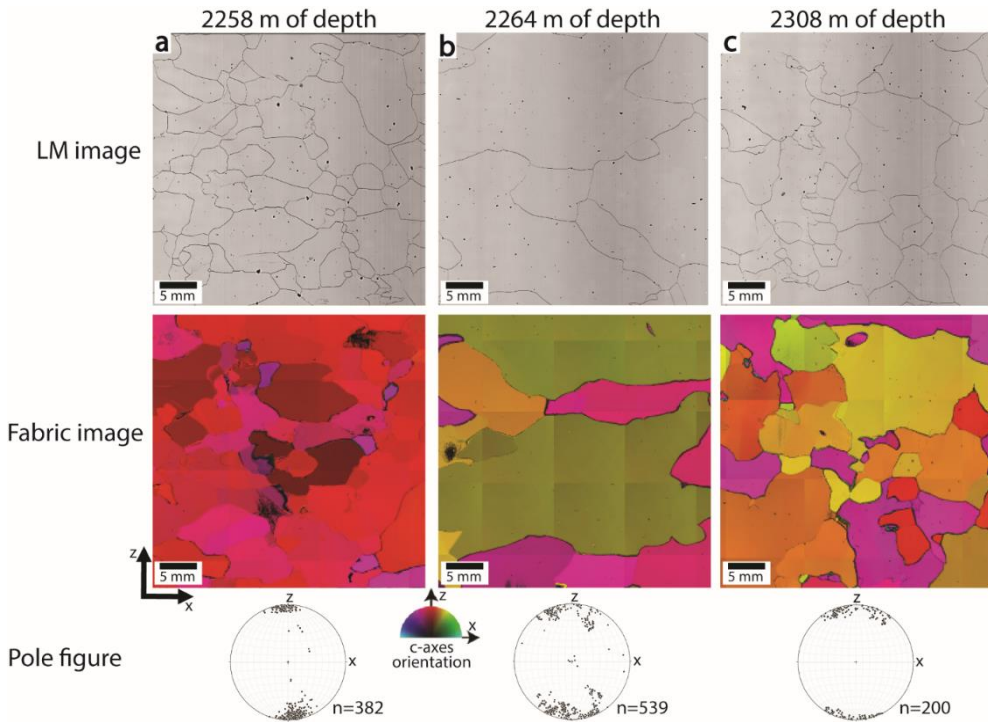


Figure 5.1: Part of vertical reflective LM images, orientation images and pole figures from three different ice core sections in the Eemian-glacial facies. The ice core sections in a) and b) are just above (2258 m of depth) and below (2264 m of depth) the stratigraphic disruption at 2262.2 m of depth, while c) is from the middle of one of the overturned layers (2308 m of depth). The z-axis is parallel to the (vertical) ice core axis. The number of grains n included in the whole (90 x 55 mm) orientation image and pole figure is provided next to the pole figure (equal area, vertical plane, one point per grain). The pole figure in (b) contains the c-axes data from six consecutive ice core sections to increase the number of grains in the pole figure.

$$T^* = T - T_m. \quad (5.6)$$

T^* was used in Equation (5.3) to calculate the strain rates in the lower part of the NEEM ice core according to Glen's flow law and the composite flow law. At the base of the 2540 m long NEEM ice core the pressure-melting point is calculated to be -2.2°C (271K). For example, the in-situ temperature at the ice-bedrock interface at NEEM is -3.4°C , which would give a T^* of -1.2°C (Equation 5.6).

The other flow law that was used in this study is Glen's flow law (Glen, 1952, 1955; Paterson, 1994), which is the flow law that is commonly used in ice sheet modelling. Glen's flow law is based on the results of uniaxial compression experiments on artificial, (initially) isotropic polycrystalline ice. Glen's flow law has the same form as Equation (5.3), but is independent of grain size (i.e., $p=0$) and is characterized by a stress exponent of $n=3$ (Glen, 1955; Paterson, 1994). Following the analysis presented in Section 4.2.3, a constant equivalent stress of 0.07 MPa was taken as input for Glen's flow law and the composite flow law.

5.3 Results

5.3.1 Ice microstructure in the Eemian-glacial facies

Figure 5.1 shows reflective LM images and orientation images with pole figures of three ice core sections at 2258 m, 2264 m, 2308 m of depth in the Eemian-glacial facies. The ice core section at 2258 m of depth in Figure 5.1a is from just above the stratigraphic disruption at 2262.2 m of depth, while the ice core section at 2264 m of depth in Figure 5.1b is from just below this stratigraphic disruption. The ice core section in Figure 5.1c is from 2308 m of depth in the middle of one of the overturned layers (NEEM community members, 2013). The ice core section in Figure 5.1a is one of the finer grained ice core sections in the Eemian-glacial facies with a mean grain size of about 5 mm and originates from the beginning of the last glacial period (NEEM community members, 2013). The orientation image and pole figure of Figure 5.1a show that, similar to the glacial ice (1419-2207 m of depth; Figure 1.8a), almost all c-axes are strongly aligned parallel to the vertical ice core axis. However, compared to the glacial ice, the grain size of the ice core section in Figure 5.1a is slightly larger and the grain shape is more irregular. The ice core section in Figure 5.1b is one of the ice core sections that was given a mean grain size of 30 mm. This ice core section originates from the end of the Eemian period (NEEM community members, 2013). The grains have an irregular shape with many millimetre sized bulges along the grain boundaries. The orientation image and pole figure show that the c-axes are distributed in a partial girdle spanning about 40° from the vertical axis. The ice core section in Figure 5.1c has a mean grain size of about 7 mm and originates from the end of the Eemian period (NEEM community members, 2013). The grain boundaries are bulging and have an irregular shape. The orientation image and pole figure show that the c-axes are distributed in a partial girdle spanning about 30° to 40° from the vertical axis.

5.3.2 Correlation mean grain diameter with type and strength of CPO

The correlation between the mean grain diameter and the type and strength of CPO in the lowest 540 m of the NEEM ice core is shown in Figure 5.2. This figure shows the first c-axes eigenvalue (Eichler et al., 2013) and the Woodcock parameter (Woodcock, 1977) versus the mean grain diameter for each orientation image in the lower part of the glacial ice (2000-2207 m of depth) and the ice in the Eemian-glacial facies (2207-2540 m of depth). The ice from the lower part of the glacial period (2000-2207 m of depth), which has a finer mean grain diameter (about 2 mm) than the ice in the Eemian-glacial facies, has a c-axes eigenvalue of >0.9 and the Woodcock parameter typically varies from 4-10. Some of the finest grained regions in the Eemian-glacial facies have a slightly larger mean grain diameter (3-5 mm) with a similar c-axes eigenvalue of >0.9 and a rather similar Woodcock parameter of about 2-10. For ice core sections with a mean grain diameter larger than about 5 mm, the eigenvalue is <0.9 with a Woodcock parameter varying from 0.3-3. However, the number of grains per orientation image decreases with increasing grain size and

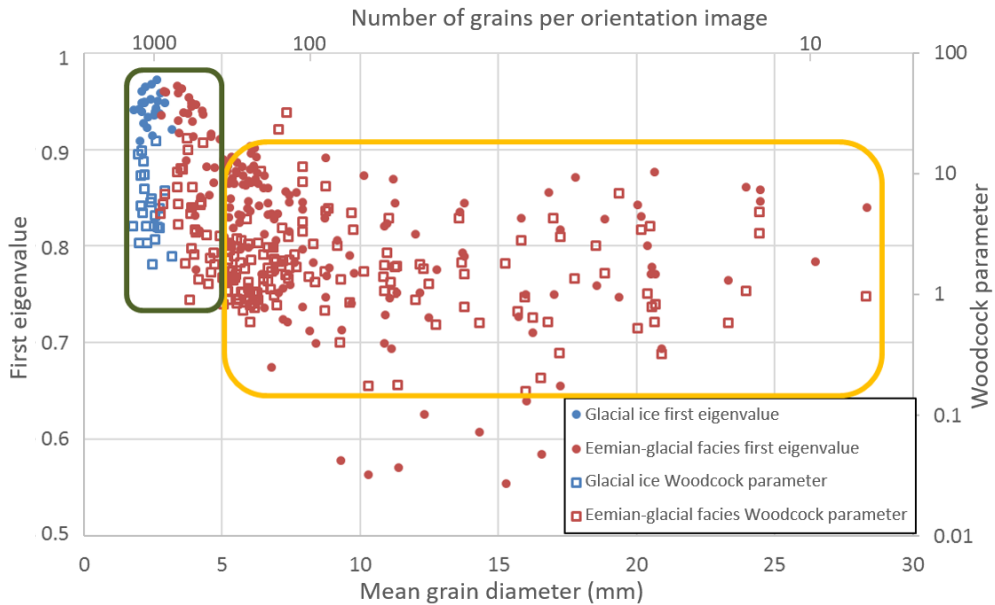


Figure 5.2: The first c-axis eigenvalue (dots) and the Woodcock parameter (open squares) per orientation image versus the mean grain diameter of the ice core sections in the lower part of the glacial ice (2000-2207 m of depth) in blue and the Eemian-glacial facies (2207-2540 m of depth) in red. The number of grains per orientation image was estimated by dividing the area of the orientation image by the mean grain area. The mean grain diameter was derived from orientation images, which gives a slightly lower mean grain diameter than the mean grain diameter derived using the Ice-image software. Two classes of grains can be distinguished based on mean grain diameter, eigenvalue and Woodcock parameter. One class (green rectangle) has a fine mean grain size <5 mm and an eigenvalue and Woodcock parameter that is comparable to the glacial ice and the other class (yellow rectangle) with a larger mean grain diameter (>5 mm) that has a lower eigenvalue and Woodcock parameter.

therefore the statistical significance of the first eigenvalue and Woodcock parameter decreases with increasing mean grain diameter. Based on Figure 5.2, two classes of grains can be distinguished based on mean grain diameter and type and strength of CPO. The first class has a relatively fine mean grain diameter of <5 mm that is comparable in eigenvalue and Woodcock parameter to the glacial ice (green rectangle). The other class has a mean grain diameter of >5 mm with a relatively low first eigenvalue and Woodcock parameter (yellow rectangle).

5.3.3 Transition temperature: NEEM results compared to other polar ice cores

Table 5.1 shows data from eight polar ice cores drilled at the Greenland and Antarctic ice sheets that contain a sudden increase in grain size and change in CPO in the lower part of the ice core. The in-situ temperature at the bottom of the boreholes varies significantly between the ice cores. The ice near the bedrock at GISP2 and GRIP was frozen to the bed, while for Byrd, EDC, EDML, NEEM and Siple dome the ice was at, or very close to, pressure-melting point. In all eight ice cores, the CPO and grain size start to change at an in-situ temperature of about -13°C (260K). For the NEEM ice core, this transition coincides with the climatic transition of the end of the Eemian period, also known as marine isotope stage (MIS) 5e, to the beginning of last glacial period (MIS 5d). The transitions to coarse grains with a multi maxima CPO in the EDML, GISP2 and GRIP ice core also coincides with a climatic transition. For the other four ice cores, the transition to a different microstructure does not coincide with a major climatic transition. The pressure corrected temperature threshold (Equation 5.4-5.6) at which this transition occurs in these polar ice cores is remarkably constant at T^* of -11°C (262K). The depth in the ice cores at which the microstructure changes to large grains and a multi maxima CPO is different for each ice core, which leads to a slightly different T^* when correcting for the change in pressure-melting point with depth (Equation 5.4-5.6). However, when taking into account the uncertainty in determining the in-situ temperature at a certain depth and the possible influence of the different impurity content between the ice cores and individual layers in the same ice core that affect the pressure-melting point, the effect of correcting the temperature at which the microstructure changes due to changes in overburden pressure is small.

The flow law parameters of the composite flow law (Goldsby and Kohlstedt, 2001) were modified to fit the temperature threshold of -11°C (262K) for premelting as derived from Table 5.1 and the experimental data points from Goldsby and Kohlstedt (2001). Another reason for modifying the dislocation creep parameters is to account for the discrepancy between the calculated strain rate for dislocation creep and the experimental data of Goldsby and Kohlstedt (2001) as explained in Chapter 4 (Figure 4.6a). Both the flow law parameters for dislocation creep and GBS-limited creep were modified and are given in Table 5.2. Since the flow law parameters for GBS-limited creep were modified to include the temperature threshold of 262K, they are different from the flow law parameters used in Table 4.2.

Table 5.1: Polar ice cores drilled at the Greenland and Antarctic ice sheets that show a sudden increase in grain size and change in CPO in the lower part of the ice core. The depth where these changes occur is given, together with ice core length, bottom borehole temperature, the in-situ temperature and the pressure-corrected temperature at the sudden grain size increase and change in CPO and the age of the ice at the transition to a sudden grain size increase and change in CPO. The age of the ice at the transition to a microstructure where temperatures are sufficient to cause premelting that would enhance GB mobility and enhance strain induced boundary migration (SIBM) is given in marine isotope stages (MIS) (Lisiecki and Raymo, 2005).

Name of ice core	Ice core length (m)	Borehole bottom T (°C)	Depth grain size increase and/or CPO change (m)	In-situ T at grain size increase and/or CPO change (°C)	Pressure-corrected temperature (T*)	Age of ice at transition to enhanced SIBM microstructure
Byrd ¹	2164	-1.6*	1810	-13	-11	MIS 3
EDC ²	3270	-2.3*	2812	-13	-11	MIS 12
EDML ³	2774	-3*	2370	-13	-11	MIS 6–MIS 5e
GISP2 ⁴	3053	-9	2950	-14	-11	MIS 6–MIS 5
GRIP ⁵	3029	-9	2790	-13	-11	MIS 5e–MIS 5d
NEEM ⁶	2540	-3.4	2207	-12	-10	MIS 5e–MIS 5d
Siple dome ⁷	1004	-1.3	605	-13	-12	MIS 1
WAIS ⁸	3405	unknown	3000	just below -10**	not applicable	MIS 3

*Subglacial water encountered during drilling close to the bedrock.

**A specific temperature was not given, only that the grain size increase started just below -10°C.

¹Gow and Williamson (1976); Hammer et al. (1994); Gow and Engelhardt (2000); Epstein et al. (2011).

²EPICA community members (2004); Augustin et al. (2007); Durand et al. (2009).

³Ruth et al. (2007); Weikusat et al. (2017).

⁴Gow et al. (1997); Suwa et al. (2006).

⁵Johnsen et al. (1995); Thorsteinsson et al. (1997); Suwa et al. (2006).

⁶NEEM community members (2013); Sheldon et al. (2014).

⁷Nereson et al. (1996); Gow and Engelhardt (2000).

⁸Fitzpatrick et al. (2014); Buizert et al. (2015).

Figure 5.3 shows the temperature versus the calculated strain rate using the original flow law parameters of Glen's flow law (Paterson, 1994) and the end members of the modified flow law parameters of the composite flow law (Table 5.2). The calculated strain rates for Glen's flow law, dislocation creep and GBS-limited creep increase with increasing temperature and show a kink at their temperature threshold of 263K (Glen's flow law) or 262K (modified composite flow law). The strain rate increase with temperature of the GBS-limited creep mechanism above the temperature threshold of 262K is considerably higher than for the dislocation creep mechanism or Glen's flow law.

5.3.4 Calculated strain rates and deformation mechanisms

Figure 5.4 shows the calculated strain rates, along with the relevant microstructural data (Binder et al., 2013; Eichler et al., 2013; NEEM community members, 2013; Binder, 2014). The modified composite flow law shows that the calculated strain rate in the lower part of the glacial ice, which reaches till a depth of 2207 m (NEEM community members, 2013), is about $2.5 \cdot 10^{-11} \text{ s}^{-1}$ and the CPO has a strong single maximum. The dominant deformation mechanism of the modified composite flow law in the lower part of the glacial ice is GBS-limited creep, with only a very small contribution of dislocation creep to bulk strain rate.

Glen's flow law predicts a higher strain rate (about 10^{-10} s^{-1}) than the modified composite flow law in the lower part of the glacial ice. At the interface between the glacial ice and Eemian-glacial facies, the calculated strain rate for the composite flow law drops by about an order of magnitude. The relative contribution of the two end members of the composite flow law changes as well with GBS-limited creep and dislocation creep contributing roughly equally to bulk strain rate. At the same depth, the CPO changes from a strong single maximum in the glacial ice to a partial girdle in the upper part of the Eemian-glacial facies. The calculated strain rate of the modified composite flow law varies by about an order of magnitude between the finer and coarser grained regions close to the stratigraphic disruptions. This variation in calculated strain rate close to the stratigraphic disruptions is produced by GBS-limited creep, which is affected by the change in grain size. The strain rate produced by dislocation creep, which is not affected by the variation in grain size, steadily increases with depth throughout the Eemian-glacial facies. Glen's flow law, which is not affected by grain size variation either, predicts an increasing strain rate with depth and a higher strain rate than the modified composite flow law in the entire Eemian-glacial facies.

The relative contribution of GBS-limited creep and dislocation creep to the bulk strain rate of the modified composite flow law is roughly equal for the ice core sections that were assigned a mean grain diameter of 30 mm just below the stratigraphic disruptions at 2209.6 m and 2262.2 m of depth. At deeper levels, the contribution of GBS-limited creep to bulk strain rate for these coarse grained ice core sections increases. The increase in relative contribution of GBS-limited creep to bulk strain rate, at the assigned constant grain size of

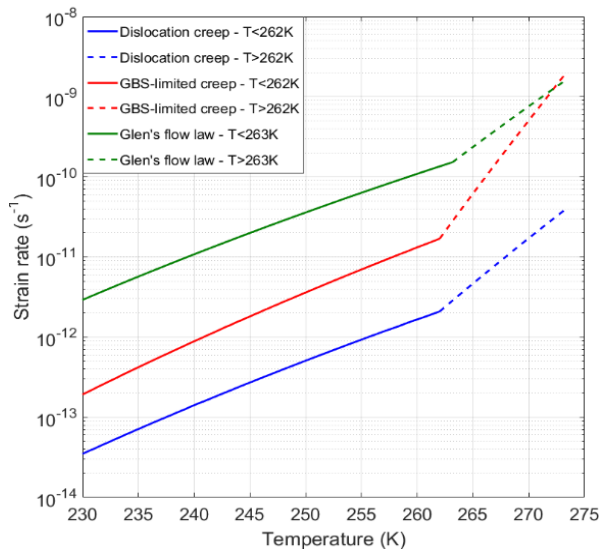


Figure 5.3: Log strain rate versus temperature for Glen's flow law and the two mechanisms (dislocation creep and GBS-limited creep) that form the end members of the modified composite flow law, using the flow law parameters from Table 5.2. A stress of 0.07 MPa (Section 4.2.3) and a mean grain diameter of 5 mm were used to calculate the strain rate.

30 mm, results from the lower activation energy at $T > 262\text{K}$ for dislocation creep compared to GBS-limited creep (Table 5.2, Figure 5.3). The difference in activation energy for Glen's flow law and the dislocation creep mechanism above their temperature thresholds is rather small (Table 5.2), which results in an almost similar strain rate increase with depth.

Table 5.2: The flow law parameters of Glen's flow law (Paterson, 1994) and the end members of the modified composite flow law for dislocation creep and GBS-limited creep.

Creep regime	A (units)	n	p	Q (kJ mol ⁻¹)
Glen's flow law ($T < 263\text{K}$)	$3.61 \cdot 10^5 \text{MPa}^{-3.0} \text{s}^{-1}$	3.0	0	60
Glen's flow law ($T > 263\text{K}$)	$1.73 \cdot 10^{21} \text{MPa}^{-3.0} \text{s}^{-1}$	3.0	0	139
Dislocation creep ($T < 262\text{K}$)*	$5.0 \cdot 10^5 \text{MPa}^{-4.0} \text{s}^{-1}$	4.0	0	64
Dislocation creep ($T > 262\text{K}$)	$6.96 \cdot 10^{23} \text{MPa}^{-4.0} \text{s}^{-1}$	4.0	0	155
GBS-limited creep ($T < 262\text{K}$)	$1.1 \cdot 10^2 \text{MPa}^{-1.8} \text{m}^{1.4} \text{s}^{-1}$	1.8	1.4	70
GBS-limited creep ($T > 262\text{K}$)	$8.5 \cdot 10^{37} \text{MPa}^{-1.8} \text{m}^{1.4} \text{s}^{-1}$	1.8	1.4	250

*These flow law parameters are similar to the modified flow law parameters in Table 4.2.

5.4 Discussion

The results show that the Eemian-glacial facies consists of layers with relatively fine grains that are alternated by layers of very coarse grains. The coarse grained layers have a strongly interlocking grain boundary structure with a partial girdle type of CPO, while the fine grained layers have a more regular grain shape and have a single maximum type of CPO (Figure 5.1 and 5.2). A comparison with other polar ice cores showed that layers with very coarse and interlocking grains with a multi maxima or partial girdle type of CPO start to appear at a T^* value of about 262K (Table 5.1). The modified composite flow law of Goldsby and Kohlstedt (2001) predicts that the strain rate in the fine grained layers, which is almost entirely produced by GBS-limited creep, is about an order of magnitude higher than the strain rate in the coarse grained layers, where GBS-limited creep and dislocation creep contribute roughly equally to bulk strain rate (Figure 5.4).

5.4.1 The role of impurities in premelted ice

It is well known that changes in impurity content correlate well with changes in mean grain size in polar ice cores (e.g. Fisher and Koerner, 1986; Paterson, 1991; Thorsteinsson et al., 1995; Cuffey et al., 2000); finer grains occur in ice with a higher impurity content. It is often assumed that impurities control grain size by pinning of grain boundaries (e.g. Fisher and Koerner, 1986; Gow et al., 1997; Durand et al., 2006), although the exact mechanism by which impurities control the mean grain size is still not understood in detail (Eichler et al., 2017). Similar to the Eemian-glacial facies in the NEEM ice core, the lower part of the GRIP ice core (Thorsteinsson et al., 1995) is likely affected by premelting (Table 5.1). In both the GRIP and NEEM ice core, the effect of impurities on grain size and shape is very large in the premelting regime (Thorsteinsson et al., 1995; NEEM community members, 2013). Due to the high impurity content in the glacial ice of the Eemian-glacial facies, the mean grain size in these layers remains relatively small. On the other hand, the Eemian ice in the Eemian-glacial facies is not (or hardly) affected by the impurity content and the

grains are much larger. The second effect of the high impurity content in the glacial layers in the Eemian-glacial facies is the melt content along grain boundaries and triple junctions is probably enhanced due to the lowering of the pressure-melting point by salts and/or impurities (e.g. Duval, 1977; Wettlaufer, 1999a, b; Döppenschmidt and Budd, 2000).

Impurities also provide additional interfaces, in addition to grain boundaries, where premelting can take place. These premelting films could act as dislocation sinks that may enhance dislocation motion in ice, preventing hardening by dislocation entanglement and thus enhance the strain rate. The type of impurity can change the effectivity of premelting, but as only few studies on particle species in solid polar ice are available so far (Ohno et al., 2005, 2006; Sakurai et al., 2009; 2011; Oyabu et al., 2015; Eichler et al.,

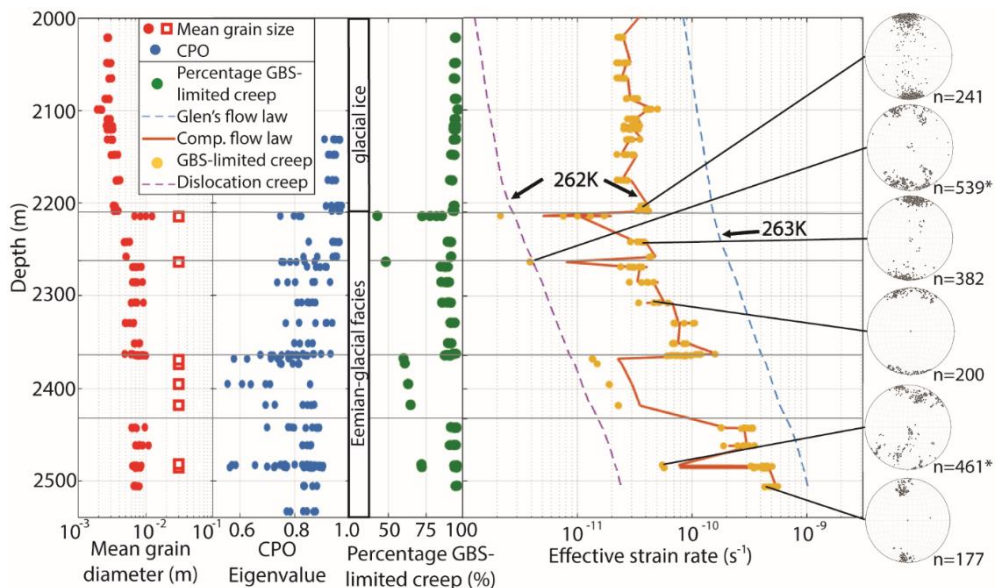


Figure 5.4: Results showing as a function of depth for the lowest 540 m of the NEEM ice core, the mean grain diameter (red dots), first CPO eigenvalues (blue dots), calculated strain rates (Table 5.2) using Glen’s flow law (blue dotted line), the modified composite flow law (orange line) and the two end-member deformation mechanisms, dislocation creep (purple dotted line) and GBS-limited creep (yellow dots), (where, the orange line shows the total strain rates made up of the dislocation creep strain rate, shown by the purple line and the GBS-limited strain rate, shown by the yellow dots). The percentage contribution of GBS-limited creep to bulk strain rate is also shown (green dots). A red open square instead of a red dot was used when the grains size was too large to determine a mean grain diameter by the Ice-image software and a mean grain diameter of 30 mm was used. The four horizontal grey lines represent the stratigraphic disruptions that were found in the NEEM deep ice core (NEEM community members, 2013). The glacial ice extends to a depth of 2207 m, with the glacial-Eemian facies continuing until the ice-bedrock interface at 2540 m depth. The depth of the temperature threshold for the modified composite flow law (262K) and Glen’s flow law (263K) are indicated. On the right, six pole figures (equal area, vertical plane, one point per grain) at different depths are shown with the number of grains (n) next to the pole figure. At two depths, indicated by an asterisk (*), the CPO data from six consecutive ice core sections were combined to increase the number of grains in the pole figure.

submitted), this argument can only be made via the total surface of impurities per volume of ice.

5.4.2 The effect of premelting on ice microstructure

Premelting is expected to initiate at grain boundaries at temperatures below, but close to, the melting point (e.g. Orem and Adamson, 1969; Döppenschmidt et al., 1998). Since premelting itself, as well as the collection of water in veins (Nye and Mae, 1972), takes place at grain boundaries and triple junctions, grain boundaries are the major ‘suspect’ that enables weakening in polycrystalline ice. As temperature increases, a water-like amorphous layer gathers in layers along grain boundaries and veins along triple junctions, the presence of a water-like amorphous layer correlates with strain rates that are faster than predicted by extrapolation of low temperature results using the Arrhenius relation with a fixed activation energy (e.g. Mellor and Testa, 1969; Nye and Mae, 1972; Duval et al., 1977; Dash et al., 1995; De la Chapelle et al., 1999). Therefore, a flow law that is calibrated at lower temperature cannot simply be applied under premelting conditions, since the mechanical properties of the material at premelting temperature, apparently, are different. Due to the higher grain boundary surface area per unit of volume in a fine grained sample, the influence of premelting on a fine grained sample is expected to be stronger than for a coarser grained sample.

A small liquid-like amorphous layer at the grain boundaries increases grain boundary mobility by about two to four orders of magnitude (Duval and Castelnau, 1995; Schulson and Duval, 2009). Since grain boundary velocity is a function of grain boundary mobility and the driving force for grain boundary migration (e.g. Higgins, 1974; Alley et al., 1986), it is expected that a strong increase in grain boundary mobility leads to an increase in grain boundary velocity, provided that the stored strain energy for SIBM in the ice polycrystal is high enough. Ice deformation tests have indeed shown that grain boundary migration rates are high close to the melting point (e.g. Wilson and Zhang, 1996; Breton et al., 2016). Microstructural changes occurring in ice close to the melting point that creates very coarse and interlocking grains, and a change in deformation behaviour, could both well be explained by the presence of a liquid-like amorphous layer that increases grain boundary mobility and consequently enhances SIBM. This enhanced SIBM would result in very coarse grains with an interlocking grain boundary structure (e.g. Duval and Castelnau, 1995; Schulson and Duval, 2009; Breton et al., 2016), as observed in the interglacial layers of the Eemian-glacial facies (Figure 5.1b).

In addition to the effect of high temperature on grain boundary mobility, the cryostatic pressure in the lower part of polar ice cores (20-23 MPa for NEEM, Equation 5.5) will further enhance grain boundary mobility (Breton et al., 2016). Directed growth of migrating grain boundaries along subgrain boundaries in specimens deformed at a cryostatic pressure of 20 MPa can lead to a smaller median grain size and a more interlocking microstructure. The smaller grain size of samples deformed at a high cryostatic pressure of 20 MPa compared to samples deformed at atmospheric pressure could be

caused by grain dissection (Breton et al., 2016; Steinbach et al., 2017), since this process also depends on SIBM.

The similarity between microstructures with coarse interlocking grains in the lower part of polar ice cores (Table 5.1, Figure 5.1b) and the ice microstructure developing during deformation tests close to the melting point suggests that these microstructures are governed by the same processes. It is therefore proposed that the sudden appearance of the coarse grains with an interlocking grain boundary structure in the lower part of polar ice cores is the result of premelting along the grain boundaries, which increases grain boundary mobility and consequently enhances SIBM.

5.4.3 Setting the temperature threshold for premelting

The in-situ temperature at which coarse and interlocking grains start to appear in polar ice sheets occurs at T^* of about -11°C (262K) (Table 5.1), falls within the temperature range (258K to 263K) of the transition to a more temperature sensitive deformation mechanism during deformation tests (Mellor and Testa, 1969; Barnes et al., 1971; Weertman, 1983; Paterson, 1994; Goldsby and Kohlstedt, 2001). The premelting temperature threshold for Glen's flow law (263K; Paterson, 1994) is 5K and 8K higher than the temperature thresholds for the dislocation creep (258K) mechanism and the GBS-limited creep mechanism (255K) applied by Goldsby and Kohlstedt (2001), respectively. Since the strain rate increase close to the melting point for dislocation creep and GBS-limited creep has been related to premelting along the grain boundaries (Goldsby and Kohlstedt, 2001), a similar temperature threshold can be expected for both deformation mechanisms.

The temperature threshold of 258K proposed by Goldsby and Kohlstedt (2001) for dislocation creep was taken from Kirby et al. (1987), who conducted ice deformation tests at a high confining pressure of 50 MPa. A confining pressure of 50 MPa lowers the pressure-melting point by 3.7K, using the pressure-melting constant for clean ice of $7.4 \cdot 10^{-8} \text{ K Pa}^{-1}$ (Hobbs, 1974; Weertman, 1983; Equation 5.4). This change in pressure-melting point due to the high confining pressure seems not to be considered by Kirby et al. (1987) and Goldsby and Kohlstedt (2001). Therefore, it is argued that the temperature threshold should have been 261.7K instead of 258K. This temperature threshold is much closer to 263K used in Glen's flow law (Paterson, 1994) and practically equal to 262K that was found by analysing ice microstructures of polar ice cores (Table 5.1). 261.7K is also closer to the temperature threshold proposed by Barnes et al. (1971), who found that the activation energy of ice is much higher between 271K and 265K (120 kJ mol^{-1}) than between 265K and 259K (78.1 kJ mol^{-1}). Similarly, 261.7K is also closer to Mellor and Testa (1969) who found that above 263K the strain rate becomes progressively more temperature dependent when approaching the melting point.

5.4.4 Recrystallization and deformation mechanisms in the Eemian-glacial facies

The strain rate calculations using the composite flow law (Figure 5.4) show that the fine grained layers in the Eemian-glacial facies deform predominantly by GBS-limited creep. It is known that the basal slip system is not significantly affected by the cryostatic pressures that are reached in polar ice sheets (e.g. Rigsby, 1958; Cole, 1996). Therefore, basal slip is the main strain producing mechanism in both the coarse and the fine grained layers, but the way basal slip is accommodated (i.e. rate-controlled) is different. Since basal slip provides only two of five independent slip systems required for homogeneous deformation, at least one additional slip system or some other mechanism is required (e.g. Von Mises, 1928; Hutchinson, 1977). Grain boundary sliding is favoured as the accommodating mechanism for basal slip in the Eemian-glacial facies, since the grain boundary area in the impurity-rich and fine grained layers is relatively high and a higher grain boundary area enhances the effect of premelting on deformation behaviour (Barnes et al., 1971). However, compared to the glacial ice between 1419 m to 2207 m of depth (Figure 4.1b), the grain boundary network in the fine grained layers in the Eemian-glacial facies is relatively irregular with many bulges (Figure 5.1a). The irregular grain boundary structure is likely a result of enhanced SIBM caused by premelting (Section 5.4.2). Still, the effect of impurities in these impurity-rich layers is strong enough to prevent the grains from growing into tens of millimetres, like the example of the coarse grained ice core section in Figure 5.1b, so grain boundary sliding remains an important accommodating mechanism. Due to the limited SIBM in these impurity-rich layers, the grains are longer-lived and can rotate towards a single maximum CPO (e.g. Van der Veen and Whillans, 1994). For these layers, the CPO is a reflection of cumulative strain, just like the CPO in the shallower parts of the ice sheet (e.g. Azuma and Higashi, 1985; Alley, 1988; Budd and Jacka, 1989; Llorens et al., 2016a, b, 2017).

For the coarse grained layers in the Eemian-glacial facies, it is predicted that GBS-limited creep and dislocation creep contribute roughly equally to bulk strain rate (Figure 5.4). However, since the grains in these layers are very coarse with an interlocking grain boundary structure (Figure 5.1b), grain boundary sliding is unlikely to be an important accommodating mechanism for basal slip. SIBM is highly active in these coarse grained layers and recovery by SIBM is probably an important accommodating mechanism for basal slip (Pimienta and Duval, 1987; De la Chapelle et al., 1999; Duval et al., 2000; Montagnat and Duval., 2000). Even though grain boundary sliding is unlikely to be an important accommodating mechanism, grain boundary sliding may locally accommodate some basal slip (Raj and Ashby, 1971). Therefore, basal slip might also be accommodated by SIBM coupled with grain boundary sliding (Drury et al., 1989). The grain size and grain shape in these impurity-depleted interglacial layers (Figure 5.1b) suggests that the grain boundaries are free to migrate at the high SIBM rates caused by premelting (Duval and Castelnau, 1995; Schulson and Duval, 2009) and are not or hardly influenced by impurities. The CPO of these coarse grained ice core sections suggests that new grains with a high

Schmidt factor nucleate continuously (e.g. Alley, 1988; Montagnat et al., 2015; Qi et al., 2017). A high Schmidt factor indicates grains with a high resolved shear stress on the basal plane, i.e. grains with a soft orientation. Normalized grain size distributions and CPO data from the premelting layer (ice at $262\text{K} < T^* < 273\text{K}$) in the EDC ice core (Durand et al., 2009) showed that small grains were much more abundant in layers with a multi maxima CPO compared to layers with a single maximum CPO. This strongly suggests that the multi maxima CPO in the premelting layer is linked to the formation of new strain free grains with soft orientations (high Schmidt factor), which grow at the expense of grains oriented in a hard orientation. This recrystallization mechanism can be described as discontinuous migration recrystallization (Wenk et al., 1989; Schulson and Duval, 2009) or SIBM-N (Faria et al., 2014).

5.4.5 Strain localization in the Eemian-glacial facies

The ice in the Eemian-glacial facies alternates between fine grained ice with a single maximum CPO and coarse grained ice with a partial girdle CPO (Figure 5.4). The differences in grain size, grain shape and CPO in the Eemian-glacial facies indicates that there are large differences in viscosity between the different layers, which is also shown by the results using the modified composite flow law (Figure 5.4). Consequently, strain localization and strain partitioning into ‘hard’ and ‘soft’ layers can be expected. Strain localization has been shown on many different scales in ice (e.g. Paterson, 1991; Wilson and Zhang, 1996; Grennerat et al., 2012; Jansen et al., 2016; Steinbach et al., 2016). In addition to a variation in grain size, the CPO has also been shown to influence strain rates (e.g. Alley, 1988; Hudleston, 2015). Deformation experiments with ice from other polar ice cores with a certain type of CPO, such as a single maximum or a multi maxima CPO, have different strain rates when the ice is deformed under different deformation modes. For example, simple shear deformation experiments on basal ice with a multi maxima CPO from Law Dome showed that the strain rates were comparable with those of isotropic ice (Russell-Head and Budd, 1979). The same study showed that samples from Law Dome with a single maximum CPO deformed much more readily than isotropic ice in simple shear (sheared in the direction of the measured surface velocity). The study of Lile (1978) with samples from Law Dome and Dome Summit showed a similar result with samples containing a single maximum CPO that were deformed in simple shear (single maximum normal to the shear plane) showing much higher strain rates compared to laboratory-prepared isotropic ice with a similar grain size. Samples with a multi maxima CPO from Dome Summit showed a similar strain rate as laboratory-prepared isotropic samples during uniaxial compression tests (Lile, 1978).

On the basis of the variation in grain size and CPO, it is hypothesized that deformation of ice in the Eemian-glacial facies is partitioned in simple shear mode with fast deformation in the fine grained layers with a single maximum CPO (e.g. Figure 5.1a), while the coarse grained layers with a partial girdle CPO (e.g. Figure 5.1b) deform more slowly in coaxial deformation or are relatively stagnant. According to the results shown in Figure 5.4, the fine grained ice is much softer than the coarse grained ice. The single maximum CPO in

the fine grained layers indicates that these layers deform by simple shear, which is expected to be the dominant deformation mode in this part of the NEEM ice core (Dansgaard and Johnsen, 1969; Montagnat et al., 2014). The likely partitioning of simple shear into the fine grained layers with a single maximum CPO results in a positive feedback loop as deformation by simple shear enhances the strength of the single maximum CPO making the ice softer in simple shear. The CPO of the coarse grained layers indicate that these layers deforms by coaxial deformation.

The composite flow law that is used in this study does not explicitly include the effect of CPO on strain rate, while it is well known that the CPO has a weakening effect on ice depending on its orientation in certain different deformation modes (e.g. Alley, 1988; Hudleston, 2015). Therefore, the partitioning of strain into layers with a certain CPO can produce additional variations in strain rate on top of the strain rate variations presented in Figure 5.4. The fine grained layers have a CPO that is compatible with the main deformation mode in this part of the NEEM ice core (simple shear), while the coarse grained layers do not have a compatible CPO and are likely relatively stagnant or deform in coaxial deformation. Therefore, it is likely that the difference in strain rate between the fine grained and coarse grained layers in the Eemian-glacial facies is even larger than shown in Figure 5.4. The relatively fine grained layer (5-10 mm) with a partial girdle CPO between 2265 m and 2365 m of depth (example in Figure 5.1c) represents a ‘mixed case’ between the two end members consisting of (i) layers with fine grain size with a single maximum CPO and (ii) layers with coarse and interlocking grains with a partial girdle CPO. Since the CPO of this layer (Figure 5.1c) is relatively hard in simple shear, which is the dominant deformation mode at this depth, it is likely that the layer between 2265 m and 2365 m of depth deforms at a lower strain rate than predicted in Figure 5.4.

The difference in microstructure between the impurity-rich glacial ice and the impurity-depleted interglacial ice poses an interesting hypothesis for the effect of premelting on ice dynamics close to the bedrock. In the case where the premelting layer consists entirely of interglacial ice (with a low impurity content) the premelting layer is expected to be relatively stagnant, provided the bedrock topography allows this, and hardly contributes to horizontal velocity, which will probably be localized above the premelting layer. In the case where glacial ice (with a high impurity content) is present in the premelting layer or the premelting layer consists entirely of glacial ice, a significant portion of the horizontal velocity will be accomplished in the premelting layer. The difference in microstructure of impurity-rich glacial and impurity-depleted interglacial ice in the premelting layer can have important consequences for ice dynamics close to the bedrock. Since the impurity content in the Greenland ice sheet is approximately 10 times higher than the impurity content in the Antarctic ice sheet (e.g. Legrand and Mayewski, 1997), this effect of strain partitioning in the premelting layer is likely to be stronger in the Greenland ice sheet than in the Antarctic ice sheet.

Borehole data from Byrd station showed that the tilting rate (deformation rate) in the premelting layer (1810 m down to the bedrock at 2164 m of depth), where grains are

coarse with a multi maxima CPO (Gow and Williamson, 1976), deformed much less than the remainder of the ice (Paterson, 1983). Borehole data from the deeper part of the EDML ice core showed that a coarse grained layer with a girdle type CPO deformed predominantly by pure shear, while the layers just above and below deformed predominantly by simple shear (Jansen et al., 2017). Both these layers show a similar microstructure compared to the Eemian-glacial facies: the layer that deforms by coaxial deformation consists of coarse grains with a multi-maxima or partial girdle type of CPO, while the layers above and below deform by simple shear and consist of finer grains with a single maximum CPO. Borehole data from the lower part of the NEEM ice core might confirm whether the strain rate variability with depth in the premelting layer is as large as predicted in Figure 5.4.

Strain partitioning between glacial and interglacial layers in the premelting zone can lead to a different rate of layer thinning. Coaxial deformation clearly leads to layer thinning, while deformation by simple shear alone, does not lead to layer thinning if the shear plane is parallel to the layering. Therefore, the layers in the coarse grained regions with a multi maxima or partial girdle type CPO could be thinning at a higher rate than the fine grained regions with a single maximum CPO. Even if in reality we can assume general shear (mixed simple shear and coaxial deformation), the relative importance or impact of a likely unequal share of both deformation modes will lead to differing thinning rates.

The heterogeneous deformation between the layers, and particularly heterogeneous layer thinning, can have important consequences for interpreting paleoclimatic records from polar ice cores, as in the deepest part of the ice core the dating tool is based on ice flow modelling describing a homogeneous transition from coaxial deformation to simple shear. It has often been shown that paleoclimatic records in the lower part of polar ice cores are disturbed (e.g. Alley et al., 1997; Gow et al., 1997; Suwa et al., 2006; Ruth et al., 2007; NEEM community members, 2013), which could be caused by heterogeneous deformation and strain partitioning between glacial and interglacial layers as described above. The suggestion of heterogeneous layer thinning as proposed above is still speculative and further research on this topic is needed.

5.5 Conclusions

In many polar ice cores the grain size, grain shape and CPO change significantly in the ice close to the bedrock, which can have a large impact on the dominant deformation mechanism and the strain rate. In this Chapter, actual temperature and grain size data of the NEEM ice core were used to apply the composite flow law of Goldsby and Kohlstedt (2001) and Glen's flow law (1955) to the lower part of the NEEM ice core with the aim of studying the effect of changes in grain size on the dominant deformation mechanism and the strain rate. Several stratigraphic disruptions are present in this part of the NEEM ice core, which causes layers of fine grained glacial ice to be alternated by layers of coarse grained Eemian ice. After a microstructural evaluation of eight different polar ice cores from the Greenland and Antarctic ice sheets, it was found that microstructures that indicate premelting start at a temperature of about 262K, which is within the temperature range at

which a more temperature sensitive deformation mechanism starts to dominate the ice rheology in deformation tests. The composite flow law of Goldsby and Kohlstedt (2001) was modified to include this premelting temperature threshold of 262K.

The modified composite flow law predicts that, as a result of the grain size variation in the Eemian-glacial facies, the strain rate varies strongly with the fine grained layers deforming about an order of magnitude faster than the coarse grained layers. In the fine grained glacial ice the dominant deformation mechanism is predicted to be GBS-limited creep. In the coarse grained interglacial ice, dislocation creep and GBS-limited creep contribute roughly equally to the bulk strain rate, with the contribution of GBS-limited creep to bulk strain rate increasing with depth. Glen's flow law, which is grain size insensitive, is unable to predict the strong variations in strain rate in the Eemian-glacial facies and predicts a steadily increasing strain rate with depth caused by an increase in temperature with depth. Glen's flow law predicts a higher strain rate than the modified composite flow law along the entire lowest 540 m of depth of the NEEM ice core.

Changes in grain size in the Eemian-glacial facies correlate strongly with changes in type and strength of CPO. The fine grained (<5 mm) impurity-rich glacial layers have a strong single maximum CPO, which is compatible with predominant simple shear deformation in this part of the NEEM ice core. The relatively fine grain size argues for GBS-limited creep to be the dominant deformation mechanism in these layers. The coarse grained (>5 mm) impurity-depleted interglacial layers have a partial girdle type of CPO, which is more compatible with coaxial deformation than with simple shear deformation. Due to the coarse grains and the interlocking grain boundary structure, these layers are likely deforming by basal slip accommodated by recovery via SIBM, which removes dislocations and stress concentrations in grains and allows further deformation to occur, or by coupled SIBM and grain boundary sliding. Therefore, strain partitioning is expected in the Eemian-glacial facies with the fine grained glacial layers with a single maximum CPO deforming at high strain rates in simple shear, while the coarse grained interglacial layers with a partial girdle type of CPO deform at much lower strain rates by coaxial deformation. The difference in microstructure, and consequently difference in viscosity, of impurity-rich glacial and impurity-depleted interglacial ice in the premelting layer can have important consequences for ice dynamics close to the bedrock.

References

- Alley, R. B. (1988) Fabrics in Polar Ice Sheets: Development and Predictions. *Science*, 240, 4851, 493-495, doi: 10.1126/science.240.4851.493.
- Alley, R. B. (1992) Flow-law hypothesis for ice sheet modeling. *Journal of Glaciology*, 38, 129, 245-256, doi: 10.1017/S002214300003658.
- Alley, R. B., Gow, A. J., Meese, D. A., Fitzpatrick, J. J., Waddington, E. D., Bolzan, J. F. (1997) Grain-scale processes, folding, and stratigraphic disturbance in the GISP2 ice core. *Journal of Geophysical Research*, 102, C12, 26819-26830, doi: 10.1029/96JC03836.

Alley, R. B., Perepezko, J. H., Bentley, C. R. (1986) Grain growth in polar ice: I. Theory. *Journal of Glaciology*, 32, 112, 415-424.

Augustin, L., Panichi, S., Frascati, F. (2007) EPICA Dome C 2 drilling operations: performances, difficulties, results. *Annals of Glaciology*, 47, 68-72, doi: 10.3189/172756407786857767.

Azuma, N., Higashi, A. (1985) Formation processes of ice fabric pattern in ice sheets. *Annals of Glaciology*, 6, 120, 130-134.

Barnes, P., Tabor, D., Walker, J. C. F. (1971) The friction and creep of polycrystalline ice. *Proceedings of the Royal Society London A.*, 324, 1557, 127-155.

Binder, T., Weikusat, I., Freitag, J., Garbe, C. S., Wagenbach, D., Kipfstuhl, S. (2013) Microstructure through an ice sheet. *Materials Science Forum*, 753, 481-484, doi: 10.4028/www.scientific.net/MSF.753.481.

Binder, T. (2014) Measurements of grain boundary networks in deep polar ice cores – A digital image processing approach. PhD thesis, University of Heidelberg, Germany.

Breton, D. J., Baker, I., Cole, D. M. (2016) Microstructural evolution of polycrystalline ice during confined creep testing. *Cold Regions Science and Technology*, 127, 25-36, doi: 10.1016/j.coldregions.2016.03.009.

Budd, W. F., Jacka, T. H. (1989) A review of ice rheology for ice sheet modelling. *Cold Regions Science and Technology*, 16, 107-144, doi: 10.1016/0165-232X(89)90014-1.

Budd, W. F., Rowden-Rich, R. J. M. (1985) Finite element analysis of two-dimensional longitudinal section flow on Law Dome. *Australian Glaciological Research; 1982-1983. ANARE Res. Notes*, 28: 153-161.

Buizert, C., Cuffey, K. M., Severinghaus, J. P., Baggenstos, D., Fudge, T. J., Steig, E. J., Markle, B. B., Winstrup, M., Rhodes, R. H., Book, E. J., Sowers, G. D., Clow, G. D., Cheng, H., Edwards, R. L., Sigl, M., McConnell, J. R., Taylor, K. C. (2015) The WAIS Divide deep ice core WD2014 chronology – Part 1: Methane synchronization (68-31 ka BP) and the gas age-ice age difference. *Climate of the Past*, 11, 2, 153-173, doi: 10.5194/cp-11-153-2015.

Catania, G. A., Neumann, T. A. (2010) Persistent englacial drainage features in the Greenland Ice Sheet. *Geophysical Research Letters*, 37, 2, 1-5, doi: 10.1029/2009GL041108.

Cole, D. M. (1996) Observations of pressure effects on the creep of ice single crystals. *Journal of Glaciology*, 42, 140, 169-175, doi: 10.1017/S0022143000030628.

Cuffey, K. M., Thorsteinsson, T., Waddington, E. D. (2000) A renewed argument for crystal size control of ice sheet strain rates. *Journal of Geophysical Research*, 105, B12, 27889-27894, doi: 10.1029/2000JB900270.

Dash, J. G., Fu, H., Wettlaufer, J. S. (1995) The premelting of ice and its environmental consequences. *Reports on Progress in Physics*, 58, 1, 115-167, doi: 10.1088/0034-4885/58/1/003.

Dash, J. G., Rempel, A. W., Wettlaufer, J. S. (2006) The physics of premelted ice and its geophysical consequences. *Reviews of Modern Physics*, 78, 3, 695-741, doi: 10.1103/RevModPhys.78.695.

- Dansgaard, W., Johnsen, S. J. (1969) A flow model and a time scale for the ice core from camp century, Greenland. *Journal of Glaciology*, 8, 53, 215-223, doi: 10.3189/S0022143000031208.
- De La Chapelle, S., Milsch, H., Castelnaud, O., Duval, P. (1999) Compressive creep of ice containing a liquid intergranular phase: rate-controlling processes in the dislocation creep regime. *Geophysical Research Letters*, 26, 2, 251-254, doi: 10.1029/1998GL900289.
- Doake, C. S. M., Wolff, E. W. (1985) Flow law for ice in polar ice sheets. *Nature*, 314, 6008, 255-257, doi: 10.1038/314255a0.
- Döppenschmidt, A., Butt, H.-J. (2000) Measuring the Thickness of the Liquid-like Layer on Ice Surfaces with Atomic Force Microscopy, *Langmuir*, 16, 18, 6709-6714, doi: 10.1021/la990799w.
- Döppenschmidt, A., Kappl, M., Butt, H. J. (1998) Surface Properties of Ice Studied by Atomic Force Microscopy. *Journal of Physical Chemistry*, 102, 40, 7813-8919, doi: 10.1021/jp981396s.
- Drury, M. R., Humphreys, F. J., White, S. H. (1989) Effect of dynamic recrystallization on the importance of grain-boundary sliding during creep. *Journal of Materials Science*, 24, 1, 154-162, doi: 10.1007/BF00660947.
- Durand, G., Svensson, A., Persson, A., Gagliardini, O., Gillet-Chaulet, F., Sjolte, J., Montagnat, M., Dahl-Jensen, D. (2009) Evolution of the texture along the EPICA Dome C ice core. *Low Temperature, Science*, 68, 91-105.
- Durand, G., Weiss, J., Lipenkov, V., Barnola, J. M., Krinner, G., Parrenin, F., Delmonte, B., Ritz, C., Duval, P., Röthlisberger, R., Bigler, M. (2006) Effect of impurities on grain growth in cold ice sheets. *Journal of Geophysical Research*, 111, F01015, 1-18, doi: 10.1029/2005JF000320.
- Durham, W. B., Stern, L. A. (2001) Rheological Properties of Water Ice – Applications to satellites of the Outer Planets. *Annual Review of Earth and Planetary Science*, 29, 295-330.
- Duval, P. (1977) The role of the water content on the creep rate of polycrystalline ice. *International Association of hydrological Sciences*, 118, 29-33.
- Duval, P., Arnaud, L., Brissaud, O., Montagnat, M., De La Chapelle, S. (2000) Deformation and recrystallization processes of ice from polar ice sheets. *Annals of Glaciology*, 30, 83-87, doi: 10.3189/172756400781820688.
- Duval, P., Castelnaud, O. (1995) Dynamic Recrystallization of Ice in Polar Ice Sheets. *Journal de Physique III*, 05, C3, 197-205, doi: 10.1051/jp4:1995317.
- Eichler, J., Weikusat, I., Kipfstuhl, S. (2013) Orientation-tensor eigenvalues along the NEEM ice core. *PANGAEA*, <https://doi.org/10.1594/Pangaea.838059>.
- Eichler, J., Kleitz, I., Bayer-Giraldi, M., Jansen, D., Kipfstuhl, S., Shigeyama, W., Weikusat, C., Weikusat, I. (2017) Location and distribution of micro-inclusions in the EDML and NEEM ice cores using optical microscopy and in situ Raman spectroscopy. *The Cryosphere*, 11, 3, 1075-1090, doi: 10.5194/tc-11-1075-2017.
- Eichler, J., Weikusat, C., Wegner, A., Twarloh, B., Behrens, M., Fischer, H., Hoerhold, M., Jansen, D., Kipfstuhl, S., Ruth, U., Wilhelms, F., Weikusat, I. (submitted) Impurity analysis and microstructure along the climatic transition from MIS 6 into 5e in the EDML ice core using cryo-Raman microscopy. Submitted to *Frontiers in Earth Science* on 07 September 2018.

- EPICA community members (2004) Eight glacial cycles from an Antarctic ice core. *Nature*, 429, 623-628, doi: 10.1038/nature02599.
- Epstein, S., Sharp, R. P., Gow, A. J. (2011) Antarctic Ice Sheet: Stable Isotope Analysis of Byrd Station Cores and Interhemispheric Climate Implications. *Science*, 168, 3939, 1570-1572, doi: 10.1126/science.168.3939.1570.
- Faria, S. H., Weikusat, I., Azuma, N. (2014) The microstructure of polar ice: Part II: State of the art. *Journal of Structural Geology*, 61, 21-49, doi: 10.1016/j.jsg.2013.11.003.
- Fitzpatrick, J. J., Voigt, D. E., Fegyveresi, J. M., Stevens, N. T., Spencer, M. K., Cole-Dai, J., Alley, R. B., Jardine, G. E., Cravens, E. D., Wilen, L. A., Fudge, T. J., McConnell, J. R. (2014) Physical properties of the WAIS Divide ice core. *Journal of Glaciology*, 69, 224, 1181-1198, doi: 10.3189/2014JG14J100.
- Fisher, D. A., Koerner, R. M. (1986) On the special rheological properties of ancient microparticle-laden northern hemisphere ice as derived from bore-hole and core measurements. *Journal of Glaciology*, 32, 112, 501-510.
- Glen, J. W. (1952) Experiments on the deformation of ice. *Journal of Glaciology*, 2, 12, 111-114.
- Glen, J. W. (1955) The creep of polycrystalline ice. *Proceedings of the Royal Society London A.*, 228, 1175, 519-538, doi: 10.1098/rspa.1955.0066.
- Goldsby, D. L., Kohlstedt, D. L. (1997) Grain boundary sliding in fine grained ice I. *Scripta Materialia*, 37, 9, 1399-1406.
- Goldsby, D. L., Kohlstedt, D. L. (2001) Superplastic deformation of ice: Experimental observations. *Journal of Geophysical Research*, 106, B6, 11017-11030, doi: 10.1029/2000JB900336.
- Goldsby D. L. (2006) *Glacier Science and environmental change* (eds. by P. G. Knight). pp. 308-314. Blackwell, Oxford.
- Gow, A. J., Engelhardt, H. (2000) Preliminary analysis of ice cores from Siple Dome, West Antarctica. In Hondoh, T., ed. *Physics of ice core records*. Sapporo, Hokkaido University Press, 63-82.
- Gow, A. J., Meese, D. A., Alley, R. B., Fitzpatrick, J. J., Anandkrishnan, S., Woods, G. A., Elder, B. C. (1997) Physical and structural properties of the Greenland Ice Sheet Project 2 ice core: A review. *Journal of Geophysical Research*, 102, C12, 26559-26575, doi: 10.1029/97JC00165.
- Gow, A. J., Williamson, T. (1976) Rheological implications of the internal structure and crystal fabrics of the West Antarctic ice sheet as revealed by deep core drilling at Byrd Station. *Bulletin of the Geological Society of America*, 87, 12, 1665-1677.
- Grennerat, F., Montagnat, M., Castelnau, O., Vacher, P., Moulinec, H., Suquet, P., Duval, P. (2012) Experimental characterization of the intragranular strain field in columnar ice during transient creep. *Acta Materialia*, 60, 8, 3655-3666, doi: 10.1016/j.actamat.2012.03.025.
- Gudlaugsson, E., Humbert, A., Kleiner, T., Kohler, J., Andreassen, K. (2016) The influence of a model subglacial lake on ice dynamics and internal layering. *Cryosphere*, 10, 2, 751-760, doi: 10.5194/tc-10-751-2016.

Hammer, C. U., Clausen, H. B., Langway, C. C. (1994) Electrical conductivity method (ECM) stratigraphic dating of the Byrd Station ice core, Antarctica. *Annals of Glaciology*, 20, 155-120, doi: 10.3189/172756494794587555.

Higgins, G. T. (1974) Grain-boundary migration and grain growth. *Metal Science*, 8, 5, 143-150, doi: 10.1179/msc.1974.8.1.143.

Hobbs, P. V. (1974) *Ice Physics*, Clarendon Press, Oxford.

Homer, D. R., Glen, J. W. (1978) The creep activation energies of ice. *Journal of Glaciology*, 21, 85, 429-444, doi: 10.3189/S0022143000033591.

Hudleston, P. J. (2015) Structures and fabrics in glacial ice: A review. *Journal of Glaciology*, 81, 1-27, doi: 10.1016/j.jsg.2015.09.003.

Humphreys, F. J., Hatherly, M. (2004) *Recrystallization and Related Annealing Phenomena*. Oxford, Elsevier.

Hutchinson, J. W. (1977) Creep and Plasticity of Hexagonal Polycrystals as Related to Single Crystal Slip. *Metallurgical Transactions A*, 8, 9, 1465-1469, doi: 10.1007/BF02642860.

IPCC. (2014) *Climate change 2014: Synthesis report. contribution of working groups i, ii, iii to the fifth assessment report of the intergovernmental panel on climate change*, IPCC, Geneva, Switzerland, 151.

Jansen, D., Llorens, M.-G., Westerhoff, J., Steinbach, F., Kipfstuhl, S., Bons, P. D., Griera, A., Weikusat, I. (2016) Small-scale disturbances in the stratigraphy of the NEEM ice core: observations and numerical model simulations. *The Cryosphere*, 10, 359-370, doi: 10.5194/tc-10-359-2016.

Jansen, D., Weikusat, I., Kleiner, T., Wilhelms, F., Dahl-Jensen, D., Frenzel, A., Stoll, N., Binder, T., Eichler, J., Faria, S. H., Sheldon, S., Panton, C., Kipfstuhl, S., Miller, H. (2017) In situ-measurement of ice deformation from repeated borehole logging of the EPICA Dronning Maud Land (EDML) ice core, East Antarctica. Poster presentation, EGU, Vienna (Austria). <https://meetingorganizer.copernicus.org/EGU2017/EGU2017-16368.pdf>

Johnsen, S. J., Dahl-Jensen, D., Dansgaard, W., Gundestrup, N. (1995) Greenland paleotemperatures derived from GRIP bore hole temperature and ice core isotope profiles. *Tellus B*, 47, 5, 624-629, doi: 10.1034/j.1600-0889.47.issue5.9.x.

Jones, J., Brunet, J. G. (1978) Deformation of ice single crystals close to the melting point. *Journal of Glaciology*, 21, 85, 445-455.

Kipfstuhl, S. (2010) Large area scan macroscope images from the NEEM ice core. Alfred Wegener Institute, Helmholtz Center for Polar and Marine Research, Bremerhaven, Pangaea, <https://doi.pangaea.de/10.1594/PANGAEA.743296> (unpublished dataset).

Kipfstuhl, S., Hamann, I., Lambrecht, A., Freitag, J., Faria, S. H., Grigoriev, D., Azuma, N. (2006) Microstructure mapping: a new method for imaging deformation induced microstructural features of ice on the grain scale, *Journal of Glaciology*, 52, 178, 398-406, doi: 10.3189/172756506781828647.

Kipfstuhl, S., Faria, S. H., Azuma, N., Freitag, J., Hamann, I., Kaufmann, P., Miller, H., Weiler, K., Wilhelms, F. (2009) Evidence of dynamic recrystallization in polar firn. *Journal of Geophysical Research: Solid Earth*, 114, 5, 1-10, doi: 10.1029/2008JB005583.

- Kirby, S., Durham, W., Beeman, M., Heard, H., Daley, M. (1987) Inelastic properties of ice I_h at low temperatures and high pressures. *Journal de Physique Colloques*, 48, C1, 227-232, doi: 10.1051/jphyscol:1987131.
- Kopp, R. E., DeConto, R. M., Bader, D. A., Hay, C. C., Horton, R. M., Kulp, S., Oppenheimer, M., Pollard, D., Strauss, B. H. (2017) Evolving understanding of Antarctic ice-sheet physics and ambiguity in probabilistic sea-level projections. *Earth's Future*, 5, 1-17, doi: 10.1002/2017EF000663.
- Krabbendam, M. (2016) Sliding of temperate basal ice on a rough, hard bed: creep mechanisms, pressure melting, and implications for ice streaming. *The Cryosphere*, 10, 1915-1932, doi: 10.5194/tc-10-1915-2016.
- Krischke, A., Oechsner, U., Kipfstuhl, S. (2015) Rapid Microstructure Analysis of Polar Ice Cores. *Optik & Photonik*, WILEY-VCH Verlag, Weinheim, 10, 32-35.
- Legrand, M., Mayewski, P. (1997) Glaciochemistry of polar ice cores: A review. *Reviews of Geophysics*, 35, 219-243, doi: 10.1029/96RG03527.
- Lile, R. C. (1978) The effect of anisotropy on the creep of polycrystalline ice. *Journal of Glaciology*, 21, 85, 475-483.
- Lisiecki, L. E., Raymo, M. E. (2005) A Pliocene-Pleistocene stack of 57 globally distributed benthic $\delta^{18}\text{O}$ records. *Paleoceanography*, 20, 1, 1-17, doi: 10.1019/2004PA001071.
- Lliboutry, L. (1976) Physical processes in temperate glaciers. *Journal of Glaciology*, 16, 76, 151-158, doi: 10.3189/S002214300003149X.
- Llorens, M.-G., Griera, A., Steinbach, F., Bons, P. D., Gomez-Rivas, E., Jansen, D., Roessiger, J., Lebensohn, R. A., Weikusat, I. (2017) Dynamic recrystallization during deformation of polycrystalline ice: insights from numerical simulations. *Philosophical Transactions A*, A375, 2086, doi: 10.1098/rsta.2015.0346.
- Llorens, M.-G., Griera, A., Bons, P. D., Roessiger, J., Lebensohn, R., Evans, L., Weikusat, I. (2016a) Dynamic recrystallisation of ice aggregates during co-axial viscoplastic deformation: a numerical approach. *Journal of Glaciology*, 62, 232, 359-377, doi: 10.1017/jog.2016.28.
- Llorens, M.-G., Griera, A., Bons, P., Lebensohn, R. A., Evans, L. A., Jansen, D., Weikusat, I. (2016b) Full-field predictions of ice dynamic recrystallization under simple shear conditions. *Earth and Planetary Science Letters*, 450, 233-242, doi: 10.1016/j.epsl.2016.06.045.
- Mellor, M., Testa, R. (1969) Effect of temperature on the creep of ice. *Journal of Glaciology*, 8, 52, 131-145.
- Montagnat, M., Chauve, T., Barou, F., Tommasi, A., Beausir, B., Fressengaes, C. (2015) Analysis of Dynamic Recrystallization of Ice from EBSD Orientation Mapping. *Frontiers in Earth Science*, 3, 81, 1-13, doi: 10.3389/feart.2015.00081.
- Montagnat, M., Duval, P. (2000) Rate controlling processes in the creep of polar ice, influence of grain boundary migration associated with recrystallization. *Earth and Planetary Science Letters*, 183, 1-2, 179-186, doi: 10.1016/S0012-821X(00)00262-4.
- Montagnat, M., Azuma, N., Dahl-Jensen, D., Eichler, J., Fujita, S., Gillet-Chaulet, F., Kipfstuhl, S., Samyn, D., Svenson, A., Weikusat, I. (2014) Fabric along the NEEM ice core, Greenland, and its comparison with GRIP and NGRIP ice core. *The Cryosphere*, 8, 1129-1138, doi: 10.5194/tc-8-1129-2014.

- Morgan, V. I. (1991) High-temperature ice creep tests. *Cold Regions Science and Technology*, 19, 3, 295-300, doi: 10.1016/0165-232X(91)90044-H.
- NEEM community members (2013) Eemian interglacial reconstructed from a Greenland folded ice core. *Nature*, 493, 489-493, doi: 10.1038/nature11789.
- Nereson, N. A., Waddington, E. D., Raymond, C. F., Jacobson, H. P. (1996) Predicted age-depth scales for Siple Dome and inland WAIS ice cores in West Antarctica. *Geophysical Research Letters*, 23, 22, 3163-3166, doi: 10.1029/96GL03101.
- Nye, J. F., Mae, S. (1972) The effect of non-hydrostatic stress on intergranular water veins and lenses in ice. *Journal of Glaciology*, 11, 61, 81-101, doi: 10.3189/S0022143000022528.
- Ohno, H., Igarashi, M., Hondoh, T. (2005) Salt inclusions in polar ice core: Location and chemical form of water-soluble impurities. *Earth and Planetary Letters*, 232, 1-2, 171-178, doi: 10.1016/j.epsl.2005.01.001.
- Ohno, H., Igarashi, M., Hondoh, T. (2006) Characteristics of salt inclusions in polar ice from Dome Fuji, East Antarctica, *Geophysical Research Letters*, 33, 8, 1-5, doi: 10.1029/2006GL025774.
- Orem, M. W., Adamson, A. W. (1969) Physical adsorption of Vapor on ice. *Journal of Colloid and Interface Science*, 31, 2, 278-286, doi: 10.1016/0021-9797(69)90337-3.
- Oyabu, I., Lizuka, Y., Fisher, H., Schüpbach, S., Gfeller, G., Svensson, A., Fukui, M., Steffensen, J. P., Hansson, M. (2015) Chemical composition of particles present in the Greenland NEEM ice core over the last 110,000 years. *Journal of Geophysical Research: Atmospheres*, 120, 9789-9813, doi: 10.1002/2015JD023290.
- Paterson, W. S. B. (1983) Deformation within polar ice sheets: an analysis of the Byrd station and Camp Century borehole-tilting measurements. *Cold Regions Science and Technology*, 8, 165-179.
- Paterson, W. S. B. (1991) Why ice-age ice is sometimes “soft”. *Cold Regions Science and Technology*, 20, 1, 75-98, doi: 10.1016/0165-232X(91)90058-O.
- Paterson, W. S. B. (1994) *The physics of glaciers*. Third edition. Oxford, Elsevier.
- Pimienta, P., Duval, P. (1987) Rate controlling processes in the creep of polar glacier ice. *Journal de Physique Colloques*, 48, C1, 243-248, doi: 10.1051/jphyscol:1987134.
- Qi, C., Goldsby, D. L., Prior, D. J. (2017) The down-stress transition from cluster to cone fabrics in experimentally deformed ice. *Earth and Planetary Science Letters*, 471, 136-147, doi: 10.1016/j.epsl.2017.05.008.
- Raj, R., Ashby, M. F. (1971) On grain boundary sliding and diffusional creep. *Metallurgical Transactions*, 2, 4, 1113-1127, doi: 10.1007/BF02664244.
- Rasmussen, S. O., Abbott, P. M., Blunier, T., Bourne, E., Brook, E., Buchardt, S. L., Buizert, C., Chappellaz, J., Clausen, H. B., Cook, E., Dahl-Jensen, D., Davies, S. M., Guillevic, M., Kipfstuhl, S., Laepple, T., Seierstad, I. K., Severinghaus, J. P., Steffensen, J. P., Stowasser, C., Svensson, A., Vallenga, P., Vinther, B. M., Wilhelms, F., Winstrup, M. (2013) A first chronology for the North Greenland Eemian Ice Drilling (NEEM) ice core. *Climate of the past*, 9, 2713-2730, doi: 10.5194/cp-9-2713-2013.
- Rigsby, G. P. (1958) Effect of hydrostatic pressure on velocity of shear deformation of single ice crystals. *Journal of Glaciology*, 3, 24, 273-278, doi: 10.3189/S0022143000023911.

Rogozhina, I., Petrunin, A. G., Vaughan, A. P. M., Steinberger, B., Johnson, J., Kaban, M. K., Calov, R., Rickers, F., Thomas, M., Koulakov, I. (2016) Melting at the base of the Greenland ice sheet explained by Iceland hotspot history. *Nature Geosciences*, 9, 366-369, doi: 10.1038/NGEO2689.

Russell-head, D. S., Budd, W. F. (1979) Ice-sheet flow properties derived from bore-hole shear measurements combined with ice-core studies. *Journal of Glaciology*, 24, 90, 117-130, doi: 10.3189/S0022143000014684.

Ruth, U., Barnola, J.-M., Beer, J., Bigler, M., Castellano, E., Fisher, H., Fundel, F., Huybrechts, P., Kaufmann, P., Kipfstuhl, S., Lambrecht, A., Morganti, A., Oerter, H., Parrenin, F., Rybak, O., Severi, M., Udisti, R., Wilhelms, F., Wolff, E. (2007) "EDML 1": a chronology of the EPICA deep ice core from Dronning Maud Land, Antarctica, over the last 150 000 years. *Climate of the Past*, 3, 475-484, doi: 10.5194/cp-3-475-2007.

Sakurai, T., Iizuka, Y., Horikawa, S., Johnsen, S., Dahl-Jensen, D., Steffensen, J. P., Hondoh, T. (2009) Direct observations of salts as micro-inclusions in the Greenland GRIP ice core. *Journal of Glaciology*, 55, 193, 777-783, doi: 10.3189/002214309790152483.

Sakurai, T., Ohno, H., Horikawa, S., Iizuka, Y., Uchida, T., Hirakawa, K., Hondoh, T. (2011) The chemical forms of water-soluble microparticles preserved in the Antarctic ice sheet during Termination I. *Journal of Glaciology*, 57, 206, 1027-1032, doi: 10.3189/002214311798843403.

Saylor, M. S., Rohrer, G. S. (1999) Measuring the Influence of Grain-Boundary Misorientation on Thermal Groove Geometry in Ceramic Polycrystals. *Journal of the American Society*, 82, 6, 1529-1536, doi: 10.1111/j.1151-2916.1999.tb01951.x.

Schulson, E. M., Duval, P. (2009) *Creep and Fracture of Ice*. Cambridge University Press, Cambridge.

Sheldon, S. G., Steffensen, J. P., Hansen, S. B., Popp, T. J., Johnsen, S. J. (2014) The investigation and experience of using ESTISOL™ 240 and COASOL™ for ice-core drilling. *Annals of Glaciology*, 55, 68, 219-232, doi: 10.3189/2014AoG68A036.

Steinbach, F., Bons, P. D., Griera, A., Jansen, D., Llorens, M.-G., Roessiger, J., Weikusat, I. (2016) Strain localization and dynamic recrystallization in the ice-air aggregate: a numerical study. *The Cryosphere*, 10, 6, 3071-3089, doi: 10.5194/tc-10-3071-2016.

Steinbach, F., Kuiper, E. N., Eichler, J., Bons, P. D., Drury, M. R., Griera, A., Pennock, G., Weikusat, I. (2017) The Relevance of Grain Dissection for Grain Size Reduction in Polar Ice: Insights from Numerical Models and Ice Core Microstructure Analysis. *Frontiers in Earth Science*, 5, 66, 1-19, doi: 10.3389/feart.2017.00066.

Suwa, M., von Fischer, J. C., Bender, M. L., Landais, A., Brook, E. J. (2006) Chronology reconstruction for the disturbed bottom section of the GISP2 and the GRIP ice cores: Implications for Termination II in Greenland. *Journal of Geophysical Research*, 111, 2, 1-12, doi: 10.1029/2005JD006032.

Thorsteinsson, T., Waddington, E. D., Taylor, K. C., Alley, R. B., Blankenship, D. D. (1999) Strain-rate enhancement at Dye 3, Greenland. *Journal of Glaciology*, 45, 150, 338-345, doi: 10.3189/002214399793377185.

Thorsteinsson, T., Kipfstuhl, J., Eicken, H., Johnsen, S. J., Fuhrer, K. (1995) Crystal size variations in Eemian-age ice from the GRIP ice core, Central Greenland. *Earth and Planetary Science Letters*, 131, 381-394, doi: 10.1016/0012-821X(95)00031-7.

- Thorsteinsson, T., Kipfstuhl, J., Miller, H. (1997) Textures and fabrics in the GRIP ice core. *Journal of Geophysical Research*, 102, C2, 26583-26599, doi: 10.1029/97JC00161.
- Van de Wal, R. S. W., Boot, W., Van den Broeke, M. R., Smeets, C. J. P. P., Reijmer, C. H., Donker, J. J. A., Oerlemans, J. (2008) Large and Rapid Melt-Induced Velocity Changes in the Ablation Zone of the Greenland Ice Sheet, *Science*, 321, 111-113, doi: 10.1126/science.1158540.
- Van der Veen, C. J., Whillans, I. M. (1994) Development of fabrics in ice. *Cold Regions Science and Technology*, 22, 1, 171-195, doi: 10.1016/0165-232X(94)90027-2.
- Von Mises, R. (1928) *Mechanik der Plastischen Formänderung von Kristallen*. *Zeitschrift für Angewandte Mathematik und Mechanik*, 8, 161-185.
- Weertman, J. (1983) Creep deformation of ice. *Annual Reviews of Earth and Planetary Sciences*, 11, 215-240.
- Weikusat, I., Jansen, D., Binder, T., Eichler, J., Faria, S. H., Wilhelms, F., Kipfstuhl, S., Sheldon, S., Miller, H., Dahl-Jensen, D., Kleiner, T. (2017) Physical analysis of an Antarctic ice core (EDML) – towards an integration of micro- and macrodynamics of polar ice. *Philosophical Transactions A*, 375, doi: 10.1098/rsta.2015.0347.
- Wenk, H.-R., Canova, A., Molinari, A., Kocks, U. F. (1989) Viscoplastic modelling of texture development in quartzite. *Journal of Geophysical Research*, 94, B12, 17895-17906, doi: 10.1029/JB094iB12p17895.
- Wettlaufer, J. S. (1999a) Ice Surfaces : Macroscopic Effects of Microscopic Structure. *Philosophical Transactions: Mathematical, Physical and Engineering Sciences*, 357, 1763, 3403-3425.
- Wettlaufer, J. S. (1999b) Impurity effects in the Premelting of Ice. *Physical Review Letters*, 82, 12, 2516-2519, doi: 10.1103/PhysRevLett.82.2516.
- Wilson, C. J. L., Zhang, Y. (1996) Development of microstructure in the high-temperature deformation of ice. *Annals of Glaciology*, 23, 293-302, doi: 10.3189/S0260305500013562.
- Wilson, C. J. L., Zhang, Y., Stüwe, K. (1996) The effects of localized deformation on melting processes in ice. *Cold Regions Science and Technology*, 24, 177-189.
- Woodcock, N. H. (1977) Specification of fabric shapes using an eigenvalue method. *Journal of Structural Geology*, 88, 9, 1231-1236, doi: 10.1130/0016-7606(1977)88<1231:SOF SUA>2.0.CO;2.
- Zwally, H. J., Abdalati, W., Herring, T., Larson, K., Saba, J., Steffen, K. (2002) Surface Melt-Induced Acceleration of Greenland Ice-Sheet Flow. *Science*, 297, 218-223, doi: 10.1126/science.1072708.

Recrystallization and deformation mechanisms in the NEEM deep ice core, Greenland

After:

Kuiper, E. N., Weikusat, I., Pennock, G. M., de Bresser, J. H. P., Drury, M. R.
Recrystallizations and deformation mechanisms in the NEEM deep ice core, Greenland.
Manuscript in preparation.

Abstract

The discharge of ice into the ocean depends on the flow of ice in polar ice sheets, which is controlled by various recrystallization and deformation mechanisms. This Chapter aims to provide an overview of the recrystallization and deformation mechanisms in the North Greenland Eemian Ice Drilling (NEEM) ice core based on (polarized) light microscopy (LM) techniques and cryogenic electron backscatter diffraction (cryo-EBSD) studies along the length of the NEEM ice core. Nine ice core sections were used for EBSD mapping in this study: three from the Holocene ice (0-1419 m of depth), four from the glacial ice (1419-2207 m of depth) and two from the Eemian-glacial facies (2207-2540 m of depth). Analysis of EBSD and LM microstructures together with crystallographic preferred orientations (CPOs) were combined with the results from Chapter 2 to 5 of this thesis and other relevant work on the NEEM ice core in order to describe which recrystallization and deformation mechanisms are active at what depth in the NEEM ice core.

In the glacial ice, the microstructures in very fine grained sub-horizontal bands indicate a process resembling microstructural shear, a process by which limited grain boundary sliding (GBS) along aligned grain boundaries produces subgrain boundaries (SGBs) in those grains that block the sliding grains: these SGBs increase in misorientation angle to become grain boundaries and become part of the aligned grain boundary structure, which acts as a positive feedback on further sliding along the aligned grain boundaries. The critical misorientation angle at which GBS can initiate was inferred to be about 5.0° - 6.0° . The very strong c-axes CPO, together with the alignment of a-axes in these fine grained sub-horizontal bands, indicates high activity of dislocation glide along the basal plane. This suggests that GBS is an accommodating mechanism for basal slip and that this grain size sensitive deformation mechanism does not destroy CPO, but strengthens it.

No evidence for GBS was found in the Holocene ice, while microstructural analyses showed evidence of extensive strain induced boundary migration (SIBM) and non-basal slip. Therefore, it is proposed that the Holocene ice deforms by basal slip accommodated by non-basal slip and SIBM, where the extent of non-basal slip is controlled by recovery via SIBM, which removes dislocations and stress concentrations in grains and allows further deformation to occur. The dominant recrystallization mechanisms and processes in the upper part of the Holocene ice are bulging recrystallization, SIBM, grain dissection and normal grain growth, whereas rotation recrystallization is expected to be relatively unimportant.

The relatively high percentage of SGBs indicative of non-basal slip in the glacial ice indicates that significant non-basal slip is activated as well as GBS, which are both mechanisms that accommodate basal slip. Microstructural analysis in the glacial ice shows that SIBM is less important than in the Holocene ice, whereas rotation recrystallization is more important.

The ice in the Eemian-glacial facies is likely affected by premelting along the grain boundaries which results in a higher grain boundary mobility. In the impurity-depleted Eemian layers in the Eemian-glacial facies, the high grain boundary mobility

results in extensive SIBM leading to very coarse and interlocking grains with a broad single maximum or small girdle circle CPO. In case of impurity-rich glacial ice in the Eemian-glacial facies, the grains remain relatively small and develop a single maximum CPO. It is expected that the impurity-depleted Eemian layers are relatively stagnant or deform by coaxial deformation at relatively low strain rates, while the impurity-rich glacial layers deform predominantly by simple shear at much higher strain rates. The difference in microstructure, and consequently in viscosity, between the glacial and interglacial ice at temperatures just below the melting point can have important consequences for ice sheet dynamics close to the bedrock.

Flow law modelling using the modified composite flow law of Goldsby and Kohlstedt (2001) (Chapter 4 and 5) predicts that GBS-limited creep is the dominant deformation mechanisms along almost the entire length of the NEEM ice core. Ice microstructures in the Holocene ice and in the coarse grained layers in the Eemian-glacial facies suggest that dislocation creep is the dominant deformation mechanism at these depths. This discrepancy could be the result of dynamic recovery and recrystallization mechanisms not being active during the deformation experiments used to calibrate the composite flow law, while these mechanisms enhance dislocation creep at high strain.

6.1 Introduction

Research into recrystallization and deformation mechanisms of polar ice has been topic of scientific studies for many decades (e.g. Mellor and Testa, 1969a, b; Duval et al., 1983; Alley, 1992; Montagnat and Duval, 2004; Faria et al., 2014a). Studying deformation mechanisms of polar ice is challenging due to the remote location of polar ice sheets and the technical challenges that come with recovering polar ice cores. Polar ice is remarkably pure compared to natural rocks (e.g. Legrand and Mayewski, 1997) and can be considered as an analogue for high temperature ($T/T_{\text{melt}} > 0.85$) rock deformation with a strong plastic anisotropy (Fukuda et al., 1987; Hondoh, 2000). The accelerating mass loss from the Greenland and Antarctic ice sheets in recent decades (e.g. IPCC, 2014) further enhances interest in recrystallization and deformation mechanisms of polar ice. Therefore, the physical properties of ice from polar ice cores, which so far have mainly been drilled for the purpose of climate reconstruction, have received more attention from glaciologists in recent decades. This Chapter provides an overview of the dominant recrystallization and deformation mechanisms with depth in the North Greenland Eemian Ice Drilling (NEEM) ice core based on cryogenic electron backscatter diffraction (cryo-EBSD) and (polarized) light microscopy (LM) techniques.

Under natural conditions on Earth, ice only occurs in the hexagonal form of I_h (e.g. Durham et al., 1997; Schulson and Duval, 2009). The ice single crystal has a very high plastic anisotropy with dislocation glide on the easy slip system, the basal plane, being at least 60 times easier to activate than dislocation glide on one of the non-basal planes, such as the prismatic and pyramidal planes (Duval et al., 1983). Since basal slip accounts for only two of the five independent slip systems needed for constant volume deformation (Von Mises, 1928), basal slip needs to be accommodated by non-basal slip or by other deformation mechanisms. It is well established that at equivalent stresses of >0.1 MPa basal slip is accommodated by non-basal slip (e.g. Schulson and Duval, 2009), also known as dislocation creep. Dislocation creep is assumed to be independent of grain size and the stress exponent, relating equivalent stress to equivalent strain rate ($\dot{\epsilon} \propto \sigma^n$), has a value of 3 during secondary creep in the stress range of 0.1-1.0 MPa (e.g. Glen, 1955; Frost and Ashby, 1982; Duval et al., 1983; Jacka, 1984; Budd and Jacka, 1989; Paterson, 1994). However, at the low stress conditions that are applicable to polar ice sheets, basal slip can be accommodated by a different mechanism than non-basal slip. An accommodating mechanism other than non-basal slip could explain the low stress exponents of $n \sim 2$ found in ice deformation tests on experimental ice (e.g. Mellor and Testa, 1969a; Pimienta and Duval, 1987; Duval and Castelnau, 1995; Goldsby and Kohlstedt, 1997, 2001) and borehole closure and flow analysis of naturally deformed polar ice sheets (e.g. Doake and Wolff, 1985; Dahl-Jensen and Gundestrup, 1987; Alley, 1992).

One of the possible accommodating mechanisms for basal slip in polar ice is grain boundary sliding (GBS). Due to the high homologous temperature of polar ice sheets ($T/T_{\text{melt}} > 0.85$), it has long been suggested that GBS could play a role in polar ice deformation, particularly at temperatures close to the melting point (Barnes et al., 1971;

Ignat and Frost, 1987; Morgan, 1991; Durham et al., 1997, 2010; Goldsby and Kohlstedt, 1997, 2001). Furthermore, it is well known that ice that originated in the glacial periods coincides with smaller grain sizes and higher borehole deformation rates (e.g. Fisher and Koerner, 1986; Paterson, 1994; Cuffey et al., 2000a), which could be explained by a grain size sensitive mechanism such as GBS. However, despite theoretical (e.g. Durham et al., 2010) and experimental evidence (Ignat and Frost, 1987; Goldsby and Kohlstedt, 1997, 2001), GBS has not yet been shown to be a relevant accommodating deformation mechanism in polar ice sheets and its importance in deformation of polar ice remains controversial (Duval and Montagnat, 2002; Goldsby and Kohlstedt, 2002).

One of the other mechanisms that has often been proposed to accommodate basal slip in polar ice is strain induced boundary migration (SIBM) associated with recrystallization (Pimienta and Duval, 1987; Montagnat and Duval, 2000; Duval et al., 2000). The build-up of internal stresses caused by strain incompatibilities can be removed by SIBM, after which deformation by basal slip can continue. Montagnat and Duval (2000) argue that a flow law with $n < 2$ could be related to recovery by SIBM, which could therefore well explain the $n \sim 2$ found in deformation tests and borehole data, as discussed above. SIBM and rotation recrystallization have been shown to be active at all depths in polar ice sheets, although the extent of these mechanisms varies strongly with depth (e.g. Duval and Castelnau, 1995; Obbard et al., 2006; Kipfstuhl et al., 2006, 2009; Weikusat et al., 2009a, 2009b; Binder, 2014).

The recrystallization mechanisms that are active in ice are similar to those in metals and rocks (e.g. Humphreys and Hatherly, 2004; Passchier and Trouw, 2005; Faria et al., 2014a). The contribution of the different recrystallization mechanisms depends on factors like temperature, impurity content, stress and deformation mode, all of which change with depth along polar ice cores (e.g. Duval et al., 1983; Alley, 1992; Faria et al., 2014a, b). The difference in contribution of the different recrystallization mechanisms controls the evolution of the ice microstructure, which in turn determines which deformation mechanisms are active at what depth. An understanding of the recrystallization and deformation mechanisms in polar ice can be used to improve the description of ice rheology in ice sheet models that are used to help predict future mass loss from the Greenland and Antarctic ice sheets.

This Chapter provides an overview of the different recrystallization and deformation mechanisms that occurred at different depths in the NEEM ice core. Large datasets of the grain boundary network (Binder et al., 2013; Binder, 2014) and crystallographic preferred orientation (CPO) (Eichler et al., 2013) were used to locate areas of interest for cryo-EBSD mapping. The results of a study of slip systems of subgrain boundaries (SGBs) of the same EBSD data set was presented in Chapter 2 and 3 of this thesis. The dataset of the grain boundary network was used to study the effect of grain size on strain rate in the NEEM ice core (Chapter 4 and 5). The results of these and other microstructure studies of the NEEM ice core (e.g. NEEM community members, 2013; Eichler et al., 2013, 2017; Binder, 2014; Montagnat et al., 2014, Jansen et al., 2016; Steinbach et al., 2017; Chapter 2-5) were combined with results from microstructural

analysis from the EBSD dataset to infer which recrystallization and deformation mechanisms were active at what depth in the NEEM ice core. Typical examples of LM images and EBSD maps at different depths are shown and analyzed in terms of recrystallization and deformation mechanisms. Hereby, the NEEM ice core was separated into three different depth intervals that coincide with certain climate periods. The three different depth intervals differ strongly in terms of grain size, grain shape, crystallographic preferred orientation (CPO), temperature and deformation mode (Figure 1.8): the Holocene ice (0-1419 m of depth), the glacial ice (1419-2207 m of depth) and the Eemian ice (2207-2540 m of depth).

6.2 Background NEEM ice core

The NEEM deep ice core (77.45°N, 51.07°W, surface elevation 2479 m, ice core length 2540 m) was drilled in the field seasons between 2008 and 2012 (Rasmussen et al., 2013). The ice core is located in the northwest of the Greenland ice sheet next to a ridge running roughly southeast-northwest (NEEM community members, 2013). The flow at NEEM is slightly divergent with the main component of the flow parallel to the ridge and a small contribution of flow perpendicular to the ridge. The horizontal flow velocity at the surface is about 6 m per year, with the average annual surface temperature being about -29°C (NEEM community members, 2013; Rasmussen et al., 2013).

The upper 1419 meters of the NEEM ice core consists of ice that was deposited during the Holocene (Holocene ice), with ice deposited during the last glacial period (glacial ice) below until a depth of 2207 m (NEEM community members, 2013). The stratigraphy of the ice below 2207 m is heavily folded, partly overturned and contains at least four stratigraphic disruptions, which were identified by measurements of oxygen stable isotope values ($\delta^{18}\text{O}_{\text{ice}}$) of H₂O and methane (CH₄) (NEEM community members, 2013). The folded and overturned parts consist of glacial and Eemian ice which result in the alternation of ice from the glacial and the Eemian. In the remainder of this Chapter, the ice below 2207 m of depth will be referred to as Eemian-glacial facies.

The mean annual layer thickness (ice equivalent) decreases from 22 cm at the surface to about 1-2 cm at 1600 m of depth and remains relatively constant in the remainder of the glacial ice (Rasmussen et al., 2013). The annual layer thickness in the Eemian-glacial facies is unknown due to the folding and stratigraphic discontinuities in this part of the NEEM ice core (NEEM community members, 2013; Westhoff, 2014).

Figure 1.8 provides an overview of the most important microstructural data (Binder et al., 2013; Eichler et al., 2013; Binder, 2014) and borehole temperature data (Sheldon et al., 2014) for analysing recrystallization and deformation mechanisms in the NEEM ice core. The CPO in the NEEM ice core shows a progressive strengthening with depth from slightly anisotropic just below the surface to a strong single maximum in the glacial ice (Eichler et al., 2013; Figure 1.8a). A weak girdle fabric (or elongated single maximum) develops in the Holocene ice, which disappears at the Holocene-glacial interface. The CPO changes suddenly at the interface between the glacial ice and the

Eemian-glacial facies and varies strongly with depth in the remainder of the Eemian-glacial facies. The mean grain area increases roughly linearly with depth from sub-millimetre size just below the surface to about 5-7 mm² at 400 m of depth (Eichler et al., 2013; Figure 1.8b). The mean grain area between about 400 and 1419 m is 5-10 mm², although variability with depth is relatively high. In the glacial ice, the mean grain area decreases to 1-3 mm². At the interface between the glacial ice and the Eemian-glacial facies, the mean grain area strongly increases and is highly variable with depth in the remainder of the Eemian-glacial facies ranging from about 20 mm² to many hundreds of mm².

The temperature in the upper ~1200 m of the ice core is equal to the average annual surface temperature of -29°C, below which the temperature steadily increases, reaching an in-situ temperature of -3.4°C at the ice-bedrock interface (Sheldon et al., 2014; Figure 1.8c). The mean grain shape, quantified using the mean perimeter ratio (Uthus et al., 2005; Hamann et al., 2007; Binder, 2014), provides a measure for the irregularity of grain boundaries, with high values (close to unity) indicating a regular grain boundary structure, while low values indicate a more irregular grain boundary structure. The mean perimeter ratio decreases from relatively high values just below the surface to a relatively low values between 600 and 1300 m of depth (Binder, 2014; Figure 1.8d). In the glacial ice, the grain shape becomes more regular with a mean perimeter ratio of >0.9. In the Eemian-glacial facies, the grain shape becomes more irregular again, although variability with depth is high until the ice-bedrock interface. The SGB density, determined by digitally analysing LM images, does not show a strong trend with depth (Binder, 2014; Figure 1.8e). Along most of the ice core, SGB density is about 0.2-0.3 mm⁻¹, although somewhat higher SGB densities of 0.5-0.6 mm⁻¹ were measured at about 400 m and 1800 m of depth and at the interface of the Holocene ice with the glacial ice and interface of the glacial ice with the Eemian-glacial facies.

6.3 Materials and methods

The EBSD dataset used in this paper was obtained from nine ice core sections in the NEEM ice core: three from the Holocene ice at 443 m, 718 m and 889 m of depth, four from the glacial ice at 1767 m, 1937 m, 1993 m and 2103 m of depth and two from the Eemian-glacial facies at 2241 and 2423 m of depth (right side of Figure 1.8). All nine sections were mapped using cryo-EBSD in the period between July 2014 and August 2016. The samples were stored (-30°C) and processed (-20°C) at the Alfred Wegener Institute (AWI) in Bremerhaven, Germany. Prior to cutting the EBSD samples (Appendix A), the samples were polished using a microtome (Pauer et al., 1999), left to controlled sublimation for thermal etching of grain boundaries, and a large area scanning microscope (LASM) (Krischke et al., 2015) image was made. After EBSD sample preparation, according to the methods of Weikusat et al. (2011a), another LM image was made of the surface of the freshly cut EBSD sample. This LM image was compared to the scanning electron microscope (SEM) images and EBSD mapped microstructures to check for microstructural changes during sample transport and storage. The EBSD samples were packed and

transported using dry ice (solid carbon dioxide, -78.5°C) to Utrecht University in the Netherlands. The EBSD samples were stored between 2 and 21 days in a -20°C storage room after which the samples were mapped using cryo-EBSD in a SEM (Appendix B). The dry ice took about a week to fully sublime, so the EBSD samples were at dry ice temperature most of the time during storage at Utrecht University.

All ice core sections, except the section at 443 m of depth, were mapped using a FEI Nova Nanolab equipped with an EBSD detector (Oxford Instruments HKL Technology, Abingdon, UK) and a cryo-stage (Quorum Technologies Ltd. Ringmer, UK). The EBSD patterns were acquired, processed and indexed using the Channel 5 software of OI_HKL Technology. The sample at 443 m of depth was mapped using a FEI Helios Nanolab G3 UC which was equipped with the same EBSD detector and cryo-stage. The EBSD patterns of this ice core section were acquired, processed and indexed using the AZTEC software (Oxford Instruments, High Wycombe, UK). SEM conditions typically were: sample stage temperature of -150°C to -100°C , working distance of 6-12 mm, beam current of 2.1-8.4 nA, accelerating voltage of 7.5-20 kV and SEM chamber pressure of 10^{-7} to 10^{-5} hPa. Conditions for EBSD collection typically were: pattern binning of 1x1 to 4x4, step size of 5-20 μm and frame averaging of 1-2. Mapping rates were between 8 to 30 pixels s^{-1} . After re-indexing the stored patterns and orientation averaging by two passes of a 3x3 filter (Humphreys et al., 2001), the majority of the EBSD maps had an index rate of $>80\%$. The angular resolution of the EBSD maps was about 0.5° . The Channel 5 software was used to analyse the EBSD maps. For a more elaborate description of the sample preparation, sample transfer into the SEM and EBSD mapping settings, the reader is referred to Weikusat et al. (2011a) and Appendix A and B.

In general, EBSD mapping of Holocene and glacial ice was successful and the microstructural features observed in the LM images, made just after EBSD sample preparation, the SEM images and the EBSD maps were the same. Occasionally, grain boundaries migrated or grains grew or shrunk during transport and storage of the samples, which happened most often with small grains. The transfer of EBSD samples from the Eemian-glacial facies into the SEM turned out to be problematic. Many EBSD samples from this depth range cracked during the SEM transfer procedure (Appendix B), which resulted in loss of the EBSD sample or severe problems with charging during EBSD mapping. Due to these problems with the EBSD samples from the Eemian-glacial facies, combined with the large grain size and low density of microstructural features in the Eemian-glacial facies (Binder, 2014; Figure 1.8), the focus of the EBSD studies was laid on the Holocene and glacial ice instead of the Eemian-glacial facies. Some of the EBSD maps were rotated relative to the LM image due to a misalignment of the EBSD sample in the SEM (e.g. Figure 6.2 and 6.4).

The EBSD maps of the ice core sections were stitched together in order to improve the statistics of the c- and a-axes distribution for each ice core section (Figure 6.5). The ice core section in the glacial ice at 1937 m of depth and the two ice core sections in the Eemian-glacial facies were excluded due to insufficient data. Orientation information (Euler angles) from misaligned EBSD samples were rotated using the Channel 5 software

so that all mapped data information was aligned to the vertical axis of the core. The EBSD dataset was also used to obtain a first order estimate of the orientation gradient in the samples. About 30 to 40 misorientation profiles were taken along the long axis of a random selection of grains in each ice core section. The total misorientation angle along the long

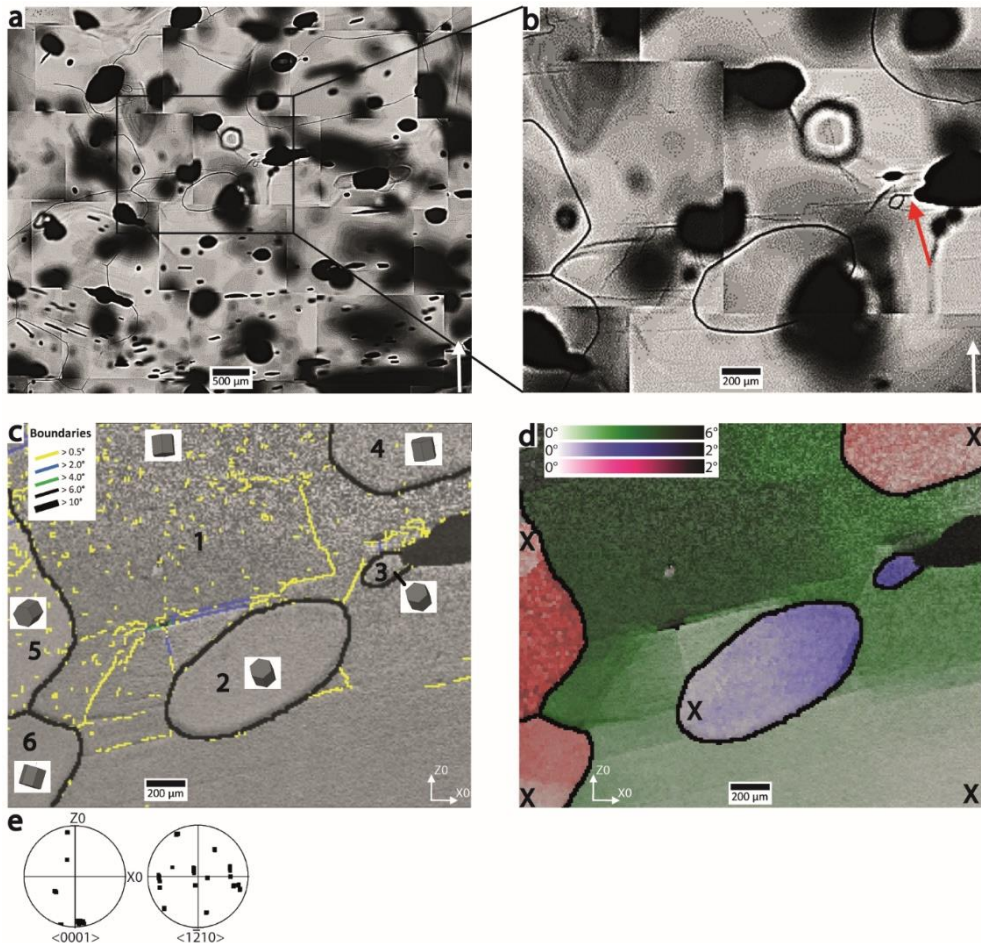


Figure 6.1: Transmitted light microscopy and corresponding EBSD data showing a typical shallow sample from the Holocene ice at 443 m of depth (NEEM 806-10) of an area where microstructures suggest that stored strain energies were high enough for SIBM to be active. (a) Transmitted LM image taken just after EBSD sample preparation with the white arrow pointing towards the top of the ice core. Black spots are air bubbles at or just below the surface of the EBSD sample. (b) Part of the same transmitted LM image showing the region mapped by cryo-EBSD. The red arrow shows a (sub)grain boundary that was consumed by the growth of grain 3 during transport and storage of the EBSD sample. (c) The corresponding EBSD map (greyscale shows pattern quality) showing the orientation of each grain in the EBSD map with a schematic of the hexagonal crystal and the boundary misorientation angle colour code. (d) Map showing the orientation difference up to 6° in green and up to 2° in blue and red in each grain relative to the spots marked with 'X'. Only the higher angle boundary misorientations of >6° are shown as black lines. (e) Pole figure (equal area, upper hemisphere projection) of the <0001> and <1210> axes of the grains in the EBSD map.

axis of the grain was plotted against the length of the misorientation profile in a scatter plot (Figure 6.6). SGBs up to 5° were included in the misorientation profile as this is expected to be the critical angle between SGBs and grain boundaries in ice (Weikusat et al., 2011b; Montagnat et al., 2015). A linear trend line through the scatter plot provides a first order estimate of the average orientation gradient in each ice core section ($^\circ \text{mm}^{-1}$). This method of estimating the orientation gradient in the ice core sections was preferred over using the grain orientation spread (GOS) or the maximum deviation from the mean orientation (MOS), since often only part of the grains was mapped with EBSD during this study.

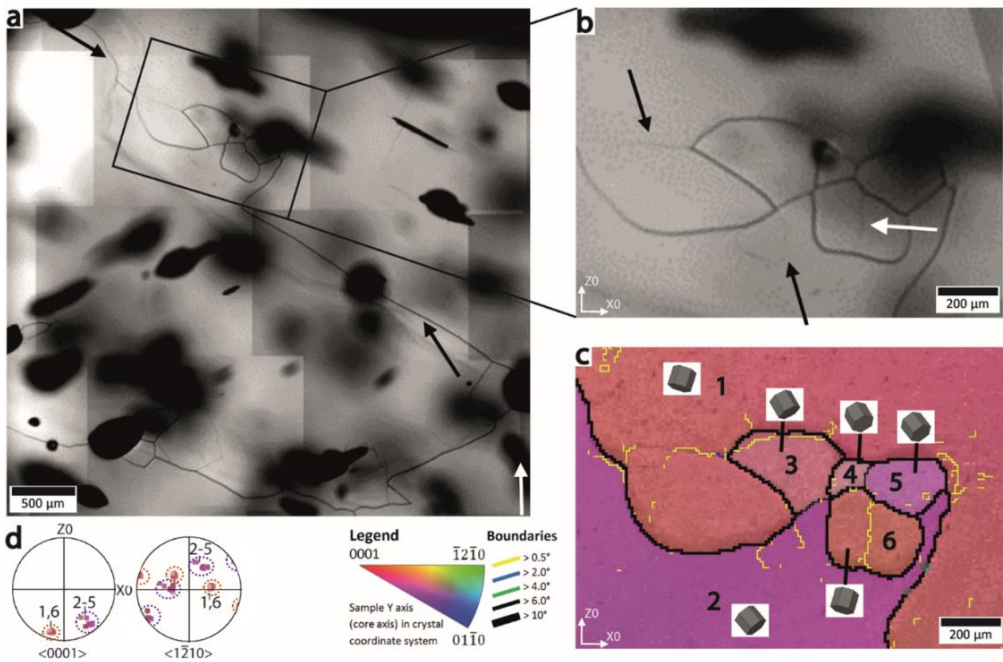


Figure 6.2: Transmitted light microscopy and corresponding EBSD data of an ice core section in the Holocene ice at 718 m of depth (NEEM 1306-50) of an area where small grains were probably formed along a grain boundary by bulging recrystallization, which isolated sections of grain 2 by SIBM and with rotation became new grains 3-5. (a) Transmitted LM image taken just after EBSD sample preparation with the white arrow pointing towards the top of the ice core. Black spots are air bubbles at or just below the surface of the EBSD sample. The image shows two large grains with a relatively straight grain boundary (black arrows) except for the boxed region where the grain boundaries bulge and small grains are present. (b) Boxed region of (a) showing one subgrain boundary indicated by the white arrow and two subgrains indicated by black arrows. (c) The corresponding EBSD map (IPF colouring) showing a schematic of the hexagonal crystal of each grain in the EBSD map and the boundary misorientation colour code. Grains 3-5 have an orientation that is close, but not similar to grain 2, while grain 6 has the same orientation as grain 1, as shown by the schematic and also shown in (d). (d) Pole figures (equal area, upper hemisphere projection) of the $\langle 0001 \rangle$ and $\langle 1\bar{2}10 \rangle$ axes of the grains in the EBSD map, with the purple and orange dotted circles indicating grains with similar $\langle 0001 \rangle$ and $\langle 1\bar{2}10 \rangle$ axes orientation.

6.4 Results

Comparing the LM images to the EBSD microstructures showed that in most cases the surface of the EBSD sample remained stable during transport and storage. The areas of the EBSD samples that showed microstructural changes were often located next to air bubbles or clathrate hydrates (Kipfstuhl et al., 2001). An example of this is shown Figure 6.1 where grain 3 is considerably larger in the EBSD map (Figure 6.1c) than in the LM image made just after sample preparation (Figure 6.1b). This small grain grew towards the air bubble during transport and storage of the EBSD sample and consumed a (sub)grain boundary in the process (red arrow Figure 6.1b). Experience showed that grain boundaries were more mobile than SGBs during transport and storage of the EBSD sample. About 25 to 45 EBSD maps were acquired of each ice core section that was mapped, except for the ice core section in the Eemian-glacial facies due to problems with cracking of the EBSD samples during the transfer procedure (Appendix B). A selection of LM images and corresponding EBSD data is presented below showing different types of microstructure at different depths in the NEEM ice core.

The transmitted LM image from 443 m of depth (Figure 6.1a) shows a typical example of the microstructure in the Holocene ice at shallow depths with a set of large (mean grain size about 5 mm) and irregular shaped grains. The EBSD mapped data shows a large grain (grain 1, Figure 6.1c) with a high number of mostly low angle SGBs (0.5° - 2.0°) located in the centre of the EBSD map. In this region of high SGB density two island grains (grain 2 and 3) are present, where the term ‘island’ means that these grains are unconnected to the surrounding grains in the 2D section. The two island grains have a similar orientation

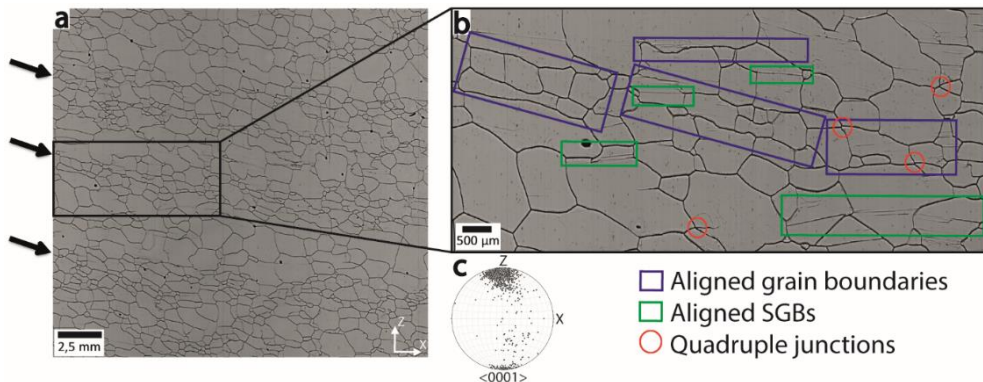


Figure 6.3: Part of a reflective LASM image of an etched ice core section in the glacial ice at 1977 m depth (NEEM 3596-30). The arrows on the left of (a) indicate fine grained sub-horizontal bands with relatively coarse grains in between. The z-axis points towards the top of the ice core. (b) Boxed region of (a) showing grain boundaries (darker lines) and SGBs (lighter lines). Several grains have aligned grain boundaries (purple rectangles). Green rectangles show locations where SGBs are aligned to the GB network. Quadruple junctions are indicated by red circles. (c) Pole figure of $\langle 0001 \rangle$ (equal area, vertical plane, one point per grain) for the whole ice core section (90 x 55 mm). LASM image taken from the PANGAEA database (doi: 10.1594/PANGAEA.743296).

(Figure 6.1c), are free of SGBs $>0.5^\circ$ and have a relatively low orientation gradient (Figure 6.1d). The orientation gradient in grain 1 (Figure 6.1d) is highest in the region between grains 5 and 6 and the island grain 2.

The maps in Figure 6.2 (Holocene ice at 718 m of depth) shows a set of four very small grains (100-300 μm in diameter) clustered at the grain boundary between two large grains. The grain boundary between grain 1 and 2 is relatively straight (black arrows, Figure 6.2a), except for the part where the four very small grains are located (boxed region in Figure 6.2a). The four small grains are next to two air bubbles, one at the surface which is in focus and a larger bubble just below the surface that is out of focus (Figure 6.2b). The c- and a-axes orientations of grain 1 and 6 are similar (orange circles in Figure 6.2d). The c- and a-axes orientation of grains 2-5 are clustered in the pole figures (purple circles in Figure 6.2d) and differ by about 10° - 15° .

The EBSD map (Figure 6.2c) shows that grain 3 contains a low angle SGB (0.5° - 2.0°) oriented parallel to the grain boundary. This SGB could not be identified in the transmitted LM image (Figure 6.2b) or SEM image (not shown), but was identified in the unprocessed EBSD map (not shown). Grain 6 does contain a low angle SGB (0.5° - 2.0°) in the middle of the grain that can also be identified in the transmitted LM image (white arrow in Figure 6.2b). Two low angle subgrains, indicated by the black arrows in Figure 6.2b, were identified in the EBSD map but were partly below the angular resolution of 0.5° of the EBSD method.

The grain size variation in the glacial ice is shown in the reflective LM image in figure 6.3 (1977 m of depth), which is from one of the finest grained depths of the glacial ice in the NEEM ice core. The mean grain area of the complete 90 x 55 mm ice core section is 1.1 mm^2 (Binder, 2014). The grain area within this ice core section is not constant but alternates between coarser and finer grained bands that are oriented sub-horizontally. The fine grained bands are indicated by the black arrows on the left side of Figure 6.3a. The mean grain area in these fine grained sub-horizontal bands is about 0.25 - 0.5 mm^2 . Besides from being one of the finest grained ice core section in the NEEM ice core, the CPO of this ice core section is very strong with an eigenvalue of 0.97 (Eichler et al., 2013). The reflective LM image at higher magnification (Figure 6.3b) shows several cases of aligned grain boundaries. A number of straight SGBs are identified that cross a grain completely and are aligned with grain boundaries on either side of the grain. Several quadruple junctions were also found in this fine grained sub-horizontal band.

A detailed EBSD map from a fine grained region in the glacial ice at 2103 m of depth is shown in Figure 6.4. The flow law modelling study of Chapter 4 predicted high strain rates produced by basal slip accommodated by GBS at this depth (2103 m of depth). The pole figures (Figure 6.4d) show that the c- and a-axes of the grains in the EBSD map are strongly aligned. The transmitted LM image and EBSD map show a large number of SGBs in grain I and II. SGBs 2 and 4-9 are N-type boundaries (Weikusat et al., 2011a, b; Chapter 2 and 3), while SGBs 3, 11 and 12 are inclined by about 15° - 20° relative to the basal plane (red bar in Figure 6.4b). The misorientation angles and the rotation axes, which are plotted as inverse pole figures (IPFs), of SGB 1-12 are given in Figure 6.4e. SGBs 4-9

and 11 have a rotation axis that is (sub-)parallel to the a-axis. The rotation axis, misorientation angle and trace orientation in the host grain (trace) of SGB 4 and 5 and of SGB 8 and 9 are also almost similar. However, SGB 4 and 8 intersect SGB 3 about 30–40 μm to the right of the intersection of SGB 5 and 9 with SGB 3. This offset is indicated by the two black arrows in the middle of Figure 6.4b. The white arrow in Figure 6.4b shows a

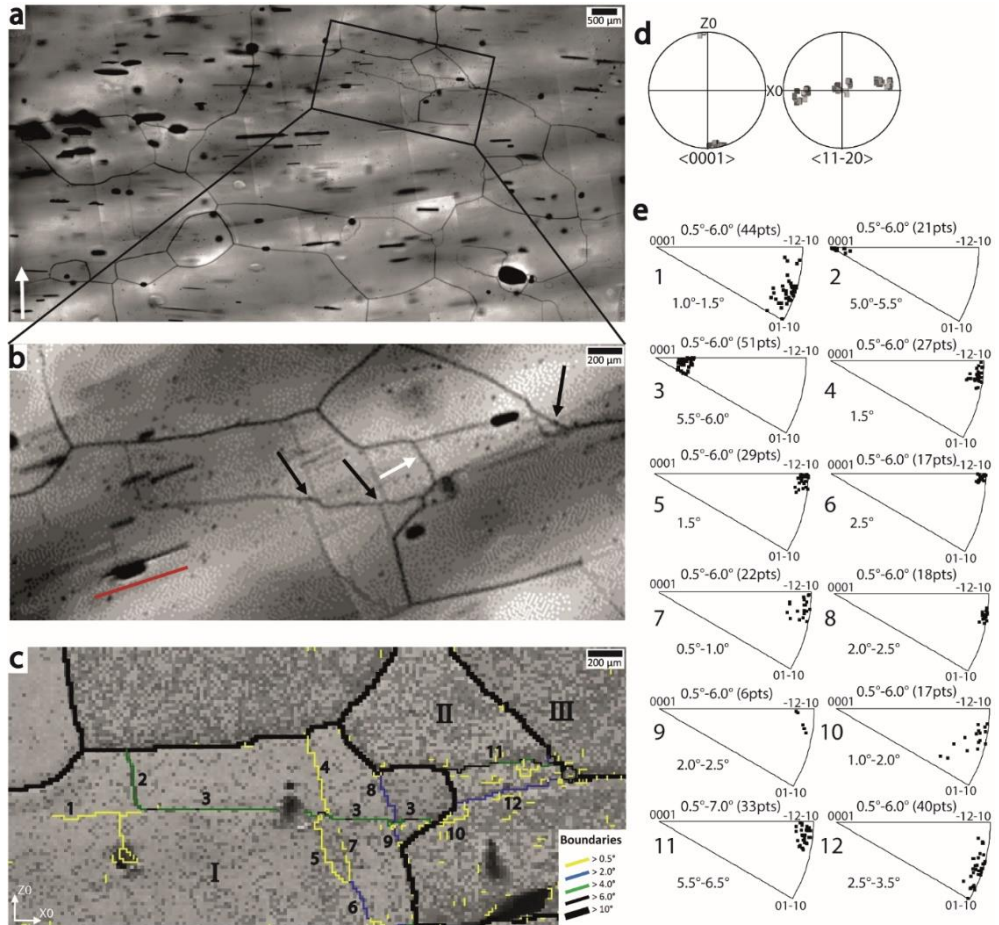


Figure 6.4: Transmitted light microscopy and corresponding EBSD data of an ice core section in the glacial ice at 2103 m of depth (NEEM 3825-10) showing a network of SGBs across two grains. (a) Transmitted LM image taken just after EBSD sample preparation showing a fine grained region in the glacial ice with the white arrow pointing towards the long (vertical) axis of the ice core. Black spots are air bubbles at or just below the surface of the EBSD sample. (b) Boxed region of (a) which is slightly rotated counter clockwise with respect to the LM image in (a). The red line drawn parallel to collapsed air bubble indicates the orientation of the basal plane. (c) the corresponding EBSD map (greyscale shows pattern quality) with the boundary misorientation colour code. (d) Pole figure (equal area, upper hemisphere projection) of the $\langle 0001 \rangle$ and $\langle 1\bar{1}20 \rangle$ axes of the grains in the EBSD map. (e) inverse pole figures (equal area, upper hemisphere projection) showing the rotation axes in crystal coordinates of SGBs 1-12. Most SGBs have misorientation angle ranging from 0.5° to 6.0°, apart from IPF 11, which has a slightly higher misorientation of about 6.0°.

bulge of grain I into grain II. Two boundaries (11 and 12) are connected to this bulge, with a very small grain present between grain II and III on the right side of SGB 11 and 12 (black arrow in the upper right corner of Figure 6.4b).

The CPO in the Holocene and glacial ice is shown in Figure 6.5. The c- and a-axes orientations of three depths in the Holocene and the glacial ice shows that the c-axes clustering parallel to the z-axis (vertical core axis) intensifies with depth in the Holocene ice and is strongly clustered in the glacial ice. The two shallowest samples in the Holocene ice (443 and 718 m of depth) have an almost random orientation of a-axes. However, the deeper sample in the Holocene ice at 889 m of depth shows a weak a-axes alignment. All three samples in the glacial ice show an a-axes alignment.

Figure 6.6 shows the orientation gradients of the grains in the Holocene ice, glacial ice and Eemian-glacial facies. A clear difference in orientation gradient in the Holocene ice occurs between 443 m of depth and 718 and 889 m of depth. The mean orientation gradient at 443 m of depth is about 1° mm^{-1} , whereas at 718 and 889 m of depth the orientation gradient is about $3.0\text{--}3.5^\circ \text{ mm}^{-1}$. Mean orientation gradient of the grains in the glacial ice is about $2.5^\circ \text{ mm}^{-1}$ for the ice core section at 1767 m of depth, while at deeper depths of 1993 m and 2103 m the orientation gradient is slightly higher at about $3.0\text{--}3.5^\circ \text{ mm}^{-1}$. The mean orientation gradient at 2241 m of depth in the Eemian-glacial facies of about $1.5^\circ \text{ mm}^{-1}$ is much lower than in the glacial ice and in the Holocene ice at 718 and 889 m of depth.

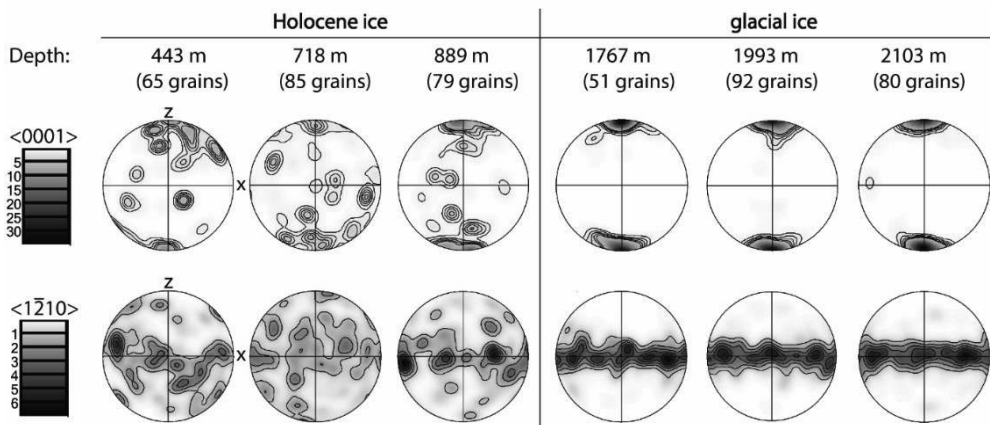


Figure 6.5: Pole figures (upper hemisphere, equal area projection) of EBSD mapped data showing c-axes, $\langle 0001 \rangle$, and a-axes, $\langle 1210 \rangle$, of three ice core sections from the Holocene ice (443 m, 718 m and 889 m of depth) and three ice core sections from the glacial ice (1767 m, 1993 m and 2103 m of depth). The misaligned EBSD samples in the SEM were rotated using the Channel 5 software so that the EBSD maps were aligned with the long (vertical) axis of the core. The number of grains included in the pole figures is indicated. Due to the difference in strength of clustering, a different grey scale was used for the pole figures showing the c-axes distribution than the a-axes distribution. A half width of 20° and a cluster size of 5° was used for all pole figures.

6.5 Discussion

A study of ice microstructures using cryo-EBSD combined with (polarized) light microscopy techniques was performed along the NEEM ice core. The microstructures were analyzed in terms of recrystallization and deformation mechanisms. In the first part of the discussion (section 6.5.1), selected and typical examples of LM images and corresponding EBSD maps will be analyzed in terms of recrystallization and deformation mechanisms. In the second part of the discussion (section 6.5.2), the dominant recrystallization and deformation mechanisms in the three depth intervals of the NEEM ice core will be discussed by combining the results from this EBSD study with earlier microstructural work on the NEEM ice core (e.g. NEEM community members, 2013; Eichler et al., 2013, 2017; Binder, 2014; Montagnat et al., 2014; Jansen et al., 2016; Steinbach et al., 2017; Chapter 2-5). In the last part of the discussion (Section 6.5.3), the results from flow law modelling (Chapter 4 and 5) are compared with the results from microstructural studies (Chapter 2, 3 and 6) and possible differences are discussed.

6.5.1 Microstructures indicating recrystallization and deformation mechanisms

6.5.1.1 SIBM and island grains at shallow depths

Figure 6.1 shows a transmitted LM image and the corresponding EBSD data of a typical microstructure in the Holocene ice of the NEEM ice core with relatively coarse grains, lobate grain boundaries and many air bubbles. The orientation gradient surrounding the two island grains (3° - 5° mm^{-1}) is much higher than the mean orientation gradient at 413 m of depth (1.0° mm^{-1} ; Figure 6.6). The high SGB density and high orientation gradient surrounding the two island grains (grain 2 and 3) in grain 1 shows that this is a region of relatively high stored strain energy (e.g. Weikusat et al., 2009b). On the other hand, the larger of the two island grain (grain 2) has a much lower orientation gradient of about 0.5° in total (Figure 6.1d), which indicates that this grain has a relatively low stored strain energy. Both island grains have a similar c- and a-axes orientation (Figure 6.1c), which makes it very likely that these island grains were part of the same parent grain in the third dimension. Therefore, the most likely explanation for the two island grains is that two migrating bulges, originating from the same parent grain, were cut by the surface of the EBSD sample. These complex grain geometries due to bulging of grain boundaries have been described in experimentally deformed ice as well as in polar ice (e.g. Hamann et al., 2007; Weikusat et al., 2009a, b; Breton et al., 2016; Steinbach et al., 2017). Bulging of grains removes localized strain. Bulging leads to complex grain shapes which creates localized stress concentrations and the process is repeated. The growth of grain 3 during transport and storage, possibly influenced by the air bubble or the change in stress configuration caused by the freshly cut surface of the EBSD sample, shows that stored strain energies were high enough for SIBM to be active in this region. The strong bulging of grain boundaries producing island grains as described above was a common observation in the three samples in the Holocene ice, particularly in the samples at 718 and 889 m of

depth where the stored strain energies are high (Figure 6.6) and the grains are irregularly shaped (Figure 1.8d). Another example of an island grain in the Holocene ice of the NEEM ice core is shown in Figure 2.4. The frequent observation of island grains and irregular shaped grains, similar to other polar ice cores (Kipfstuhl et al., 2006, 2009; Faria et al., 2009, 2010), shows that recovery by SIBM, which removes dislocations and stress concentrations and allows further deformation to occur, is an important mechanism in the Holocene ice of the NEEM ice core.

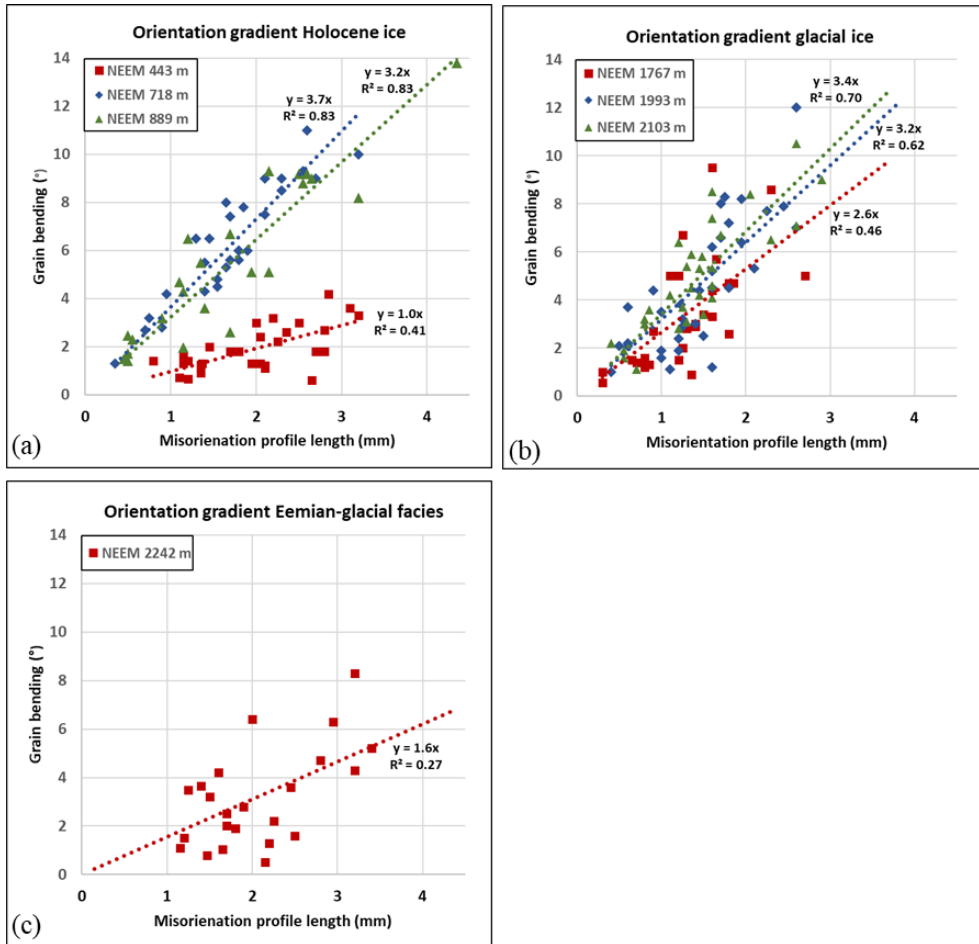


Figure 6.6: Scatterplots showing the orientation gradient (total grain bending along the long axis of a grain in $^{\circ}$ versus the length of the misorientation profile in mm) of a random selection of grains in the ice core sections that were studied using EBSD in (a) the Holocene ice, (b) the glacial ice and (c) the Eemian-glacial facies. A linear fit for each ice core section is shown with dotted lines, where R^2 is the correlation coefficient. Between 30 and 40 grains of each ice core section were included in the scatterplots.

6.5.1.2 Recrystallization of new grains along grain boundaries by grain boundary bulging and subgrain rotation

Evidence of new grains forming by bulging recrystallization was found in the Holocene ice (Figure 6.2). Due to the similar crystallographic orientation of grain 1 and 6, it is likely that grain 6 is a remnant of grain 1. This is supported by the subgrain boundary in the middle of grain 6. If grain 6 was a newly nucleated grain, it would have been relatively free of dislocations and therefore free of SGBs (e.g. Humphreys and Hatherly, 2004). Grains 3-5 all have a slightly different crystallographic orientation, although the crystallographic orientations of grain 3-5 are close to the crystallographic orientation of grain 2 (Figure 6.2d). Therefore, it is likely that grains 3-5 were formed by bulging recrystallization which isolated sections of grain 2 by SIBM and, with continued deformation, rotated into three new grains (Stipp et al., 2002; Faria et al., 2014a).

A very similar microstructure as shown in Figure 6.2 with newly nucleated grains and ‘remnant’ grains at the boundary of two larger grains was recently shown by Chauve et al. (2017, Figure 5 therein) in artificially produced ice deformed in the laboratory. Even though the conditions during the deformation tests (stress of 0.5 MPa, temperature of -7°C , strain rate of $3 \cdot 10^{-7} \text{s}^{-1}$) were very different from the deformation conditions at 718 m of depth in the NEEM ice core (estimated stress ~ 0.07 MPa, temperature of -29°C , estimated strain rate of $3.2 \cdot 10^{-12} \text{s}^{-1}$) (Gillet-Chaulet et al., 2011; Montagnat et al., 2014; Sheldon et al., 2014; Section 4.2.3), the microstructures are remarkably similar. The similarity in microstructures supports the hypothesis of Chauve et al. (2017) that the role of strain and stress heterogeneities observed in ice deformation experiments may also be important at the low strain rates in polar ice sheets. Strongly localized deformation, frequently combined with a high SGB density (Figure 6.1), high orientation gradients (Figure 6.1) or bulging recrystallization (Figure 6.2), were observed in the Holocene ice while they were absent in the glacial ice.

6.5.1.3 Microstructures indicating GBS-limited creep

Several microstructural features can be interpreted as providing evidence for GBS in the ice. These microstructural features include: (i) elongated blocky grains (“brick-wall pattern”, Faria et al., 2009) (Figure 4.1 and 6.3), (ii) grain boundaries aligned parallel to the shear plane (Figure 4.1 and 6.3), (iii) SGBs aligned to the grain boundary network (Drury and Humphreys, 1988; Faria et al., 2009; Figure 6.3), (iv) rotation axes of low angle grain boundaries not related to host crystallography (e.g. Fliervoet and White, 1995; Bestmann and Prior, 2003; Chapter 3). The reflective LM image in Figure 6.3 contains microstructural features that can be interpreted as evidence for GBS. This sample is from a depth where high strain rates were predicted using the grain size sensitive composite flow law of Goldsby and Kohlstedt (1997, 2001) in Chapter 4. Another exemplary depth region (2103 m) for which high strain rates were predicted by the flow law modelling study of Chapter 4 was investigated using transmitted LM imaging and cryo-EBSD is shown in Figure 6.4.

The strong c-axes alignment of the grains in the EBSD map (Figure 6.4d), and generally strong c-axes alignment in the glacial ice of the NEEM ice core ((Eichler et al.,

2013; Montagnat et al., 2014; Figure 1.8a and 6.5), shows that strain is mainly produced by intracrystalline dislocation glide (e.g. Azuma and Higashi, 1985; Alley, 1992; Azuma, 1994). The alignment of a-axes (Figure 6.4d and 6.5) indicates that basal slip along the easy slip system of $\langle 1\bar{2}10 \rangle / (0001)$ is the dominant slip system in this part of the NEEM ice core (Kamb, 1961; Hondoh, 2000). The alignment of a-axes also indicates that plane strain deformation, such as simple shear, at this depth is dominant.

In the example shown in Figure 6.4, the rotation axis of SGB 2 is parallel to the c-axis and the trace of this boundary is normal to the basal plane. This SGB is therefore classified as an N[c] type SGB (Miyamoto et al., 2005, 2011; Weikusat et al., 2011a, b; Chapter 2 and 3) and was likely formed by an array of edge dislocations with Burgers vector $\mathbf{b} = (1/3)\langle 1\bar{2}10 \rangle$ gliding on a non-basal plane (Figure 3.2 number 2a). SGB 3 on the other hand is closest to a P[c] boundary but deviations of the trace by about 15° - 20° and the rotation axis of about 15° suggests a more general SGB type (Chapter 3). Another interesting feature of this EBSD map is that SGB 4 and 5 and SGB 8 and 9 have the same rotation axis, trace and misorientation angle. The exact rotation axis of SGB 9 is uncertain since the IPF contains only 6 pixels. However, the rotation axis of this SGB is, just like SGB 8, is close to $\langle 1\bar{2}10 \rangle$. All four SGBs intersect with SGB 3 at the same angle with an offset of about 30-40 μm between SGB 4 and 5 and between SGB 8 and 9, respectively. Sliding along newly formed SGB 3 could have disconnected SGB 4 from SGB 5 and SGB 8 from SGB 9 along this boundary. It is possible that both SGB pairs were continuous SGBs that became displaced by sliding along SGB 3 in a dextral shear sense. A sliding boundary would indicate that SGB 3 is actually a grain boundary instead of a SGB, which, based on its misorientation angle (5.5° - 6.0°), agrees with the SGB-grain boundary critical angle of 5° found by Weikusat et al. (2011b) and Montagnat et al. (2015). The strain incompatibly between grain I and II and grain II and III, as a results of sliding along SGB 3, likely resulted in the formation of the bulge (white arrow Figure 6.4b) and to the boundary 11 and 12 and could have been responsible for the formation of the small grain between grain II and III.

The rotation axis of SGB 3 could be explained by the activation of multiple slip systems with different rotation axes contributing to the formation, as was proposed for the ‘general’ rotation axes of high angle SGBs (4.0° - 6.5°) in the glacial ice (Chapter 3). However, for this particular example, such a mixed boundary type cannot explain the offset of SGB 4 and 5 and SGB 8 and 9 along SGB 3. The development of a general rotation axes of boundaries that have been formed by subgrain rotation and initiated sliding along that boundary was first proposed by Fliervoet and White (1995) and convincingly shown in natural rocks by Bestmann and Prior (2003). Sliding along newly formed SGB 3 could have resulted in the development of the general rotation axis of SGB 3. With respect to the results from flow law modelling, which predict high strain rates produced by GBS-limited creep at this depth (Chapter 4), the observation of the general rotation axis of SGB 3 could be attributed to enforced SGB formation in grain 1 to enable local GBS.

Sliding along grain boundaries in fine grained bands could also explain the aligned subgrain boundaries observed in Figure 6.3 and SGB 11 and 12 in Figure 6.4. If sliding is

allowed along aligned grain boundaries, then a grain blocking this alignment will experience an accumulation of stress and strain at the triple junction where the aligned grain boundaries meet with the blocking grain. Therefore, the dislocation density in the blocking grain will increase as a result of the strain incompatibility (e.g. Drury and Humphreys, 1988; Bons and Jessel, 1999; Faria et al., 2009). When these dislocations recover into a SGB, the SGB will originate at the location of highest strain incompatibility. With progressive sliding along the grain boundaries ahead of the blocking grain, the SGB eventually rotates to become a grain boundary and can contribute to sliding along the aligned grain boundaries. This process produces SGBs with a preferred orientation not controlled by the intrinsic slip systems of ice but by the external (local) stress configuration. These enforced SGBs are produced in blocking grains and could explain the small grain size and flattening in the fine grained bands with aligned grain boundaries compared to the neighbouring coarser grained bands (Figure 6.3). Since these aligned SGBs are not controlled by the crystallography of the host crystal but by strain incompatibility with surrounding grains, it is expected that these SGBs will not have a rotation axis and/or a trace that is controlled by the (intrinsic) slip systems of the host grain. In Chapter 3 it was shown that the glacial ice in the NEEM ice core contains a significant number of high angle SGBs (4.0° - 6.5°) with a general rotation axis and/or an oblique trace. SGB 3 in Figure 6.4c is such a boundary with a general rotation axis and oblique trace. SGB 11 and 12 in Figure 6.4 could also have been formed by this process as these SGBs are aligned with the local grain boundary network, although their rotation axes are not 'general' rotation axes like SGB 3. Part of the high angle SGBs (4.0° - 6.5°) in the glacial ice with a general rotation axis and/or trace could have been formed in a similar way to SGB 3 in Figure 6.4c. These types of boundaries were not found in the Holocene ice where GBS is less likely to occur due to the coarser grain size and interlocking grains (Chapter 4).

It is often stated that a grain size sensitive deformation mechanism such as GBS-limited creep destroys CPO (e.g. Duval et al., 2000; Duval and Montagnat, 2002; Bestmann and Prior, 2003). However, in the glacial ice of the NEEM ice core, the c-axes are strongly clustered into a single maximum CPO (Eichler et al., 2013; Montagnat et al., 2014). Furthermore, the a-axes are also aligned in this part of the glacial ice (Figure 6.4d and 6.5). This suggests that basal slip and GBS operate simultaneously at this depth, a mechanism which was proposed by Goldsby and Kohlstedt (1997, 2001). Furthermore, SGB 2 in Figure 6.4c is a N[c] type boundary and likely formed by an array of edge dislocations with Burgers vector $\mathbf{b}=(1/3)\langle 1\bar{2}10 \rangle$ gliding on a non-basal plane. This could be interpreted as GBS, basal slip and non-basal slip operating simultaneously within the same grain.

Premelting is expected to enhance grain boundary processes, like GBS (e.g. Barnes et al., 1971; Schulson and Duval, 2009). It is interesting to note that the in-situ temperature of the samples shown in Figure 6.3 (255K) and Figure 6.4 (258K) is below the expected temperature threshold for the onset of premelting in ice of 262K (Chapter 5). The high impurity content in the glacial ice (Kuramoto et al., 2011; Eichler et al., 2017) could

lead to premelting occurring at lower temperatures in these samples, which enhances grain boundary processes such as GBS.

During their ice deformation experiments Goldsby and Kohlstedt (1997; 2001) argued for a deformation mechanism where GBS is the accommodating mechanism for basal slip (from here on called GBS-limited creep), and thus GBS may contribute only slightly to total deformation. In case of limited contribution of GBS to the bulk strain rate, intragranular slip accommodated by GBS can strengthen instead of weaken the CPO as was shown by the modelling studies of Zhang et al. (1994). Aligned grain boundaries, similar to the grain boundary alignment in Figure 6.3, were also observed during the deformation experiments on aluminium-magnesium alloys of Drury and Humphreys (1986, 1988). During these experiments, strain was predominantly produced by intergranular dislocation creep, with only 10-15% of strain being produced by GBS. This shows that, even though the contribution to bulk strain is low, GBS can have a significant effect on microstructural development. A strengthening of CPO caused by the accommodation of basal slip by GBS could explain the exceptionally high CPO eigenvalue of 0.97 in the very fine grained sample in Figure 6.3. Furthermore, GBS-limited creep strengthening CPO could explain why the CPO is often stronger in the fine grained glacial regions than in the coarser grained interglacial regions, as has been shown in many different polar ice cores (e.g. Paterson, 1991; DiPrinzio et al., 2005; Durand et al., 2009; Montagnat et al., 2012; Eichler et al., 2013; Faria et al., 2014b; Fitzpatrick et al., 2014; Weikusat et al., 2017).

6.5.1.4 Alignment of a-axes

Numerical simulations of polycrystalline ice have shown that in pure shear an alignment of a-axes can form (e.g. Llorens et al., 2016, 2017). The flow of ice in the upper part of the NEEM ice core is slightly divergent with the main flow component parallel to the ridge and a small contribution of flow perpendicular to the ridge (Montagnat et al., 2014) and can therefore, strictly speaking, not be considered as pure shear deformation. The ice core sections at 443 m and 718 m of depth do not show an a-axes alignment. However, an alignment of a-axes was found in the sample at 889 m of depth, which could indicate that at this depth the ice starts to deform increasingly by a different deformation mode. Since all three samples from the glacial ice show an alignment of a-axes, it is likely that deformation by simple shear is responsible for the a-axes alignment at 889 m of depth in the Holocene ice and in the glacial ice. The higher total strain at 889 m of depth and in the three glacial samples compared to the samples at 443 m and 718 m of depth could also have had an effect on the formation of the a-axes alignment. A different explanation for why an a-axes alignment was found at 889 m and not at 443 m and 718 m of depth is the difference in slip system activity as was shown by the slip system analysis of SGBs in Chapter 3. The basal-to-non-basal slip ratio of the sample at 889 m of depth (71% to 29%) is much higher than that of the samples at 718 m of depth (54% to 46%) and 443 m of depth (50% to 50%) (Table 3.2). As an alignment of a-axes is caused by preferred slip along $\langle 1\bar{2}10 \rangle / \{0001\}$ (Kamb, 1961; Hondoh, 2000), the a-axes alignment in the sample at 889 m of depth could also be explained in terms of higher dislocation glide along the basal plane.

Alignment of a-axes in natural ice has been observed before by Miyamoto et al. (2005) in three out of eight samples from the glacial ice in the GRIP ice core. The GRIP ice core is located at an ice dome (Thorsteinsson et al., 1997), whereas the NEEM core is located next to a ridge. Therefore, strain rates and the component of simple shear are expected to be higher in the NEEM ice core than in the GRIP ice core (Montagnat et al., 2014). This could explain why an a-axes alignment was found in all three ice core sections in the glacial ice of the NEEM ice core, while only three out of the eight ice core sections in the GRIP ice core showed an alignment of a-axes (Miyamoto et al., 2005).

6.5.1.5 Internal strain energy by geometrically necessary dislocations as driver for SIBM

Figure 6.6 shows that there is a clear difference in mean orientation gradient between the different depths that were mapped by EBSD along the NEEM ice core. The orientation gradient of a grain is a proxy for the density of geometrically necessary dislocations (GNDs), which are stored to accommodate strain gradients (e.g. Nye, 1953; Ashby, 1970). The density of dislocations that trap each other randomly, which are referred to as statistically stored dislocations (Nye, 1953; Ashby, 1970), is much lower than the density of GNDs in ice according to Montagnat et al. (2003a, b). Therefore, as a first order approximation, mean orientation gradient can be considered as a proxy for the mean stored strain energy in a certain ice core section. However, it has to be noted that the type of dislocations that are stored in the lattice are important as well, since basal dislocations store up to 3,5 times less energy than non-basal dislocations in the ice lattice (e.g. Hondoh, 2000; Schulson and Duval, 2009).

The increase in mean orientation gradient between 443 m and 718-889 m of depth coincides with a change in the mean perimeter ratio of the grains (Figure 1.8d). The more irregular grain shape at 600-1300 m of depth can therefore be explained by the higher stored strain energy, which, due to the high plastic anisotropy of ice, leads to local differences in stored strain energy (e.g. Schulson and Duval, 2009), and consequently more extensive SIBM. Interestingly, the mean orientation gradient in the Holocene ice at 718 and 889 m of depth and in the three glacial ice core sections is roughly equal. This indicates that stored strain energy is roughly equal in these depth regions, which in the glacial ice, however, does not lead to extensive SIBM. Pinning by impurities of grain boundaries in the glacial ice (e.g. Weiss et al., 2002) could be an explanation for the lack of SIBM in the glacial ice even though dislocation densities are relatively high. Eichler et al. (2017) showed that impurities in the Holocene ice of the NEEM ice core had no pinning effect on grain boundaries. However, cryo-EBSD in combination with optical microscopy showed that in the glacial ice of the NEEM ice core, impurities in the interior of the grains and at the grain boundaries were aligned along nearly straight lines (Shigeyama et al., 2018), which suggests that the grain boundaries were pinned by impurities in the glacial ice of the NEEM ice core.

The mean orientation gradient in the Eemian-glacial facies is much lower than in the glacial ice and in the Holocene ice at 714 m and 889 m of depth. However, the mean

perimeter ratio (Figure 1.8d) shows that the grain boundary structure is about as irregular at 2241 m of depth as in the samples at 718 and 889 m of depth. The microstructures showing extensive SIBM at 2241 m of depth, while stored strain energies are relatively low, could well be explained by the higher grain boundary mobility expected from premelting in the Eemian-glacial facies as well as from the higher ice temperatures at this depth (Chapter 5).

6.5.2 Recrystallization and deformation mechanisms in the NEEM ice core

In this section, the results from the Chapter 2-5 and Section 6.5.1 of this thesis will be combined with earlier microstructural work on the NEEM ice core (e.g. NEEM community members, 2013; Eichler et al., 2013, 2017; Binder, 2014; Montagnat et al., 2014; Jansen et al., 2016; Steinbach et al., 2017) to discuss the dominant recrystallization and deformation mechanisms in the three depths intervals of the NEEM ice core: the Holocene ice (Section 6.5.2.1), the glacial ice (Section 6.5.2.2) and the Eemian-glacial facies (Section 6.5.2.3).

6.5.2.1 The Holocene ice

Normal grain growth is the major contributor to grain size increase in the upper part of polar ice sheets (e.g. Alley, 1992; Thorsteinsson et al., 1997). However, other mechanisms such as subgrain formation and SIBM are already active at only a few tens of meters of depth (Mathiesen et al., 2004; Kipfstuhl et al., 2006, 2009; Durand et al., 2008). At about 250 m of depth in the NEEM ice core, the grain boundaries become more irregular with depth (Figure 1.8d), suggesting that SIBM becomes progressively more important. The mean orientation gradient in the Holocene ice (Figure 6.6) indicates that the stored strain energy is considerably higher at 718 and 889 m of depth than at 443 m of depth. This leads to enhanced SIBM, which is driven by differences in stored strain energy, at 718 and 889 m of depth. As the mean perimeter ratio remains low in the middle and lower part of the Holocene ice (Figure 1.8d), stored strain energies due to dislocation densities and SIBM activity in this region is probably similar to the ice core sections at 718 and 889 m of depth. The lowest values of grain perimeter ratio may be influenced by bubble relaxation in the brittle zone (between 600 and 1160 m of depth): after retrieval of the core from the borehole irregularities in the grain boundary network may appear where bubbles near grain boundaries relax (Binder, 2014). These irregularities give lower grain perimeter values that are not caused by SIBM. However, the coincidence of an increase in the mean orientation gradient (443 m and 718 and 889 m of depth) with a change in the mean perimeter ratio of the grains confirms that a change in stored strain energy occurs.

The mean grain area increases in the upper 400 m of the NEEM ice core to about 5-7 mm² after which the mean grain area remains relatively stable in the remainder of the Holocene ice (Figure 1.8b). Several grain size reducing mechanisms have been shown to be active in the Holocene ice, such as grain dissection (Steinbach et al., 2017), bulging recrystallization with local rotation of the lattice in the bulge (Figure 6.2) and rotation recrystallization (Eichler et al., 2013; Chapter 2 and 3). The relatively low number of low angle SGBs (0.5°-2.0°) that rotate into high angle SGBs (4.0°-6.5°) (Figure 3.7a) as well as the low SGB densities between 600 and 1200 m of depth (Figure 1.8e) indicate that rotation

recrystallization is relatively unimportant in the Holocene ice compared to the glacial, except for local rotation across a bulge that leads to the formation of new grains (Figure 6.2). The activity of grain dissection and bulging recrystallization as grain size reducing mechanisms is probably high since these mechanisms are closely related to SIBM. Normal grain growth (grain boundary surface energy driven) and SIBM without the formation of new grains referred to as SIBM-O by Faria et al., (2014a) are both active in the Holocene ice. Based on the approximately linear increase in grain area with depth in the upper 400 m (Figure 1.8b), normal grain growth could be considered as the dominant grain size increasing mechanism in the upper part of the Holocene ice (Gow, 1969). However, as discussed by means of the recrystallization diagram by Faria et al. (2014a), SIBM can lead to dynamic grain growth if no new grains are formed. The onset of SIBM at about 250 m of depth as indicated by the decrease of the mean perimeter ratio below 250 m of depth (Figure 1.8d) argues for dynamic grain growth as a more valid description for grain size evolution in the upper few hundreds of meters of the NEEM ice core. The increasing irregular grain shape in the remainder of the Holocene ice indicates that SIBM as a grain growth mechanism is becoming progressively more important with depth in the Holocene ice.

The application of the modified grain size sensitive composite flow law of Goldsby and Kohlstedt (2001) to NEEM grain size distributions (Chapter 4) suggested that the dominant deformation mechanism in the Holocene ice is GBS-limited creep (basal slip accommodated by GBS) with a very small contribution from dislocation creep (basal slip accommodated by non-basal slip). However, ice microstructures of the Holocene ice do not support these results. Although locally some accommodation of basal slip by GBS might be achieved (Raj and Ashby, 1971), the large and interlocking grains in the Holocene ice (Figure 1.8b, d and 6.1) argue against GBS as the dominant accommodating mechanism for basal slip in the Holocene ice. Furthermore, no fine grained bands or grain boundary alignment, as observed in the glacial ice (Figures 6.3 and 6.4), were found in the Holocene ice. The reason for the absence of fine grained bands is typically attributed to the low impurity load in Holocene ice compared to glacial ice which has about 50 to 100 times higher dust load (Kuramoto et al., 2011; Eichler et al., 2017). High angle subgrain boundaries (4.0° - 6.5°) with a general rotation axis, which could be produced by GBS, were regularly found in the glacial ice but were absent in the Holocene ice (Figure 3.6, 3.7f and 6.4).

The results of slip system analysis of SGBs in the Holocene ice (Chapter 3) showed that the percentage of SGBs likely formed by non-basal slip decreases for samples that indicate extensive SIBM. This strongly suggests that SIBM controls the amount of non-basal slip that is activated by removing strain incompatibilities from which non-basal slip is activated. In the Holocene ice, basal slip is likely to be the dominant deformation mechanism, with recovery by SIBM (Pimienta and Duval, 1987). However, even at the depth with the most irregular shaped grain boundaries (889 m of depth; Figure 1.8d), still 29% of SGBs were indicative of non-basal slip (Table 3.2). This shows that basal slip with recovery via SIBM is not the only deformation mechanism that is active in the Holocene ice

as considerable amounts of non-basal slip are still activated, even at depths where SIBM rates are high.

It is therefore proposed that deformation of Holocene ice of the NEEM ice core is mainly produced by basal slip accommodated by recovery via SIBM and non-basal slip. The amount of non-basal slip that is activated depends on the extent of SIBM, which increases below 250 m of depth. GBS is not an important accommodating mechanism for basal slip in the Holocene ice of the NEEM ice core.

6.5.2.2 The glacial ice

The mean grain area in the glacial ice is relatively small at 1-3 mm² and varies slightly with depth (Figure 1.8b). SIBM is less active in the glacial ice than in the middle and lower part of the Holocene ice shown by the relatively high mean perimeter ratio in the glacial ice (Figure 1.8d) and by the low percentage of low angle SGBs (0.5°-2.0°) (Figure 3.7a). It is therefore unlikely that recovery by SIBM is an important accommodating mechanism for basal slip in the glacial ice, as described above for the Holocene ice. Due to this low extent of SIBM in the glacial ice it is unlikely that grain dissection and bulging recrystallization are effective as grain size reducing processes in the glacial ice. Therefore, rotation recrystallization is likely the more important grain size reducing mechanism, which is supported by the high number of high angle SGBs (4.0°-6.5°) in the glacial ice compared to the Holocene and Eemian ice (Figure 3.7a).

The higher strain rates often observed in glacial ice compared to interglacial ice (e.g. Paterson, 1991) have been ascribed to grain size and/or impurity content (e.g. Thorsteinsson et al., 1999; Peltier et al., 2000; Cuffey et al., 2000a, b). These studies concluded that the strong single maximum CPO alone cannot be responsible for the viscosity change between the Holocene ice and the glacial ice. In the following it is argued that GBS is an important accommodating mechanism for basal slip in the glacial ice and can be responsible for the high strain rates measured by borehole logging studies in glacial ice. Microstructures indicating GBS-limited creep (Section 6.5.1.3) are frequently observed in the fine grained sub-horizontal bands (Figure 6.3), particularly where the composite flow law study predicts high strain rates produced by GBS-limited creep. These microstructures resemble microstructural shear (cf. Drury and Humphreys, 1988; Bons et al., 1999), which involves GBS and produces aligned grain boundaries parallel to the shear plane and likewise SGBs in grains that are blocking the sliding boundaries (Figure 6.3 and 6.4). If the misorientation angle of SGBs formed by microstructural shear continues to increase, the SGB will rotate into a grain boundary along which GBS can occur. The misorientation angle at which sliding appears to initiate in ice is rather low (5.0°-6.0°). GBS could also explain the relatively high number of high angle SGBs (4.0°-6.5°) in the glacial ice with a general rotation axis (Chapter 3). Weikusat et al. (2011b) and Montagnat et al. (2015) inferred a similar misorientation angle threshold for SGB behaviour to grain boundary behaviour in natural and artificial ice. The threshold for SGB behaviour is related to the intrinsic grain boundary energies in ice which increase rapidly with increasing misorientation (Suzuki and Kuroiwa, 1972). However, the misorientation threshold is also

dependent on the type of dislocations that have accumulated to form the boundary (Weikusat et al., 2011b), since non-basal dislocations contain up to 3,5 times more energy than basal dislocations (Hondoh, 2000). However, even though there is evidence for GBS in the glacial ice of the NEEM ice core, still a significant percentage of the SGBs in the glacial ice indicate non-basal slip (Figure 3.7d and Table 3.2). Therefore, basal slip is only partly accommodated by GBS with a significant amount of basal slip being accommodated by non-basal slip.

Here we conclude that GBS is an important accommodating mechanism in the glacial ice of the NEEM ice core, particularly in the finer grained sub-horizontal bands. However, similar to the Holocene ice, significant amounts of non-basal slip are still activated as was shown in Chapter 3. Therefore, GBS-limited creep is not the only deformation mechanism in the glacial ice, but there is still a considerable contribution of dislocation creep. Basal slip accommodated by recovery via SIBM is not an important deformation mechanism in the glacial ice.

6.5.2.3 The Eemian-glacial facies

The stratigraphy in the lower part of the NEEM ice core is heavily folded and disturbed (NEEM community members, 2013). The folded and partly overturned layers consist of glacial ice and Eemian ice, which causes the grain size to vary strongly with depth, ranging from a few millimetres to a couple of centimetres in diameter (Figure 1.8b and 5.4). Due to the high temperature in this part of the NEEM ice core (Sheldon et al., 2014), the ice is likely affected by premelting (Table 5.1). The irregular shape of the grains (Figure 1.8d and 5.1) in this part of the ice sheet could well be explained by enhanced grain boundary mobility caused by premelting along the grain boundaries (Duval et al., 1983; Dash et al., 1995; Duval and Castelnau, 1995).

The application of a modified version of the composite flow law of Goldsby and Kohlstedt (2001) (Table 5.2) to the NEEM ice core showed that the effect of grain size on calculated strain rate is particularly strong in the Eemian-glacial facies (Figure 5.4). The variation in strain rate by GBS-limited creep is largest near the stratigraphic disruptions. The modified composite flow law predicts that GBS-limited creep produces almost all strain in the fine grained layers, while for the coarse grained layer dislocation creep and GBS-limited creep contribute roughly equally to bulk strain (Figure 5.4). However, similar to the results of flow law modelling in the Holocene ice (Chapter 4, Section 6.5.2.1), the very coarse and interlocking grains in the Eemian-glacial facies argue against GBS as an important accommodating mechanism for basal slip.

Changes in grain size strongly correlate with changes in type and strength of CPO with the fine grained regions (grain size <5 mm) having a strong single maximum CPO and the coarser grained regions (>5 mm) having a broad single maximum or small circle girdle type CPO (Figure 5.1 and 5.2). As discussed in Chapter 5, the regions with a fine grain size and strong single maximum CPO likely deform by simple shear at relatively high strain rates, which is expected to be the dominant deformation mode in the lower part of the NEEM ice core (Dansgaard and Johnson, 1969; Montagnat et al., 2014). The coarse grained

regions with a broad single maximum or small girdle CPO likely deform by pure shear or are relatively stagnant.

Due to the relatively small grain size and premelting along the grain boundaries, the fine grained regions with a single maximum CPO likely deform by GBS-limited creep in combination with SIBM. The presence of premelting along grain boundaries is expected to increase basal slip and reduce non-basal slip activity in the dislocation creep regime (De la Chapelle et al., 1999). Evidence for this was found by slip system analysis of SGBs in a relatively fine grained (5 mm) ice core section at 2241 m in the Eemian-glacial facies (Chapter 3). The slip system analysis of SGBs showed that considerably fewer SGBs in this ice core section were indicative of non-basal slip compared to the shallower and colder parts of the NEEM ice core, which is best explained by the presence of premelting along the grain boundaries or enhanced SIBM caused by premelting. The low orientation gradient (Figure 6.6c) and high percentage of low angle (0.5° - 2.0°) SGBs (Figure 3.7a) further argue for SIBM being extensive in this part of the NEEM ice core. The coarser grained regions with a broad single maximum or a small circle girdle CPO are less likely affected by GBS due to the large grain size and interlocking grain boundaries. In these coarse grained layers new strain free grains with soft orientations nucleate continuously and grow at the expense of grains with a hard orientation (Chapter 5), also known as SIBM-N (Faria et al., 2014a) or discontinuous migration recrystallization (Wenk et al., 1989; Schulson and Duval, 2009). In these regions basal slip is predominantly accommodated by recovery via SIBM, which is extensive due to premelting along the grain boundaries and the low impurity content.

The difference in microstructure between the glacial and interglacial ice close to the melting point can have important implications for ice sheet dynamics close to the bedrock, with interglacial ice being relatively stagnant and hardly contributing to horizontal velocity, while glacial ice deforms at high strain rates and contributes considerably to horizontal velocity.

6.5.3 Discrepancy between results of flow law modelling and microstructural analysis

The results from flow law modelling using the modified grain size sensitive composite flow law from Goldsby and Kohlstedt (2001) predicts that GBS-limited creep is the main strain producing mechanism along almost the entire length of the NEEM ice core (Chapter 4 and 5). Only for the coarsest grained regions in the Eemian-glacial facies it is predicted that dislocation creep and GBS-limited creep have roughly the same strain rate (Figure 5.4). However, slip system analysis from SGBs (Chapter 2 and 3) suggests that considerable amounts of non-basal slip are activated along the entire length of the NEEM ice core. Furthermore, dominant GBS-limited creep is not consistent with the microstructures in the Holocene ice (Section 6.5.2.1) and the coarse grained regions in the Eemian-glacial facies (Section 6.5.2.3). It is therefore likely that the modified composite flow law underestimates the rate of dislocation creep, as was also pointed out in Chapter 4. In Chapter 4, the absence

of SIBM during the deformation experiments of Goldsby and Kohlstedt (1997, 2001) was proposed as an explanation for the low strain rates predicted for dislocation creep.

A related explanation for the low strain rate calculated for dislocation creep was provided by Stern et al. (1997) and is shown in Figure 6.7. These authors showed, using constant temperature and constant strain rate deformation tests, that the fine grained ice (grain size $1-3 \mu\text{m}$) did not go through a peak stress, while the standard ice (grain size $300 \pm 50 \mu\text{m}$) did go through a peak stress at about one percent of strain. The temperature, stress and grain size conditions in both the fine and coarse grained deformation tests during the experiments of Goldsby and Kohlstedt (1997, 2001) were roughly similar to the temperature, stress and grain size conditions of Stern et al. (1997). Goldsby and Kohlstedt (1997, 2001) took their stress-strain rate data points during secondary creep at a few percent strain. Figure 6.7 shows that the fine grained ice is relatively soft at 1-2% strain, while the standard ice is relatively hard at 1-2% strain. Therefore, the flow law parameters derived from Goldsby and Kohlstedt's experimental results could describes ice that is relatively soft in the grain size sensitive regime (GBS-limited creep), while the flow law parameters describe ice that is relatively hard in the grain size insensitive regime (dislocation creep). Dynamic recovery and recrystallization processes that are activated after secondary creep at 1-2% strain (e.g. Jacka, 1984; Montagnat et al., 2009; Schulson and Duval, 2009) results in the enhancement of dislocation creep rates, which is not included in the composite flow law of Goldsby and Kohlstedt (2001). The enhancement factor for higher strain in tertiary creep depends on deformation mode and stress (e.g. Budd and Jacka, 1989; Treverrow et al., 2012) and can have a value of up to 10 for high stress and simple shear deformation experiments (Treverrow et al., 2012).

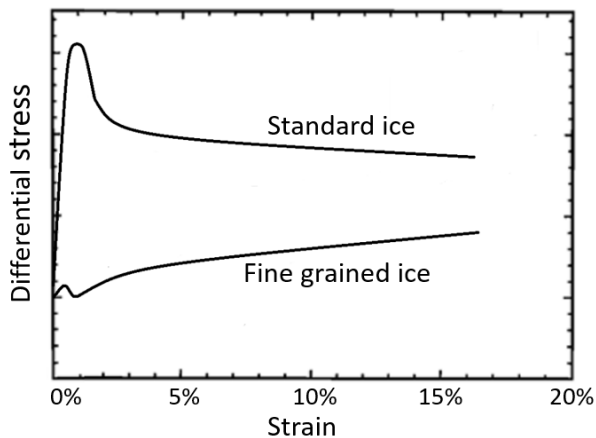


Figure 6.7: Schematic stress-strain curves of deformation tests at constant temperature and constant strain rate for fine grained ice ($1-3 \mu\text{m}$) and standard ice ($300 \pm 50 \mu\text{m}$). Standard ice samples go through peak stress at about 1% strain, while fine grained samples are much weaker and do not go through a peak stress at about 1% strain. Figure after Stern et al. (1997).

6.6 Conclusions

On the basis of (polarized) LM techniques, cryo-EBSD, flow law modelling and earlier work on ice microstructure in the NEEM ice core, the following conclusions were made.

The Holocene ice likely deforms by basal slip accommodated by recovery via SIBM and non-basal slip. In the middle and lower part of the Holocene ice, non-basal slip is less often activated compared to the shallow part of the Holocene ice. Here, SIBM controls the amount of non-basal slip that is activated by reducing strain incompatibilities that activate non-basal slip. The dominant recrystallization mechanisms and processes in the Holocene ice are grain dissection, bulging recrystallization, SIBM and normal grain growth which is limited to the upper 250 meters. Rotation recrystallization is expected to be relatively unimportant in the Holocene ice.

In the glacial ice a process resembling microstructural shear was identified in fine grained sub-horizontal bands. This process includes GBS and the formation of SGBs in grains that are blocking sliding along aligned grain boundaries. Microstructures suggest that these SGBs might contribute to sliding when a misorientation angle of 5.0° - 6.0° is reached. Glacial ice shows a strong single maximum CPO. The a-axes in the glacial ice were also aligned. This suggests that GBS and basal slip are operating simultaneously where basal slip is accommodated by GBS. This deformation mechanism does not destroy, but strengthens CPO. The high percentage of SGBs indicative of non-basal slip in the glacial ice shows that GBS is not the only accommodating mechanism for basal slip, but significant amounts of basal slip are also accommodated by non-basal slip. In the glacial ice rotation recrystallization is more important and SIBM is less important compared to the Holocene ice.

Deformation of ice in the Eemian-glacial facies is expected to be strongly dependent on grain size, grain shape and CPO, all of which vary strongly with depth. The fine grained impurity-rich regions with a strong single maximum CPO likely to deform by simple shear at relatively high strain rates, whereas the coarse grained impurity-poor regions are likely to deform by coaxial deformation at relatively low strain rates. The extensive SIBM, which is likely enhanced by premelting along the grain boundaries, results in a relatively low stored strain energy in the Eemian-glacial facies compared to the other part of the NEEM ice core and in low activity of dislocation glide along the non-basal planes.

The results from flow law modelling and analysis of ice microstructures in the Holocene and the coarse grained layers in the Eemian-glacial facies suggests that the modified composite flow law of Goldsby and Kohlstedt (1997, 2001) underestimates the strain rate produced by dislocation creep. The underestimation of dislocation creep can be explained by dynamic recovery and recrystallization mechanisms not being active during the deformation experiments used to calibrate the composite flow law, while these mechanisms enhance dislocation creep at the high strains that are relevant for polar ice sheets.

References

- Alley, R. B. (1992) Flow-law hypotheses for ice-sheet modeling. *Journal of Glaciology*, 38, 129, 245-256.
- Ashby, M. F. (1970) The deformation of plastically non-homogeneous materials. *The Philosophical Magazine*, 21, 170, 399-424, doi: 10.1080/14786437008238426.
- Azuma, N. (1994) A flow law for anisotropic ice and its application to ice sheets. *Earth and Planetary Science Letters*, 128, 601-614, doi: 10.1016/0012-821X(94)90173-2.
- Azuma, N., Higashi, A. (1985) Formation processes of ice fabric pattern in ice sheets. *Annals of Glaciology*, 6, 120, 130-134.
- Barnes, P., Tabor, D., Walker, J. C. F. (1971) The friction and creep of polycrystalline ice. *Proceedings of the Royal Society London A.*, 324, 1557, 127-155.
- Bestmann, M., Prior, D. J. (2003) Intragranular dynamic recrystallization in naturally deformed calcite marble: diffusion accommodated grain boundary sliding as a result of subgrain rotation recrystallization. *Journal of Structural Geology*, 25, 10, 1597-1613, doi: 10.1016/S0191-8141(03)00006-3.
- Binder, T., Weikusat, I., Freitag, J., Garbe, C. S., Wagenbach, D., Kipfstuhl, S. (2013) Microstructure through an ice sheet. *Materials Science Forum*, 753, 481-484, doi: 10.4028/www.scientific.net/MSF.753.481.
- Binder, T. (2014) Measurements of grain boundary networks in deep polar ice cores – A digital image processing approach. PhD dissertation, University of Heidelberg, Germany, 141 pages.
- Bons, P. D., Jessell, M. W. (1999) Micro-shear zones in experimentally deformed octachloropropane. *Journal of Structural Geology*, 21, 3, 323-334, doi: 10.1016/S0191-8141(98)90116-X.
- Breton, D. J., Baker, I., Cole, D. M. (2016) Microstructural evolution of polycrystalline ice during confined creep testing. *Cold Regions Science and Technology*, 127, 25-36, doi: 10.1016/j.coldregions.2016.03.009.
- Budd, W. F., Jacka, T. H. (1989) A review of ice rheology for ice sheet modelling. *Cold Regions Science and Technology*, 16, 107-144, doi: 10.1016/0165-232X(89)90014-1.
- Chauve, T., Montagnat, M., Barou, F., Hidas, K., Tommasi, A., Mainprice, D. (2017) Investigation of nucleation processes during dynamic recrystallization of ice using cryo-EBSD. *Philosophical Transactions of the Royal Society A*, 375, 20150345, doi: 10.1098/rsta.2015.0345.
- Cuffey, K. M., Thorsteinsson, T., Waddington, E. D. (2000a) A renewed argument for crystal size control of ice sheet strain rates. *Journal of Geophysical Research*, 105, B12, 27889-27894, doi: 10.1029/1000JB900270.
- Cuffey, K. M., Conway, H., Gades, A., Hallet, B., Raymond, C. F., Whitlow, S. (2000b) Deformation properties of subfreezing glacial ice: Role of crystal size, chemical impurities, and rock particles inferred from in situ measurements. *Journal of Geophysical Research*, 105, B12, 27895-27915, doi: 10.1029/2001JB900014.
- Dahl-Jensen, D., Gundestrup, N. S. (1987) Constitutive properties of ice at Dye 3, Greenland. *The Physical Basis of Ice Sheet Modelling*, 170, 31-43.

- Dansgaard, W., Johnson, J. (1969) A flow model and time scale for the ice core from camp century, Greenland. *Journal of Glaciology*, 8, 53, 215-223.
- Dash, J. G., Fu, H., Wettlaufer, J. S. (1995) The premelting of ice and its environmental consequences. *Reports on Progress in Physics*, 58, 1, 115-167, doi: 10.1088/0034-4885/58/1/003.
- De La Chapelle, S., Milsch, H., Castelnaud, O., Duval, P. (1999) Compressive creep of ice containing a liquid intergranular phase: rate-controlling processes in the dislocation creep regime. *Geophysical Research Letters*, 26, 2, 251-254, doi: 10.1029/1998GL900289.
- Diprinzio, C. L., Wilen, L. A., Alley, R. B., Fitzpatrick, J. J., Spencer, M. K., Gow, A. J. (2005) Fabric and texture at Siple Dome, Antarctica. *Journal of Glaciology*, 51, 173, 281-290, doi: 10.3189/172756505781829359.
- Doake, S. S. M., Wolff, E. W. (1985) Flow law for ice in polar ice sheets. *Nature*, 314, 6008, 255-257.
- Drury, M. R., Humphreys, F. J. (1986) The development of microstructure in Al-5% Mg during high temperature deformation. *Acta Metallurgica*, 34, 11, 2259-2271, doi: 10.1016/0001-6160(86)90171-9.
- Drury, M. R., Humphreys, F. J. (1988) Microstructural shear criteria associated with grain-boundary sliding during ductile deformation. *Journal of Structural Geology*, 10, 1, 83-89, doi: 10.1016/0191-8141(88)90130-7.
- Durand, G., Persson, A., Samyn, D., Svensson, A. (2008) Relation between neighbouring grains in the upper part of the NorthGRIP ice core – Implication for rotation recrystallization. *Earth and Planetary Science Letters*, 265, 3-4, 666-671, doi: 10.1016/j.epsl.2007.11.002.
- Durand, G., Svensson, A., Persson, A., Gagliardini, O., Gillet-Chaulet, F., Sjolte, J., Montagnat, M., Dahl-Jensen, D. (2009) Evolution of the texture along the EPICA Dome C ice core. *Low Temperature Science*, 68, 91-105.
- Durham, W. B., Kirby, S. H., Stern, L. A. (1997) Creep of water ices at planetary conditions: A compilation. *Journal of Geophysical Research*, 102, E7, 16293-16302, doi: 10.1029/97JE00916.
- Durham, W. B., Prieto-Ballesteros, O., Goldsby, D. L., Kargel, J. S. (2010) Rheological and Thermal Properties of Icy Materials. *Space Science Reviews*, 153, 273-298, doi:10.1007/s111214-009-9619-1.
- Duval, P., Ashby, M. F., Anderman, I. (1983) Rate-Controlling Processes in the Creep of Polycrystalline Ice. *Journal of Physical Chemistry*, 87, C1, 4066-4074, doi: 10.1021/j100244a014.
- Duval, P., Arnaud, L., Brissaud, O., Montagnat, M., De La Chapelle, S. (2000) Deformation and recrystallization processes of ice from polar ice sheets. *Annals of Glaciology*, 30, 83-87, doi: 10.3189/172756400781820688.
- Duval, P., Castelnaud, O. (1995) Dynamic Recrystallization of Ice in Polar Ice Sheets. *Journal de Physique III*, 05, C3-197-C3-205, doi: 10.1051/jp4:1995317.
- Duval, P., Montagnat, M. (2002) Comment on “Superplastic deformation of ice: Experimental observations” by D. L. Goldsby and D. L. Kohlstedt. *Journal of Geophysical Research*, 107, B4, 1-2, doi: 10.1029/2001JB000946.

- Eichler, J., Weikusat, I., Kipfstuhl, S. (2013): Orientation-tensor eigenvalues along the NEEM ice core. PANGAEA, <https://doi.org/10.1594/Pangaea.838059>.
- Eichler, J., Kleitz, I., Bayer-Giraldi, M., Jansen, D., Kipfstuhl, S., Shigeyama, W., Weikusat, C., Weikusat, I. (2017) Location and distribution of micro-inclusions in the EDML and NEEM ice cores using optical microscopy and in situ Raman spectroscopy. *The Cryosphere*, 11, 3, 1075-1090, doi: 10.5194/tc-11-1075-2017.
- Faria, S. H., Freitag, J., Kipfstuhl, S. (2010) Polar ice structure and the integrity of ice-core paleoclimate records. *Quaternary Science Reviews*, 29, 1-2, 338-351, doi: 10.1016/j.quascirev.2009.10.016.
- Faria, S. H., Kipfstuhl, S., Azuma, N., Freitag, J., Weikusat, I., Murshed, M. M., Kuhs, W. F. (2009) Multiscale Structures in the Antarctic Ice Sheet Part I: Inland Ice. *Physics of Ice Core Records II, Supplement Issue of Low Temperature Science*, 68, 2, 39-59.
- Faria, S. H., Weikusat, I., Azuma, N. (2014b) The microstructure of polar ice. Part I: Highlights from ice core research. *Journal of Structural Geology*, 61, 2-20, doi: 10.1016/j.jsg.2013.09.010.
- Faria, S. H., Weikusat, I., Azuma, N. (2014a) The microstructure of polar ice. Part II: State of the art. *Journal of Structural Geology*, 61, 21-49, doi: 10.1016/j.jsg.2013.11.003.
- Fisher, D. A., Koerner, R. M. (1986) On the special rheological properties of ancient microparticle-laden northern hemisphere ice as derived from bore-hole and core measurements. *Journal of Glaciology*, 32, 112, 501-510.
- Fitzpatrick, J. J., Voigt, D. E., Fegyveresi, J. M., Stevens, N. T., Spencer, M. K., Cole-Dai, J., Alley, R. B., Jardine, G. E., Cravens, E. D., Wilen, L. A., Fudge, T. J., McConnell, J. R. (2014) Physical properties of the WAIS Divide ice core. *Journal of Glaciology*, 60, 224, 1181-1198, doi: 10.3189/2014JoG14J100.
- Fliervoet, T. F., White, S. H. (1995) Quartz deformation in a very fine grained quartzofeldspathic mylonite: a lack of evidence for dominant grain boundary sliding deformation. *Journal of Structural Geology*, 17, 8, 1095-1109, doi: 10.1016/0191-8141(95)00007-Z.
- Frost, H. J., Ashby, M. F. (1982) *Deformation-Mechanism Maps for Metals and Alloys*. Oxford: Pergamon Press.
- Fukuda, A., Hondoh, T., Higashi, A. (1987) Dislocation mechanisms of plastic deformation of ice. *Journal de Physique Colloques*, 48, C1, 163-173, doi: 10.1051/jphyscol:1987124.
- Gillet-Chaulet, F., Hindmarsh, R. C. A., Corr, H. F. J., King, E. C., Jenkins, A. (2011) In-situ quantification of ice rheology and direct measurement of the Raymond Effect at Summit, Greenland using a phase-sensitive radar. *Geophysical Research Letter*, 38, 24, 1-6, doi: 10.1029/2011GL049843.
- Glen, J. W. (1955) The creep of polycrystalline ice. *Proceedings of the Royal Society A: Mathematical, Physical and Engineering Sciences*, 228, 1175, 519-538, doi: 10.1098/rspa.1955.0066.
- Goldsby, D. L., Kohlstedt, D. L. (1997) Grain boundary sliding in fine grained ice I. *Scripta Materialia*, 37, 9, 1399-1406.
- Goldsby, D. L., Kohlstedt, D. L. (2001) Superplastic deformation of ice: Experimental observations. *Journal of Geophysical Research*, 106, B6, 11017-11030, doi: 10.1029/2000JB900336.

- Goldsby, D. L., Kohlstedt, D. L. (2002) Reply to comment by P. Duval and M. Montagnat on “Superplastic deformation of ice: Experimental observations.” *Journal of Geophysical Research*, 107, B11, 1-5, doi: 10.1029/2002JB001842.
- Gow, A. J. (1969) On the rates of growth of grains and crystals in south polar firn. *Journal of Glaciology*, 8, 53, 241-252, doi: 10.3189/S0022143000031233.
- Hamann, I., Weikusat, C., Azuma, N., Kipfstuhl, S. (2007) Evolution of ice crystal microstructure during creep experiments. *Journal of Glaciology*, 53, 182, 479-489, doi: 10.3189/002214307783258341.
- Hondoh, T. (2000) Nature and behavior of dislocations in ice. In Hondoh, T., ed. *Physics of ice core records*. Sapporo, Hokkaido University Press, 3-24.
- Humphreys, F. J., Bate P.S., Hurley, P.J. (2001) Orientation averaging of electron backscattered diffraction data. *Journal of Microscopy*, 201, 1, 50–58, doi: 10.1046/j.1365-2818.2001.00777.x.
- Humphreys, F. J., Hatherly, M. (2004) *Recrystallization and Related Annealing Phenomena*. Second ed. Pergamon, Oxford.
- Ignat, M., Frost, H. J. (1987) Grain boundary sliding in ice. *Le Journal de Physique Colloques*, 48, 9, C1-189-C1-195, doi: 10.1051/jphyscol:1987127.
- IPCC. (2014) *Climate change 2014: Synthesis report. contribution of working groups i, ii, iii to the fifth assessment report of the intergovernmental panel on climate change*, IPCC, Geneva, Switzerland, 151.
- Jacka, T. H. (1984) The time and strain required for development of minimum strain rates in ice. *Cold Regions Science and Technology*, 8, 261-268, doi: 10.1016/0165-232X(84)90057-0.
- Jansen, D., Llorens, M. -G., Westhoff, J., Steinbach, F., Kipfstuhl, S., Bons, P. D., Griera, A., Weikusat, I. (2016) Small-scale disturbances in the stratigraphy of the NEEM ice core: observations and numerical model simulations. *The Cryosphere*, 10, 359-370, doi: 10.5194/tc-10-359-2016.
- Kamb, W. B. (1961) The glide direction in ice. *Journal of Glaciology*, 3, 30, 1097-1106.
- Kipfstuhl, S., Faria, S., Azuma, N., Freitag, J., Hamann, I., Kaufmann, P., Miller, H., Weiler, K., Wilhelms, F. (2009) Evidence of dynamic recrystallization in polar firn. *Journal of Geophysical Research*, 114, 5, 1-10, doi: 10.1029/2008JB005583.
- Kipfstuhl, S., Hamann, I., Lambrecht, A., Freitag, J., Faria, S. H., Grigoriev, D., Azuma, N. (2006) Microstructure mapping: a new method for imaging deformation-induced microstructural features of ice on the grain scale. *Journal of Glaciology*, 52, 178, 298-406, doi: 10.3189/172756506781828647.
- Kipfstuhl, S., Pauer, F., Kuhs, W. F., Shoji, H. (2001) Air bubbles and clathrate hydrates in the transition zone of the NGRIP ice core. *Geophysical Research Letters*, 28, 4, 591-594, doi: 10.1029/1999GL006094.
- Krischke, A., Oechsner, U., Kipfstuhl, S. (2015) Rapid Microstructure Analysis of Polar Ice Cores. *Optik & Photonik*, 10, 2, 32-35, doi: 10.1002/opph.201500016.
- Kuramoto, T., Goto-Azuma, K., Hirabayashi, M., Miyake, T., Motoyama, H., Dahl-Jensen, D., Steffensen, J. P. (2011) Seasonal variation of snow chemistry at NEEM, Greenland. *Annals of Glaciology*, 52, 58, 193-200, doi: 10.3189/172756411797252365.

- Legrand, M., Mayewski, P. (1997) Glaciochemistry of polar ice cores: A review. *Reviews of Geophysics*, 35, 3, 219-243, doi: 10.1029/96RG03527.
- Llorens, M.-G., Griera, A., Bons, P. D., Roessiger, J., Lebensohn, R., Evans, L., Weikusat, I. (2016) Dynamic recrystallization of ice aggregates during co-axial viscoplastic deformation: a numerical approach. *Journal of Glaciology*, 62, 232, 359-377, doi: 10.1017/jpg.2016.28.
- Llorens, M.-G., Griera, A., Steinbach, F., Bons, P. D., Gomez-Rivas, E., Jansen, D., Roessiger, J., Lebensohn, R. A., Weikusat, I. (2017) Dynamic recrystallization during deformation of polycrystalline ice: insights from numerical simulations. *Philosophical transactions A*, 375, doi: 10.1098/rsta.2015.0346.
- Mathiesen, J., Ferkinghoff-Borg, J., Jensen, M. H., Levinsen, M., Olesen, P., Dahl-Jensen, D., Svensson, A. (2004) Dynamics of crystal formation in the Greenland NorthGRIP ice core. *Journal of Glaciology*, 50, 170, 325-328, doi: 10.3189/172756504781829873.
- Mellor, M., Testa, R. (1969a) Creep of ice under low stress. *Journal of Glaciology*, 8, 52, 147-152.
- Mellor, M., Testa, R. (1969b) Effect of temperature on the creep of ice. *Journal of Glaciology*, 8, 52, 131-145.
- Miyamoto, A., Shoji, H., Hori, A., Hondoh, T., Clausen, H. B., Watanabe, O. (2005) Ice fabric evolution process understood from anisotropic distribution of *a*-axis orientation on the GRIP (Greenland) ice core. *Annals of Glaciology*, 42, 47-52, doi: 10.3189/172756405781812501.
- Miyamoto, A., Weikusat, I., Hondoh, T. (2011) Instruments and Methods Complete determination of ice crystal orientation using Laue X-ray diffraction method. *Journal of Glaciology*, 57, 201, 103-110, doi: 10.3189/002214311795306754.
- Montagnat, M., Azuma, N., Dahl-Jensen, D., Eichler, J., Fujita, S., Gillet-Chaulet, F., Kipfstuhl, S., Samyn, D., Svenson, A., Weikusat, I. (2014) Fabric along the NEEM ice core, Greenland, and its comparison with GRIP and NGRIP ice cores. *The Cryosphere*, 8, 1129-1138, doi: 10.5194/tc-8-1129-2014.
- Montagnat, M., Buiron, D., Arnaud, L., Broquet, A., Schlitz, P., Jacob, R., Kipfstuhl, S. (2012) Measurements and numerical simulation of fabric evolution along the Talos Dome ice core, Antarctica. *Earth and Planetary Science Letters*, 357-358, 168, 178, doi: 10.1016/j.epsl.2012.09.025.
- Montagnat, M., Chauve, T., Barou, F., Tommasi, A., Beausir, B., Fressengeas, C. (2015) Analysis of Dynamic Recrystallization of Ice from EBSD Orientation Mapping. *Frontiers in Earth Science*, 3, 81, 1-13, doi: 10.3389/feart.2015.00081.
- Montagnat, M., Durand, G., Duval, P. (2009) Recrystallization processes in granular ice. *Low Temperature Science, Physics of ice core records II*, 68, 81-90.
- Montagnat, M., Duval, P. (2000) Rate controlling processes in the creep of polar ice, influence of grain boundary migration associated with recrystallization. *Earth and Planetary Science Letters*, 183, 1-2, 179-186, doi: 10.1016/S0012-821X(00)00262-4.
- Montagnat, M., Duval, P. (2004) Dislocations in Ice and Deformation Mechanisms: from Single Crystals to Polar Ice. *Defect and Diffusion Forum*, 229, 43-54.
- Montagnat, M., Duval, P., Bastie, P., Hamelin, B., Lipenkov, V. Y. (2003a) Lattice distortion in ice crystals from the Vostok core (Antarctica) revealed by hard X-ray

diffraction: implication in the deformation of ice at low stress. *Earth and Planetary Science Letters*, 214, 369-378, doi: 10.1016/S0012-821X(03)00364-9.

Montagnat, M., Duval, P., Bastie, P., Hamelin, B. (2003b) Strain gradients and geometrically necessary dislocations in deformed ice single crystals. *Scripta Materialia*, 49, 5, 441-415, doi: 10.1016/S1359-6462(03)00303-8.

Morawiec, A. (1995) Misorientation-angle distribution of randomly oriented symmetric objects. *Journal of Applied Crystallography*, 28, 3, 289-293.

Morgan, V. I. (1991) High-temperature ice creep tests. *Cold Regions Science and Technology*, 19, 295-300.

NEEM community members. (2013) Eemian interglacial reconstructed from a Greenland folded ice core. *Nature*, 493, 489-494, doi: 10.1038/nature11789.

Nye, J. F. (1953) Some geometrical relations in dislocated crystals. *Acta Metallurgica*, 1, 2, 153-162, doi: 10.1016/0001-6160(53)90054-6.

Obbard, R., Baker, I., Sieg, K. (2006) Using electron backscatter diffraction patterns to examine recrystallization in polar ice sheets. *Journal of Glaciology*, 52, 179, 546-557, doi: 10.3189/172756506781828458.

Passchier, C. W., Trouw, R. A. J. (2005) *Microtectonics*, Springer, Berlin.

Paterson, W. S. B. (1991) Why ice-age ice is sometimes “soft”. *Cold Regions Science and Technology*, 20, 1, 75-98.

Paterson, W. S. B. (1994) *The physics of glaciers*, Third edition. Oxford, Elsevier.

Pauer, F., Kipfstuhl, S., Kuhs, W. F., Shoji, H. (1999) Air hydrates crystals from the GRIP deep ice core, Greenland: a number- size- and shape-distribution study. *Journal of Glaciology*, 45, 149, 22-30.

Peltier, W. R., Goldsby, D. L., Kohlstedt, D. L., Tarasov, L. (2000) Ice-age ice-sheet rheology; constraints from the Last Glacial Maximum form of the Laurentide ice sheet. *Annals of Glaciology*, 30, 163-176, doi: 10.3189/172756400781820859.

Pimienta, P., Duval, P. (1987) Rate controlling processes in the creep of polar glacier ice. *Journal de Physique*, 48, C1, 243-248, doi: 10.1051/jphyscol:1987134.

Raj, R., Ashby, M. F. (1971) On Grain Boundary Sliding and Diffusional Creep. *Metallurgical Transactions*, 2, 4, 1113-1127, doi: 10.1007/BF02664244.

Rasmussen, S. O., Abbott, P. M., Blunier, T., Bourne, A. J., Brook, E., Buchardt, S. L., Buizert, C., Chappellaz, J., Clausen, H. B., Cook, E., Dahl-Jensen, D., Davies, S. M., Guillevic, M., Kipfstuhl, S., Laepple, T., Seierstad, I. K., Severinghaus, J. P., Steffensen, J. P., Stowasser, C., Svensson, A., vallelonga, P., Vinther, B. M., Wilhelms, F., Winstrup, M. (2013) A first chronology for the North Greenland Eemian Ice Drilling (NEEM) ice core. *Climate of the Past*, 9, 2713-2730, doi: 10.5194/cp-9-2713-2013.

Schulson, E. M., Duval, P. (2009) *Creep and Fracture of Ice*. Cambridge University Press.

Sheldon, S. G., Steffensen, J. P., Hansen, S. B., Popp, T. J., Johnsen, S. J. (2014) The investigation and experience of using ESTISOL™ 240 and COASOL™ for ice-core drilling. *Annals of Glaciology*, 55, 68, 219-232, doi: 10.3189/2014AoG68A036.

Shigeyama, W., Nagatsuka, N., Homma, T., Takata, M., Goto-Azuma, K., Weikusat, I., Drury, M. R., Kuiper, E. N., Pennock, G. M., Mateiu, R. V., Azuma, N., Dahl-Jensen, D. (2018) In-situ observations of solid particles in a deep ice core from Greenland. *Japan*

Geosciences Union Meeting 2018, Makuhari Messe Chiba, Japan.

<https://conft.atlas.jp/guide/event/jpgu2018/subject/ACC29-08/advanced>

Steinbach, F., Kuiper, E. N., Eichler, J., Bons, P. D., Drury, M. R., Griera, A., Pennock, G., Weikusat, I. (2017) The Relevance of Grain Dissection for Grain Size Reduction in Polar Ice: Insights from Numerical Models and Ice Core Microstructure Analysis.

Frontiers in Earth Science, 5, 66, 1-19, doi: 10.3389/feart.2017.00066.

Stern, L. A., Durham, W. B., Kirby, S. H. (1997) Grain-size-induced weakening of H₂O ice I and II and associated anisotropic recrystallization. *Journal of Geophysical Research*, 102, B3, 5313-5325.

Stipp, M., Stunitz, H., Heilbronner, R., Schmid, S. M. (2002) Dynamic recrystallization of quartz: correlation between natural and experimental conditions. *Geological Society, London, Special Publications*, 200, 1, 171-190.

Suzuki, S. Kuroiwa, D. (1972) Grain-boundary energy and grain-boundary groove angles in ice. *Journal of Glaciology*, 11, 62, 265-277.

Thorsteinsson, T., Waddington, E. D., Taylor, K. C., Alley, R. B., Blankenship, D. D. (1999) Strain-rate enhancement at Dye 3, Greenland. *Journal of Glaciology*, 45, 150, 338-345, doi: 10.3189/002214399793377185.

Thorsteinsson, T., Kipfstuhl, J., Miller, H. (1997) Textures and fabrics in the GRIP ice core. *Journal of Geophysical Research*, 102, C12, 26583-26599, doi: 10.1029/97JC00161.

Treverrow, A., Budd, W. F., Jacka, T. H., Warner, R. C. (2012) The tertiary creep of polycrystalline ice: experimental evidence for stress-dependent levels of strain-rate enhancement. *Journal of Glaciology*, 58, 208, 301-314, doi: 10.3189/2012JoG11J149.

Uthus, L., Hoff, I., Horvli, I. (2005) Evaluation of grain shape characterization methods for unbound aggregates. *Seventh International Conference on the Bearing Capacity of Road*, Trondheim.

Von Mises, R. (1928) *Mechanik der Plastischen Formänderung von Kristallen*. *Zeitschrift für Angewandte Mathematik und Mechanik*, 8, 161-185.

Weikusat, I., de Winter, D. A. M., Pennock, G. M., Hayles, M., Schneiderberg, C. T. W. M., Drury, M. R. (2011a) Cryogenic EBSD on ice: preserving a stable surface in a low pressure SEM. *Journal of Microscopy*, 242, 3, 295-310, doi: 10.1111/j.1365-2818.2010.03471.x.

Weikusat, I., Jansen, D., Binder, T., Eichler, J., Faria, S. H., Wilhelms, F., Kipfstuhl, S., Sheldon, S., Miller, H., Dahl-Jensen, D., Kleiner, T. (2017) Physical analysis of an Antarctic ice core – towards an integration of micro- and macrodynamics of polar ice. *Philosophical transactions A*, 375, doi: 10.1098/rsta.2015.0347.

Weikusat, I., Kipfstuhl, S., Faria, S., Azuma, N., Miyamoto, A. (2009a) Deformation Microstructures in an Antarctic ice core (EDML) and in Experimentally Deformed Artificial Ice. *Physics of Ice Core Records II*, 68, 115-123.

Weikusat, I., Kipfstuhl, S., Faria, S. H., Azuma, N., Miyamoto, A. (2009b) Subgrain boundaries and related microstructural features in EDML (Antarctica) deep ice core. *Journal of Glaciology*, 55, 191, 461-472, doi: 10.3189/002214309788816614.

Weikusat, I., Miyamoto, A., Faria, S. H., Kipfstuhl, S., Azuma, N., Hondoh, T. (2011b) Subgrain boundaries in Antarctic ice quantified by X-ray Laue diffraction, 57, 201, 85-94, doi: 10.3189/002214311795306628.

Weiss, J., Vidot, J., Gay, M., Arnaud, L., Duval, P., Petit, J. R. (2002) Dome Concordia ice microstructure: Impurities effect on grain growth. *Annals of Glaciology*, 35, 552-558, doi: 10.3189/172756402781816573.

Wenk, H.-R., Canova, A., Molinari, A., Kocks, U. F. (1989) Viscoplastic modelling of texture development in quartzite. *Journal of Geophysical Research*, 94, B12, 17895-17906, doi: 10.1029/JB094iB12p17895.

Westhoff, J. (2014) Small Scale Folding in NEEM Ice Core. Bachelor Thesis, Eberhard Karls Universität Tübingen and Alfred Wegener Institute, Bremerhaven, Germany.

Zhang, Y., Hobbs, B. E., Jessell, M. W. (1994) The effect of grain-boundary sliding on fabric development in polycrystalline aggregates. *Journal of Structural Geology*, 16, 9, 1315-1325, doi: 10.1016/0191-8141(94)90072-8.

Chapter 7

Summary and suggestions for further research

Summary

Introduction

Global mean sea level (GMSL) rise is expected to accelerate in the next decades and centuries due to anthropogenic climate change. The highest uncertainty in long term GMSL predictions is the melting of the Greenland and Antarctic ice sheets, which contain enough water to raise GMSL by 7 and 61 meters, respectively. One of the uncertainties in the ice sheet models that are used to predict the contribution of the polar ice sheets to GMSL rise is the flow of ice by internal deformation. To model the flow of ice in polar ice sheets Glen's flow law (Glen, 1955; Paterson, 1994) is often used, which is a flow law derived in secondary creep with artificially produced (initially) isotropic ice at relatively high stress (0.1-1.0 MPa) compared to natural ice conditions. It has been shown that ice at these relatively high stress levels deforms by the easy slip system (basal slip) and is accommodated by the harder slip systems (non-basal slip), a deformation mechanism also known as dislocation creep. However, ice deformation tests and microstructural studies of polar ice have shown that, at the low stress conditions in polar ice sheets, ice can deform by other deformation mechanisms, such as a mechanism that includes recovery by strain induced boundary migration (SIBM) or a grain size sensitive mechanism (e.g. Alley, 1992; Pimienta and Duval, 1987; Goldsby and Kohlstedt, 1997, 2001; Montagnat and Duval, 2000). The dominant deformation mechanism under certain boundary conditions depends on the microstructure of the ice, which in turn is determined by the balance of the different recovery and recrystallization mechanisms. The recrystallization and deformation mechanisms in ice depend on many different factors such as crystallographic preferred orientation (CPO), grain size, driving stress, deformation mode, temperature and impurity content, which all vary strongly throughout polar ice sheets. The uncertainty about which deformations mechanisms are active in polar ice complicates attempts to replace or improve Glen's flow law in ice sheet models. The aim of this PhD project is to study the recrystallization and deformation mechanisms of polar ice and the effect of these processes on ice sheet flow laws and ice sheet dynamics so that ice sheet models can be improved.

Microstructural information from the North Greenland Eemian Ice Drilling (NEEM) ice core in northwest Greenland were studied. Recrystallization and deformation mechanisms in the NEEM ice core were studied using two different methods: (i) microstructural studies were carried out using cryogenic electron backscatter diffraction (cryo-EBSD) in combination with (polarized) light microscopy (LM) studies (Chapter 2, 3 and 6) and (ii) two different flow law models were applied to polar ice constrained by actual grain size and temperature data from the NEEM ice core (Chapter 4 and 5). In order to obtain an overview of the dominant recrystallization and deformation mechanisms with depth in the ice core, the results of these two methods were combined with the results from earlier ice microstructural studies on the NEEM ice core (Chapter 6). For this overview, the NEEM ice core was divided into three different depth intervals that differ significantly in

temperature, CPO, grain size, grain shape and deformation mode: the Holocene ice (0-1419 m of depth), the glacial ice (1419-2207 m of depth) and the Eemian-glacial facies (2207-2540 m of depth).

Microstructural results

In total, nine different ice core sections along the NEEM ice core were used for EBSD sample preparation. More than a thousand subgrain boundaries (SGBs) were mapped using cryo-EBSD and categorized based on misorientation angle, rotation axis and trace orientation of the boundary plane (trace). Slip system analyses using the trace and rotation axis showed that SGBs indicative of dislocations with Burgers vector $\mathbf{b}=(1/3)\langle 1\bar{2}10 \rangle$ ($\mathbf{b}=\langle \mathbf{a} \rangle$) gliding on the basal plane are the most common type of SGBs in the Holocene and glacial ice (both about 40%) and the Eemian-glacial facies (about 60%) (Chapter 2 and 3). A small percentage of SGBs (<5%) along the length of the NEEM ice core were analyzed in terms of prism $\mathbf{b}=\langle \mathbf{a} \rangle$ slip and slip of $\mathbf{b}=\langle \mathbf{a} \rangle$ screw dislocations on the basal plane. About 30-35% of SGBs in the Holocene and glacial ice and 15% of SGBs in the Eemian-glacial facies were indicative of $\mathbf{b}=[0001]$ or $\mathbf{b}=(1/3)\langle 11\bar{2}3 \rangle$ dislocations gliding on prism and/or pyramidal planes and are therefore likely formed by non-basal slip. These non-basal type of SGBs were found in every sample that was mapped with cryo-EBSD, showing that non-basal slip is activated along the entire length of the NEEM ice core. However, two regions in the NEEM ice core contained considerably fewer SGBs indicative of non-basal slip: the middle and lower part of the Holocene ice and the Eemian-glacial facies. The grain boundary network in these two regions indicates considerable activity of SIBM, which strongly suggests that the amount of non-basal slip that is activated is controlled by the removal of strain incompatibilities by SIBM (Chapter 3).

Along the entire NEEM ice core, about 20% of SGBs could not easily be related to slip system activity in the host grain. Of these not-classified SGBs, 1% had a high misorientation angle (4.0° - 6.5°) in the Holocene ice, while in the glacial ice 36% of these not-classified SGBs had a high misorientation angle (4.0° - 6.5°). Two explanations are provided for this difference: (i) sliding along the newly formed high angle SGBs in the glacial ice results in ‘general’ rotation axes and (ii) multiple slip systems with different rotation axes were involved in the formation of the SGB, which leads to a general rotation axis (Chapter 3).

The data on misorientation angles of the SGBs showed that all SGBs that were analyzed had a misorientation angle $<6.5^\circ$. In all three depth intervals, low angle SGBs (0.5° - 2.0°) were the most common, with the highest percentage in the Eemian-glacial facies, followed by the Holocene ice and the glacial ice. This low angle range of subgrain boundary misorientations can be explained by the high rates of SIBM in the Holocene ice and especially in the Eemian-glacial facies, which consumes many SGBs before they can rotate into higher angle SGBs or grain boundaries (Chapter 3).

EBSD data showed that a clear difference in the mean orientation gradient of the grains between different depths in the NEEM ice core (Chapter 6). The mean orientation gradient is relatively low (1.0° - $1.5^{\circ} \text{ mm}^{-1}$) in the sample at 413 m of depth in the shallow part of the Holocene ice and at 2241 m of depth in a fine grained layer in the Eemian-glacial facies, while the mean orientation gradient is much higher (2.5° - $3.5^{\circ} \text{ mm}^{-1}$) in the middle and lower part of the Holocene ice and in the glacial ice. The increase in mean orientation gradient in the Holocene ice between 413 m and 718-889 m of depth coincides with an increase in the extent of SIBM, as indicated by the more irregular grain boundary networks in the Holocene ice (Chapter 3). In the Eemian-glacial facies, the low mean orientation gradient is likely a result of extensive SIBM, which is enhanced by premelting along the grain boundaries.

Analysis of LM images and the EBSD data set identified a process resembling microstructural shear in very fine grained sub-horizontal bands in the glacial ice (Chapter 6). Microstructural shear includes grain boundary sliding (GBS) along aligned grain boundaries and the formation of SGBs in the grains that are blocking the sliding grains. When a critical misorientation angle of about 5.0° - 6.0° is reached, the SGB has rotated into a sliding boundary and becomes part of the aligned grain boundary structure, which acts as a positive feedback for further sliding. A strong alignment of c- and a-axes observed in fine grained sub-horizontal bands in the glacial ice suggests that GBS is an accommodating mechanism for basal slip in the glacial ice of the NEEM ice core.

Results from flow law modelling

The composite flow law of Goldsby and Kohlstedt (1997, 2001) describes ice deformation by two different deformation mechanisms: dislocation creep and basal slip accommodated by GBS. For both mechanisms basal slip is assumed to be the main strain-producing mechanism, which is either accommodated by non-basal slip (dislocation creep) or by GBS (GBS-limited creep). The composite flow law was modified in order to obtain a better agreement between the experimental data for dislocation creep and the calculated strain rates for the dislocation creep mechanism (Chapter 4). The composite flow law was also modified to fit a new temperature threshold of 262K for the onset of premelting in polar ice, which was found after a survey of ice microstructures close to the melting point in eight different polar ice cores (Chapter 5). The modified composite flow law, together with Glen's flow law (Glen, 1955; Paterson, 1994), were used to calculate the strain rates along the NEEM ice core using actual temperature and grain size data from the NEEM ice core, which were obtained by automated image analysis of LM images (Chapter 4). The grain size data in the Holocene and glacial ice were described using a mean grain size and a full grain size distribution. The grain size distribution allowed for the application of two different model end members: (i) the micro-scale constant stress model, where each grain experiences the same stress but deforms at a different strain rate and (ii) the micro-scale constant strain rate model, where each grain deforms by the same (bulk) strain rate but supports a different stress. The grain size in the Eemian-glacial facies is highly variable

with depth due to the stratigraphic disruptions in this part of the NEEM ice core (NEEM community members, 2013), which causes the fine grained glacial ice to be alternated by the coarse grained Eemian ice. Due to the very large grain size in parts of the Eemian-glacial facies it was not possible to determine a grain size distribution, so only a mean grain size was used to calculate the strain rate produced by GBS-limited creep.

The results show that Glen's flow law predicts a higher strain rate than the modified composite flow law along the entire length of the NEEM ice core (Chapter 4 and 5). Glen's flow law is grain size insensitive and shows a steady increase in strain rate with depth resulting from an increase in temperature with depth. Applying the modified composite flow law to the Holocene and glacial ice, the strain rate predicted by GBS-limited creep is about an order of magnitude higher than the strain rate predicted by dislocation creep (Chapter 4). The average strain rate predicted by the modified composite flow law in the fine grained glacial ice is four to five times higher than in the coarser grained Holocene ice. The strain rate variability with depth, resulting from a variability in grain size, is relatively small in the Holocene ice, but is much larger in the glacial ice, showing two strain rate peaks at about 1980 and 2100 m of depth. The difference between the micro-scale constant stress model and the micro-scale constant strain rate model is relatively small, with the micro-scale constant stress model predicting slightly higher strain rates and a higher contribution of GBS-limited creep to bulk strain rate than the micro-scale constant strain rate model.

The Eemian-glacial facies is likely affected by premelting along the grain boundaries (the premelting layer), which enhances grain boundary processes such as GBS and SIBM (Chapter 5). The modified composite flow law predicts that the strain rate in the fine grained glacial layers in the Eemian-glacial facies is about an order of magnitude higher than in the coarse grained Eemian layers. The fine grained glacial layers deform almost entirely by GBS-limited creep. In the coarse grained layers dislocation creep and GBS-limited creep contribute roughly equally to bulk strain rate, although the calculated strain rate for GBS-limited creep depends on the mean grain size that was assigned to coarsest grained layers (30 mm).

There is a strong correlation between changes in grain size and type and strength of CPO in the Eemian-glacial facies (Chapter 5). The impurity-rich glacial ice consists of relatively fine grains (<5 mm diameter) with a strong single maximum CPO, while the impurity-depleted Eemian ice consists of coarser (>5 mm diameter) and more interlocking grains with a multi maxima or partial girdle type of CPO. Due to the difference in CPO between the glacial and Eemian ice, it is expected that the fine grained glacial ice deforms predominantly by simple shear, which is the dominant deformation mode in this part of the NEEM ice core, while the coarse grained interglacial ice deforms predominantly by coaxial deformation or is relatively stagnant. The difference in microstructure, and consequently in viscosity, between the glacial and interglacial ice at temperatures just below the melting point can have important consequences for ice sheet dynamics close to the bedrock. It is expected that the premelting layer hardly contributes to horizontal velocity if the premelting layer consists of impurity-depleted interglacial ice, while it is expected that a premelting

layer consisting of impurity-rich glacial ice contributes significantly to horizontal velocity (Chapter 5).

Synthesis of the recrystallization and deformation mechanisms in the NEEM ice core

The relatively coarse and irregular shaped grains in the Holocene ice argue against GBS as an important accommodating mechanism for basal slip (Chapter 6). Instead, basal slip is accommodated by recovery via SIBM in the Holocene ice, which removes strain incompatibilities after which basal slip can proceed. However, slip system analysis from SGBs (chapter 2 and 3) shows that significant non-basal slip is activated in the Holocene ice, even in the samples that show extensive SIBM. Therefore, it is proposed that the Holocene ice deforms by recovery via basal slip accommodated by SIBM and non-basal slip, where the activation of non-basal slip is regulated by the extent of SIBM.

Microstructural analysis indicates that the dominant recrystallization mechanisms and processes in the Holocene ice are bulging recrystallization, grain dissection and SIBM. Normal grain growth is an important mechanism in the upper 250 m of the ice core. Rotation recrystallization is expected to be relatively unimportant in the Holocene ice.

Microstructures in the glacial ice indicate that GBS is an important accommodating mechanism for basal slip, particularly in the fine grained sub-horizontal bands (Chapter 6). However, slip system analysis from SGBs indicates that significant amounts of non-basal slip are activated in the glacial ice. It is therefore proposed that the glacial ice deforms by basal slip accommodated by GBS and non-basal slip. The strong *c*-axes alignment in the glacial ice, particularly in the fine grained sub-horizontal bands, indicates that GBS as an accommodating mechanism for basal slip does not destroy but strengthens CPO. The grain boundary network shows that SIBM is relatively unimportant in the glacial ice, while rotation recrystallization is more important in the glacial ice than in the Holocene ice.

The effect of grain size on strain rate is predicted to be very large in the Eemian-glacial facies, with the fine grained glacial layers deforming about an order of magnitude faster than the coarse grained Eemian layers. Changes in grain size correlate strongly with type and strength of CPO in the Eemian-glacial facies with the fine grained layers having a single maximum CPO and the coarse grained layers a multi maxima or a partial girdle type CPO. It is therefore expected that the fine grained layers deform predominantly by simple shear at high strain rates, while the coarse grained layers deform at much lower strain rates and hardly contribute to horizontal velocity.

Flow law modelling using the modified composite flow law (Chapter 4 and 5) predicts that GBS-limited creep is the dominant deformation mechanism along almost the entire NEEM ice core. However, microstructures indicate that dislocation creep is the dominant deformation mechanism in the Holocene ice and the coarse grained layers in the Eemian-glacial facies (Chapter 6). Furthermore, significant non-basal slip is activated all along the NEEM ice core (Chapter 2 and 3). It is therefore proposed that the modified

composite flow law underestimates the strain rate produced by dislocation creep. This underestimation can best be explained by the absence of dynamic recrystallization mechanisms and recovery by SIBM in the experiments used to calculate the parameters of the composite flow law of Goldsby and Kohlstedt (1997, 2001), while these mechanisms are present in polar ice sheets and enhance the strain rate produced by dislocation creep at high strain.

Suggestions for further research

Ice deformation at, or close to, the pressure-melting point is of high importance for ice sheet dynamics. Modelling studies and borehole tilt data have shown that most of the horizontal movement is accommodated in the lowest 10-20% of polar ice sheets. However, most research into ice deformation mechanisms of natural ice samples so far has focused on the colder and shallower ice that is not affected by premelting. The study presented in Chapter 5 shows that there is a large difference in the dominant deformation mechanism and strain rate in the premelting layer (ice at $262\text{K} < T^* < 273\text{K}$, where T^* is the pressure-adjusted temperature) between impurity-rich glacial ice and impurity-depleted interglacial ice. Therefore, a suggestion for further research would be to perform more cryo-EBSD studies on ice from the premelting layer of NEEM or other polar ice cores. Since Chapter 3 showed that significantly less non-basal slip was activated in the fine grained glacial ice in the premelting layer, it would be interesting to study the slip system activity in both the glacial and interglacial ice in the premelting layer. In order to achieve this, a larger EBSD sample size is required than the $8 \times 8 \times 5$ mm sized EBSD samples that were used during this PhD project. The methods proposed by Prior et al. (2015) could be used to prepare and map larger samples with cryo-EBSD. Different methods to study slip system activity from EBSD data could also be considered, such as HR-EBSD (e.g. Britton and Wilkinson, 2011; Wallis et al., 2016) or the application of the Weighted Burgers Vector (e.g. Wheeler et al., 2009; Chauve et al., 2017). These methods have the advantage to study all geometrically necessary dislocations instead of only the dislocations that have recovered into subgrain boundaries.

Chapter 4, 5 and 6 showed that the composite flow law of Goldsby and Kohlstedt (1997, 2001) likely underestimates the strain rate produced by dislocation creep. A suggestion for further research would be to perform more deformation tests in the dislocation creep regime in order to adjust the flow law parameters for dislocation creep in the composite flow law. If the explanation provided in Section 6.5.3 why dislocation creep is so slow is correct, then simply continuing the deformation experiments beyond peak stress at about 1-2% strain (Figure 6.7) should improve the accuracy of the flow law parameters for dislocation creep. However, there are some complications with this approach. The timescale involved in deformation tests that continue to tertiary creep is much longer, potentially beyond what practically can be achieved in the laboratory. Part of this can be overcome by starting the deformation experiments at higher temperature and subsequently decrease the temperature when secondary creep is passed (e.g. Russel-head,

1979; Treverrow et al., 2012). Another complication is that if the deformation experiments in the dislocation creep regime continue beyond secondary creep, dynamic recovery and recrystallization will change the ice microstructure (e.g. Poirier, 1985; Budd and Jacka, 1989). The change in CPO, grain size and grain shape resulting from dynamic recovery and recrystallization will change the viscosity of the ice and therefore change the new flow law parameters for dislocation creep. In this case, the new parameters for dislocation creep will describe ice that has recrystallized and has a CPO, while the old parameters for GBS-limited creep describe ice that has not recrystallized and does not have a CPO. Furthermore, Treverrow et al. (2012) showed that the stress exponent is higher in tertiary creep than in secondary creep, which potentially induces an error when extrapolating back to the low stress levels that are relevant for ice sheets. Therefore, improving the flow law parameters of the dislocation creep mechanism of the composite flow law of Goldsby and Kohlstedt (2001) is not straightforward.

The East Greenland Ice-Core Project (EastGRIP) ice core (<https://eastgrip.org/>) is currently being drilled during the summer seasons. The drill site is located on top of the largest ice stream of the Greenland ice sheet: the North East Greenland Ice Stream (NEGIS). Contrary to other polar ice cores (e.g. Faria et al., 2014), this ice core is drilled at a site that is dynamically very active, moving at about 50 meters per year. The driving stress at the location of the EastGRIP ice core is much higher than the driving stress at the location of other Greenlandic ice cores (Sergienko et al., 2014), which are mainly drilled at low stress sites such as domes and flanks (Faria et al., 2014). The EastGRIP ice core provides an opportunity to study ice recrystallization and deformation mechanisms at a dynamically active site in the Greenland ice sheet. Recent analysis shows that the stress exponent that best describes the flow at NEGIS is different from the stress exponent in the remainder of the north Greenland ice sheet (Bons et al., 2018), which suggests that ice deforms by a different mechanism along the EastGRIP ice core compared to the other ice cores drilled at the Greenland ice sheet. However, it is likely that a large part of the horizontal velocity at the EastGRIP site is produced by sliding over the bedrock due to the high geothermal heat flux (Rogozhina et al., 2016). At the bedrock near EastGRIP, climatic undisturbed layers could be detected till 50,000 years before present (Dahl-Jensen, personal communication), which means that this ice was deposited during the last glacial period. Future borehole data combined with microstructure analysis from the ice close to the bedrock at EastGRIP can be used to study the deformation of glacial ice at high temperature and high stress. This way, the hypothesis of the different development of ice microstructure between the glacial and interglacial ice in the premelting layer, as proposed in Chapter 5, can be verified.

References

- Alley, R. B. (1992) Flow-law hypothesis for ice-sheet modelling. *Journal of Glaciology*, 38, 129, 245-256.
- Bons, P. D., Kleiner, T., Llorens, M.-G., Prior, D. J., Sachau, T., Weikusat, I., Jansen, D. (2018) Greenland Ice Sheet: Higher Nonlinearity of ice Flow Significantly Reduces Estimated Basal Motion. *Geophysical Research Letters*, 45, 13, 6542-6548, doi: 10.1029/2018GL078356.
- Britton, T. B., Wilkinson, A. J. (2011) Measurement of residual elastic strain and lattice rotations with high resolution electron backscatter diffraction. *Ultramicroscopy*, 111, 8, 1395-1404, doi: 10.1016/j.ultramic.2011.05.007.
- Budd, W. F., Jacka, T. H. (1989) A review of ice rheology for ice sheet modelling. *Cold Regions Science and Technology*, 16, 107-144, doi: 10.1016/0165-232X(89)90014-1.
- Chauve, T., Montagnat, M., Piazzolo, S., Journaux, B., Wheeler, J., Barou, F., Mainprice, D., Tommasi, A. (2017) Non-basal dislocations should be accounted for in simulating ice mass flow. *Earth and Planetary Science Letters*, 473, 247-255, doi: 10.1016/j.epsl.2017.06.020.
- Faria, S. H., Weikusat, I., Azuma, N. (2014) The microstructure of polar ice. Part I: Highlights from ice core research. *Journal of Structural Geology*, 61, 2-20, doi: 10.1016/j.jsg.2013.09.010.
- Glen, J. W. (1955) The creep of polycrystalline ice. *Proceedings of the Royal Society A: Mathematical, Physical and Engineering Sciences*, 228, 1175, 519-538, doi: 10.1098/rspa.1955.0066.
- Goldsby, D. L., Kohlstedt, D. L. (1997) Grain boundary sliding in fine grained ice I. *Scripta Materialia*, 37, 9, 1399-1406.
- Goldsby, D. L., Kohlstedt, D. L. (2001) Superplastic deformation of ice: Experimental observations. *Journal of Geophysical Research*, 106, B6, 11017-11030, doi: 10.1029/2000JB900336.
- Montagnat, M., Duval, P. (2000) Rate controlling processes in the creep of polar ice, influence of grain boundary migration associated with recrystallization. *Earth and Planetary Science Letter*, 183, 1-2, 179-186, doi: 10.1016/S0012-821X(00)00262-4.
- NEM community members. (2013) Eemian interglacial reconstructed from a Greenland folded ice core. *Nature*, 493, 489-494, doi: 10.1038/nature11789.
- Paterson, W. S. B. (1994) *The physics of glaciers*, Third edition. Oxford, Elsevier.
- Pimienta, P., Duval, P. (1987) Rate controlling processes in the creep of polar glacier ice. *Journal de Physique Colloques*, 48, C1, 243-248, doi: 10.1051/jphyscol:1987134.
- Poirier, J. P. (1985) *Creep of Crystals*. Cambridge University Press, Cambridge, 260 pp.
- Prior, D. J., Lilly, K., Seidemann, M., Vaughan, M., Becroft, L., Easingwood, R., Diebold, S., Obbard, R., Daghlian, C., Baker, I., Caswell, T., Golding, N., Goldsby, D., Durham, W. B., Piazzolo, S., Wilson, C. J. L. (2015) Making EBSD on water ice routine. *Journal of Microscopy*, 00, 0, 1-20, doi: 10.1111/jmi.12258.
- Rogozhina, I., Petrunin, A. G., Vaughan, A. P. M., Steinberger, B., Johnson, J. V., Kaban, M. K., Calov, R., Rickers, F., Thomas, M., Koulakov, I. (2016) Melting at the base of the

Greenland ice sheet explained by Iceland hotspot history, 9, 366-372, doi: 10.1038/ngeo2689.

Russel-Head, D. S. (1979) Ice sheet flow from borehole and laboratory studies. MSc Thesis, University of Melbourne.

Sergienko, O. V., Creyts, T. T., Hindmarsh, R. C. A. (2014) Similarity of organized patterns in driving and basal stresses of Antarctic and Greenland ice sheets beneath extensive areas of basal sliding. *Geophysical Research Letters*, 41, 11, 3925-3932, doi: 10.1002/2014GL059976.

Treverrow, A., Budd, W. F., Jacka, T. H., Warner, R. C. (2012) The tertiary creep of polycrystalline ice: experimental evidence for stress-dependent levels of strain-rate enhancement. *Journal of Glaciology*, 58, 208, 301-314, doi: 10.3189/2012JoG11J149.

Wallis, D., Hansen, L. N., Britton, T. B., Wilkinson, A. J. (2016) Geometrically necessary dislocation densities in olivine obtained using high-angular resolution electron backscatter diffraction. *Ultramicroscopy*, 168, 34-45, doi: 10.1016/j.ultramic.2016.06.002.

Wheeler, J., Mariani, E., Piazzolo, S., Prior, D. J., Trimby, P., Drury, M. R. (2009) The weighted Burgers vector: a new quantity for constraining dislocation densities and types using electron backscatter diffraction on 2D sections through crystalline materials. *Journal of Microscopy*, 233, 3, 482-494, doi: 10.1111/j.1365-2818.2009.03136.x.

Nederlandse samenvatting

Introductie

De stijging van de mondiale zeespiegel zal naar verwachting de komende decennia en eeuwen versnellen als gevolg van antropogene klimaatverandering. De grootste onzekerheid in de lange termijn voorspellingen van de mondiale zeespiegel is het smelten van de ijskappen van Groenland en Antarctica, waar genoeg water ligt opgeslagen voor een mondiale zeespiegelstijging van respectievelijk 7 en 61 m. Eén van de onzekerheden in de modellen die worden gebruikt om de bijdrage van de ijskappen aan de mondiale zeespiegelstijging te voorspellen is de stroming van ijs als gevolg van de interne vervorming van het ijs. De meest gebruikte stromingswet in modellen van ijskappen is de vloeiwet van Glen (Glen, 1955; Paterson, 1994). Deze vloeiwet is afgeleid in secundaire kruip met kunstmatig geproduceerd (initieel) isotroop ijs onder relatief hoge spanning (0.1-1.0 MPa) vergeleken met de spanning in natuurlijk ijs. Het is aangetoond dat ijs onder deze relatief hoge spanning vervormt door middel van het gemakkelijke schuifstelsel (*basal slip*) en geacommodeerd door het harde schuifstelsel (*non-basal slip*), een vervormingsmechanisme bekend als dislocatiekruip. Ijs vervormingstesten en microstructuurstudies van polair ijs hebben echter aangetoond dat, bij de lage spanning in polaire ijskappen, het ijs kan vervormen door middel van andere mechanismen, zoals een mechanisme dat gedreven wordt door herstel van vervorminggedreven korrelgrensmigratie (VGKM) of een mechanisme dat afhankelijk is van de korrelgrootte (bijv. Alley, 1992; Pimienta en Duval, 1987; Goldsby en Kohlstedt, 1997, 2001; Montagnat en Duval, 2000). De dominante vervormingsmechanismen onder bepaalde randvoorwaarden zijn afhankelijk van de microstructuur van ijs. Deze microstructuur wordt bepaald door de balans tussen de verschillende herstel- en rekristallisatiemechanismen. De rekristallisatie- en vervormingsmechanismen in ijs zijn afhankelijk van veel verschillende factoren, zoals de kristallografische voorkeursoriëntatie (KVO), korrelgrootte, spanning, vervormingsmodus, temperatuur en de onzuiverheidsgraad, die allen sterk variëren door de gehele ijskap heen. De onzekerheid over welke vervormingsmechanismen actief zijn in polair ijs bemoeilijkt de pogingen om de vloeiwet van Glen in de modellen van polaire ijskappen te verbeteren of te vervangen. Het doel van dit PhD-project was het bestuderen van de rekristallisatie- en vervormingsmechanismen van polair ijs en het effect van deze mechanismen op de vloeiwetten en de dynamica van ijskappen, zodat modellen van ijskappen kunnen worden verbeterd.

De *North Greenland Eemian Ice Drilling* (NEEM) ijskern uit het noordwesten van Groenland werd gebruikt voor het verkrijgen van ijskernmonsters en microstructuurdata van ijs. Twee verschillende methodes werden gebruikt voor het bestuderen van ijs rekristallisatie- en vervormingsmechanismen: (i) microstructuurstudies werden uitgevoerd door middel van *cryogenic electron backscatter diffraction* (*cryo-EBSD*) in combinatie met (gepolariseerd) licht microscopie (LM) studies (Hoofdstuk 2, 3 en 6) en (ii) twee

verschillende vloeiwetmodellen werden toegepast op poolijs, gebruikmakend van werkelijke korrelgrootte- en temperatuurdata uit de NEEM ijskern (Hoofdstuk 4 en 5). De resultaten van deze twee methodes werden gecombineerd met de resultaten van eerdere ijs microstructuurstudies van de NEEM ijskern om een overzicht te verkrijgen van welke rekristallisatie- en vervormingsmechanismen dominant zijn op welke diepte (Hoofdstuk 6). Voor dit overzicht werd de NEEM ijskern opgedeeld in drie verschillende diepte-intervallen die significant verschillen in temperatuur, KVO, korrelgrootte, korrelvorm en vervormingsmodus: het Holoceen ijs (0-1419 m diepte), het glaciaal ijs (1419-2207 m diepte) en de Eemien-glaciaal faciës (2207-2540 m diepte).

Microstructuur resultaten

In totaal werden negen ijskernsegmenten uit de NEEM ijskern werden gebruikt voor het prepareren van EBSD-monsters. Meer dan duizend sub-korrelgrenzen (SKG's) zijn opgemeten door middel van cryo-EBSD en gecategoriseerd op basis van misoriëntatiehoek, rotatieassen en de oriëntatie van het grensvlak. Analyses van schuifsystemen door middel van de oriëntatie van het grensvlak en de rotatieassen toonden aan dat SKG's indicatief voor dislocaties met Burgers vector $\mathbf{b}=(1/3)\langle 1\bar{2}10 \rangle$ ($\mathbf{b}=\langle \mathbf{a} \rangle$), schuivend op de *basal plane*, het meest voorkomende type SKG's zijn in het Holoceen en het glaciaal ijs (beiden ongeveer 40%) en het Eemien-glaciaal faciës (ongeveer 60%) (Hoofdstuk 2 en 3). Een klein percentage van de SKG's (<5%) in de NEEM ijskern werden geanalyseerd in termen van prismatisch $\mathbf{b}=\langle \mathbf{a} \rangle$ glijding en glijding van $\mathbf{b}=\langle \mathbf{a} \rangle$ schroefdislocaties op de *basal plane*. Ongeveer 30-35% van de SKG's in het Holoceen en glaciaal ijs en 15% van de SKG's in het Eemien-glaciaal faciës waren indicatief voor $\mathbf{b}=[0001]$ or $\mathbf{b}=(1/3)\langle 11\bar{2}3 \rangle$ dislocaties op de prismatische of piramidale glijvlakken en zijn daarom indicatief voor *non-basal slip*. Dit *non-basal* type SKG's werden gevonden in elk monster dat werd opgemeten met cryo-EBSD, wat aantoont dat *non-basal slip* wordt geactiveerd langs de gehele lengte van de NEEM ijskern. Twee gedeeltes in de NEEM ijskern bevatten echter aanzienlijk minder SKG's die indicatief zijn voor *non-basal slip*: het middel en lagere gedeelte van het Holoceen ijs en het Eemien-glaciaal faciës. Het korrelgrensnetwerk van deze gedeeltes suggereert hoge activiteit van VGKM, wat er sterk op duidt dat de activatie van *non-basal slip* wordt gereguleerd door het verwijderen van vervormingsincompatibiliteiten door middel van VGKM (Hoofdstuk 3).

Ongeveer 20% van de SKG's in gehele NEEM ijskern kon niet gemakkelijk gerelateerd worden aan schuifstelsel activiteit in de moederkorrel. Van deze niet-geclassificeerde SKG's had 1% een grote misoriëntatiehoek (4.0°-6.5°) in het Holoceen ijs, terwijl in het glaciaal ijs 36% van deze niet-geclassificeerde SKG's een grote misoriëntatiehoek (4.0°-6.5°) had. Voor dit verschil worden twee verklaringen gegeven: (i) schuiving langs de nieuw gevormde SKG's met een hoge misoriëntatiehoek in het glaciaal ijs resulteert in 'algemene' rotatieassen en (ii) meerdere schuifsystemen met verschillende rotatieassen waren betrokken in de vorming van de SKG's, wat leidde tot algemene rotatieassen (Hoofdstuk 3).

De data van misoriëntatiehoeken van de SKG's toonden aan dat alle SKG's die werden geanalyseerd een misoriëntatiehoek hadden van $<6.5^\circ$. In alle drie de diepte-intervallen waren SKG's met een kleine misoriëntatiehoek (0.5° - 2.0°) het meest voorkomend met het hoogste percentage in het Eemien-glaciaal faciës, gevolgd door het Holoceen en het glaciaal ijs. Deze verdeling van misoriëntatiehoeken kan worden verklaard met VGKM in het Holoceen ijs en vooral in het Eemien-glaciaal faciës, doordat VGKM veel SKG's consumeert voordat ze kunnen roteren in SKG's met een grote misoriëntatiehoek of korrelgrenzen (Hoofdstuk 3).

Data van de gemiddelde oriëntatiegradiënt van de korrels in de EBSD-afbeeldingen toonden aan dat er een duidelijk verschil is tussen de verschillende dieptes in de NEEM ijskern (Hoofdstuk 6). De gemiddelde oriëntatiegradiënt is relatief laag (1.0° - $1.5^\circ \text{ mm}^{-1}$) in het ondiepe monster van 413 m diepte van het Holoceen ijs en op 2241 m diepte in een fijnkorrelige laag in het Eemien-glaciaal faciës, terwijl de gemiddelde oriëntatiegradiënt veel hoger (2.5° - $3.5^\circ \text{ mm}^{-1}$) is in het midden en diepere gedeelte van het Holoceen ijs en van het glaciaal ijs. De toename van de gemiddelde oriëntatiegradiënt in het Holoceen ijs tussen 413 m en 718-889 m diepte komt overeen met een toename van VGKM, wat te zien is aan het meer onregelmatige korrelgrensnetwerk in het Holoceen ijs (Hoofdstuk 3). De lage gemiddelde oriëntatiegradiënt in het Eemien-glaciaal faciës is waarschijnlijk het resultaat van omvangrijke VGKM, wat wordt versterkt door de voorsmeltlaag langs de korrelgrenzen.

De analyse van LM-afbeeldingen en de EBSD dataset identificeerde een proces dat lijkt op microstructuurschuif in zeer fijnkorrelige sub-horizontale lagen in het glaciaal ijs (Hoofdstuk 6). Microstructuurschuif omvat korrelgrensschuiving (KGS) lang korrelgrenzen met dezelfde oriëntatie en de formatie van SKG's in de korrels die de schuiving langs de korrels blokkeren. Wanneer een kritische misoriëntatiehoek van ongeveer 5.0° - 6.0° is bereikt, is de SKG geroteerd tot een schuivende korrelgrens en wordt onderdeel van het korrelgrensnetwerk met dezelfde oriëntatie, wat fungeert als een positieve terugkoppeling op verdere korrelschuiving. De sterke clustering van c- en a-assen in de fijnkorrelige horizontale lagen suggereert dat KGS een accommoderend mechanisme is voor *basal slip* in het glaciaal ijs van de NEEM ijskern.

Resultaten modelleren van vloeiwetten

De samengestelde vloeiwet van Goldsby en Kohlstedt (1997, 2001) beschrijft de vervorming van ijs door middel van twee verschillende vervormingsmechanismen: dislocatiekruip en *basal slip* geaccommodeerd door KGS. De aanname voor beide mechanismen is dat *basal slip* het dominante vervormingsmechanisme is, dat ofwel wordt geaccommodeerd door *non-basal slip* (dislocatiekruip) ofwel door KGS (*KGS-gelimiteerde kruip*). De samengestelde vloeiwet werd aangepast voor een betere overeenkomst tussen de experimentele data voor dislocatiekruip en de berekende vervormingssnelheid voor dislocatiekruip (Hoofdstuk 4). De samengestelde vloeiwet werd ook aangepast om de nieuwe temperatuurdrempel van 262K, waarbij voorsmelten in polair ijs begint, in te

passen. Deze temperatuurdrempel werd gevonden na een onderzoek van ijs microstructuren vlak bij het smeltpunt in acht verschillende polaire ijskernen (Hoofdstuk 5). De aangepaste samengestelde vloeiwet werd samen met de vloeiwet van Glen (Glen, 1955; Paterson, 1994) gebruikt om de vervormingssnelheden te berekenen langs de NEEM ijskern, gebruikmakend van temperatuur- en korrelgrootedata van de NEEM ijskern, die werden verkregen door geautomatiseerde afbeeldingsanalyse van LM-afbeeldingen (Hoofdstuk 4). De korrelgrootte data van het Holoceen en glaciaal ijs werden beschreven door middel van een gemiddelde korrelgrootte en een volledige korrelgroottedistributie. De korrelgroottedistributie gaf de mogelijkheid om twee verschillende eindmodellen toe te passen: (i) het microschaal constante spanningsmodel, waarin elke korrel dezelfde spanning ervaart, maar met een andere snelheid vervormt en (ii) het microschaal constante vervormingsmodel, waarin elke korrel dezelfde vervormingssnelheid heeft, maar een andere spanning ondersteunt. De korrelgrootte in de Eemien-glaciaal faciës is zeer variabel door de diepte heen, door de stratigrafische onderbrekingen in dit gedeelte van de NEEM ijskern (NEEM community members, 2013), wat tot gevolg heeft dat het fijnkorrelige glaciaal ijs wordt afgewisseld door het grofkorrelige Eemien ijs. Door de zeer grote korrelgrootte in het Eemien ijs was het niet mogelijk om een volledige korrelgroottedistributie te bepalen, waardoor alleen een gemiddelde korrelgrootte kon worden gebruikt voor de berekening van de vervormingssnelheid die wordt geproduceerd door KGS-gelimiterde kruip.

De resultaten laten zien dat de vloeiwet van Glen een hogere vervormingssnelheid voorspelt dan de aangepaste samengestelde vloeiwet langs de gehele lengte van de NEEM ijskern (Hoofdstuk 4 en 5). De vloeiwet van Glen is onafhankelijk van korrelgrootte en laat een regelmatige toename in vervormingssnelheid met diepte zien als gevolg van een toename in temperatuur met diepte. In het Holoceen en glaciaal ijs is de voorspelde vervormingssnelheid van KGS-gelimiterde kruip ongeveer tien keer hoger dan de vervormingssnelheid die wordt voorspeld door dislocatiekruip (Hoofdstuk 4). De gemiddelde vervormingssnelheid die wordt voorspeld door de aangepaste samengestelde vloeiwet in het fijnkorrelige glaciaal ijs is vier tot vijf keer hoger dan in het meer grofkorrelige Holoceen ijs. De variatie van de vervormingssnelheid met de diepte, wat het gevolg is van een variatie in korrelgrootte, is relatief klein in het Holoceen ijs, maar is veel groter in het glaciaal ijs met twee pieken in vervormingssnelheid op ongeveer 1980 en 2100 m diepte. Het verschil tussen het microschaal constante spanningsmodel en het microschaal constante vervormingsmodel is relatief klein, waarbij het microschaal constante spanningsmodel een iets hogere vervormingssnelheid en een groter aandeel van KGS-gelimiterde kruip aan de totale vervormingssnelheid voorspelt.

Het Eemien-glaciaal faciës wordt waarschijnlijk beïnvloed door het effect van voorsmelten langs de korrelgrenzen (de voorsmeltlaag), waardoor korrelgrensprocessen zoals KGS en VGKM worden versterkt (Hoofdstuk 5). De aangepaste samengestelde vloeiwet voorspelt dat de vervormingssnelheid in het fijnkorrelige glaciaal ijs in de Eemien-glaciaal faciës ongeveer tien keer hoger is dan in de grofkorrelige Eemien lagen. De fijnkorrelige glaciale lagen vervormen vrijwel geheel door middel van KGS-

gelimiteerde kruip. In de grofkorrelige Eemien lagen is de bijdrage van dislocatiekruip en KGS-gelimiteerde kruip aan de totale vervormingssnelheid ongeveer gelijk, hoewel de berekende vervormingssnelheid van KGS-gelimiteerde kruip afhankelijk was van de gemiddelde korrelgrootte die was toegewezen aan de grofkorreligste lagen (30 mm).

Er is een sterke correlatie tussen de verandering in korrelgrootte en het type en de sterkte van de KVO in het Eemien-glaciaal faciës (Hoofdstuk 5). Het onzuivere glaciaal ijs is relatief fijnkorrelig (<5 mm in diameter) met een sterke enkel maximum KVO, terwijl het onzuiverheid-arme Eemien ijs bestaat uit grovere (>5 mm in diameter) en meer vervlochten korrels met meerdere maxima of gedeeltelijke gordel type KVO. Als gevolg van het verschil in KVO tussen het glaciaal en Eemien ijs is het de verwachting dat het fijnkorrelige glaciaal ijs voornamelijk vervormt door schuif (*simple shear*), wat de dominante vervormingsmodus is in dit deel van de NEEM ijskern, terwijl het grofkorrelige interglaciaal ijs voornamelijk vervormt door coaxiale deformatie of relatief stilstaand is. Het verschil in microstructuur, en als gevolg daarvan het verschil in viscositeit, tussen het glaciaal en interglaciaal ijs bij temperaturen net onder het vriespunt kan belangrijke consequenties hebben voor de dynamica van ijskappen dicht bij het gesteente. Het is de verwachting dat de voorsmeltlaag nauwelijks aan de horizontale snelheid bijdraagt wanneer hij bestaat uit onzuiverheid-arm interglaciaal ijs, terwijl het de verwachting is dat wanneer de voorsmeltlaag geheel uit onzuiver glaciaal ijs bestaat deze significant bijdraagt aan de horizontale snelheid (Hoofdstuk 5).

Synthese van de rekristallisatie- en vervormingsmechanismen in de NEEM ijskern

De relatief grove en onregelmatig gevormde korrels in het Holoceen ijs pleiten tegen KGS als een belangrijk accommoderend mechanisme voor *basal slip* (Hoofdstuk 6). In plaats daarvan wordt in het Holoceen ijs *basal slip* geaccommodeerd door middel van herstel via VGKM, wat de vervormings incompatibiliteiten verwijdert, waarna *basal slip* voort kan gaan. Analyse van schuifsystemen van SKG's (Hoofdstuk 2 en 3) toont echter aan dat een significante hoeveelheid *non-basal slip* wordt geactiveerd in het Holoceen ijs, zelfs in de monsters die wijdverbreid VGKM laten zien. Daarom wordt voorgesteld dat het Holoceen ijs vervormt door middel van *basal slip* geaccommodeerd door middel van herstel via VGKM en *non-basal slip*, waarbij de activering van *non-basal slip* wordt gereguleerd door de mate van VGKM. Microstructuuranalyse duidt erop dat de dominante rekristallisatiemechanismen en processen in het Holoceen ijs bestaan uit *bulging recrystallization*, *grain dissection* en VGKM. *Normal grain growth* is een belangrijk mechanisme in de bovenste 250 m van de ijskern. Rotatie rekristallisatie is naar verwachting relatief onbelangrijk in het Holoceen ijs.

De microstructuur in het glaciaal ijs wijst erop dat KGS een belangrijk accommoderend mechanisme is voor *basal slip*, in het bijzonder in de fijnkorrelige sub-horizontale lagen (Hoofdstuk 6). Analyse van schuifsystemen van SKG's toont echter aan dat een significante hoeveelheid *non-basal slip* wordt geactiveerd in het glaciaal ijs.

Daarom wordt gesuggereerd dat het vervormen van glaciaal ijs gebeurt door middel van *basal slip* geaccommodeerd door KGS en *non-basal slip*. De sterke clustering van c-assen in het glaciaal ijs, in het bijzonder in de fijnkorrelige sub-horizontale lagen, tonen aan dat KGS als een accommoderend mechanisme voor *basal slip* de KVO niet vernietigt maar versterkt. Het korrelgrensnetwerk toont aan dat VGKM relatief onbelangrijk is in het glaciaal ijs, terwijl rotatie rekristallisatie belangrijker is in het glaciaal ijs dan in het Holoceen ijs.

Het verwachte effect van korrelgrootte op vervormingssnelheid is zeer groot in het Eemien-glaciaal-faciës, met een ongeveer tien keer zo grote vervormingssnelheid in de fijnkorrelige glaciële lagen dan in de grofkorrelige Eemien lagen. De verandering in korrelgroottes correleert sterk met het type en de sterkte van de KVO in het Eemien-glaciaal faciës waarin de fijnkorrelige lagen een enkel maximum KVO hebben en de grofkorrelige lagen meerdere maxima of een gedeeltelijke gordel type KVO. Hierdoor is de verwachting dat de fijnkorrelige lagen voornamelijk vervormen door middel van schuif (*simple shear*) bij hoge vervormingssnelheden, terwijl de grofkorrelige lagen met veel lagere snelheden vervormen en nauwelijks bijdragen aan de horizontale snelheid van de ijsskap.

Het modelleren door middel van de aangepaste samengestelde vloeiwet (Hoofdstuk 4 en 5) voorspelt dat KGS-gelimiteerde kruip het dominante vervormingsmechanisme is langs vrijwel de gehele NEEM ijskern. De microstructuren geven echter aan dat dislocatiekruip het dominante vervormingsmechanisme is in het Holoceen ijs en in de grofkorrelige lagen in het Eemien-glaciaal faciës (Hoofdstuk 6). Tevens worden significante hoeveelheden *non-basal slip* geactiveerd langs de gehele NEEM ijskern (Hoofdstuk 2 en 3). Daarom wordt voorgesteld dat de aangepaste samengestelde vloeiwet de vervormingssnelheid als gevolg van dislocatiekruip onderschat. Deze onderschatting kan het beste verklaard worden door het ontbreken van dynamische rekristallisatiemechanismen en herstel door middel van VGKM tijdens de experimenten die werden gebruikt om de parameters te berekenen van de samengestelde vloeiwet van Goldsby en Kohlstedt (1997, 2001), terwijl deze mechanismen actief zijn in polaire ijsskappen en de vervormingssnelheid van dislocatiekruip versterken bij grote totale vervorming.

Appendices

Appendix A: EBSD sample preparation from ice core sections

A1. Remarks and preparations

The ice core sections that you want to process often need to be transported from partner ice core labs to the Alfred Wegener Institute (AWI) in Bremerhaven. Make sure that the ice core sections have arrived before you start working in the cold lab. The dry ice (solid carbon dioxide, -78.5°C) that is needed to transport the EBSD samples to Utrecht University should be ordered a couple of days before packing the EBSD samples (contact the AWI ice laboratory technician). About 15-20 kilos of dry ice is required to transport the EBSD samples by car to Utrecht University. The distance from Utrecht to the AWI in Bremerhaven is 350 kilometres and takes about three and a half to four hours by car.

The preparation of ten to fifteen EBSD samples out of one ice core section takes about two days. Make a planning in the beginning of the week and try to stick to it. Make sure that you include at least two or three breaks a day to warm up. It is best to take a break just after polishing (microtoming) the surface of an EBSD sample or thick section so that the surface can sublime during the break. It is not allowed to stay in the cold room unaccompanied for a long time. Wear a scarf or buff to protect the microtomed surface from the moisture (condense) coming from your breath. The pair of gloves that you are not wearing can be stored in the warm cabinet for measurement computers in the cold lab. Do not leave the gloves, the hat or the scarf on the working bench; they will be cold within minutes. If you have to stand behind the same working bench for some time, try to stand on a piece of styrofoam to insulate your boots from the cold metal floor. Pens don't work in the cold lab due to the low temperature, so using pencils is advisable.

Be aware that the cold rooms (-20°C) are a risky working place. Responsible behavior with respect to your own health and safety, but also to other's health and safety is expected. Never stay in the cold lab while feeling cold, the longer you stay in the cold lab while being cold, the longer it takes to recover. Be careful when handling the band saws or sharp microtome blades.

A2. Logging and cutting

Each ice core section is packed in a transparent plastic bag with the name of the ice core and the number of the ice core section written on it. Every bag and sample also have an arrow



Figure A1: Packed ice core sections (90 x 55 mm) from the NEEM ice core.

written on it, which indicates the top of the ice core. Make sure that you always know which part of the ice core section or EBSD sample is the top. Draw on the ice core section an arrow with a pencil to indicate the top of the ice core and draw an arrow with a black marker on the glass plates that are used when microtoming the surface. Also, make sure that the top of the ice core always points in the same direction when using the microtome, light microscope and storing of the sample.

In case of the NEEM ice core, each ice core unit is 55 cm long and is divided up into six parts of about 9 cm. The top part of each core section is labelled '10' and the sixth part is labelled '60'. When storing one of these 9 cm ice core sections, make sure to write down the name of the ice core, the number of the ice core section and the arrow that indicates the top of the ice core on the plastic bag. Use staples to close the bag when storing the 9 cm core section. This prevents the sample from sliding in the plastic bag.

If you start working with a 55 cm ice core section, the ice core section first needs to be cut into 6 parts of about 9 cm. The cutting is done using one of the bands saws in the cold lab. After having used the band saw, the housing of the band saw should be opened and the ice residue removed with a brush. Leave the housing open so that the residue that hasn't been removed with the brush can sublime away.

A3. Preparing the thick section

Ice core sections (thick sections) are polished using a microtome. A microtome consists of a sledge with a glass plate glued on top of it that can be pushed back and forth. This way, the stage moves beneath a sharp blade that scrapes away a thin layer of ice each repetition. The thickness of the layer that is scraped away can be controlled by a dial. Before using the microtome, it is advisable to spray some lubricant (e.g. WD-40) on the tracks and move the stage back and forth a couple of times to spread the lubricant. This will make it easier for the stage to slide over the tracks. It is



Figure A2: A microtome with a glass plate and an ice core section glued to it with the black cloth between the glass plate and the ice core section.

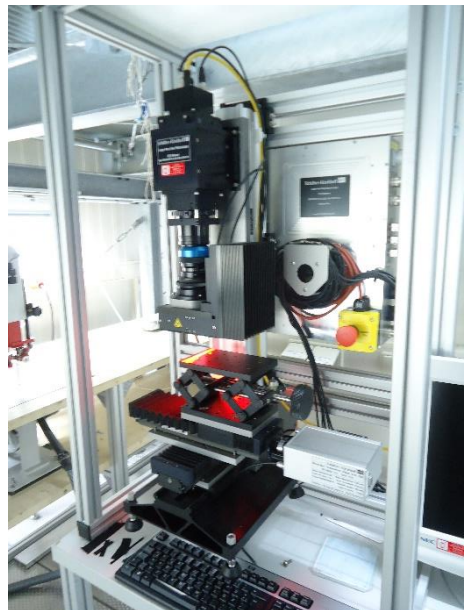


Figure A3: The large area scanning microscope (LASM).

important to replace the blade regularly, this will prevent scratches on the surface of the microtomed sample.

Take a piece of black cloth that has the same dimension as the surface of the thick section (roughly 9 by 6 cm). Take a glass plate with an arrow on it that indicates the top of the ice core and glue the glass plate to the stage of the microtome using a droplet of water on each of the four corners of the glass plate.

Whenever gluing, make sure that you suck the excess water back in the flask; this limits the amount of water that is used to glue the sample to the glass plate, which reduces the stress caused by the expansion of the freezing water turning into ice.

After securing the glass plate to the stage of the microtome, place the convex side of the thick section on top of the glass plate with the black cloth between the thick section and the glass plate. Move the stage carefully upwards till the thick section hits the blade and the surface of the thick section is parallel to the blade. Glue the thick section to the glass plate (not to the black cloth) at the top and the bottom of the thick section where the convex side touches the glass plate. When the thick section is glued to the glass plate with the surface parallel to the blade, lower the stage so that the stage can slide back and forth below the blade without the ice touching the blade. Start to raise the stage in steps of $\sim 30 \mu\text{m}$ each time you move the stage back and forth until the blade scratches away a thin layer of ice across the entire surface of the thick section. Each push of the sledge should be steady and continuous and while pulling the sledge back to the front, the stage should be lowered slightly to prevent the blade from damaging the surface of the thick section. To make sure that the microtomed surface of the thick section was not affected by previous sawing with the band saw, it is advised to microtome away about one millimetre of the surface of the thick section. Do this in steps of about $20\text{-}30 \mu\text{m}$. Use a brush to clean the blade regularly from the ice that scratches away during the microtoming. Make sure that the hairs of the brush do not touch the microtomed surface. The hairs will cause scratches that are clearly visible in the LM image. Decrease the step size to $10 \mu\text{m}$ and finish off with a few microtoming steps of $2\text{-}3 \mu\text{m}$. Make sure that the blade and the surface of the thick section is as clean as possible during the last microtoming steps. Sometimes the blade in the microtome is damaged, which caused scratches along the length of the surface of the thick section. In this case, the blade should be replaced and the surface of the thick section should be microtomed again till the scratches have disappeared.



Figure A4: The fabric analyser.

A4. Large area scanning microscope

The freshly microtomed surface of the thick section needs to sublime for 60 to 120 minutes to show the (sub)grain boundaries and other microstructural features. When the thick

section is subliming, place it under one of the plastic boxes to protect the surface from dust. The sublimation step of the thick section is a good moment to take a break and warm up. After the surface of the thick section has sublimed, the large area scanning microscope (LASM) image can be made. The top of the thick section should point to the right when making the LASM image. This way the top of the thick section aligns with the top of the LASM image. Adjust the focus so that the spikes of the greyscale are maximal. When the surface of the thick section is in focus, make a quick scan to see if the surface has sublimed long enough and whether the blade of the microtome didn't produce any artefacts. Check also the brightness of the LM image during this step. Then, make a LASM scan of the entire surface and save the image on the computer.

This is the moment to make a thin section for the fabric analyser to map the c-axes distribution. Keep in mind that making a thin section removes a layer of about one to two millimetres from the thick section. In case the thick section is thinner than about 10 millimetres, it is advisable to skip this step as the thick section will become too thin for making EBSD samples. Appendix B in Kerch (2016) provides a protocol for making thin sections and using the fabric analyser.

A5. Cutting EBSD samples

The LASM image of the thick section gives an indication of the grain size and shape, whereas the fabric analyser shows the c-axes orientation of the grains. Try to locate the areas of interest on the thick section and prepare the EBSD samples out of these areas.

EBSD samples are always cut with the surface of the sample parallel to the core axis. When sawing the EBSD samples, make sure that you write with a pencil a 'B' on the bottom side and a 'T' on the top side of the EBSD sample. This way you can still identify the microtomed surface and the orientation of the EBSD sample in case the EBSD sample tips over during transport or when mounting the EBSD sample on the stub holder (Appendix B). Also, whenever gluing an EBSD sample to a glass plate or to one of the metal boxes (for transport), make sure that you only glue the bottom side of the EBSD sample.



Figure A5: Sawing 8 mm thick bars perpendicular to the core axis.



Figure A6: Overview of the location of the EBSD samples in the 90 x 55 mm ice core section.

The bottom side of the EBSD sample is the side that sticks out when the EBSD sample is mounted on the stub holder, while the top side leans on the stub holder and should therefore be straight (Appendix B).

A handsaw is used to saw the thick section into cubes of roughly 8 x 8 mm (sample surface). Start off by sawing 8 mm bars perpendicular to the core axis. It is easiest to take a notepad with a 5 x 5 mm grid spacing and place the flat surface of the thick section on top of it. This will make it easier to saw the thick section into right-angled EBSD samples.

Also, the piece of paper can be used as a one to one overview of the thick section, which makes it easy to identify the location of an EBSD sample in the thick section later on.

Start by sawing the convex surface while gently pushing the thick section on the piece of paper. Be careful that the warmth coming from your hands does not partially melt the thick section when holding it in place. After having produced a couple of bars of ice (perpendicular to the core axis), the bars can be sawed into 8 mm x 8 mm blocks. The left and right side of the bars are too thin (due to the convex shape of the thick section) to use for EBSD sample preparation. Try to saw two or three samples (depending on the height of the bar) out of every 8 mm thick bar. Be careful when sawing these small EBSD samples, since they tend to crack and shoot away when too much force is applied when using the handsaw.

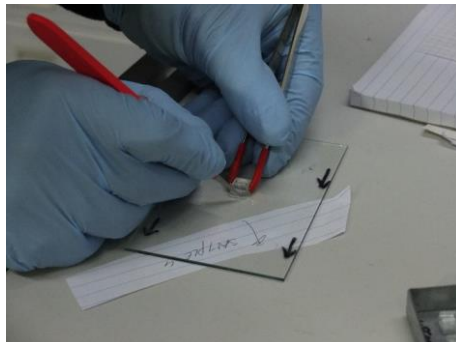


Figure A7: Removing the EBSD sample from the glass plate after microtoming the surface of the sample.

A6. Microtoming and sublimation

Glue the EBSD sample (8mm x 8mm) to a glass plate such that the convex side can be microtomed. Make sure that you only glue the bottom side of the EBSD sample. Continue to microtome the EBSD sample until the surface is level and the EBSD sample has a thickness of about 6 to 7 mm. Let the freshly microtomed EBSD sample sublime for about one hour. Then, turn the EBSD sample over so that you can microtome the surface for EBSD measurements. Continue to microtome the surface until the EBSD sample has a thickness of about 5 to 6 mm. The microtoming procedure is the same as explained in Section A3 where the step size is progressively decreased to steps of 2-3 μm . After having microtomed the surface of the EBSD sample, the EBSD sample needs to sublime for one to two hours. This is a good time to take a break and warm up. Remember that, whenever working with a microtomed surface, the rubber gloves should be worn and a scarf or buff to protect the surface of the EBSD sample from the condense coming from your breath.

A7. LM scan of the EBSD samples

A manual for using the light microscope is available and should lie next to the light microscope. Make sure that the top of the sample is aligned with the top of the LM image. The light microscope can also be focused below the surface of the EBSD sample. This can be useful when you are planning to do EDS measurements on the EBSD sample. This way the particles just below the surface can be mapped that can be revealed in the SEM after sublimation. A scan that is focused just below the surface can also be useful to determine the angle that grain boundaries make with respect to the surface of the EBSD sample.



Figure A8: Storing the EBSD samples in a metal box for transport to Utrecht University.

The light microscope takes a number of partly overlapping LM images of about 2 by 2 mm each. These images need to be stitched together to form one larger LM image of the entire surface of the EBSD sample. Check whether all microstructural features such as (sub)grain boundaries, shear bands and air bubbles are clear in the LM images. If these microstructural features are not clear, the EBSD sample should either be microtomed again or the surface of the EBSD sample should sublime longer.

A8. Packing of the EBSD samples

To protect the surface of the EBSD samples from sublimation and condensation, the EBSD samples need to be packed after the LM images have been made. If the EBSD samples remain unpacked in the lab overnight, they will over-sublime and the surface will become too irregular for proper EBSD mapping.

Take one of the small metal boxes provided by the AWI and make sure that the boxes are clean and that the relevant information such as the name of the ice core, the number of the ice core section, the number of the EBSD sample and top and bottom are written on the box with a permanent marker. Glue the EBSD samples (again, only on the bottom side) to the metal box. Then, gently close the box and wrap the box in two plastic zip-bags (bags that can be closed airtight). When closing the bag with the zipper, leave as little air in the bag as possible to minimize sublimation. Gently place the box on one of the shelves in the cold lab or place the box in the styrofoam box with dry ice.

A9. Transport of the EBSD samples

To transport the EBSD samples, they need to be packed in dry ice. Take a large styrofoam box and fill the lower third of the box with dry ice. Then, take the metal boxes containing

the EBSD samples and gently place them in the middle of the styrofoam box on top of the dry ice. The remainder of the dry ice can now be used to fill the styrofoam box. Due to the constantly subliming dry ice, the styrofoam box should never be closed airtight.

Place the box in the back of the car and make sure that the box cannot move or tip over during the ride. Place something heavy on top of the lid so that the lid is secure. Leave one of the windows of the car a bit open during the ride to make sure that the sublimed carbon dioxide gas can escape. As long as the lid stays on top of the styrofoam box, the dry ice doesn't fully sublime for a couple of days. When arriving at Utrecht University, the styrofoam box should be placed in the -20°C cold room. The cold room in the David de Wied (DDW) building at the Utrecht University science park (Uithof) is located on the sixth floor and is run by the Chemistry department.

References

Kerch, J. (2016) Crystal-orientation fabric variations on the cm-scale in cold Alpine ice: Interaction with paleo-climate proxies under deformation and implications for the interpretation of seismic velocities. PhD thesis, University of Heidelberg.

Appendix B: Cryo-EBSD on polar ice in a low pressure SEM

B1. Remarks and preparations

This Appendix follows up on Appendix A, which describes EBSD sample preparation from polar ice core sections. The methods described here are intended for cryo-EBSD studies using an FEI Helios Nanolab G3 UC equipped with an EBSD detector of Oxford Instruments HKL Technology (Abingdon, UK) and a Quorum Technologies Ltd. (Ringmer, UK) cryo-stage. The methods for EBSD sample transfer and EBSD mapping using different instruments might differ from the methods described here. Due to the size of the sledge and the size of the vacuum tube in the advanced transfer unit, it is important that the EBSD samples have the right dimensions of 8 mm x 8 mm (sample surface) by 5-6 mm (sample thickness). A day of cryo-EBSD work with this setup requires at least 50 liter of liquid nitrogen (LN). Temporarily heating of the system in absence of LN will destroy the ongoing experiment, so make sure that there is sufficient LN available at the beginning of the day.

There are three dewars that need to be refilled with LN regularly during the day: two smaller dewars that are attached on top of the preparation chamber and one larger dewar that is used for the heat-exchange-core that cools the nitrogen gas. Check and refill the dewars every one to two hours with LN. The temperature of the SEM stage will slowly rise if there isn't enough LN in the dewar to cool the heat-exchange-core.

In case the styrofoam box that is used to transport and store the EBSD samples (Appendix A) still contains dry ice (-78.5°C), the EBSD samples need to warm up from dry ice temperatures to -20°C. It takes about half an hour for the samples to heat up to -20°C, so this should be done before cooling down the cryo-stage in the morning. Simply place the metal box that contains the EBSD sample out of the styrofoam box in the -20°C cold room and start with cooling down the SEM stage and the preparation chamber. The metal box containing the EBSD samples should be kept in the plastic bags to avoid condensation depositing on the metal box or the EBSD samples.

B2. Installing the cryo-stage and cooling down the system

The cold trap and the cryo-stage of the SEM need to be installed at least one day before the start of the EBSD campaign. It takes a day for the vacuum pump to remove the moisture that deposits in the SEM chamber during the installation of the cryo-stage. If the EBSD sample is transferred to the SEM chamber just after installing the cryo-stage, the moisture in the chamber will deposit on the EBSD sample and the cold trap.

Flush the gas tubes with nitrogen gas at least 15 minutes before cooling down the system. Fill the preparation chamber dewars and the dewar for the heat-exchange-core with LN. Slowly lower the heat-exchange-core in the large dewar. Set the temperature of the cryo-stage to the desired temperature during SEM work (generally -150°C to -100°C) and set the temperature of the cold trap 20°C lower than the temperature of the cryo-stage. Due to the lower temperature of the cold trap, the moisture in the SEM chamber will deposit on the cold trap instead of on the EBSD sample or sample holder. Check regularly during EBSD mapping whether the cold trap and the cryo-stage are at the desired temperature. The temperature can be affected by the amount of LN in the dewars and possible leaks in the gas tubes.

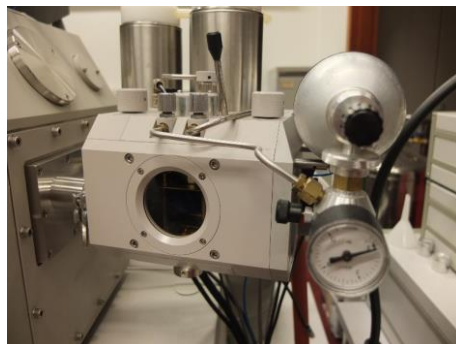


Figure B1: The preparation chamber with the two small dewars.

B3. Mounting the EBSD sample on the stub

All the material and equipment that come into contact with the EBSD sample or LN should be clean and dry. The LN that is used to transport and transfer the EBSD sample to the preparation chamber should be filtered using a piece of filter paper to remove the frost particles in the LN. Fill the thermos with filtered LN and close the lid of the thermos. Due to the constantly evaporating LN, the thermos should never be closed airtight. Take the thermos, a set of tweezers, a Stanley knife, the sledge, the plastic test-tube and thin gloves with rubber gloves over it to the cold room (-20°C) where the EBSD samples are stored. Preheat the sledge by keeping it in contact with your skin (below your watch for example).

When entering the cold room, start by placing the tweezers and the plastic test-tube on the table or shelves so that they can cool down to -20°C . Carefully remove the plastic bags from the metal box that contain the EBSD samples. Make sure to wear a scarf or buff to prevent your breath from contaminating the EBSD sample and always wear rubber gloves when handling the EBSD sample. Take the lid of the metal box and gently scrape away the gluing water of one of the EBSD samples with the Stanley knife while holding the EBSD sample in place with one of the tweezers. Place the warm (body temperature) sledge on top of one of the cold



Figure B2: The cryo-stage with the white tubes carrying the cooled nitrogen gas to the cryo-stage and the red and yellow wires for the thermometer. The cold trap is installed next to the pole piece.

metal boxes (-20°C) and wait for 35 to 40 seconds before placing the EBSD sample on top of the sledge. The heat from the sledge will melt the bottom part of the EBSD sample and will quickly refreeze when the heat from the sledge is conducted away via the cold metal box. Make sure to wait exactly 35 to 40 seconds before placing the EBSD sample on the sledge. Waiting not long enough will cause the bottom of the EBSD sample to melt too much, while waiting for too long will prevent the bottom part of the EBSD sample from melting at all. Make sure that the top of the EBSD sample (the side marked with a 'T', appendix A) is facing downwards on the pre-tilted stub. This way the upper part of the EBSD sample will be aligned with the upper part of the SEM images and the EBSD maps. Try to align the edge of the EBSD sample parallel with the edge of the stub. Even a small rotation of the EBSD sample relative to the stub will cause a severe distortion in the SEM images and EBSD maps when the sample is 70° tilted in the SEM.

Place the sledge in the test-tube and slowly lower the test-tube with the sledge in the thermos with filtered LN. If it turns out that other EBSD samples cracked during this procedure or during the transfer of the EBSD sample to the preparation chamber (Section B4), it is advisable to wait for 10-15 minutes to let the EBSD sample 'relax' before lowering the test-tube with the EBSD sample in the thermos with filtered LN. Screw the lid on top of the thermos with the string stuck between the lid and the thermos. Be careful that the string, and with it the sledge containing the EBSD sample, does not fall into the filtered LN. Close the metal box with the remaining EBSD samples and pack the metal box in the plastic bags to prevent further sublimation. Place the metal box back in the styrofoam box that contain the other EBSD samples.

The coarsest grained samples from the bottom part of the NEEM ice core (grain size of a couple of centimetres) tended to crack very easily when lowered in the thermos with filtered liquid nitrogen. The cracking is likely resulting from the difference in thermal contraction between the ice and the stub caused by the temperature shock. The stress that this difference in thermal contraction produces can induce cracks that can easily travel to the surface of the sample since the sample is probably only one grain thick. The finer grained samples (grain size a couple of millimetres) hardly ever cracked when lowered into the thermos with filtered liquid nitrogen. In case you want to do cryo-EBSD on course grained samples you can consider trying out a new method of sample transfer, such as the methods proposed by Prior et al. (2015).

B4. EBSD sample transfer to preparation chamber

Make sure that the tweezers and the gloves that you used in the cold room are heated up to room temperature and that the condensation and frost particles on them are removed. Also,



Figure B3: Mounting of the EBSD sample on the stub while holding the EBSD sample in place with a tweezer.

make sure that the transfer rod is lubricated with a drop of vacuum oil. Fill the styrofoam cup in the advanced transfer unit with filtered LN. Place the lid on top and pump down the advanced transfer until the filtered LN stops bubbling. Vent the system with nitrogen gas and prepare the transfer of the test-tube that contains the EBSD sample to the advanced transfer unit. The test-tube that contains the EBSD sample should be placed in the styrofoam cup with filtered LN. Try to do this as quickly as possible as the air condenses around the cold test-tube.

Take one of the clean and dry tweezers and place the sledge in the holder. Be careful while doing this, the EBSD sample can easily separate from the stub and fall into the filtered LN. Screw the tip of the transfer rod in the sledge. Evacuate the advanced transfer unit for about a minute before retracting the sledge into the vacuum tube. Close the vacuum tube after the rod is fully retracted. Take the advanced transfer unit and place it on the preparation chamber opening. Make sure that the EBSD sample is always facing upwards while doing this and does not touch the wall of the vacuum tube. Evacuate the air in the housing of the advanced transfer unit and open the first valve of the preparation chamber. Slide the sledge into the sledge holder of the preparation chamber.

B5. Sublimation and sample transfer to the SEM chamber

Depending on the amount of frost and condensation, the EBSD sample needs to sublime for about four to eight minutes at -90°C in the preparation chamber. Start with letting the EBSD sample sublime for about four minutes. Make sure that the valve between the SEM chamber and the preparation chamber is closed during sublimation so that the water molecules cannot enter the SEM chamber. Check during sublimation of the EBSD sample if the electron beam is switched off and if the cryo-stage and the cold trap are at the desired temperature. Open the second valve after four minutes and slide the sledge into the cryo-stage holder. Unscrew the transfer rod from the sledge, retract the rod and close both valves of the preparation chamber. Check whether the heater in the preparation chamber is switched off and whether the vacuum pump of the preparation chamber is switched on.

In most cases, four minutes of sublimation at -90°C is not enough to remove all the frost particles and condensation from the surface of the EBSD sample. In this case, the sledge should be retracted to the



Figure B4: The advanced transfer unit with the temperature regulators for the cryo-stage and the cold trap and an indicator for the SEM chamber pressure. Below is the turbo pump.

preparation chamber and the EBSD sample should sublime for a couple of more minutes at -90°C . Try to make sure that the EBSD sample does not sublime for too long in the preparation chamber, this will cause the surface of the EBSD sample, and particularly the grain boundaries, to become too irregular for proper EBSD mapping.

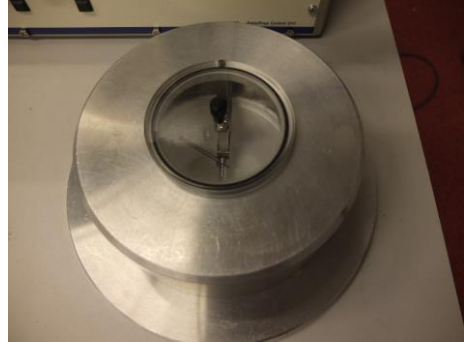


Figure B5: The advanced transfer unit when pumping down.

B6. SEM/EBSD work

The stage can be rotated in order to align the top of the EBSD sample with the tilt axis of the SEM. However, do not rotate the stage more than 5° in any direction since the tubes that carry the cooled nitrogen gas to the cryo-stage are stiff and can leak nitrogen gas if the stage is rotated too much. Before starting with SEM work, it is necessary to know the exact pre-tilt angle of the surface of the EBSD sample. Due to the melting and refreezing of the bottom of the EBSD sample during the mounting procedure (Section B3), the pre-tilt of the surface of the EBSD sample is often lower than pre-tilt of the stub, which is 23° . The tilt of the surface of the EBSD sample can be estimated by focusing the electron beam on the lower and upper part of the EBSD sample and using the y- and z-coordinates to calculate the pre-tilt according to:

$$\theta = \tan^{-1}(\Delta z/\Delta y), \quad (\text{A.1})$$

where θ is the pre-tilt of the EBSD sample, Δz is the difference in working distance and Δy is the difference in y-coordinate (sample length). This is the pre-tilt angle that should be used when tilting the EBSD sample to 70° and for the tilt correction.

Lower the stage to $z=0$ and switch off the beam before tilting the stage. The calculated pre-tilt and the tilt of the stage should add up to 70° for EBSD. Tilt the stage in steps of 10° and watch the stage and the EBSD sample with the CCD camera during tilting. When the stage is fully tilted, the EBSD detector can be driven in. Make a number of SEM images at different magnitudes of the area that you want to map using EBSD.

The optimum SEM conditions for cryo-EBSD on ice are: a stage temperature of -150°C to -100°C , a cold trap temperature 20°C lower than the stage temperature, a working distance of 6-12 mm, a beam current of 2.1-8.4 nA, an accelerating voltage of 7.5-20 kV and a SEM chamber pressure of 10^{-7} - 10^{-5} hPa. The optimum EBSD collection conditions are binning of 1x1 to 4x4, a step size of 5-20 μm , a frame averaging of 1-2 and static and auto background switched on.

Often, the surface of the EBSD sample suffers from drifting and charging during EBSD mapping. The following settings can be adjusted to reduce charging of the surface: increase the stage temperature, increase the tilt of the stage, reduce the accelerating voltage, reduce the dwell time or defocus the beam. In most cases, defocusing the beam is the best option to try first, since the resolution that is lost due to defocusing is irrelevant for the

coarse grained ice. Due to the coarse grain size of polar ice, the processed EBSD maps are often stitched together for microstructural analysis. Therefore, it is advisable to use step sizes of 5 μm , 10 μm , 15 μm or 20 μm , since maps with these step sizes can easily be stitched together later. It is also advisable to save the EBSD patterns as these can later be used for HR-EBSD or re-indexed to improve the angular resolution of the EBSD maps.

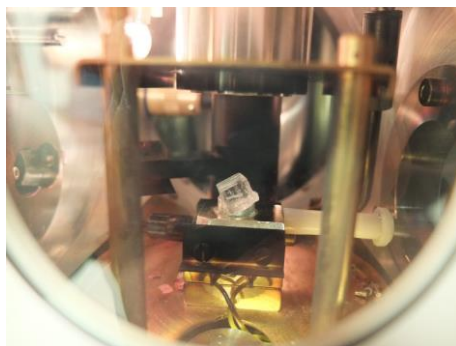


Figure B6: View through the glass of the preparation chamber with the EBSD sample mounted on the pre-tilted stub.

B7. Removal of the EBSD sample and heating up the system

When finished with EBSD mapping, retract the EBSD detector first. Lower the stage to $z=0$ and tilt the stage back in steps of 10° while monitoring the EBSD sample using the CCD camera. Set the stage to home position ($x=0$, $z=0$) and switch off the electron beam. Place the housing of the transfer unit on the preparation chamber and evacuate the air. Open the first valve and wait for ten seconds till the air in the preparation chamber is evacuated. Open the second valve and retract the sledge using the transfer rod. Close both valves before removing the advanced transfer unit from the preparation chamber. Check whether the turbo pump that evacuates the preparation chamber is switched on.

Before leaving, the system needs to heat up. Start by taking the heat-exchange-core out of the dewar filled with LN. Be careful not to leak water droplets (from condensation) on the equipment and instruments in the SEM room. The cold trap releases the condensation that was deposited during the EBSD mapping when it reaches a temperature of about -30°C . When the cold trap releases this moisture, the SEM chamber pressure increases rapidly. Stay to monitor the SEM chamber pressure until the cold trap has released the water vapour. It often happens that the system suspects a leak when the cold trap releases the water vapour and starts to vent the SEM chamber. If this happens, the SEM chamber should be evacuated immediately. You can leave when the temperature of the cryo-stage and cold trap is above 0°C and the chamber pressure in the SEM is stable.

References

Prior, D. J., Lilly, K., Seidemann, Vaughan, M., Becroft, L., Easingwood, R., Diebold, S., Obbard, R., Daghlian, C., Baker, I., Caswell, T., Golding, N., Goldsby, D., Durham, W. B., Piazzolo, S., Wilson, C. J. L. (2015) Making EBSD on water ice routine. *Journal of Microscopy*, 00, 0, 1-20, doi: 10.1111/jmi.12258.

Appendix C: Terminologies describing ice microstructures in different fields

The metallurgy, geological and glaciological communities all use a slightly different terminology to describe a certain microstructure or microstructural process. This appendix gives an overview of the most important terms in these three fields of science, in order to avoid confusion about which term is used for which microstructural process. Several key publications in each of the three fields of science were used for this overview. The superscripts (1-7) refer to the reference of each definition. The terminology from the metallurgy community was taken from Humphreys and Hatherly (2004)¹.

The geological terminology was taken from Drury and Urai (1990)², De Meer et al. (2002)³ and Passchier and Trouw (2005)⁴, while the glaciology terminology was taken from Alley (1992)⁵, Schulson and Duval (2009)⁶, Faria et al. (2014)⁷. Throughout this thesis, the most appropriate terminology has been used, which are the underlined terms in this appendix. For the case of basic dislocation structures and processes the original materials science terminology is preferred. For the case of recrystallization mechanisms, a combination of the geological and glaciology terminology was used to describe ice microstructures and microstructural processes. Terms such as fabric and texture, which have different meanings in the different fields of science, were avoided.

C1. Material science terminology

Annealing: ¹*Recovery and static recrystallization* by thermally activated processes induced by passive heating of a previously deformed material.

Continuous (dynamic) recovery/recrystallization: See *recovery/recrystallization*.

Discontinuous (dynamic) recovery/recrystallization: See *recovery/recrystallization*.

Dynamic recovery/recrystallization: See *recovery/recrystallization*.

Geometric dynamic recrystallization: ¹This mechanism involves the formation of new grains from the original high-angle grain boundaries once the original grains have flattened to approximately the diameter of the subgrain size, without involvement of rotation recrystallization.

Grain boundary migration (GBM): ¹The migration of a grain boundary through a crystal removing dislocations and subgrain boundaries, often at relatively high temperature. The driving force for *grain boundary migration* can be driven by the curvature of energetic grain boundaries or the reduction in stored strain energy.

Grain growth: ¹The elimination of small grains by the growth of larger grains. The qualifiers *discontinuous* and *continuous* denote phenomena occurring throughout the material that are distributed heterogeneously and uniformly, respectively.

Microstructure: ¹Grain size, grain shape, internal structure within grains and arrangement of grains in a polycrystal.

Nucleation: ¹Recrystallization processes involving the formation of a new nuclei (tiny strain free new grains).

Recovery: ¹The annihilation and rearrangement of dislocations. The qualifiers *dynamic* and *static* denote recovery phenomena occurring *during* and *prior/after* deformation, respectively. The qualifiers *discontinuous* and *continuous* denote phenomena occurring throughout the material that are distributed heterogeneously and uniformly, respectively.

Recrystallization: ¹The formation of new dislocation-free grains within a deformed or recovered structure, which grow and consume the old grains resulting in a new grain structure with low dislocation density. Recrystallization can occur *during* the processes of deformation (*dynamic*) or during annealing *following* deformation (*static* or *annealing recrystallization*). To refer to the continuity of the process, the terms *discontinuous* and *continuous* are used.

Polygonization: ¹The organization of geometrically necessary dislocations by recovery into a 2D structure (dislocation wall).

Strain induced (grain) boundary migration (SIBM): ¹Bulging of part of a pre-existing grain boundary, leaving a region behind the migrating boundary with a lower dislocation content.

Static recovery/recrystallization: See *recovery/recrystallization*.

Texture: ¹Statistically preferred orientation of the crystalline lattices of a population of grains.

C2. Geological terminology

Bulging recrystallization (BLG): ⁴Also called *low-temperature grain boundary migration*. Bulging of a grain boundary into a crystal with high dislocation density and formation of new, independent small crystals.

Crystallographic preferred orientation (CPO): ²Statistically preferred orientation of the crystalline lattices of a population of grains.

Classical nucleation recrystallization: ²During *classical nucleation recrystallization* a cluster of atoms spontaneously takes on a new orientation owing to the action of thermally activated fluctuations.

Continual recrystallization: See *recrystallization*.

Discontinual recrystallization: See *recrystallization*.

Dynamic recovery/recrystallization: See *recovery/recrystallization*.

Fabric: ⁴The complete spatial and geometrical configuration of all those components that make up a rock. It covers concepts such as *texture*, *structure* and *crystallographic preferred orientation*.

General recrystallization mechanisms: ²Mechanisms at which both *grain boundary migration* and *new grain boundary formation* are involved in the transformation of the microstructure.

Grain boundary migration (GBM): ^{2,4}The migration of grain boundaries with respect to a material point driven by the reduction in stored strain energy. Involves the transfer of material across the boundary.

Lattice preferred orientation (LPO): See *crystallographic preferred orientation*.

Microstructure: See *texture*.

Migration recrystallization: ²Recrystallization dominated by *grain boundary migration*.

Nucleation: ⁴Recrystallization processes that involves the formation of a new nuclei that is relatively strain-free.

Polygonization: ⁴The glide and climb of dislocations during *static* or *dynamic recovery* into a planar array forming a *subgrain boundary*.

Recovery: ⁴Processes that lead to a decrease in the total length of dislocations and rearrangement of dislocations into subgrain boundaries. The qualifier *dynamic* is used to refer to *recovery* during active deformation, while the qualifier *static* is used to refer to *recovery* prior/after deformation.

Recrystallization: ²Reworking of material with a change in grain size, shape and orientation within the same mineral. *Recrystallization* is divided into *rotation mechanisms*, *migration mechanisms* and *general recrystallization mechanisms* which involve both processes. The qualifier *dynamic* is used to refer to *recrystallization* during active deformation (including *bulging recrystallization*, *subgrain rotation recrystallization* and grain boundary migration), while the qualifier *static* is used to refer to *recrystallization* prior/after deformation. To refer to the continuity of the process, the terms *continual/discontinual* are used.

Rotation recrystallization: ^{2,3}Also called *continual recrystallization*. The dominant processes involved in transformation of the microstructure is the formation of new high angle grain boundaries either by progressive rotation of subgrains or by subgrain boundary migration in a region of lattice curvature.

Static recovery/recrystallization: See *recovery/recrystallization*.

Structure: ⁴The presence of compositional layering, folds, foliation, lineation, etc.

Subgrain rotation recrystallization (SGR): See *rotation recrystallization*.

Texture: ⁴Also called *microstructure*. The geometrical aspects of the component particles of a rock including size, shape and arrangement.

C3. Glaciology literature

Classical nucleation: See *nucleation*.

Continuous (dynamic) recrystallization: See *recrystallization*.

Crystal orientation fabric (COF): See *fabric*.

Crystallographic preferred orientation (CPO): See *fabric*.

Discontinuous (dynamic) recrystallization: See *migration recrystallization*.

Dynamic grain growth (DGG): ⁷Class of phenomenological processes of grain coarsening in polycrystals during deformation.

Dynamic recrystallization: ⁷See *recrystallization*.

Fabric: ⁶Also called *lattice preferred orientation (LPO)*, *crystallographic preferred orientation (CPO)*, *crystal-orientation fabric (COF)*, *c-axis fabric* or *texture*. Statistically preferred orientation of the crystalline lattices of a population of grains. For ice, almost always only the c-axes orientations are meant by these terms.

Grain boundary migration: ⁷The migration of a boundary with respect to material points. Includes both *normal grain growth* and *strain induced boundary migration (SIBM)*.

Lattice preferred orientation (LPO): See *fabric*.

Microstructure: ⁷Collection of all microscopic deformation related structures, inclusions, and the orientation stereology of a polycrystal.

Migration recrystallization: 1) ⁶Also called *discontinuous (dynamic) recrystallization*. The rapid migration of grain boundaries between dislocation-free nuclei and deformed grains, inducing a new orientation of grains. Occurs at high temperatures of $>-15^{\circ}\text{C}$.

2) *Strain induced grain boundary migration (SIBM)*. ⁷Grain boundary motion driven by stored strain energy.

Normal grain growth (NGG): ⁷Phenomenological recrystallization process of grain coarsening in polycrystals, driven by the curvature of energetic grain boundaries. Tends to reduce the grain boundary area per unit volume.

Nucleation: ⁷Class of phenomenological recrystallization processes involving the formation of a new nuclei (tiny strain free new grains). During *classical nucleation* a cluster of atoms/molecules forms under the action of high internal stresses and thermally-activated fluctuations. During *pseudo-nucleation* a special combination of elementary recrystallization processes (e.g. SIBM, subgrain rotation and growth) takes place within a small crystalline region with high stored strain energy giving rise to a small strain-free grain.

Polygonization: 1) ⁷Special type of recovery mechanism for the formation of tilt boundaries. In ice, polygonization is often used in reference to the bending of basal planes.

2) ⁵The formation of new grains by subdividing the old grains by the reorganization of dislocations into *subgrain boundaries* and eventually into *grain boundary*.

Pseudo-nucleation: See *nucleation*.

Recovery: ⁷Release of the stored strain energy by any thermo-mechanical process of microstructural change other than *recrystallization*. The qualifiers *dynamic* and *static* denote recrystallization phenomena occurring *during* and *prior/after* deformation, respectively.

Recrystallization: ⁷Any re-orientation of the lattice caused by grain boundary migration and/or formation of new grain boundaries (*rotation recrystallization*). The qualifiers *dynamic* and *static* denote recrystallization phenomena occurring *during* and *prior/after* deformation, respectively. To refer to the continuity of the process, the terms *continuous/discontinuous* are used.

Rotation recrystallization (RRX): ⁷Phenomenological recrystallization process responsible for the formation of new *grain boundaries*.

Static recrystallization: See *recrystallization*.

Strain induced (grain) boundary migration (SIBM): ⁷Elementary recrystallization process of grain boundary motion driven by minimization of the stored strain energy. Defined as *SIBM-N* when the formation of a new grain (*nucleus*) is involved or *SIBM-O* when no formation of a new grain is involved.

SIBM-N: See *strain induced boundary migration and nucleation*.

SIBM-O: See *strain induced boundary migration*.

Texture: See *fabric*. ⁵*Texture* is sometimes used to denote grain size, shape and orientation.

References

⁵Alley, R. B. (1992) Flow-law hypothesis for ice sheet modeling. *Journal of Glaciology*, 38, 129, 245-256, doi: 10.1017/S0022143000003658.

³De Meer, S., Drury, M. R., De Bresser, J. H. P., Pennock, G. M. (2002) Current issues and new developments in deformation mechanisms, rheology and tectonics. Geological Society, London, Special Publications, 200, 1-27, doi: 10.1144/GSL.SP.2001.200.01.01.

²Drury, M. R., Urai, J. L. (1990) Deformation-related recrystallization processes. *Tectonophysics*, 172, 235-253.

⁷Faria, S., Weikusat, I., Azuma, N. (2014) The microstructure of polar ice. Part II: State of the art. *Journal of Structural Geology*, 61, 21-49, doi: 10.1016/j.jsg.2013.11.003.

¹Humphreys, F. J., Hatherly, M. (2004) *Recrystallization and Related Annealing Phenomena*. Elsevier, 574 pages.

⁴Passchier, C. W., Trouw, R. A. J. (2005) *Microtectonics*, Springer, Berlin.

⁶Schulson, E. M., Duval, P. (2009) *Creep and Fracture of Ice*. Cambridge University Press.

Afterword/Acknowledgements

En dan is het opeens zo ver: het schrijven van het dankwoord. Het is alweer bijna vijf jaar geleden dat ik, terwijl ik nog druk bezig was met mijn masterscriptie, solliciteerde voor deze promotieplek. Ik had in de vacature gezien dat het onderzoeksgebied op de grens van geologie en klimatologie lag, wat toevallig de twee richtingen van mijn bachelor en master waren. Stiekem werd mijn interesse toch ook wel versterkt doordat er een mogelijkheid was om mee te gaan op een expeditie naar Groenland en/of Antarctica. Nu realiseer ik me dat de laatste vijf jaar mij zoveel meer hebben gebracht dan ik me op dat moment kon bedenken. Ik ben ontzettend dankbaar voor de vrijheid en mogelijkheden die ik heb gekregen om met veel 'trial and error' een schat aan kennis en ervaring op te doen en ben blij dat ik door middel van dit proefschrift mijn steentje heb kunnen bijdragen aan de (klimaat)wetenschap. Zonder de hulp, steun en expertise van mijn familie, (co)promotoren, collega's en vrienden was me dit nooit gelukt en daarvoor ben ik bijzonder dankbaar.

Allereerst wil mijn promotor **Martyn** bedanken. My sincerest thanks for all your efforts, Martyn. In the beginning of my PhD project I had to get used to the freedom that you gave me, but after almost five years I realize that this is the best way to become a scientist and develop a scientific attitude. I learned a lot from you in countless aspects like geology, material science, scientific writing, but most of all the scientific method in general. You always made time to discuss data and results and could, like no other, provide me with new insights. Many thanks for supervising my PhD project.

Hans. Bedankt voor al je hulp, in het bijzonder bij het ontwikkelen en afronden van de twee composite flow law hoofdstukken. Jouw inzicht en hulp bij dit onderdeel van mijn proefschrift was onmisbaar en zelfs bij de laatste versies van deze hoofdstukken wist je toch nog nét die paar verbeterpunten te vinden. Ondanks dat je zo druk bent lukte het je toch altijd om tijd vrij te maken bij het afronden van mijn proefschrift. Heel erg bedankt hiervoor.

Gill. Many thanks for your countless hours of help with the SEM and data analysis in the beginning of my PhD project. Without that I would never have been able to acquire the skill set that I needed to finish this project. Also, many thanks for proofreading so many different versions of all the chapters of this PhD thesis. Your attention to detail was essential while writing this PhD thesis.

Auch einen großen Dank an **Ilka**. Während der vergangenen fünf Jahre warst du ein essenzielles Bindeglied zwischen Glaziologie und (Struktur) Geologie. Ich bewundere deine Hingabe für deine Forschung und bin dankbar für die Zeit die du dir für mich, und auch die anderen Doktoranden unserer Gruppe genommen hast. Während unserer 'Gruppentreffen' in Tübingen, Heidelberg, Bremerhaven und Utrecht hast du immer für eine entspannte und familiäre Atmosphäre gesorgt. Darüber hinaus bin ich besonders dankbar dass du es mir ermöglicht hast Felderfahrung in den Alpen und im EastGRIP

letzten Sommer zu sammeln. Ich habe beide Expeditionen sehr genossen.

Many thanks to **Chris, Matthijs** and **Sergei** for helping me countless times with the electron microscope. Without your insights, help and repairs of the SEM I would never have been able to do my lab work at the UU.

All people from the Structural Geology and Tectonics group at the UU, **David, Oliver, Maartje, Markus, Leo, Vasileios, Yang, Maartje, Herman, Helen, Reinout, Magda, Arjen, Nina, Paul, Claudia** and so many more. Thanks for being such nice colleagues! I enjoyed our (scientific) discussions, group meetings and the beers we had together a lot.

To my PhD colleagues from the 'Helmholtz Junior Research Group' **Gema, Johanna, Jan** and **Florian**. I am proud of what we have achieved during the years that we worked together. Each of us approached the study of ice deformation from a different angle and I learned a lot from each of you. I also enjoyed the group meetings in Tübingen, Bremerhaven, Heidelberg and Utrecht a lot!

Daniela, Tobias, Nico, Pia and **Madda**. Many thanks for the nice cooperation during the last years and during my stay at EastGRIP.

Bas. Bedankt voor al je hulp en het samenwerken tijdens de eerste jaren van mijn master. Ik kijk met erg veel plezier terug op onze fietstocht naar Rome een paar jaar geleden.

Beste **Keitjes**, bedankt dat ik zo fijn bij jullie heb kunnen wonen in de eerste paar jaar van mijn promotie onderzoek.

Roel, Elke, Matthijs, Nard, Willem, Hanna en **Linde**. Bedankt voor het geweldige bestuursjaar, alle mooie en vooral ook grappige herinneringen. Elke (Elke! Elke!) keer als we elkaar weer zien voelt het als vanouds. Wat mij betreft blijven we nog jaren lang elk jaar weer op bestuursweekend gaan. Ook bedankt namens Nico en Jos!

Koen, Lex, Johanna and **Marieke**. You introduced me to climate activism during those many Friday afternoon working sessions in the UU library. I learned a lot from you guys and your energy and positive attitude inspired me to stay active in the climate movement.

Joris. Wat een mooie tocht hebben we in Nepal gemaakt om het Annapurna massief. Ik waardeer dat je nooit moe wordt van mijn verhalen over klimaat en duurzaamheid. Daarnaast is het fijn dat er altijd iemand is die me regelmatig herinnert aan die ene rode kaart die ik ooit heb gepakt ;-). Bedankt dat je mijn paranimf wilde zijn!

Dear **Alex**. What an asset to have some Australian 'laid back' mentality in the family. It's great to see how easily you've found your way in Amsterdam and how (seemingly) easily you've completed your master's. I hope I can borrow your PlayStation for a while after I'm finished with this PhD project ;-).

Beste **Ev**. Wat fijn dat Wiets zo'n geweldig reismaatje heeft gevonden. Ik bewonder hoe gemotiveerd je bent om jezelf altijd maar te blijven ontwikkelen en je de ene na de andere cursus en studie succesvol afsluit. ευχαριστώ που είμαι ο φωτογράφος κατά τη διάρκεια της υπεράσπισης του PhD!

Beste **Vin, Cato** en **Sam**. Wat word ik altijd vrolijk als ik jullie samen in ABC of Velp

zie. Jullie energie en vrolijkheid werkt aanstekelijk. Sam en Cato, jullie boffen maar met zo'n chille vader!

Lot. Ik kijk met heel veel plezier terug op ons weekje touren in 'the meth machine' in Tasmanië! Bedankt nog dat je me er toen regelmatig aan herinnerde dat ze links rijden in Australië ;-). Wat knap dat het je allemaal zo goed af gaat in je opleiding tot advocaat!

Wiets. Wat mooi om te zien dat je samen met Ev de ene na de andere reis maakt. Je open en nuchtere karakter waardeert ik enorm. Fijn dat onze band de laatste jaren zo sterk is geworden! Heel erg bedankt dat je mijn paranimf wilde zijn.

Jus. Mijn promotie-maatje binnen de familie. Nu ik zelf een proefschrift heb geschreven, heb ik nóg meer bewondering gekregen voor hoe jij dat twee jaar geleden hebt gedaan naast je nieuwe baan, zorgen voor Cato en zoeken naar een nieuw huis. Ik bewonder hoe goed het je allemaal af gaat en dat je zo'n leuke moeder bent voor Sam en Cato!

Als laatste wil ik mijn ouders **Hans** en **Paula** bedanken. Ik had me geen fijnere en onbezorgdere jeugd kunnen wensen. Bedankt voor alle mogelijkheden die jullie me hebben gegeven om te studeren, reizen, sporten en zoveel meer! Ook bedankt voor jullie steun tijdens het schrijven van dit proefschrift, ik had het zo nu en dan zeker nodig...

Mams. Altijd meedenken, gevraagd en ongevraagd (als ik weer eens te eigenwijs ben) advies geven. Je stabiliteit en je positieve kijk op het leven waren, en zijn nog steeds, onmisbaar voor me. Je weet hoe en wanneer je me een zetje in de juiste richting moet geven. Ook nog bedankt voor het doorsturen van de vacature voor deze promotieplek vijf jaar geleden :-).

Pa. Je interesse in mijn onderzoek (*oud ijs glijdt beter*), humor, stabiliteit en altijd nuchtere blik op de wereld zijn ontzettend belangrijk voor me. Er is niemand met wie ik zoveel gemeen heb als jij. Onze gezamenlijke passie voor wetenschap, reizen, fietsen en lange gesprekken over van alles en nog wat koester ik. Je bent en blijft altijd *daddy cool*.

Lieve **Pa** en **Ma**, dit proefschrift is voor jullie.

Curriculum Vitae

Sept 2000 to Aug 2006	Atheneum. Profiel: Natuur & Gezondheid. Arentheem college, Arnhem
Sept 2007 to Aug 2011	Bachelor of Science (BSc) in 'Earth Sciences' Dept. of Earth Sciences, Utrecht University
Sept 2011 to May 2014	Master of Science (MSc) in 'Meteorology, Physical Oceanography and Climate' Dept. of Physics, Utrecht University
Mar 2014 to Feb 2019	PhD candidate Dept. of Earth Sciences, Utrecht University

Ernst-Jan Nicolaas Kuiper was born on the 26th of April 1988 in Rheden, Gelderland, the Netherlands. After finishing his Athenaeum at the Arentheem College in Arnhem in 2006 he travelled for eight months in South America with a friend. The next year he moved to Utrecht to study Earth Sciences at Utrecht University. He completed his BSc degree in 2011 on a thesis entitled "Changes in the binding capacity of heavy metals by soil organic matter due to climate change in the Netherlands" supervised by Dr. Marcel van der Perk. In September 2011 he started with the MSc programme "Meteorology, Physical Oceanography and Climate" at the department of Physics at Utrecht University. His MSc thesis, entitled "The effect of bromine chemistry on tropospheric ozone concentration using a modified CB05 approach", was written at the Royal Netherlands Meteorological Institute (KNMI) and supervised by Thomas Röckmann, Geert-Jan Roelofs and Jason Williams. Afterwards he started with a PhD research as part of the Helmholtz Junior Research group 'The effect of deformation mechanisms for ice sheet dynamics', which culminated in the present thesis.

List of publications

As of 21 December 2018.

Manuscripts in preparation:

Kuiper, E. N., Drury, M. R., Pennock, G. M., de Bresser, J. H. P., Weikusat, I.
Recrystallization and deformation mechanisms in the NEEM deep ice core, Greenland.

Kuiper, E. N., Pennock, G. M., Kilian, R., de Bresser, J. H. P., Weikusat, I., Drury, M. R.
Variation in non-basal slip activity controlled by strain induced migration in the NEEM deep ice core, Greenland.

Manuscripts submitted:

Kuiper, E. N., Weikusat, I., de Bresser, J. H. P., Jansen, D., Pennock, G. M., Drury, M. R.
Using a composite flow law to model deformation in the NEEM deep ice core, Greenland:
Part 1 the role of grain size and grain size distribution on the deformation of Holocene and glacial ice.

Kuiper, E. N., de Bresser, J. H. P., Drury, M. R., Eichler, J., Pennock, G. M., Weikusat, I.
Using a composite flow law to model deformation in the NEEM deep ice core, Greenland:
Part 2 the role of grain size and premelting on ice deformation at high homologous temperature.

Papers published:

Steinbach, F., **Kuiper, E. N.**, Eichler, J., Bons, P. D., Drury, M. R., Grier, A., Pennock, G. M., Weikusat, I. (2017) The relevance of grain dissection for grain size reduction in polar ice: insights from numerical models and ice core microstructure analysis. *Frontiers in Earth Science*, 5, 66, 1-19, doi: 10.3389/feart.2017.00066.

Weikusat, I., **Kuiper, E. N.**, Pennock, G. M., Kipfstuhl, S., Drury, M. R., (2017) EBSD analysis of subgrain boundaries and dislocation slip systems in Antarctic and Greenland Ice. *Solid Earth*, 8, 5, 883-898, doi: 10.5194/se-8-883-2017.

